ELECTRON-PHONON INTERACTION

EFFECTS OF THE ELECTRON-PHONON INTERACTION IN HEXAGONAL CLOSE-PACKED METALS

By

PAUL THOMAS TRUANT, B.Sc., M.Sc.

A Thesis

Submitted to the School of Graduate Studies

in Partial Fulfilment of the Requirements

for the Degree

Doctor of Philosophy

McMaster University

March 1972

DOCTOR OF PHILOSOPHY (1972) McMASTER UNIVERSITY
(Physics) Hamilton, Ontario.

TITLE: Effects of the Electron-Phonon Interaction in Hexagonal Close-Packed Metals

AUTHOR: Paul Thomas Truant

B.Sc. (University of British Columbia)

M.Sc. (University of British Columbia)

SUPERVISOR: Professor J. P. Carbotte

NUMBER OF PAGES: v, 241

SCOPE AND CONTENTS:

A unified approach, employing effective phonon frequency distributions, is used to investigate effects of phonon anisotropy in the hcp metals.

Phonon information is included by means of empirical force constant models, and pseudopotentials are used to describe the electron-ion interaction.

Zinc and thallium superconducting gaps are determined as a function of position on the Fermi surface. The gap anisotropy is used to calculate thermodynamic properties.

The normal state electron-phonon mass enhancement and the imaginary part of the electron self-energy are calculated as a function of temperature and Fermi surface position. Anisotropic transport scattering times are defined, calculated and used to obtain the polycrystalline and single crystal resistivities. Comparison is made with resistivities obtained by the variational approach.

ACKNOWLEDGEMENTS

I wish to thank Dr. J. P. Carbotte, my research supervisor, for his patient guidance and constant encouragement.

I also wish to thank Dr. C. R. Leavens for his help during the preliminary stages of this work, and Mr. B. Hayman for many interesting discussions.

Many thanks go to Miss Erie Long for typing the manuscript, and Mrs. Danielle Grange for her assistance in preparing the drawings.

The financial assistance of the National Research Council and the McMaster Physics Department is gratefully acknowledged.

TABLE OF CONTENTS

CHAPTER I

INTRODUCTION

1.1 HISTORICAL INTRODUCTION - SUPERCONDUCTIVITY

The liquefaction of helium in 1908 by H. K. Onnes led to his discovery in 1911 of superconductivity in mercury [1]. For the next four decades the understanding of this phenomenon was based on thermodynamic and phenomenological arguments. In 1933 Meissner and Ochsenfeld [2] observed that a bulk superconductor expels a magnetic field, leading to a stable state which can be described by the laws of thermodynamics. A two-fluid model was advanced by Gorter and Casimir [3] in 1934 to describe the thermodynamic properties; and in 1935 London and London [4] proposed a phenomenological theory for the electromagnetic properties. The London theory was extended in 1950 by Ginsburg and Landau [5] to include a spacially dependent superfluid density; and in 1953 by Pippard [6] who proposed a nonlocal form for the theory.

In 1950 Fröhlich [7] recognized the importance of the interactions between electrons and phonons (quantized lattice vibrations) in forming the superconducting state. He showed that this interaction could lead to an effective electron-electron interaction which is attractive for electrons near the Fermi surface. In the same year Fröhlich's proposal was confirmed by the experimental observation of the isotope

effect by Maxwell [8] and independently by Reynolds et al. [9] The specific heat experiments of Corak and Satterthwaite [10] and Corak et al. [11] indicated that there is an energy gap for excitations from the superconducting ground state.

In 1956 Cooper [12] investigated the problem of a pair of electrons of zero total momentum and spin interacting with each other via an attractive two-body interaction in the presence of an inert Fermi sea. He considered a model interaction of constant strength when the electron energies were within an "average" phonon energy of the Fermi surface, and zero strength otherwise. He found that an electron pair in such a system would form a bound state, no matter how weak the attractive interaction was. This indicated that in the presence of an attractive electron-electron interaction the Fermi sea would be unstable with respect to the formation of electron pairs. Cooper's result along with the mechanism for the attractive interaction proposed by Fröhlich cleared the way for the theory of Bardeen, Cooper and Schrieffer [13], hereafter referred to as BCS.

The BCS theory treats the electron-ion system in terms of electrons in Block states and noninteracting phonons, with a residual two-body interaction between the electrons. This residual interaction is composed of a repulsive Coulomb part, and a phonon part which is attractive between electrons for which the energy difference between electron states is less than the phonon energy. When the residual interaction

is attractive the Fermi sea becomes unstable with respect to the formation of Cooper pairs, and a new ground state of the system is formed. The model interaction of Cooper was used to show that this new state gave good agreement with a wide range of superconducting phenomena. This BCS model introduces the total effect of the phonons by means of a single adjustable parameter, which is the interaction strength times the density of electron states at the Fermi surface. Thus, it predicts a law of corresponding states among superconductors, and shows good agreement with experiment for a wide range of superconducting properties and materials [14,15].

The superconducting state energy gap was directly measured in 1960 by Giaever [16], who used electron tunneling through metal-insulator-superconductor films. This tunneling technique has been refined [17,18] such that the current-voltage characteristics can provide information on the "superconducting phonon density of states" [19-21]. To account for these and other observed deviations from the BCS theory, the detailed nature of the electron-phonon and Coulomb interactions had to be included in the theory. This was accomplished by Eliashberg [22], Nambu [23], Morel and Anderson [24], and Scalapino, Schrieffer and Wilkins [25], with work based on Migdal's [26] approach for normal metals and Gor'kov's [27] Green's function method. A number of thorough discussions of superconductivity have been published [28,29]; and calculations of energy gaps, transition

temperatures, and other superconducting properties have been reported [24,30-38].

In a pure single-crystal superconductor the energy gap is a function of position on the Fermi surface. The most direct measure of this effect is provided by tunneling experiments. The directional gaps have been measured in lead [39,40] and tin [41,42]. A number of theoretical investigations have been carried out both for anisotropic effective electron-electron interactions [43,44] and anisotropic band structure [45]. More recent calculations by Bennett for lead [46] included phonon anisotropy resulting from the phonon spectrum, while neglecting anisotropy arising from the electron-phonon interaction. He found that the phonon contribution was the dominant source of energy gap anisotropy in lead, rather than band structure effects. Bennett later extended his calculations to include tin [47]. Calculations including the full effect of phonon anisotropy have been performed by Balsley in tin [48,49] and Leavens and Carbotte [50,51] in aluminum.

1.2 SCOPE OF THESIS

On the basis of reasonable assumptions [52] it is possible to express any motion of atoms in a crystal as a superposition of normal vibrations. These vibrations, or phonon modes, are described by a propagation vector, a frequency, and a direction of displacement; all of which are characteristic of the crystal and depend upon the atomic geometry and interatomic forces. In a metal the conduction electrons interact with the ions; thus the electronic properties of both the superconducting and normal states will be dependent upon the phonon modes. There is some evidence to suggest that phonon effects may account for most of the observed anisotropy in:

1) the superconducting gaps of face-centred cubic aluminum [50] and lead [46], and tetragonal white tin [47,48,49].
2) the normal state resistivity of white tin [48,49].

In this thesis we present the results of a detailed numerical investigation of the effects of phonon anisotropy on the properties of the hexagonal close-packed metals zinc and thallium. By "phonon anisotropy" we refer to that anisotropy which arises from both the directional dependence of the phonon frequency distributions and the electron-phonon

interaction. The rather artificial separation of these two effects is not considered. Zinc was initially chosen for these calculations because:

a) it appears to be highly anisotropic [53],

b) an accurate empirical pseudopotential is available [54],

c) rather extensive phonon measurements have been performed and force constant models derived [55].

The calculations were later extended to include thallium because of the availability of superconducting tunneling information [56,57], and recent measurements of the phonon dispersion curves [58] along some of the high symmetry directions in the reciprocal lattice.

Within the accurate [20] "strong-coupling" [25,28,59] theory of superconductivity, the superconducting state is completely specified by means of a frequency (ω) and wave-vector ($\underline{k}$) dependent gap and renormalization function. These quantities are determined by a set of nonlinear integral equations - the Eliashberg gap equations. These equations may be expressed in a form where all of the essential normal state information is contained in a set of directional dependent distribution functions.

$$\alpha^2(\omega,\underline{k})F(\omega,\underline{k}) = \int_{S_F'} \frac{d^2\underline{k}'}{(2\pi)^3|\underline{v}_{\underline{k}'}|} \sum_j |g_{\underline{k}\underline{k}'j}|^2 \delta(\omega-\omega_{\underline{k}-\underline{k}'j}) \tag{1.1}$$

where δ denotes the Dirac delta function. The wavevectors $\underline{k}$ and $\underline{k}'$ are on the Fermi surface, $\underline{v}$ is the electron velocity vector, and the integral extends over the entire Fermi surface. The electron-phonon coupling constant, $g_{\underline{k}\underline{k}'j}$ of section 2.2, depends upon the electron-ion pseudopotential and the phonon: wavevector $\underline{k}-\underline{k}'$, frequencies $\omega_{\underline{k}-\underline{k}'j}$, and polarization vectors. We have used j to denote the phonon branch index. The average of equation (1.1) over all $\underline{k}$ directions, $\alpha^2(\omega)F(\omega)$; may be thought of as a product of the phonon frequency distribution $F(\omega)$ and a quantity $\alpha^2(\omega)$ which describes, in an average way, the strength of the coupling between the electrons and the phonons.

All of the properties discussed in this thesis may be expressed in terms of two sets of distribution functions, those given by equation (1.1) and another very closely related set, $\alpha^2_{tr}(\omega,\underline{k})F(\omega,\underline{k})$. The $\alpha^2_{tr}F$ functions are given by equation (1.1) with $|g_{\underline{k}\underline{k}'j}|^2$ multiplied by a simple function of the electron velocities $v_{\underline{k}}$ and $v_{\underline{k}'}$. They both involve normal state information through the phonons and the electron-ion interaction. The treatment of the normal state data and the subsequent calculation of these functions will be the subject of Chapters II and III.

Detailed experimental phonon information is included in our calculations by the use of Born-von Kármán force constant models [52], which describe the lattice dynamics of the metals. The effects of electronic band structure are

included by the use of an isotropic band mass approximation, in which the density of electron states at the Fermi surface is changed from its free electron value. Any anisotropy arising from the band structure is ignored.

In section 2.1 and 2.2 the Born-von Kármán theory and the electron-phonon interaction respectively, are discussed for metals with more than one atom per unit cell.

Section 3.1 describes the particular force constant model which we use to describe the hexagonal close-packed metals. The actual force constants and pseudopotentials employed in our zinc and thallium calculations are given in sections 3.3 and 3.4 respectively. Two models are used to describe each metal. The zinc models have the same pseudopotential, but different force constants; while the thallium models have the same force constants, but different pseudopotentials. Section 3.2 outlines the calculation of the functions defined by equation (1.1) for each of the four models mentioned above. Once this has been accomplished the superconducting results of Chapter IV and the normal state results of Chapter V follow in a relatively straightforward manner.

The isotropic $\alpha^2(\omega)F(\omega)$'s are used in section 4.1 to calculate superconducting properties in the isotropic or "dirty" limit. From the directional $\alpha^2(\omega,\underline{k})F(\omega,\underline{k})$'s we determine the superconducting gaps as a function of position on the Fermi surface, which may be compared with experiment.

The resulting gap anisotropy allows us to calculate the transition temperature, the gap at the gap edge, the low temperature specific heat, and the nuclear spin relaxation rate for a pure single crystal superconductor. The above results are discussed in section 4.2 for zinc and section 4.3 for thallium.

Also, in section 5.1 we obtain the electron-phonon mass enhancement parameters and scattering times as a function of temperature and position on the Fermi surface. In section 5.2 we investigate the anisotropy in the temperature variation of the electron-phonon mass enhancement on the zinc third band lens. The use of a "scattering time approximation" in section 5.3 enables us to calculate the directional large-angle scattering times as a function of temperature and conduction electron wavevector direction. These scattering times may be expressed in terms of the $\alpha^2_{tr}(\omega,\underline{k})F(\omega,\underline{k})$ functions mentioned previously. From these quantities we obtain the phonon-limited resistivities parallel and perpendicular to the c-axis. The resistivities are also calculated using the variational approach; and the results of the two methods are compared.

In Chapter VI conclusions are drawn from our calculated results and the comparisons with experiment discussed in Chapters III, IV and V.

CHAPTER II

PHONONS AND THE ELECTRON-PHONON INTERACTION

2.1 PHONONS AND BORN-VON KÁRMÁN THEORY

Inelastic slow neutron scattering [60] provides the most detailed information about phonon modes, usually for wavevectors in high symmetry directions. Born-von Kármán theory [52] assumes that the lattice dynamics of a crystal can be expressed in terms of effective interionic potentials or force constants. These force constants are adjusted to give the best possible fit to measured phonon dispersion curves and any other relevant data. Then the fitted force constants are used to generate the frequencies and polarization vectors for any desired phonon wavevector.

In a crystal the ionic motion consists of small oscillations about the equilibrium positions. Since the electrons move much faster than the ions, the adiabatic approximation [61] states that the electronic motion may be considered as contributing to the effective interionic forces, and need not be explicitly included in the dynamical problem. Thus, the total crystal potential energy Φ can be expressed as a function of the instantaneous ion positions. In a crystal with N unit cells and p ions per unit cell, we write the position vector $\underline{R}(\ell\kappa;t)$ of the κ^{th} ion in the ℓ^{th} unit cell at time t as

$$\underline{R}(\ell\kappa;t) = \underline{R}^0(\ell\kappa) + \underline{U}(\ell\kappa;t) \quad ,$$

where $\underline{R}^0$ is the equilibrium position and $\underline{U}$ gives the excursion from equilibrium.

Since the ionic displacements are small, the harmonic approximation is invoked, whereby Φ is expanded in a Taylor's series. The expansion is made in powers of the displacements; and only terms up to second order are retained. Thus [62],

$$\Phi = \Phi_0 + \sum_{\ell\kappa\alpha} \Phi_\alpha^\kappa(\ell) U_\alpha(\ell\kappa;t) + \frac{1}{2} \sum_{\substack{\ell\kappa\alpha \\ \ell'\kappa'\beta}} \Phi_{\alpha\beta}^{\kappa\kappa'}(\ell,\ell') \times U_\alpha(\ell\kappa;t) U_\beta(\ell'\kappa';t) \qquad (2.1)$$

with

$$\Phi_\alpha^\kappa(\ell) = \frac{\partial \Phi}{\partial U_\alpha(\ell\kappa;t)} \Big|_0 \qquad (2.2)$$

and

$$\Phi_{\alpha\beta}^{\kappa\kappa'}(\ell,\ell') = \frac{\partial^2 \Phi}{\partial U_\alpha(\ell\kappa;t)\, \partial U_\beta(\ell'\kappa';t)} \Big|_0 \qquad (2.3)$$

where $\alpha,\beta = 1, 2, 3$ are the Cartesian components, the subscript 0 denotes evaluation at the equilibrium positions, and Φ_0 is the static crystal potential energy. The term $\Phi_\alpha^\kappa(\ell)$ gives the force in the α-direction acting on the $(\ell\kappa)$ ion, and at equilibrium this must vanish

$$\Phi_\alpha^\kappa(\ell) = 0 \quad .$$

The crystal Hamiltonian in the harmonic approximation becomes

$$H = \frac{1}{2} \sum_{\ell\kappa\alpha} M_\kappa \dot{U}^2_\alpha(\ell\kappa;t) + \Phi_0$$

$$+ \frac{1}{2} \sum_{\substack{\ell\kappa\alpha \\ \ell'\kappa'\beta}} \Phi^{\kappa\kappa'}_{\alpha\beta}(\ell,\ell') U_\alpha(\ell\kappa;t) U_\beta(\ell'\kappa';t) \quad (2.4)$$

where the first term is the total kinetic energy of the lattice and M_κ is the mass of the κ type ion.

The force constant $\Phi^{\kappa\kappa'}_{\alpha\beta}(\ell,\ell')$ is the force in the α-direction acting on the $(\ell\kappa)^{th}$ ion, due to a unit displacement of the $(\ell'\kappa')^{th}$ ion in the β-direction. From the definition (2.3), commutation of the derivatives gives

$$\Phi^{\kappa\kappa'}_{\alpha\beta}(\ell,\ell') = \Phi^{\kappa'\kappa}_{\beta\alpha}(\ell',\ell) \quad .$$

Throughout this section we implicitly assume an infinite periodic crystal made up of macrocrystals with N unit cells. Therefore, translation of the entire crystal by a lattice vector must leave the crystal potential energy unchanged. This implies that the force constants can only depend upon the relative cell index $\ell-\ell'$, or

$$\Phi^{\kappa\kappa'}_{\alpha\beta}(\ell,\ell') = \Phi^{\kappa\kappa'}_{\alpha\beta}(\ell-\ell',0) \quad . \quad (2.5)$$

From Hamilton's equations and the crystal Hamiltonian (2.4) the equations of motion for the lattice are

obtained,

$$M_\kappa \ddot{U}_\alpha(\ell\kappa;t) = - \sum_{\ell'\kappa'\beta} \Phi^{\kappa\kappa'}_{\alpha\beta}(\ell,\ell') U_\beta(\ell'\kappa';t) \qquad (2.6)$$

The time dependence is removed by setting

$$\underline{U}(\ell\kappa;t) = \underline{U}(\ell\kappa) e^{-i\omega t} \quad .$$

The resulting equation

$$\omega^2 M_\kappa U_\alpha(\ell\kappa) = \sum_{\ell'\kappa'\beta} \Phi^{\kappa\kappa'}_{\alpha\beta}(\ell,\ell') U_\beta(\ell'\kappa') \qquad (2.7)$$

may be simplified by assuming a solution of the form

$$U_\alpha(\ell\kappa) = \frac{U^\kappa_\alpha(\underline{k})}{\sqrt{M_\kappa}} \; e^{i\underline{k}\cdot(\underline{R}^0_\ell + \underline{\rho}(\kappa))} \qquad (2.8)$$

where we have written the ionic equilibrium positions as

$$\underline{R}^0(\ell\kappa) = \underline{R}^0_\ell + \underline{\rho}(\kappa)$$

where $\underline{R}^0_\ell$ is the position of the origin of the ℓ^{th} unit cell, $\underline{\rho}(\kappa)$ is the position of the κ^{th} ion with respect to the origin of the unit cell, and $\underline{k}$ is a wavevector with N allowed values uniformly distributed throughout the first Brillouin zone. Upon substituting (2.8) into (2.7) the equations of

motion become

$$\omega^2 U_\alpha^\kappa(\underline{k}) = \sum_{\kappa',\beta} D_{\alpha\beta}^{\kappa\kappa'}(\underline{k}) U_\beta^{\kappa'}(\underline{k}) \tag{2.9}$$

where the elements

$$D_{\alpha\beta}^{\kappa\kappa'}(\underline{k}) = \sum_{\ell'} e^{-i\underline{k}\cdot(\underline{R}_\ell^0+\underline{\rho}(\kappa))} \frac{\Phi_{\alpha\beta}^{\kappa\kappa'}(\ell,\ell')}{\sqrt{M_\kappa M_{\kappa'}}} e^{i\underline{k}\cdot(\underline{R}_{\ell'}^0+\underline{\rho}(\kappa'))} \tag{2.10}$$

define the dynamical matrix $D(\underline{k})$.

We initially set out to determine the motion of the ions expressed in terms of 3pN ($N \approx 10^{23}$) coupled differential equations (2.6). The set of linear homogeneous equations (2.9) has reduced the problem to one of diagonalizing a 3p by 3p matrix $D(\underline{k})$. The eigenvalues $\omega_{\underline{k}j}^2$, $j = 1, 2, \ldots, 3p$, are the squares of the phonon frequencies and the eigenvectors are the phonon polarization vectors, corresponding to the phonon of wavevector $\underline{k}$. To make explicit the correspondence between the eigenvalues and the eigenvectors, we write the latter as $\underline{\varepsilon}^\kappa(\underline{k},j)$. The convention of Born and Huang [52] is adopted, whereby

$$\varepsilon_\alpha^\kappa(\underline{k},j) = (\varepsilon_\alpha^\kappa(-\underline{k};j))^* \quad ;$$

and in all that follows we assume that the eigenvectors are orthonormal

$$\sum_{\kappa\alpha} (\varepsilon_\alpha^\kappa(\underline{k},j))^* \varepsilon_\alpha^\kappa(\underline{k},j') = \delta_{j,j'}$$

$$\sum_{j} (\varepsilon_\beta^{\kappa'}(\underline{k},j))^* \varepsilon_\alpha^\kappa(\underline{k},j) = \delta_{\alpha,\beta}\delta_{\kappa,\kappa'}$$

where * denotes the complex conjugate and δ is the Kronecker delta.

The equations of motion (2.9) may now be written in standard form [62,63] as

$$\omega_{\underline{k}j}^2 \, \varepsilon_\alpha^\kappa(\underline{k};j) = \sum_{\kappa'\beta} D_{\alpha\beta}^{\kappa\kappa'}(\underline{k}) \varepsilon_\beta^{\kappa'}(\underline{k};j) \quad ; \tag{2.11}$$

and using relation (2.5) the elements of the dynamical matrix become

$$D_{\alpha\beta}^{\kappa\kappa'}(\underline{k}) = \sum_{\ell} e^{-i\underline{k}\cdot\underline{R}_\ell^0} \frac{\Phi_{\alpha\beta}^{\kappa\kappa'}(\ell,0)}{\sqrt{M_\kappa M_{\kappa'}}} e^{-i\underline{k}\cdot(\underline{\rho}(\kappa)-\underline{\rho}(\kappa'))} \tag{2.12}$$

From these two equations it follows that for any reciprocal lattice vector $\underline{H}_n$

$$\underline{\varepsilon}^\kappa(\underline{k} + \underline{H}_n;j) = e^{-i\underline{H}_n\cdot\underline{\rho}(\kappa)} \underline{\varepsilon}^\kappa(\underline{k};j) \tag{2.13}$$

In general the ionic displacements may be expressed as a superposition of normal modes $(\underline{k},j)$

$$U_\alpha(\ell\kappa) = \frac{1}{\sqrt{NM_\kappa}} \sum_{\underline{k}j} Q(\underline{k};j)\varepsilon_\alpha^\kappa(\underline{k};j) \, e^{i\underline{k}\cdot(\underline{R}_\ell^0 + \underline{\rho}(\kappa))} \tag{2.14}$$

The normal coordinates $Q(\underline{k};j)$ are chosen to diagonalize the crystal Hamiltonian (2.4). They may be expressed in terms of phonon creation (a^+) and annihilation (a) operators as [62,64]

$$Q(\underline{k};j) = \left(\frac{\hbar}{2\omega_{\underline{k}j}}\right)^{1/2} \left(a^+_{-\underline{k}j} + a_{\underline{k}j}\right) \qquad (2.15)$$

where $\hbar$ is Planck's constant divided by 2π, with

$$[a_{\underline{k}j},\ a^+_{\underline{k}'j'}] = \delta_{\underline{k},\underline{k}'}\ \delta_{j,j'}$$

and

$$[a_{\underline{k}j},\ a_{\underline{k}'j'}] = [a^+_{\underline{k}j},\ a^+_{\underline{k}'j'}] = 0 \quad .$$

The above formalism will be used throughout this work. However, it should be mentioned that for a crystal with more than one atom per unit cell, there exists an alternative definition for the dynamical matrix which has also been discussed by Born and Huang [52]. In this approach the elements of the dynamical matrix are defined as

$$D^{\kappa\kappa'}_{\alpha\beta}(\underline{k})_{B.H.} = \sum_{\ell'} e^{-i\underline{k}\cdot\underline{R}^0_{\ell}} \frac{\Phi^{\kappa\kappa'}_{\alpha\beta}(\ell,\ell')}{\sqrt{M_\kappa M_{\kappa'}}} e^{i\underline{k}\cdot\underline{R}^0_{\ell'}} \qquad (2.16)$$

The eigenvalue equation then becomes

$$\omega^2_{\underline{k}j}\ \varepsilon^{\kappa}_{\alpha}(\underline{k};j)_{B.H.} = \sum_{\kappa'\beta} D^{\kappa\kappa'}_{\alpha\beta}(\underline{k})_{B.H.}\ \varepsilon^{\kappa'}_{\beta}(\underline{k};j)_{B.H.} \qquad (2.17)$$

where the polarization vectors satisfy

$$\underline{\varepsilon}^{\kappa}(\underline{k} + \underline{H}_n; j)_{B.H.} = \underline{\varepsilon}^{\kappa}(\underline{k}; j)_{B.H.} \quad , \tag{2.18}$$

and the expansion for the ionic displacements becomes

$$U_{\alpha}(\ell\kappa) = \frac{1}{\sqrt{NM_{\kappa}}} \sum_{\underline{k}j} Q(\underline{k}; j)\ \varepsilon_{\alpha}^{\kappa}(\underline{k}; j)_{B.H.}\ e^{i\underline{k}\cdot\underline{R}_{\ell}^{0}} \tag{2.19}$$

Finally, we may make the connection between these two conventions by observing that

$$\underline{\varepsilon}^{\kappa}(\underline{k}; j) = e^{-i\underline{k}\cdot\underline{\rho}(\kappa)}\ \underline{\varepsilon}^{\kappa}(\underline{k}; j)_{B.H.} \quad . \tag{2.20}$$

In the literature $\underline{\varepsilon}^{\kappa}$ and $\underline{\varepsilon}^{\kappa}_{B.H.}$ are both referred to as polarization vectors. The convention followed must be specified if this terminology is to be unambiguous.

Although the Born-von Kármán description of lattice dynamics is complete, in application it may not be entirely accurate. The experimental data is, of necessity, limited; and this in turn restricts the number of force constants which may be assigned meaningful values [60]. Also, the elements of the dynamical matrix (2.12) consist of a sum over all lattice vectors; but in practice the series is truncated after a number (usually less than nine) of nearest neighbour shells have been included. This keeps the calculation tractable; and it is reasonable because the forces between

ions are expected to decrease with increasing distance. However, there is some indication [65] that longer range forces may play a role in the lattice dynamics of metals. Thus, different sets of force constants may give comparable fits to the measured dispersion curves [66]; but they may differ significantly in their predictions for other directions. This effect has been discussed previously for lead [67,68], and we shall see more evidence of it in our zinc (section 3.3) and thallium (section 3.4) results.

2.2 THE ELECTRON-PHONON INTERACTION

In this section we will derive an expression for the electron-phonon coupling, which describes the interaction between the lattice vibrations and the conduction electrons in a metal. Pseudopotential theory, which has been extensively discussed by Harrison [69], Heine [70] and others [71-73], will be used.

For the simple metals we may separate the electron states into two distinct groups [74]: localized core states and nonlocal conduction band states. The Pauli exclusion principle dictates that the conduction and core states must be orthogonal. The essence of the pseudopotential method is to write the effect of this orthogonalization as an extra repulsive term which is added to the original attractive ion-electron potential; and both of these act upon a pseudo electron wavefunction. There is a large cancellation between the attractive and repulsive terms, and the resulting pseudopotential is weak. Thus, the pseudo wavefunction may be expanded in a small number of plane waves. If one employs n plane waves in this expansion, then the calculations are said to be done in the n orthogonalized plane wave (OPW) approximation. By using this formalism we can describe the scattering of conduction electrons by the "strong" ionic potentials in terms of plane wave scattering by a weak effective potential.

Rather than attempt the calculation of pseudopotentials from first principles, the usual procedure is to obtain them by fitting to experimental data [75]. This fitting is accomplished either by directly adjusting some starting form for the pseudopotential, or by assuming some simple model interaction and varying the parameters. We shall take the attitude that the ionic pseudopotential is a given potential which is obtained from experiment.

In the diffraction model [61,69] the potential energy $W(\underline{r})$ of an electron at $\underline{r}$ is given by

$$W(\underline{r}) = \sum_{\ell\kappa} w(\underline{r} - \underline{R}(\ell\kappa))$$

where w is the electron-ion pseudopotential, and all ions in the crystal are assumed to be identical. We shall work in the one OPW approximation in which each pseudo conduction band state is described by a single plane wave $|\underline{k}\rangle$. The scattering of an electron from a state $|\underline{k}\rangle$ to a state $|\underline{k}+\underline{q}\rangle$ is determined by

$$\langle \underline{k}+\underline{q}|W(\underline{r})|\underline{k}\rangle = \frac{1}{V}\int e^{-i(\underline{k}+\underline{q})\cdot\underline{r}} \sum_{\ell\kappa} w(\underline{r}-\underline{R}(\ell\kappa)) e^{i\underline{k}\cdot\underline{r}}\, d^3\underline{r}$$

where V is the total crystal volume. This may be rewritten as

$$\langle \underline{k}+\underline{q}|W(\underline{r})|\underline{k}\rangle = S(\underline{q})\ \langle \underline{k}+\underline{q}|w|\underline{k}\rangle$$

where

$$S(\underline{q}) = \frac{1}{pN} \sum_{\ell\kappa} e^{-i\underline{q}\cdot\underline{R}(\ell\kappa)} \tag{2.21}$$

is the structure factor and

$$\langle \underline{k}+\underline{q}|w|\underline{k}\rangle = \frac{1}{\Omega_0} \int e^{-i(\underline{k}+\underline{q})\cdot\underline{r}}\, w(\underline{r})\, e^{i\underline{k}\cdot\underline{r}}\, d^3\underline{r}$$

with Ω_0 being the volume per ion, and $\langle \underline{k}+\underline{q}|w|\underline{k}\rangle$ is the pseudopotential form factor.

In its most general form the pseudopotential is a nonlocal operator [69,70,75]. That is, the matrix elements $\langle \underline{k}+\underline{q}|w|\underline{k}\rangle$ depend upon the initial and final momenta and the energy as well as the momentum transfer $\hbar\underline{q}$. In the one OPW approximation we only consider scattering on the Fermi sphere. Thus, only the momentum transfer dependence remains and we may write

$$\langle \underline{k}+\underline{q}|w|\underline{k}\rangle = w(q)$$

where $0 \leq q \leq 2k_F$, and k_F is the Fermi wavevector.

The electron-ion Hamiltonian [36] is given by

$$\sum_{\substack{\underline{q}\underline{k} \\ \sigma}} \langle \underline{k}+\underline{q}|W|\underline{k}\rangle\, C^{+}_{\underline{k}+\underline{q}\sigma}\, C_{\underline{k}\sigma} \tag{2.22}$$

where the operator $C^{+}_{\underline{k}\sigma}$ ($C_{\underline{k}\sigma}$) creates (annihilates) an electron of wavevector $\underline{k}$ and spin σ. To obtain the electron-phonon

contribution (H_{el-ph}) to the Hamiltonian (2.22), the structure factor (2.21) is expanded to first order in the ionic displacements

$$S(\underline{q}) = S^{(0)}(\underline{q}) + S^{(1)}(\underline{q})$$

where the static crystal structure factor is

$$S^{(0)}(\underline{q}) = \frac{1}{pN} \sum_{\ell\kappa} e^{-i\underline{q}\cdot(\underline{R}_\ell^0 + \underline{\rho}(\kappa))}$$

and the scattering term is given by

$$S^{(1)}(\underline{q}) = -\frac{i}{pN} \sum_{\ell\kappa} \underline{q}\cdot\underline{U}(\ell\kappa)\, e^{-i\underline{q}\cdot(\underline{R}_\ell^0 + \underline{\rho}(\kappa))} .$$

Next, the displacements $\underline{U}(\ell\kappa)$ are expanded in normal coordinates (2.14), and using the relation

$$\frac{1}{N} \sum_{\ell} e^{i\underline{k}\cdot\underline{R}_\ell^0} = \sum_{\underline{H}_n} \delta_{\underline{k},\underline{H}_n}$$

we obtain

$$H_{el-ph} = -\frac{i}{p} \sum_{\substack{\underline{q}\underline{k} \\ \kappa j\sigma}} \frac{1}{\sqrt{NM}}\, \underline{q}\cdot\underline{\varepsilon}^{\kappa}(\underline{q};j)Q(\underline{q};j)w(q)C^{+}_{\underline{k}+\underline{q}\sigma}C_{\underline{k}\sigma}$$

where $M=M_\kappa$ for all κ. From relation (2.15) this may be written as

$$H_{el\text{-}ph} = \sum_{\substack{\underline{q}\underline{k} \\ j\sigma}} g_{\underline{k}+\underline{q},\underline{k};j}\ C^{+}_{\underline{k}+\underline{q}\sigma}\ C_{\underline{k}\sigma}(a^{+}_{-\underline{q}j} + a_{\underline{q}j})$$

where g is the electron-phonon coupling, which in the one OPW approximation is

$$g_{\underline{k}+\underline{q},\underline{k};j} = -i\left(\frac{\hbar}{2NM\omega_{\underline{q}j}}\right)^{1/2} w(q)\ \frac{1}{p}\ \sum_{\kappa}\ \underline{q}\cdot\underline{\varepsilon}^{\kappa}(\underline{q};j) \quad . \tag{2.23}$$

If we write

$$\underline{q} = \underline{q}_R + \underline{H}_n$$

where the reduced wavevector $\underline{q}_R$ is in the first Brillouin zone and $\underline{H}_n$ is a reciprocal lattice vector, then the use of equation (2.13) gives us

$$g_{\underline{k}+\underline{q},\underline{k};j} = -i\left(\frac{\hbar}{2NM\omega_{\underline{q}_R j}}\right)^{1/2} w(|\underline{q}_R+\underline{H}_n|)\frac{1}{p}\ \sum_{\kappa}(\underline{q}_R+\underline{H}_n)\cdot\underline{\varepsilon}^{\kappa}(\underline{q}_R;j)$$
$$\times e^{-i\underline{H}_n\cdot\underline{\rho}(\kappa)} \quad . \tag{2.24}$$

We shall make use of both expressions (2.23) and (2.24) in our calculations.

It should be mentioned that the expression for g, in terms of the alternative dynamical matrix defined by equations (2.16) through (2.19), is given by the substitution of relation (2.20) into the above equations.

CHAPTER III

FORCE CONSTANTS AND PSEUDOPOTENTIALS FOR ZINC AND THALLIUM

3.1 LATTICE DYNAMICS OF THE HEXAGONAL CLOSE-PACKED METALS - THE MAS MODEL

The arrangement of ions in the hexagonal close-packed (hcp) metals consists of two interpenetrating simple hexagonal sublattices. This crystal structure may be analyzed in terms of a unit cell containing two ions, with the lattice basis vectors given by

$$\underline{a}_1 = a(0,1,0)$$

$$\underline{a}_2 = a(-\frac{\sqrt{3}}{2}, -\frac{1}{2}, 0)$$

$$\underline{a}_3 = c(0,0,1) \quad .$$

The $\underline{a}_i$ have been expressed in terms of the Cartesian coordinate system shown in figure 3.1.1. c is the distance along the z-axis between alternate planes, which are perpendicular to the z-axis; and a is the distance between nearest neighbour ions in any such plane.

For convenience we choose one atom to be at the origin of the unit cell

$$\underline{\rho}(1) = (0,0,0) \quad . \tag{3.1}$$

Then the position of the second ion is

$$\underline{\rho}(2) = \frac{1}{3}\,\underline{a}_1 + \frac{2}{3}\,\underline{a}_2 + \frac{1}{2}\,\underline{a}_3 = \left(-\frac{a}{\sqrt{3}}, 0, \frac{c}{2}\right) \quad . \tag{3.2}$$

These two inequivalent lattice sites give rise to six vibrational modes which, in the long wavelength limit, may be classified as three acoustic and three optic branches.

The locations of the unit cell origins throughout the crystal are

$$\underline{r}(\ell) = m_1\underline{a}_1 + m_2\underline{a}_2 + m_3\underline{a}_3 \quad ,$$

where the m_i assume integer values. Reciprocal lattice vectors $\underline{H}_n$ are generated by

$$\underline{H}_n = n_1\underline{b}_1 + n_2\underline{b}_2 + n_3\underline{b}_3 \quad ,$$

where the n_i are integers; and the basis vectors for the reciprocal lattice are given in Cartesian coordinates as

$$\underline{b}_1 = \frac{2\pi}{a}\left(-\frac{1}{\sqrt{3}}, 1, 0\right)$$

$$\underline{b}_2 = \frac{2\pi}{a}\left(-\frac{2}{\sqrt{3}}, 0, 0\right)$$

$$\underline{b}_3 = \frac{2\pi}{a}\left(0, 0, \frac{1}{\gamma}\right)$$

with $\gamma = c/a$.

The resulting hexagonal first Brillouin zone (FBZ) is shown in figure 3.1.1, where the irreducible 1/24th is drawn in detail. The labeling of the high symmetry points follows the convention of Koster [76]. However, we have adopted the Cartesian coordinate system of DeWames et al. [77], which is rotated by 90° from that of Koster. In any discussion of hcp metals it is common usage to refer to the direction defined by our z-axis as the c-axis.

A number of force constant models have been proposed to describe the lattice dynamics of hcp metals: the Slutsky and Garland [78] model includes third neighbour forces, and the tensor force model of Collins [79] extends to fourth nearest neighbours. We note in passing that the ordering of neighbour shells depends upon the ratio c/a. In particular, the ordering of zinc neighbours differs from the ideal hcp structure by interchanging the fourth and sixth shells.

We shall use the six neighbour "modified axially symmetric" (MAS) model, which was originally proposed by DeWames, Wolfram and Lehman [77] (hereafter referred to as DWL) to analyze experimental data in Be and Zn. The most general description would have six independent force constants

between neighbouring ions. In the MAS model the forces between neighbours are expressed in terms of three independent force constants: a bond-stretching term along the line joining two ions, and two bond-bending force constants corresponding to restoring forces in the basal (xy) plane and normal to the plane (in the z-direction). This model is an extension of an earlier axially symmetric force constant model, proposed by the same authors for Cu and Al [80], and also white Sn [81]. In the original model the two bond-bending terms were assumed to be equal.

First we briefly discuss the axially symmetric model; then the modifications needed to convert this to the MAS model will be given. It is assumed that the potential energy of interaction associated with the κ^{th} ion in the 0^{th} unit cell is

$$V(0,\kappa) = \frac{1}{2} \sum_{n\kappa'} |\underline{R}_n^{\kappa'\kappa}|^{-2} [C_1(n;\kappa\kappa')(\underline{R}_n^{\kappa'\kappa}\cdot\underline{U}_n^{\kappa'\kappa})^2 + C(n;\kappa\kappa')(\underline{R}_n^{\kappa'\kappa}\times\underline{U}_n^{\kappa'\kappa})^2]$$

where

$$\underline{R}_n^{\kappa'\kappa} = \underline{R}^\circ(n\kappa') - \underline{R}^\circ(0\kappa) = \underline{R}_n^\circ + \underline{\rho}(\kappa') - \underline{\rho}(\kappa)$$

is the vector from the κ^{th} ion in the 0^{th} unit cell to the κ'^{th} ion in the n^{th} unit cell. Similarly for the displacements

from equilibrium

$$\underline{U}_n^{\kappa'\kappa} = \underline{U}(n\kappa') - \underline{U}(0\kappa) \quad .$$

The parameters $C_1(n;\kappa\kappa')$ and $C(n;\kappa\kappa')$ are the effective bond-stretching and bond-bending force constants respectively, associated with the interaction between the (0κ) ion and the $(n\kappa')$ ion.

Since there are two ions per unit cell the dynamical matrix is 6 by 6, and from (2.12) the elements are given by

$$D_{\alpha\beta}^{\kappa\kappa'}(\underline{q}) = \frac{1}{M}\left(\delta_{\kappa\kappa'} \sum_{\sigma=1}^{2} A_{\alpha\beta}^{\kappa\sigma}(0) - A_{\alpha\beta}^{\kappa\kappa'}(\underline{q})\right)$$

with

$$A_{\alpha\beta}^{\kappa\kappa'}(\underline{q}) = \sum_S \{-K(S,\kappa\kappa')\left|\underline{R}_{n(S)}^{\kappa'\kappa}\right|^{-2} \frac{\partial^2}{\partial q_\alpha \partial q_\beta}$$

$$+ C(S,\kappa\kappa')\delta_{\alpha\beta}\}G(S,\kappa\kappa') \qquad (3.3)$$

where

$$K(S,\kappa\kappa') = C_1(S,\kappa\kappa') - C(S,\kappa\kappa') \qquad (3.4)$$

and

$$G(S,\kappa\kappa') = \sum_{n(S)} e^{i\underline{q}\cdot\underline{R}_{n(S)}^{\kappa'\kappa}} \quad . \qquad (3.5)$$

We have written $\underline{R}_{n(S)}^{\kappa'\kappa}$ to indicate the vector between a κ and a κ' ion, with the κ' ion in the S^{th} shell about the κ ion. In (3.5) the sum is restricted to the S^{th} shell of ions. The notation used has closely followed that of reference 80.

The conversion to the MAS model is accomplished the simple substitution in equation (3.3) of

$$C(S,\kappa\kappa')\delta_{\alpha\beta} \rightarrow C_{\alpha}(S,\kappa\kappa')\delta_{\alpha\beta}$$

to give

$$A_{\alpha\beta}^{\kappa\kappa'}(\underline{q}) = \sum_{S} \{-K(S,\kappa\kappa')|\underline{R}_{n(S)}^{\kappa'\kappa}|^{-2} \frac{\partial}{\partial q_{\alpha}\partial q_{\beta}}$$

$$+ C_{\alpha}(S,\kappa\kappa')\delta_{\alpha\beta}\}G(S,\kappa\kappa')$$

and using

$$C_{x}(S,\kappa\kappa') = C_{y}(S,\kappa\kappa') \quad .$$

The above substitution is not made in the K force constant, which also contains a C factor (equation (3.4)). In appendix A of DWL the authors give explicit expressions for $G(S,\kappa\kappa')$ and $D_{\alpha\beta}^{\kappa\kappa'}(\underline{q})$, for interactions extending to six nearest neighbours. It has been pointed out by McDonald et al. [55] that there is a misprint in DWL and the expression for G(4,1-1)

should read

$$G(4,1\text{-}1) = 2C_{2z} \quad .$$

Before proceeding on to a discussion of calculations using this model it seems advisable to point out that the derivation of a Born-von Kármán model for hcp metals is considerably more involved, and probably less accurate, than for cubic systems. The dispersion relations along major symmetry directions of cubic metals may be expressed in terms of linear combinations of interionic force constants [60]. This is not possible in hcp metals because of the two interpenetrating sublattices; thus, the fitting procedures become considerably more complex. Moreover, the experimental measurements, which have been used to derive force constant models, in both Zn and Tl have been restricted to the basal plane and along the c-axis; and a large portion of the FBZ remains unexplored. This greatly reduces the reliability of the force constant fits.

FIGURE CAPTION - SECTION 3.1

FIGURE 3.1.1: The first Brillouin zone for hexagonal close-packed structures. The labeling of the high symmetry points of the irreducible 1/24th follows the convention of Koster [76]. The Cartesian coordinate system is given by $\underline{x}$, $\underline{y}$ and $\underline{z}$. The angles θ and ϕ define the angular coordinate system, where ϕ is the angle in the xy plane.

Figure 3.1.1

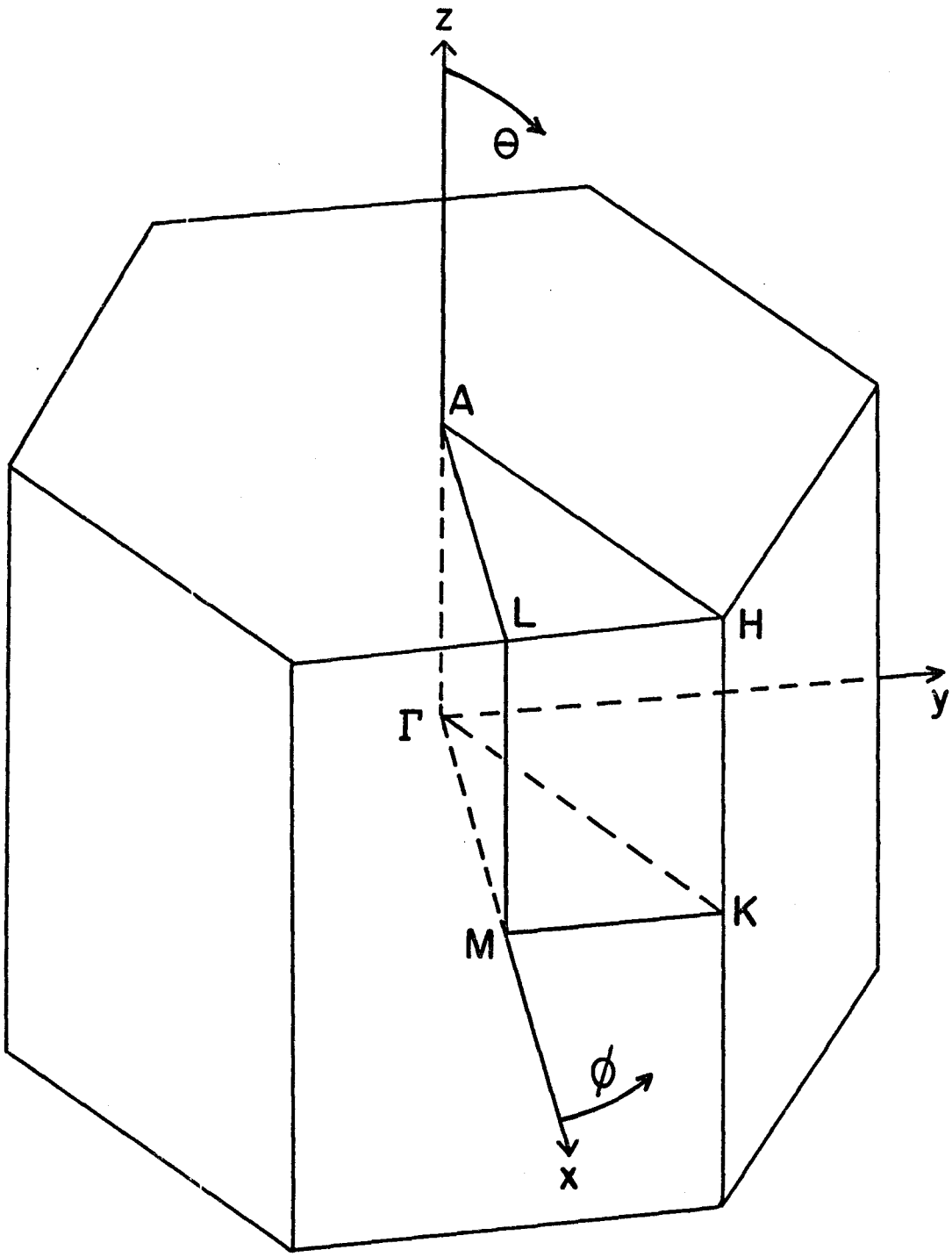

3.2 CALCULATION OF THE α^2F AND $\alpha^2_{tr}F$ FUNCTIONS - DIRECTIONAL AND ISOTROPIC

In section 1.2 we have indicated that most of our results follow directly from two sets of directional distribution functions, which we now write as

$$\alpha^2(\omega,\underline{k})F(\omega,\underline{k}) \equiv \alpha^2F(\omega,\underline{k})$$

and

$$\alpha^2_{tr}(\omega,\underline{k})F(\omega,\underline{k}) \equiv \alpha^2_{tr}F(\omega,\underline{k}) \quad .$$

This change in notation is made purely for the sake of convenience. We emphasize that this does not imply that we consider $\alpha^2(\omega,\underline{k})$ to be independent of direction, as was the case in Bennett's calculation [46].

The Fermi surface averages of these functions will also be needed, and it is through these averages that the connection is made with the more familiar frequency distributions. We shall use two procedures to obtain these average, or isotropic, functions. One method, to be discussed later in this section, consists of first calculating the directional functions; and then taking a Fermi surface average. However, this method consumes a large amount of computer time. If

only the isotropic function is desired then a more efficient method, which we now discuss, is based on a modification of existing frequency distribution computer programmes.

Computer programmes have been developed which calculate the phonon frequency distributions, $F(\omega)$, from Born-von Kármán force constant models for the cubic [82], hcp [83,84] and tetragonal [85] metals. The hcp program of Raubenheimer and Gilat [83,84] (hereafter referred to as RG) uses the MAS force constant model of DWL, as described in the previous section, to calculate the density of phonon states per unit frequency

$$F(\omega) = \frac{V}{N} \sum_j \int_{FBZ} \frac{d^3\underline{q}}{(2\pi)^3} \delta(\omega-\omega_{\underline{q}j}) \quad , \tag{3.6}$$

where V is the total crystal volume. The numerical method is described in great detail by RG, and we only give a brief outline here.

The integral (3.6) need only be performed over the irreducible 1/24th of the FBZ, which is further subdivided into a "uniform" mesh. For phonon wavevectors corresponding to the "center" of each mesh volume, the frequencies and polarization vectors are determined by diagonalizing the dynamical matrix. The frequencies for each elemental volume, obtained by extrapolation from the center evaluation, are then entered into the appropriate histogram channels of $F(\omega)$. The normalization of $F(\omega)$ can be determined by the sum rule [62]

$$\int_0^\infty F(\omega)\,d\omega = 6 \quad , \tag{3.7}$$

corresponding to the number of degrees of freedom per unit cell.

The integral of equation (1.1) is over the true Fermi surface. Direct measurements of the Fermi surface dimensions have been made using the de Haas-van Alphen effect. They show that the nearly free electron approximation is reasonable for the larger pieces of the Fermi surface in both zinc [86] and thallium [87,88]. Throughout this work we replace the actual Fermi surface by a spherical one, even though for certain regions the true shape may be considerably distorted from the spherical model. Including the actual Fermi surface would greatly increase the complexity of these calculations. However, the effects of electronic band structure may be included in an approximate way by the use of an isotropic band mass m_B, which compares the actual density of electron states at the Fermi level with the free electron value. The band mass is

$$m_B = \frac{N(0)}{N(0)_{F.E.}} \tag{3.8}$$

where $N(0)$ is the band mass electronic density of states of single spin at the Fermi energy, and the free electron value

is [89]

$$N(0)_{F.E.} = \frac{V}{2\pi^2}\frac{mk_F}{\hbar^2} \quad . \tag{3.9}$$

The parameter m_B may be obtained from band structure calculations [90], or from experimental data such as the specific heat [38].

Equation (1.1) may be written, in the spherical Fermi surface approximation, as [50]

$$\alpha^2F(\omega,\underline{k}) = N(0)\int_{FS}\frac{d\Omega_{\underline{k}'}}{4\pi}\sum_j |g_{\underline{k}\underline{k}'j}|^2\,\delta(\omega-\omega_{\underline{k}-\underline{k}'j}) \quad , \tag{3.10}$$

with the isotropic function given by

$$\alpha^2F(\omega) = \int_{FS}\frac{d\Omega_{\underline{k}}}{4\pi}\,\alpha^2F(\omega,\underline{k}) \quad . \tag{3.11}$$

Similarly, the second set of distribution functions, to be used in the resistivity calculations, become

$$\alpha^2_{tr}F(\omega,\underline{k}) = N(0)\int_{FS}\frac{d\Omega_{\underline{k}'}}{4\pi}\,(1-\cos(\underline{k},\underline{k}'))\sum_j|g_{\underline{k}\underline{k}'j}|^2\delta(\omega-\omega_{\underline{k}-\underline{k}'j}) \tag{3.12}$$

where $\cos(\underline{k},\underline{k}')$ is the cosine of the angle between $\underline{k}$ and $\underline{k}'$; and

$$\alpha^2_{tr}F(\omega) = \int_{FS}\frac{d\Omega_{\underline{k}}}{4\pi}\,\alpha^2_{tr}F(\omega,\underline{k}) \quad . \tag{3.13}$$

For the remainder of this section we will refer to the calculation of the α^2F functions; however, the same techniques and remarks hold for the calculation of $\alpha^2_{tr}F$.

The double surface integral implied in equation (3.11) may be converted to the volume integral

$$\alpha^2F(\omega) = \frac{V}{N} \sum_j \int_{q<2k_F} \frac{d^3\underline{q}}{(2\pi)^3} L(\underline{q};j)\delta(\omega-\omega_{\underline{q}j}) \tag{3.14}$$

with

$$L(\underline{q};j) = m_B \frac{mw^2(q)}{4Mk_F q\hbar\omega_{q_R j}} \left| \frac{1}{2} \sum_{\kappa=1}^{2} \underline{q}\cdot\underline{\varepsilon}^{\kappa}(\underline{q}_R;j) e^{-i\underline{H}_n\cdot\underline{\rho}(\kappa)} \right|^2 , \tag{3.15}$$

where m is the bare electron mass, $|w^2(q)|$ is the pseudopotential form factor, and the vectors $\underline{\rho}(\kappa)$ are given by equations (3.1) and (3.2). We have written the one OPW coupling constant $g_{kk'j}$ in the form (2.24) where

$$\underline{k} - \underline{k}' = \underline{q} = \underline{q}_R + \underline{H}_n \quad .$$

Upon comparing (3.6) and (3.14), it is clear that the RG computer program which gives $F(\omega)$ may be modified to calculate $\alpha^2F(\omega)$ if:

1) the $\underline{q}$ integration is extended from the FBZ to a sphere of radius $2k_F$, and
2) the weighting of the phonon modes is changed from unity to $L(\underline{q};j)$ of equation (3.15).

Carbotte and Dynes [36] have discussed these modifications for the cubic metal case, we extend their technique to the hexagonal close-packed metals. To describe how the $\underline{q}$ integration is extended, let us consider one of the mesh volumes in the irreducible part of the FBZ which is used to calculate $F(\omega)$. The dynamical matrix is diagonalized for $\underline{q}_c$ at the center, and the phonon frequencies and polarization vectors are obtained. Within the sphere of integration, all other "equivalent" positions $\underline{q}'_c$ and the corresponding frequencies and polarization vectors may be obtained by the hcp symmetry operations [76] and translations by reciprocal lattice vectors. Using this information, the weights $L(\underline{q}_c;j)$ and all $L(\underline{q}'_c;j)$ may be calculated from (3.15). Then the frequencies obtained by extrapolation throughout the original and translated mesh volumes are weighted with the corresponding L and are entered into the appropriate $\alpha^2F(\omega)$ histogram channels, as determined by the δ-functions.

The total volume integral is generated by repeating the above procedure for all mesh volumes in the irreducible part of the FBZ; and the normalization is determined by the use of equation (3.7). Furthermore, symmetry allows us to restrict the volume integral to the 1/24th part found by extending the irreducible part of the FBZ. In terms of the angular coordinate system (θ,ϕ) defined in figure 3.1.1 the integration volume is given by the conditions $0°\leq\theta\leq90°$, $0°\leq\phi\leq30°$ and $0\leq|\underline{q}(\theta,\phi)|\leq2k_F$.

Some of the above points may be clarified by reference to figure 3.2.1. Here we have drawn the basal plane of the hcp reciprocal lattice with the origin at 0, and one reciprocal lattice vector $\underline{H}_1 = 2\pi/a(2/\sqrt{3},0,0)$. The thick solid lines define the projection on the plane of the volume of integration, where the radius of the solid arc is $2k_F$ (drawn for zinc). The irreducible part of the FBZ has been shaded in.

Because there are two inequivalent lattice sites, the determination of the polarization vectors is not quite as straightforward as it is for cubic systems. RG follow DWL in writing the dynamical matrix as a supermatrix

$$D(\underline{q}) = \begin{bmatrix} D^{11}(\underline{q}) & , & D^{12}(\underline{q}) \\ D^{12}(\underline{q})^*, & & D^{11}(\underline{q}) \end{bmatrix} \qquad (3.16)$$

The $D^{KK'}(\underline{q})$ are 3x3 matrices whose elements are $D^{KK'}_{\alpha\beta}(\underline{q})$, where $\alpha = x,y,z$ is the row index and $\beta = x,y,z$ is the column index. Diagonalization of $D(\underline{q})$ gives six eigenvectors $\underline{\varepsilon}(\underline{q};j)$, each having six components. Referring back to the set of equations (2.11), we see that they will be obtained in the form

$$\underline{\varepsilon} = \begin{bmatrix} \\ \underline{\varepsilon}^{(1)} \\ \\ \text{----} \\ \\ \underline{\varepsilon}^{(2)} \\ \\ \end{bmatrix} = \begin{bmatrix} \varepsilon_x^{(1)} \\ \varepsilon_y^{(1)} \\ \varepsilon_z^{(1)} \\ \varepsilon_x^{(2)} \\ \varepsilon_y^{(2)} \\ \varepsilon_z^{(2)} \end{bmatrix} \tag{3.17}$$

where the (q;j) dependence has been suppressed.

However, to simplify the diagonalization subroutine RG actually work with the real matrix

$$\tilde{D}(\underline{q}) = u^{+} D(\underline{q}) u$$

where

$$u = \frac{1}{\sqrt{2}} \begin{bmatrix} I & , & -iI \\ \\ -iI & , & I \end{bmatrix} \tag{3.18}$$

and I is a 3x3 identity matrix. Thus, for a given $\underline{q}$ the RG program gives the eigenvectors $\tilde{\underline{\varepsilon}}(\underline{q};j)$ obtained by diagonalizing $\tilde{D}(\underline{q})$. From these the polarization vectors may be obtained by noting that

$$\underline{\varepsilon}(\underline{q};j) = u\, \tilde{\underline{\varepsilon}}(\underline{q};j)$$

and using (3.17). In the RG paper [83] u and u^+ are interchanged, where u is given by (3.18).

In all our calculations, using this method to obtain the isotropic $\alpha^2F(\omega)$, the irreducible 1/24th of the FBZ has been subdivided into 1539 and 1710 mesh volumes for Zn and Tl respectively. The difference in mesh numbers is due to the different c/a values. The frequency channel widths are approximately $\omega_c/100$, where ω_c is the maximum phonon frequency.

To calculate the directional functions we neglect any anisotropy in the Fermi surface or in the electronic density of states at the Fermi surface, which gives [50]

$$\alpha^2F(\omega,\theta,\phi) = N(0)\int \frac{d\Omega_{\underline{k}'}}{4\pi} \sum_j |g_{kk'j}|^2 \delta(\omega-\omega_{\underline{k}-\underline{k}'j}) \quad . \quad (3.19)$$

The variable θ,ϕ refer to the angular coordinates of the wavevector $\underline{k} = (k_F,\theta,\phi)$ expressed relative to the spherical coordinate system of figure 3.1.1. The element of solid angle centred at $\underline{k}'$ may be expressed as $\Omega_{\underline{k}'} = \sin\theta'd\theta'd\phi'$. For these calculations expression (2.23) for the one OPW coupling constant is more convenient, and equation (3.19) becomes

$$\alpha^2F(\omega,\theta,\phi) = \int \frac{d\Omega_{\underline{k}'}}{4\pi} \sum_j L(\underline{q};j)\delta(\omega-\omega_{\underline{q};j}) \quad (3.20)$$

where

$$L(\underline{q};j) = m_B \frac{3Z\, m\, w^2(q)}{2k_F^2\, M\, \hbar\, \omega_{\underline{q}j}} \left| \frac{1}{2} \sum_{\kappa=1}^{2} \underline{q}\cdot\underline{\varepsilon}^{\kappa}(\underline{q};j) \right|^2 \quad (3.21)$$

and we have used $\underline{k} - \underline{k}' = \underline{q}$ along with equations (3.8) and (3.9).

The numerical evaluation of $\alpha^2F(\omega,\theta,\phi)$ is straightforward, following the method of Leavens and Carbotte [51]. The frequency range $0<\omega<\omega_c$ is divided into 100 channels. The surface of the Fermi sphere is subdivided into 4050 mesh areas by forty-five lines of latitude 4° apart and ninety lines of longitude also 4° apart. A random point (k_F,θ',ϕ') is generated inside each mesh area, and $\underline{q} = \underline{k} - \underline{k}'$ is determined. The dynamical matrix $D(\underline{q})$ is diagonalized to give the phonon frequencies and polarization vectors. From these the weights $L(\underline{q};j)\sin\theta'$ are calculated, which are then added to the appropriate frequency channels as determined by the delta functions. The directional histograms which are presented as figures in the following chapters are calculated using 16,200 mesh areas.

To normalize the histogram we define

$$N(\omega,\theta,\phi) = \int \frac{d\Omega_{\underline{k}'}}{4\pi} \sum_j \delta(\omega-\omega(\underline{q};j)) \quad , \tag{3.22}$$

which may be considered as a directional frequency distribution for phonons of wavevector $\underline{q} = \underline{k} - \underline{k}'$ emitted in the scattering of an electron in initial state $\underline{k}$ on the Fermi surface to every other state $\underline{k}'$ on the surface. The sum rule operating on $N(\omega,\theta,\phi)$ is analogous to (3.7) whereby for a

crystal structure with six degrees of freedom per unit cell

$$\int_0^\infty N(\omega,\theta,\phi)d\omega = 6 \tag{3.23}$$

Therefore, as $\alpha^2F(\omega,\theta,\phi)$ is calculated one also computes $N(\omega,\theta,\phi)$ in the same manner, then from (3.23) the normalization of both functions is obtained.

To determine the directional variation of $\alpha^2F(\omega,\theta,\phi)$ these functions were calculated at 44 points on the "irreducible 1/24th of the Fermi surface". The points are given by (k_F,θ_I,ϕ_J) where

$$\theta_I = 9^\circ\ I \quad ; \quad I = 0,1,2, \ldots ,10$$

and

$$\phi_J = 10^\circ\ J \quad ; \quad J = 0,10,20,30 \quad .$$

By symmetry these evaluations determine the directional variation over the entire Fermi surface.

These directional functions may also be used to obtain the isotropic $\alpha^2F(\omega)$, equation (3.11). The simplest averaging procedure may be written as

$$\alpha^2F(\omega) = \Big[\sum_{I,J} W_{IJ}\sin(\theta_I)\alpha^2F(\omega,\theta_I,\phi_J)\Big]\Big/\Big[\sum_{I,J} W_{IJ}\sin(\theta_I)\Big] \tag{3.24}$$

where the weights $W_{IJ} = 1,2$ or 4 are for the point (k_F,θ_I,ϕ_J) on the "corner", boundary or interior of the irreducible part

of the Fermi surface. The averages (3.24) were performed and compared to the results of the RG method, no significant differences were observed. However, for consistency when comparing isotropic and directional results we use (3.24), and when only the isotropic function is needed (fitting, etc.) the RG method is used.

It should be noted that the computing time is mainly determined by the number of matrix diagonalizations. Thus, if the directional functions are not required, equation (3.24) represents a much greater investment ($\approx 1.6\ 10^5$ diagonalizations) as compared to equation (3.14) ($\approx 1.6\ 10^3$ diagonalizations).

One further point remains to be discussed relating to the calculation of the α^2F and $\alpha^2_{tr}F$ functions. The one OPW approximation is not adequate to describe an electron state near a Bragg reflection plane. This defect shows up as an unphysical divergence in the electron-phonon coupling constant, equation (2.24), for acoustic modes with momentum transfer $\underline{q}$ approximately equal to a reciprocal lattice vector $\underline{H}_n \neq 0$. The straightforward way of removing this difficulty is to use a many OPW approximation [48,91]. In fact, it has been shown [61] that in the two OPW approximation the coupling constant approaches zero as the reduced momentum transfer approaches zero. However, these calculations are of much greater complexity than those using the one OPW approximation.

In a recent calculation Allen and Cohen [92] give a simple modification, of the one OPW result for $\alpha^2F(\omega)$, which

may be used to simulate the effect of a multiple OPW calculation. They suggest that the lower 1/5 of the frequency histogram should be multiplied by $5\omega/\omega_c$, or some higher power of this factor. This is reasonable because one OPW calculations in Al [36] and our Zn and Tl results show a linear behaviour for small ω, while it is believed that $\alpha^2F(\omega)$ should approach zero approximately as ω^2 [20,68]. Since, in our calculations, the strongest weight given to the low frequencies is much weaker than $1/\omega^2$, the low ω regions will be unimportant as long as they show roughly the correct behaviour. We utilize this suggestion, with slight modifications, and give the details of the renormalizations used in the appendix. Also, we follow Leavens and Carbotte [51] and apply this low frequency renormalization to the directional functions.

It is interesting to note that for some $\underline{k}$ directions the one OPW calculation of $\alpha^2F(\omega,\underline{k})$ and $\alpha^2_{tr}F(\omega,\underline{k})$ is entirely adequate and the above renormalization is of little significance. While for other directions this approximation breaks down. Figure 3.2.1 illustrates how this arises. The dashed circle of radius k_F (for zinc) is the intersection of the basal plane and the "scattering sphere" $\underline{k} - \underline{k}'$, where $\underline{k} = (k_F, 90°, 0°)$ and $\underline{k}'$ varies over the Fermi surface. Let us only consider the reciprocal lattice point $\underline{H}_1$. In this position the dashed circle is not close to $\underline{H}_1$ and the one OPW calculation will hold for this $\underline{k}$ direction. However, as θ and ϕ are varied it is apparent that the scattering sphere

will intersect $\underline{H}_1$. It is for these values of θ and ϕ that lead to intersection (or close approach) of the scattering sphere and any reciprocal lattice vector that the one OPW approximation fails, and the low frequency renormalization becomes necessary.

We emphasize that the phonons which must be renormalized are those acoustic umklapp processes of small reduced momentum transfer $\underline{q}_R$; but the particular renormalization chosen is not significant, as long as it is roughly correct (see the appendix). However, we will stress the importance of the low frequency phonon branches to our anisotropy calculations. These modes occur for larger reduced momentum transfer, they introduce structure in the distribution functions and are not renormalized.

FIGURE CAPTION - SECTION 3.2

FIGURE 3.2.1: Basal plane of the hcp reciprocal lattice with the origin at 0 and one reciprocal lattice vector $\underline{H}_1 = 2\pi/a(2/\sqrt{3},0,0)$. The shaded region is the irreducible part of the FBZ. The thick solid lines define the projection of the RG method volume of integration. The dashed circle of radius k_F (zinc) is the intersection of the $\underline{k} = (k_F,90°,0°)$ scattering sphere and the basal plane.

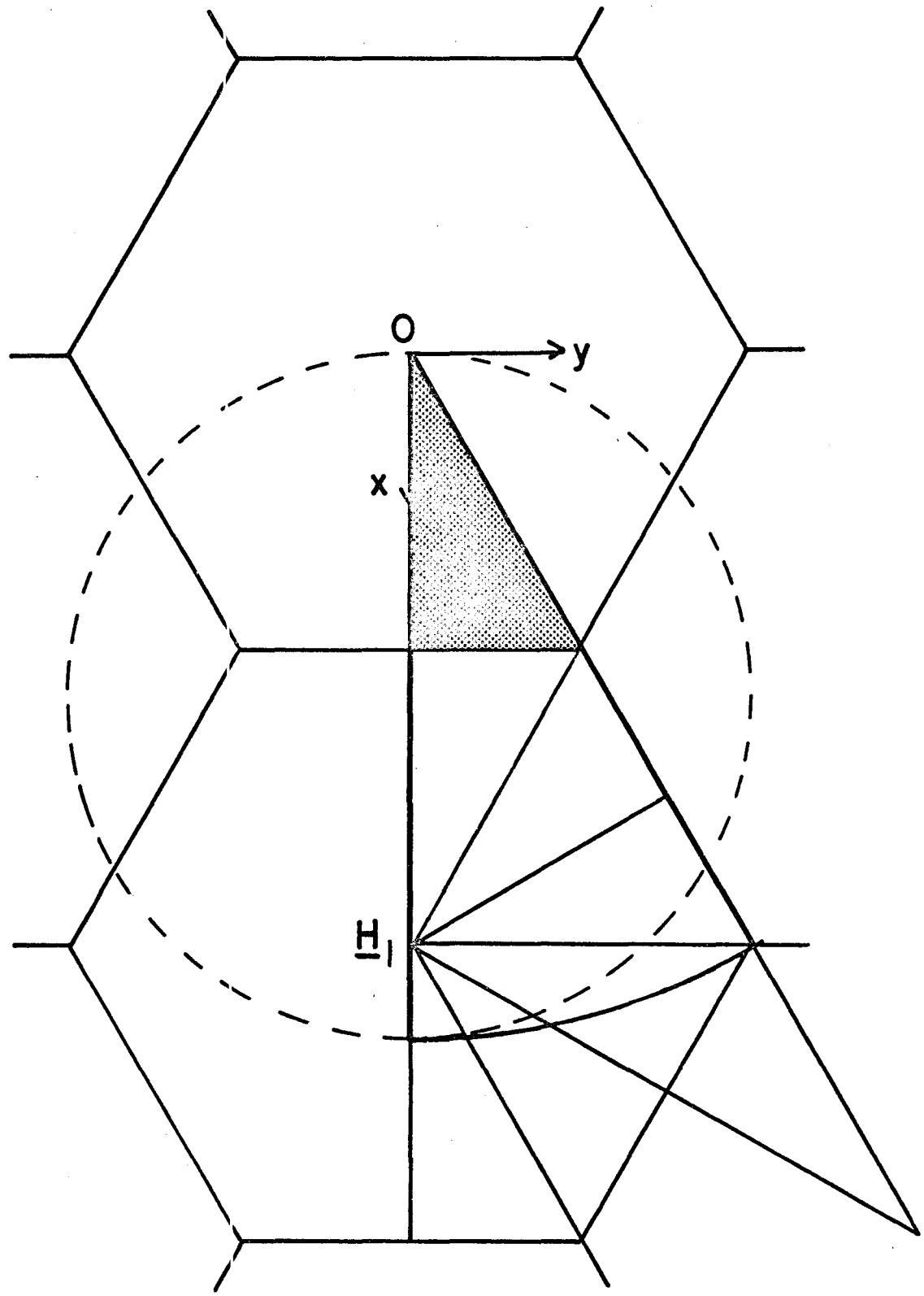
O
y
x
$\underline{H}_1$

3.3 PSEUDOPOTENTIAL AND FORCE CONSTANTS: ZINC

The essential raw materials of our calculations are the force constants, which give the crystal lattice vibrations; and the pseudopotential, which describes the interaction between the conduction electrons and the ions. The zinc pseudopotential is well determined. The neutron measurements from which force constant models have been derived, although rather extensive, are not what could be considered as complete. Therefore, as we shall see in this section, zinc is a convenient system in which to investigate the importance of the low frequency phonon branches to phonon anisotropy.

Stark and Falicov [54] have proposed an accurate empirical nonlocal pseudopotential for zinc. This pseudopotential was determined by fitting the calculated Fermi surface extremal cross-sectional areas to measured de Haas-van Alphen results. Agreement with experiment was obtained to within a few percent. Determination of other Fermi surface properties has also yielded good agreement [90]. Since we only consider scattering on the Fermi sphere, just the OPW form factors $w(q)$ are needed; these [93] are shown in figure 3.3.1. They were determined by using the full nonlocal pseudopotential to calculate $w(\underline{H}_n)$; and then a smooth curve was interpolated between these values and the point $w(0) = -2/3\ E_F$, where E_F is the Fermi energy. The resulting local form, which we use

throughout our zinc calculations, has been shown to yield good agreement with experimental determinations of the electron-phonon mass enhancement [90].

The most recent and complete set of neutron inelastic scattering measurements of the zinc phonon dispersion curves, from which a force constant model has been derived, is that reported by McDonald, Elcombe and Pryor [55] (hereafter referred to as MEP). They used a triple-axis neutron spectrometer to determine the phonon modes along the directions ΓM, MK, KΓ (all in the basal plane), and ΓA (along the c-axis). The directions are shown in figure 3.1.1. A least-squares fit to their data was used to generate a set of seventeen independent MAS model force constants. The resulting fit, shown in figure 3 of MEP, appears to be quite good. However, we have observed that these force constants predict imaginary frequencies for phonon wavevectors in the region of the H-point in reciprocal space.

Since the MEP fit to experiment is quite good, it was decided that these force constants (table 2 of MEP) should be modified to remove the incorrect behaviour at the H-point, while causing as little change as possible to the fit along the measured directions. This was accomplished by changing the MEP value of $K(6,11) = -3053$ dyn cm^{-1} to $K(6,11) = -2500$ dyn cm^{-1}; the reasons for this choice will be discussed below. We refer to this set of force constants with the modified K(6,11) value as MEPM. The lattice parameters [77] are taken to be $a = 2.6648$ Å and $c = 4.9467$ Å.

Along the measured directions, the only effect of this modification is to cause a slight upward shift of two branches along the ΓA direction, as shown in figure 3.3.2. Figure 3.3.3 gives the phonon dispersion curves calculated using MEPM force constants, along the high symmetry directions measured by MEP. The dots are the lowest observed phonon branches in the basal plane. We emphasize that all the ΓM, MK, KΓ and two of the ΓA branches are identical to those predicted by the original MEP force constants.

However, the situation along the unmeasured directions is quite different, as seen in figure 3.3.4. The solid lines are obtained from MEPM force constants, and the dashed curves are the predictions of the original MEP model. The modification of K(6,11), although leaving the higher frequency branches almost unchanged, has drastically altered the lowest branch. In particular, the low frequency mode at H is very sensitive to the value of K(6,11).

To determine a reasonable value for this force constant, we imposed the constraint that the calculated and empirical electron-phonon mass enhancement parameters λ should be in reasonable agreement. The effective increase in electron mass due to its interaction with the lattice ions is given by the parameter [59]

$$\lambda = 2 \int_0^\infty \frac{d\omega}{\omega} \alpha^2 F(\omega) \qquad (3.25)$$

Thus, the use of this constraint incorporates information about $\alpha^2F(\omega)$ in an average way; even though the detailed $\alpha^2F(\omega)$'s for weak coupling superconductors, such as zinc, have not been measured.

The solid curve of figure 3.3.5 shows the calculated $\alpha^2F(\omega)$ using the local form of the Stark-Falicov pseudopotential, the MEPM force constants, and the calculated [90] band mass value

$$m_B(\text{zinc}) = 0.59 \quad . \tag{3.26}$$

From equation (3.25), we obtain

$$\lambda = 0.425 \quad .$$

Allen and Cohen [38] have used specific heat data to derive an empirical value of $\lambda_{Expt} = 0.43$, agreement between these two values is excellent; and both of our constraints have been satisfied by our choice of K(6,11).

However, the above agreement should not be taken too seriously. Neglecting electron-electron effects, which are believed to be small [38,94], the specific heat mass is given by

$$m^* = m_B(1 + \lambda) \tag{3.27}$$

and

$$m^* = \frac{\gamma_{Expt.}}{\gamma_{F.E.}} \tag{3.28}$$

where $\gamma_{F.E.}$ is the free-electron specific heat coefficient [89]. One determination of the experimental electronic specific heat coefficient is given by Garland and Silverman [95] as $\gamma_{Expt.} = 1.56 \times 10^{-4}$ cal. mole^{-1} deg.$^{-2}$. These authors reanalyzed the results of two previous experiments by Seidel and Keesom [96] and Phillips [97]. If we use this value in the above equations we obtain $\lambda_{Expt.} = 0.47$; and the agreement between λ and $\lambda_{Expt.}$, although not as good, is still within 10%.

We have also carried through our superconductivity calculations with another older set of force constants proposed by DWL, which are also listed in table 2 of MEP. These were determined by a fit to neutron data along the ΓM and ΓA directions. The resulting dispersion curves are given in figures 3.3.6 and 3.3.7. The dots are the experimental results of MEP for the lowest phonon branches in the basal plane. These DWL branches are considerably higher than experiment, while the MEPM model is in much better agreement. Comparing figures 3.3.7 and 3.3.4, the lowest branch in the H-point region is also higher for the DWL model. Of course, all of the other branches have shifted somewhat; but for our purposes the above mentioned differences are the most relevant.

The solid curve of figure 3.3.8 gives the calculated $\alpha^2F(\omega)$ using the DWL force constants. The structure is very similar to that seen for the MEPM result of figure 3.3.5. The most significant points to notice are that the onset of structure and the position of the low frequency peak have been shifted upwards in energy, about 3 meV and 2 meV respectively, relative to the MEPM results. Apparently, in both our zinc models, the onset of structure is determined by the lowest H-point frequency, and the peak position is determined by the "flat" portions of the lowest frequency branches in the basal plane directions. We point out that the DWL value of $\lambda = 0.338$ is much lower than the empirical values. This is to be expected since the DWL low frequency modes have been shifted upwards in energy, and these are the modes which are most heavily weighted in (3.25).

A number of other deductions may be made from the figures presented in this section. The large energy difference between the two lowest acoustic modes in the ΓM direction (figures 3.3.3 and 3.3.6) illustrates the highly anisotropic nature of zinc. Since, they correspond to lattice waves vibrating in different directions, one in the basal plane and one normal to it.

The dashed curves of figures 3.3.5 and 3.3.8 are the frequency distributions for MEPM and DWL force constants respectively. Comparison of $F(\omega)$ with the corresponding $\alpha^2F(\omega)$, the solid curve, shows that these function are qualitatively similar in zinc. However, the presence of

umklapp processes tends to enhance the importance of the lower frequency region of $\alpha^2 F(\omega)$ over that of $F(\omega)$. Thus, the coupling function $\alpha^2(\omega)$ will decrease with frequency, at least over the lower energy range. The assumption which is sometimes made [98], that $\alpha^2(\omega)$ = constant, is obviously not a particularly accurate approximation for zinc; but it may be adequate for qualitative comparisons.

During the writing of this thesis a comprehensive determination of the zinc phonon dispersion relations has been published by Almqvist and Stedman [99]. The result which is of most significance to our work is that the lowest frequency at the H-point is considerably higher than that predicted by either the MEPM or DWL models. This would seem to imply that the MEPM force constants will give an upper limit on the effects of phonon anisotropy in zinc, unless the pseudopotential is modified.

In summary, this section has dealt with the pseudopotential and phonons to be used in our zinc calculations. We use the local form of the accurate empirical Stark-Falicov pseudopotential. Two force constant models, MEPM and DWL, have been discussed. The MEPM force constants give a good fit to the measured dispersion curves of MEP, and also the electron-phonon mass enhancement λ. The DWL force constants predict low frequency phonon branches which are generally higher than those of MEPM; and the DWL value of λ is much smaller than the experimental value.

FIGURE CAPTIONS - SECTION 3.3

FIGURE 3.3.1: Local form of the zinc Stark-Falicov pseudopotential form factors.

FIGURE 3.3.2: Two zinc phonon branches along the ΓA direction. The experimental data (⧫) is from reference 55. These are the only two measured branches which are affected by the change from (---)MEP force constants to (———)MEPM force constants.

FIGURES 3.3.3 and 3.3.4: Zinc phonon dispersion curves as calculated with the MEPM force constants (solid lines). The dots are the lowest measured [55] phonon branches in the basal plane. The dashed curves are the original MEP model results in the AL, LH and HA directions.

FIGURE 3.3.5: The phonon frequency dependence of the Fermi surface averaged $\alpha^2 F(\omega)$ (solid line) and the frequency distribution $F(\omega)$ (dashed line) for zinc, using MEPM force constants.

FIGURES 3.3.6 and 3.3.7: Zinc phonon dispersion curves as calculated with the DWL force constants. The dots are the lowest measured [55] phonon branches in the basal plane.

FIGURE 3.3.8: The phonon frequency dependence of $\alpha^2 F(\omega)$ (solid line) and the frequency distribution $F(\omega)$ (dashed line) for zinc, using DWL force constants.

Figure 3.3.1

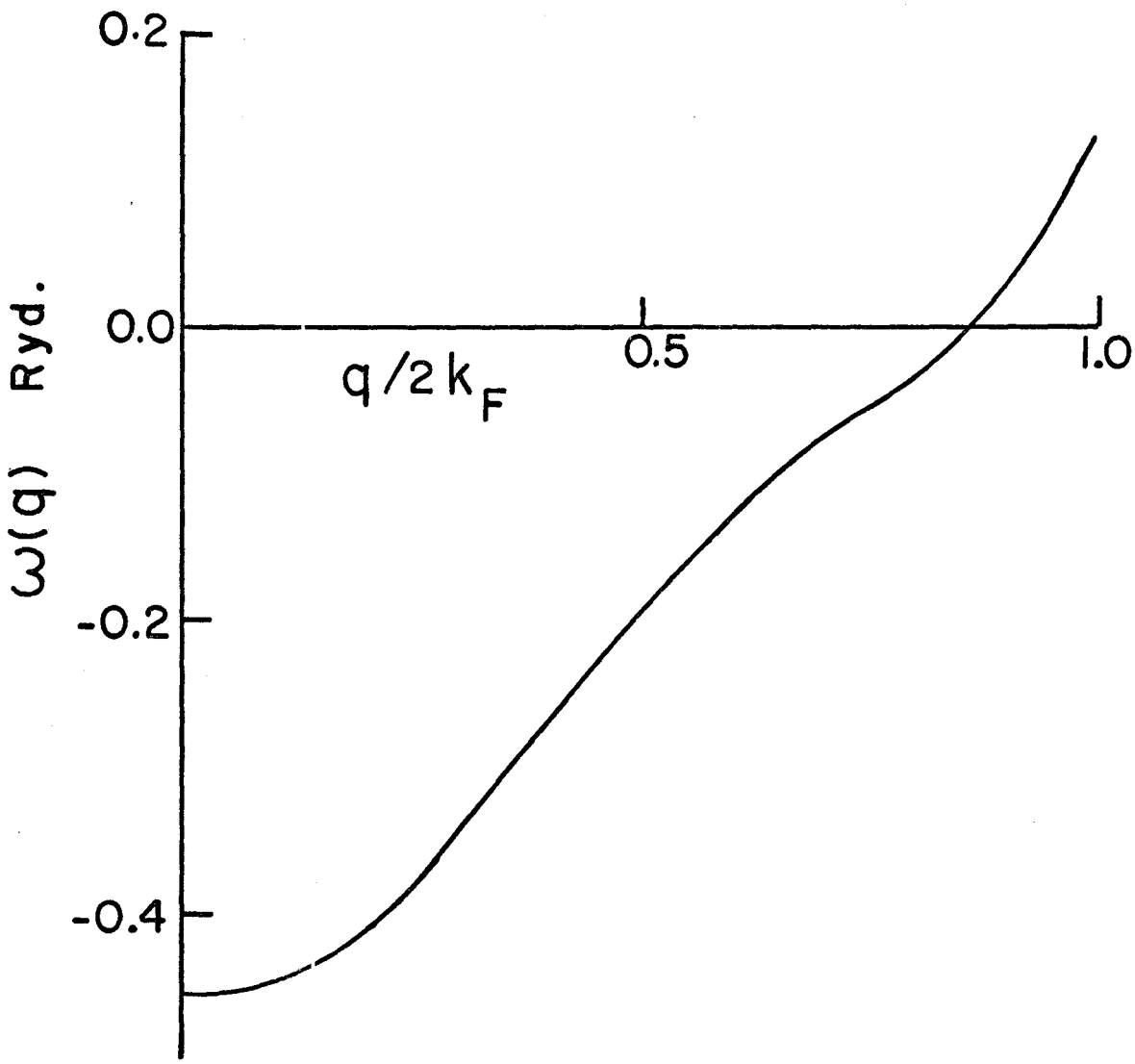

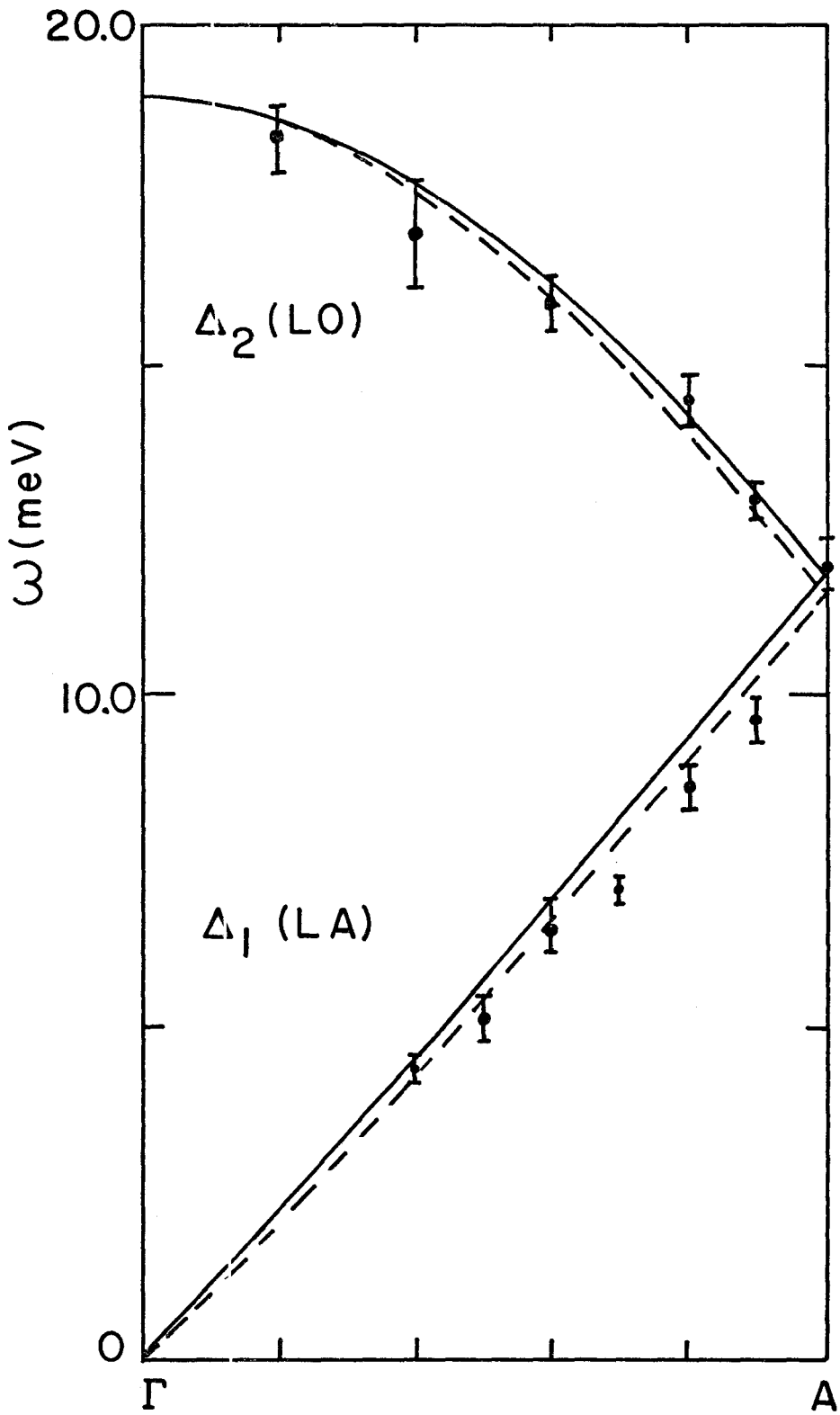
20.0
10.0
0
ω(meV)
Δ2 (LO)
Δ1 (LA)
Γ
A

Figure 3.3.3

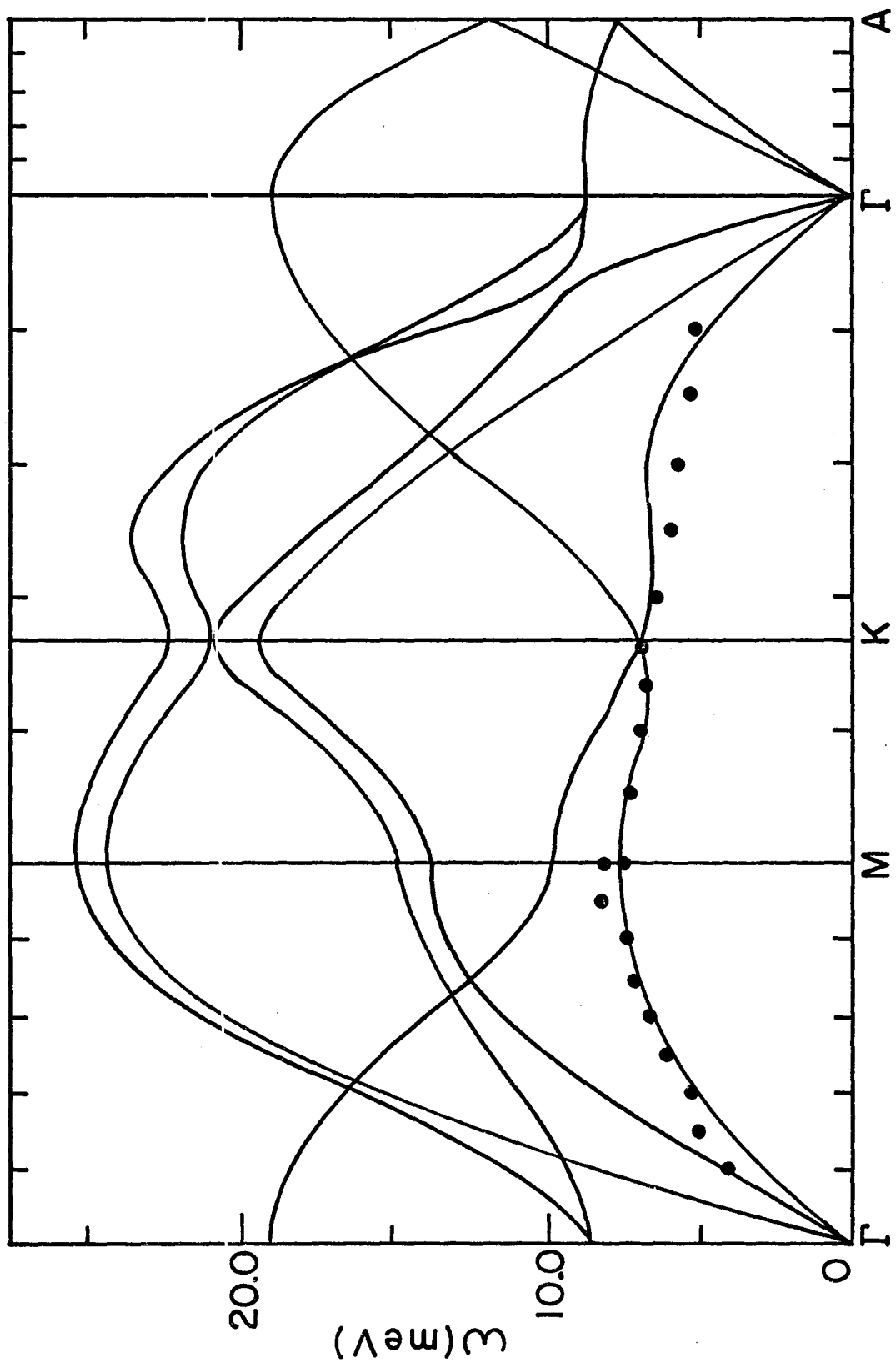

Figure 3.3.4

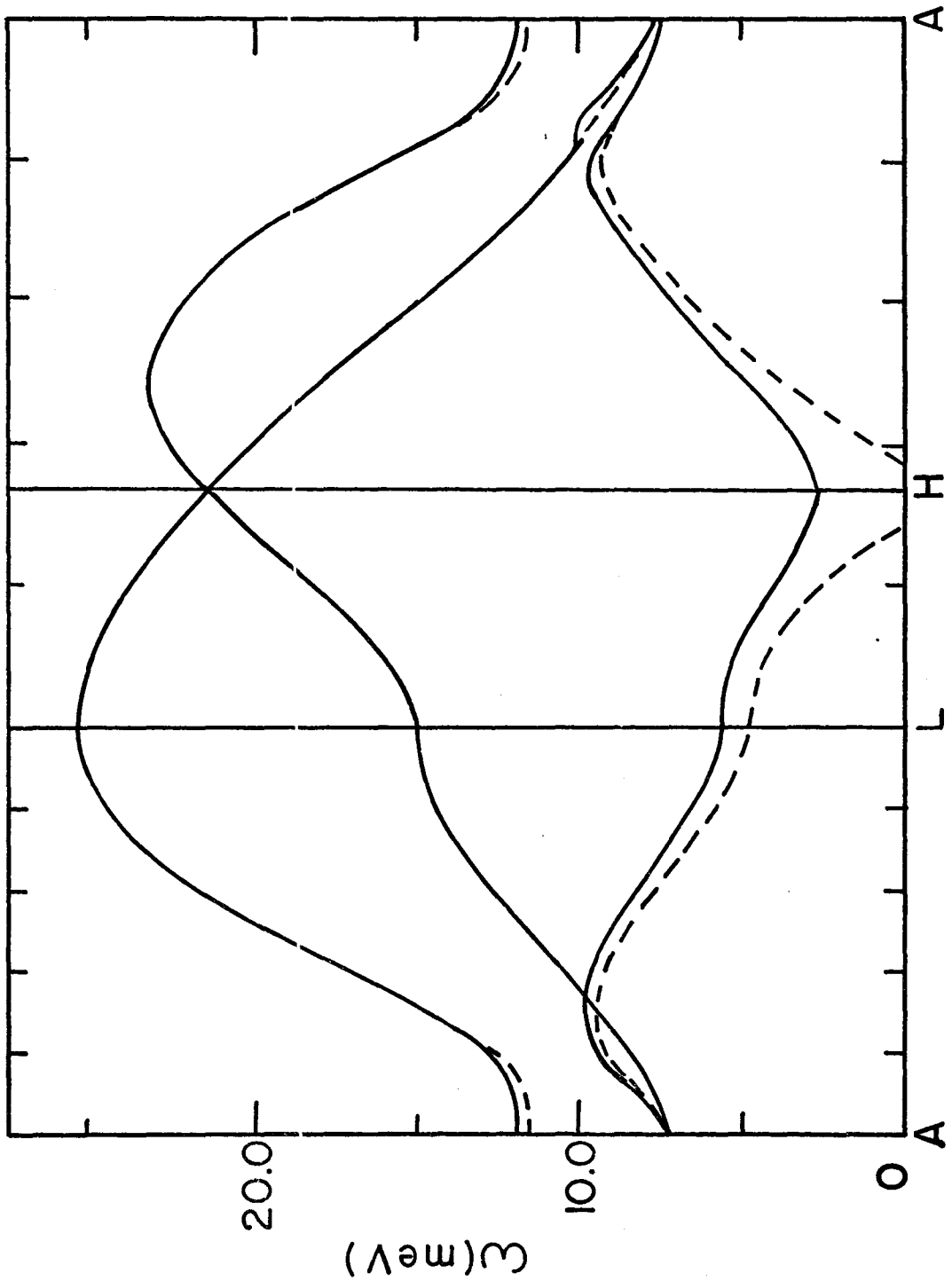

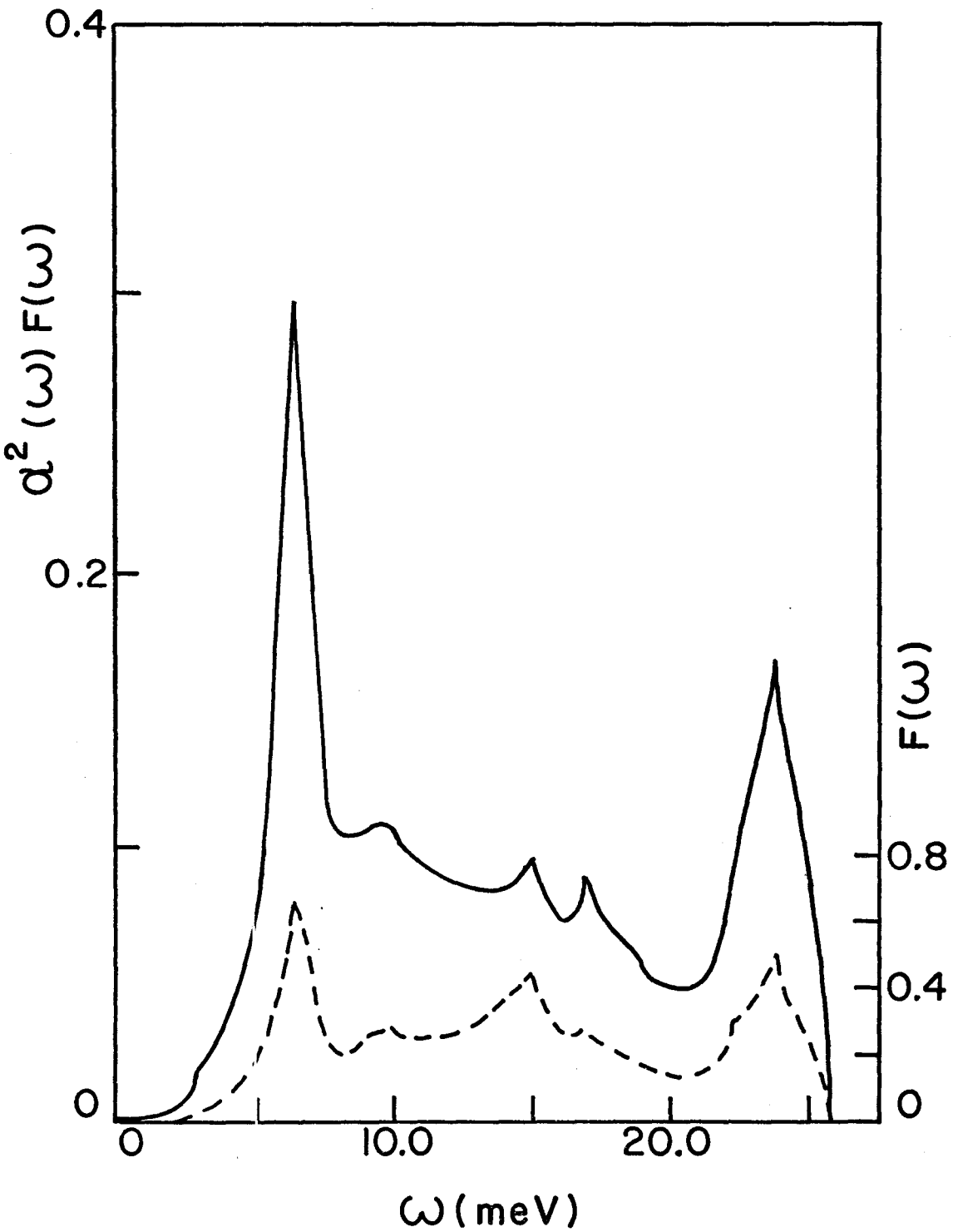
0.4
0.2
0
$\alpha^2(\omega)F(\omega)$
F(ω)
0.8
0.4
0
0
10.0
20.0
ω(meV)

Figure 3.3.6

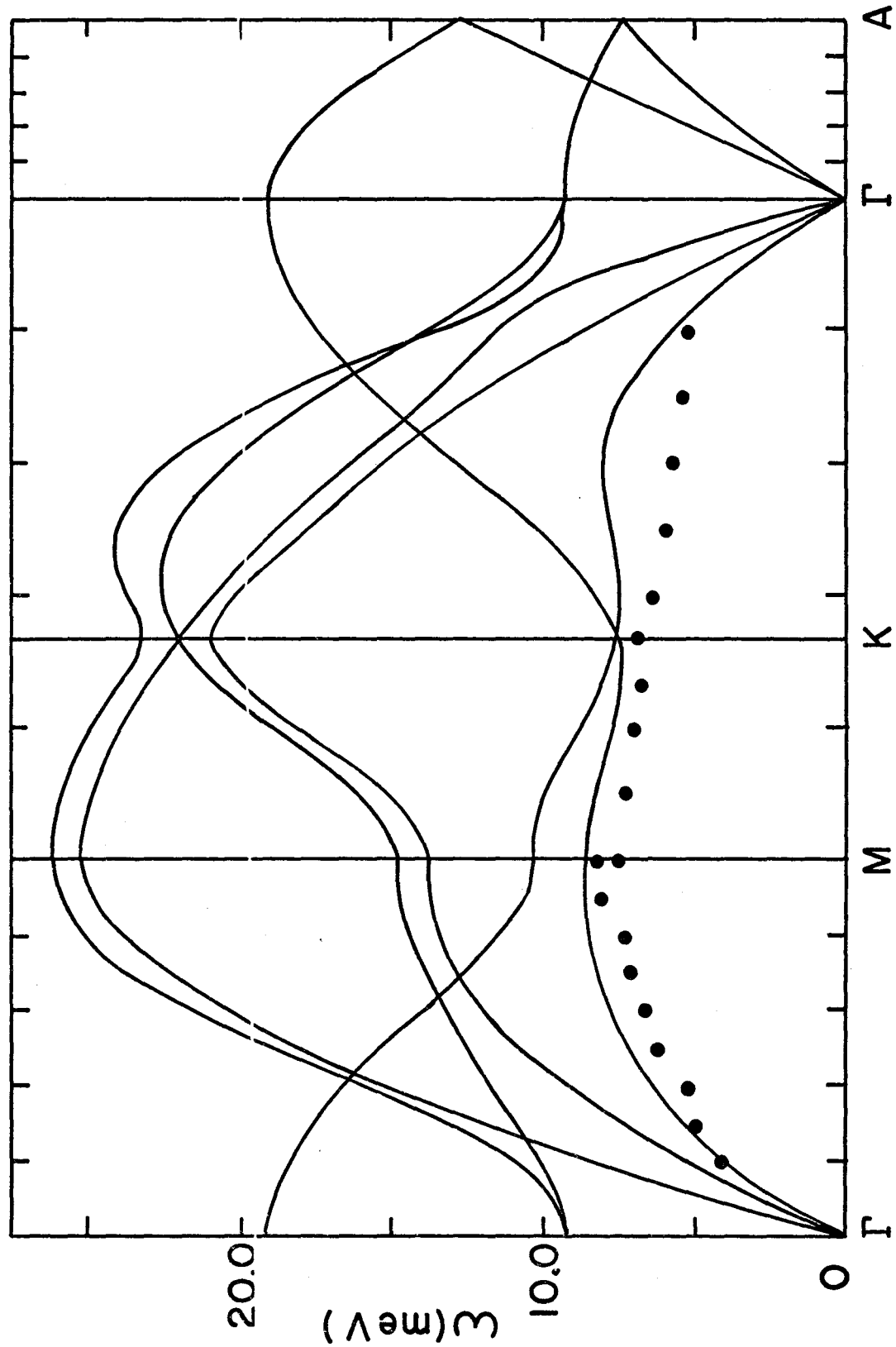

Figure 3.3.7

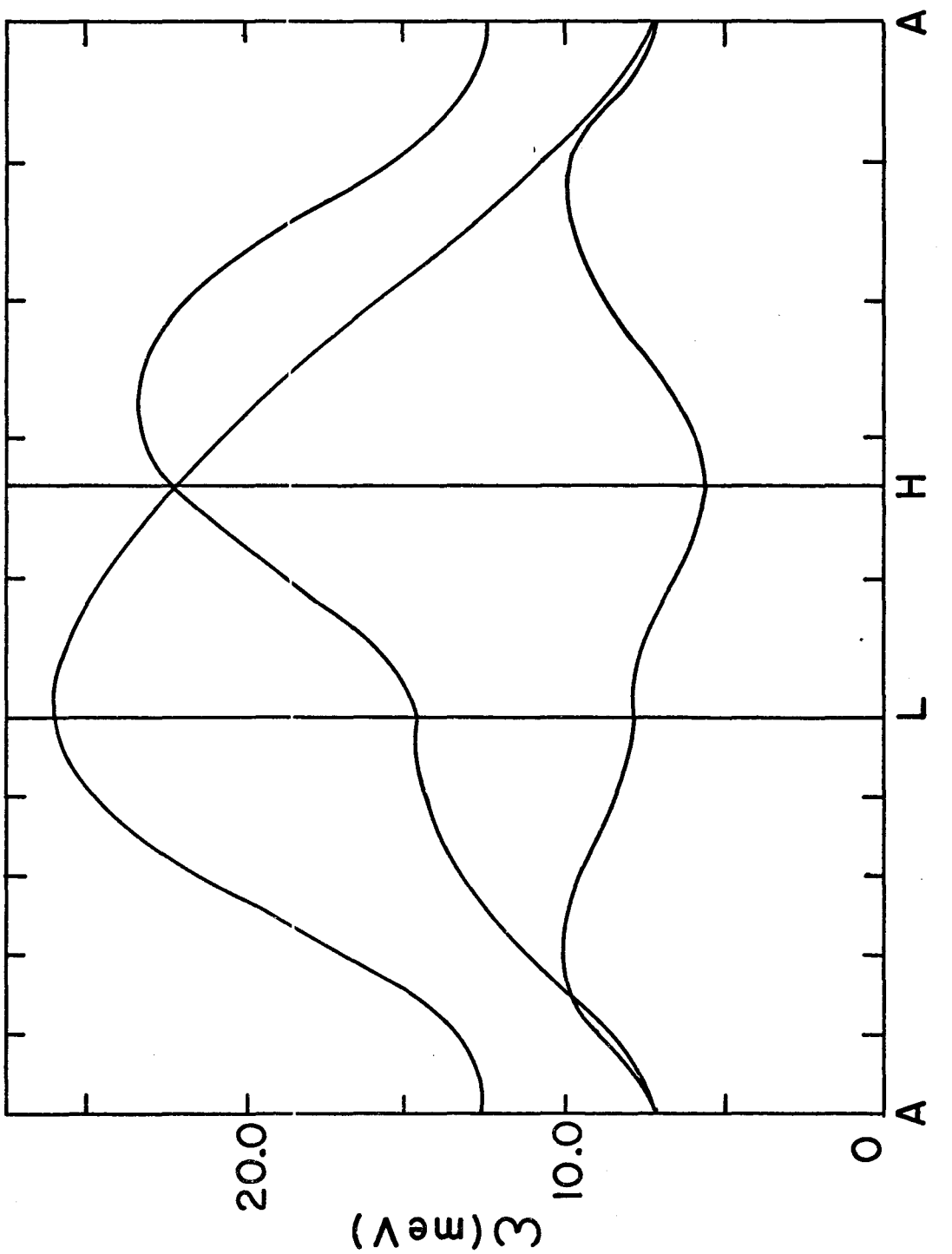

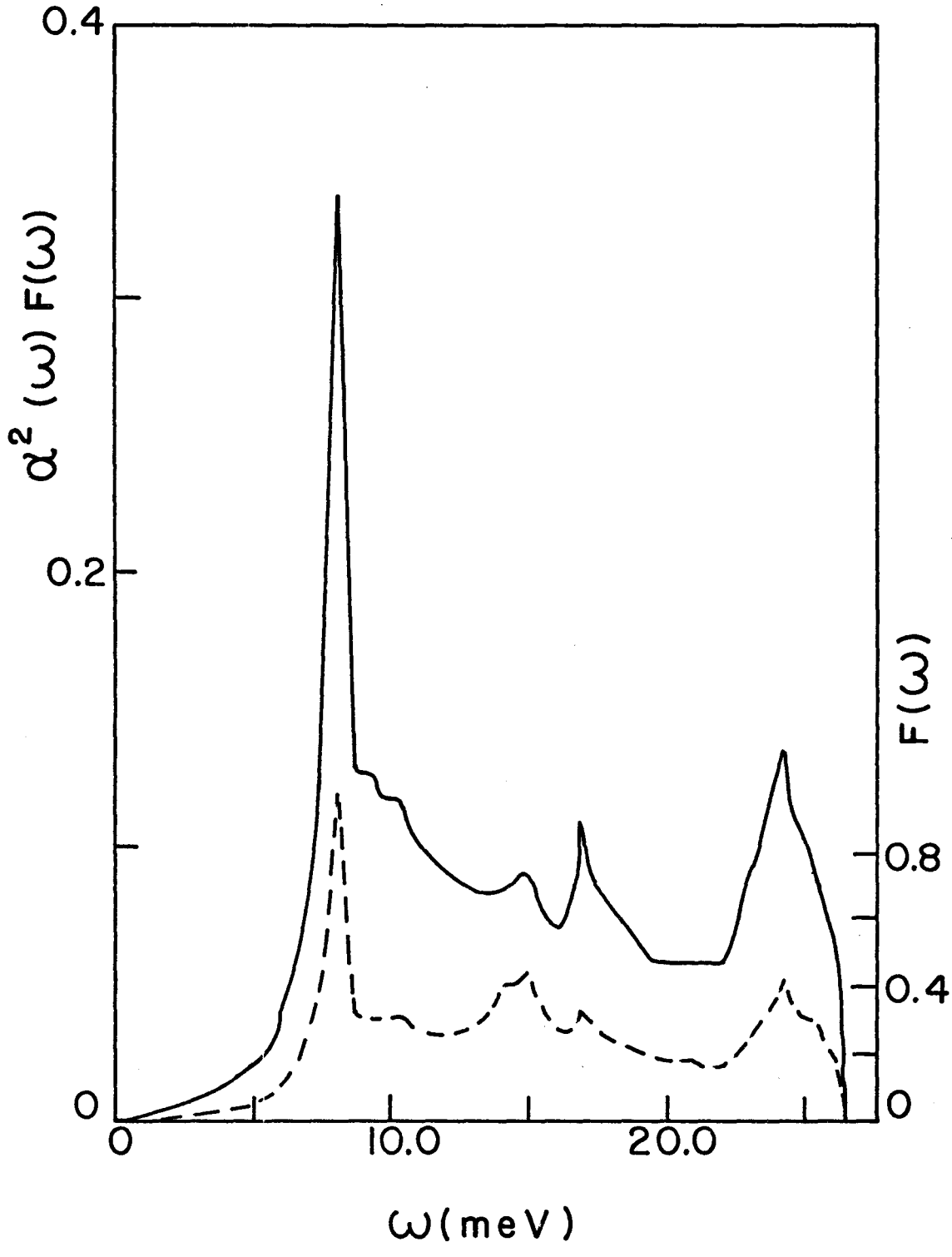
0.4
0.2
0
$\alpha^2(\omega)F(\omega)$
0
10.0
20.0
ω(meV)
F(ω)
0.8
0.4
0

3.4 PSEUDOPOTENTIALS AND FORCE CONSTANTS: THALLIUM

A good deal of agreement is found to exist between the phonon spectrum derived from superconducting tunneling experiments and that obtained by inelastic neutron scattering data. However, some discrepancy apparently exists in thallium. In this section, we discuss the reasons for these differences, and show how they can be largely eliminated. While, at the same time, determining the force constants and pseudopotentials to be used throughout our calculations.

Inelastic neutron scattering yields the phonon dispersion curves in metals and other systems, usually along high symmetry directions. These are fit by a Born-von Kármán force constant model, which is then used to generate the phonon frequency distribution $F(\omega)$. For a strong coupling superconductor, such as thallium, there exists an independent method of obtaining very much the same information. It is superconducting tunneling [20,21] on diodes involving strong coupling systems. In the current-voltage characteristics of such devices there exists an image of the phonons.

The I-V data can be "inverted" by the technique of McMillan and Rowell [20] to yield the phonon function $\alpha^2F(\omega)$. As mentioned previously, this function may be thought of as a product of some average electron-phonon coupling strength $\alpha^2(\omega)$, times the phonon frequency distribution $F(\omega)$. In as

much as the assumption that $\alpha^2(\omega)$ does not vary significantly with energy is valid, we obtain an independent measure of $F(\omega)$ which can be compared with neutron data.

A review of such comparisons has been made by Rowell and Dynes [98]. Generally, a considerable degree of agreement is obtained between these two techniques. At the moment, however, Tl appears to be an exception.

Worlton and Schmunk [58] (hereafter referred to as WS) have recently used neutron inelastic scattering to measure the Tl phonon dispersion curves in the ΓM and ΓA directions, at 77°K and 296°K. They analyzed their data in terms of the MAS model (section 3.1), and used a least-squares fit to derive the force constants. Since we are primarily interested in low temperature calculations we restrict our attention to their 77°K results, for which WS present three force constant models. We discuss model 1A [58], because its fit to experiment is as good or better than the other two models.

The dispersion curves as predicted by the WS model 1A are given in figures 3.4.1 and 3.4.2, where we have used the lattice parameters [100] a = 3.4496 Å and c = 5.5137 Å. It is interesting to note that the more than linear increase in some of the acoustic modes, for small q, has been predicted by van der Hoeven and Keesom [101] on the basis of specific heat measurements in Tl.

The frequency distribution, calculated using the 1A model, is shown in figure 3.4.3 by the dashed line. The I-V characteristics of thallium have been measured [56,57], and the dots in this figure correspond to the inverted data of Dynes [57,102]. There is almost no agreement between $F(\omega)$ and the experimental $\alpha^2F(\omega)$. The position and magnitude of the peaks are different, and in particular there is a marked difference in the low energy structure.

However, the comparison should actually be made between the experimental data and $\alpha^2F(\omega)$ calculated from the 1A force constants. In addition to the phonons, this calculation requires the pseudopotential and the band mass. The band mass may be estimated from the experimental value [101] of the coefficient of the electronic specific heat $\gamma_{Expt.} = 1.47$ mJ mole^{-1} deg^{-2}, which, from equation (3.28) implies that $m^*_{Expt.} = 1.13$. The use of Dyne's value [57] $\lambda_{Expt.} = 0.78$ in equation (3.27) gives

$$m_B(\text{Expt.}) = 0.64 \quad . \tag{3.29}$$

For the time being, we take $m_B = 0.64$ to be one of the constraints imposed on our pseudopotential fit to the experimental $\alpha^2F(\omega)$.

The initial pseudopotential used is that of Animalu and Heine [103] calculated by the Heine-Abarenkov [104] method, and tabulated in Harrison [69]. In this method the

pseudopotential is fitted to spectroscopic data on the free ions. It has been found that these form factors generally give satisfactory results for the electronic properties, although not in all cases. The dashed curve of figure 3.4.4 shows the Tl Heine-Abarenkov form factors. Using the above quantities we are able to calculate $\alpha^2F(\omega)$, which is shown in figure 3.4.3 as the solid line.

Unfortunately, agreement with experiment is no better for the calculated $\alpha^2F(\omega)$ than it was for $F(\omega)$; and, if anything, it is actually worse; since, the low frequency structure has been decreased in importance relative to the high frequency peaks. However, the absolute magnitude of the calculated and experimental results appear to be in agreement, and this implies that the chosen m_B value is adequate.

To see how these discrepancies can be removed we compare $F(\omega)$ and $\alpha^2F(\omega)$ in figure 3.4.3, and also the zinc results of figures 3.3.5 and 3.3.8. In general, inclusion of the coupling function $\alpha^2(\omega)$ modulates the heights of the $F(\omega)$ peaks; but it does not affect the peak number or position. Therefore, to bring the Tl calculated and experimental $\alpha^2F(\omega)$'s into agreement, both the pseudopotential and the force constants must be modified.

In WS it was assumed that the force constants in the z-direction were proportional to those describing forces in

the basal plane. DWL found that, although Be data could be fit with this assumption, it had to be dropped for Zn. Thus, there is no real reason to apply this constraint to Tl, and this would affect the least squares fit of WS. The Tl dispersion curves show large changes as the temperature is decreased from 296°K to 77°K, therefore, the 77°K phonons may not be entirely representative of the phonons at superconducting temperatures. Also, WS required that the 1A model should reproduce the elastic constants. Section 3.2 and the appendix stress that these phonons are of little importance to our results. Finally, some of the experimental error bars are quite large. For these reasons, and the sensitivity of the MAS model, we feel that we are justified in modifying the force constants.

The 1A model force constants were adjusted with the idea that the resulting peak structure of $F(\omega)$ should correspond to the experimental $\alpha^2F(\omega)$. Also, the fit to the measured phonon branches should be comparable to that obtained by the original 1A model. The modified force constants chosen (which we shall refer to as WSM) are listed in table 3.1, along with the corresponding 1A values. Figure 3.4.5 compares the resulting WSM fit (solid lines) and the original 1A fit (dashed lines) to the experimental data of WS. The major change occurs for the Σ_3 optic branch, for which agreement has been improved. The Δ_5 and

TABLE 3.1

MAS* Force Constants	T1-1A** (10^4 dyn. cm.$^{-1}$)	T1-WSM (10^4 dyn. cm.$^{-1}$)
K(1)	1.02475	1.02475
C_x(1)	-0.19278	-0.19278
C_z(1)		0.41769
K(2)	1.05406	1.19332
C_x(2)	-0.00733	-0.14659
C_z(2)		-0.21445
K(3)	-0.23860	-0.14592
C_x(3)	0.08603	0.05470
C_z(3)		-0.12602
K(4)	-0.14887	-0.30554
C_x(4)	-0.02527	-0.02527
C_z(4)		0.04833
K(5)	0.18162	0.18162
C_x(5)	0.00314	0.00314
C_z(5)		-0.04518
K(6)	-0.11599	0.02327
C_x(6)	0.01008	0.01008
C_z(6)		0.11127

* The (κ,κ') dependence has been dropped.

** This column is from reference (58), where $C_z = \sigma_B C_x$ with $\sigma_B = -1.91267$.

Δ_6 branches remain unchanged, and the fits to the other branches are not very different.

Figures 3.4.6 and 3.4.7 show the high symmetry dispersion curves as given by our WSM model. Comparing with the 1A model results, figures 3.4.1 and 3.4.2, it is apparent that the branches along the unmeasured ΓK and MK directions have been considerably shifted. This is particularly noticeable at the point K. Also, the lowest H-point frequency has been decreased and phonon modes in this region will now contribute to the low energy peak in $F(\omega)$ and $\alpha^2F(\omega)$.

Figure 3.4.8(b) gives $\alpha^2F(\omega)$ as calculated using our WSM force constants and the Heine-Abarenkov pseudopotential. Agreement with experiment (dots) has been considerably improved, with the peaks occurring at approximately the correct energies. However, large differences still exist in the peak magnitudes.

To remove this remaining discrepancy the pseudopotential must be changed. We choose one of the simplest models, the "empty-core model" [75] proposed by Ashcroft [105], which assumes the following form for the ionic pseudopotential

$$v^{ion}(r) = 0 \qquad \text{for } r < R_c$$
$$= -\frac{Ze^2}{r} \qquad \text{for } r > R_c \quad . \tag{3.29}$$

R_c is an adjustable parameter to be determined from experiment, and Z is the ionic charge in units of the electronic charge e. Then the pseudopotential form factor is given by

$$w(q) = \frac{Z}{\Omega_0} \frac{4\pi e^2}{q^2} \frac{\cos(qR_c)}{\varepsilon(q)} \quad , \tag{3.30}$$

where we have included the Hartree self-consistent screening [69]

$$\varepsilon(q) = 1 + \frac{e^2 k_F}{\pi q^2} \{1 + \frac{1}{qk_F}(k_F^2 - (q/2)^2) \ln|\frac{q+2k_F}{q-2k_F}|\} \quad ; \tag{3.31}$$

and k_F is the Fermi wavevector.

The function $\alpha^2F(\omega)$ was calculated using the experimental estimate $m_B = 0.64$, the WSM force constants, and the above Ashcroft pseudopotential. The parameter R_c was varied until good agreement with experiment was obtained. This was achieved with $R_c = 0.875$ Å, where figure 3.4.9 compares the calculated $\alpha^2F(\omega)$ (solid line) with the experimental result of Dynes (dots). It seems fair to say that the overall agreement is very good. However, it should be remembered that the force constants and pseudopotential have been adjusted with just this result in mind.

The $R_c = 0.875$ Å pseudopotential form factors are given in figure 3.4.4. They are very different from the Heine-Abarenkov curve. This result need not be unreasonable as may be seen by referring to figure 2 of reference 38,

where the Heine-Abarenkov form factors for cadmium are compared to accurate empirical results derived by the Stark-Falicov method. In this case, also, the differences are very large.

Holtham and Priestley [106] have recently obtained a good fit to thallium de Haas-van Alphen data by using a local pseudopotential. Their pseudopotential Fourier coefficients are given in figure 3.4.4 by the black dots, where these values were determined by adjusting the Heine-Abarenkov form factors (dashed line). We decided to attempt to fit the experimental $\alpha^2F(\omega)$ with another pseudopotential, whose form factors are more similar to the Holtham-Priestley results. However, in this case it was found that both R_c and m_B had to be adjusted to $m_B = 0.44$ and $R_c = 0.435$ Å to obtain the very good agreement with experiment shown in figure 3.4.10. These form factors are also given in figure 3.4.4.

We note that the $\alpha^2F(\omega)$'s given by our pseudopotentials Tl(0.875) and Tl(0.435) are almost identical. However, the band masses are different and they will give different values for the specific heat mass. Figure 3.4.8(a) has been included in this section to illustrate that agreement with experiment cannot be obtained by just varying the pseudopotential and leaving the 1A force constants unchanged.

From figure 3.4.8(b) one can roughly predict the sort of change in the pseudopotential (from the Heine-Abarenkov form) which is needed to obtain agreement with the experimental

$\alpha^2F(\omega)$. It appears as if the strength of the umklapp (large q) process must be increased to build up the low energy peak. This may be done by increasing the value of $|w(q)|^2$ near $2k_F$; which corresponds to shifting the node of the form factors to the left (figure 3.4.4) or farther to the right, past $2k_F$.

If we shift to the left, then the umklapp processes will be built up - hopefully at the expense of higher frequency contributions. This is essentially what has been accomplished by the Ashcroft Tl(0.875) pseudopotential. If the shift is to the right, the low frequency peak will be increased; but the high frequency peak will also be built up, as $|w(q)|^2$ is increased throughout the whole $0 \leq q \leq 2k_F$ range. Therefore, a shift to the right may reproduce the shape of $\alpha^2F(\omega)$; but the magnitude will be too large. A decrease of the band mass parameter m_B will then be needed to obtain agreement with experiment. This is what has occurred for our Tl(0.435) model.

In summary, it has been shown that there is no real discrepancy between the superconducting tunneling and inelastic neutron scattering results. The original poor agreement shown in figure 3.4.3 is apparently due to the force constant model and pseudopotential used to process the neutron data. A set of force constants (WSM) has been found which reproduces the observed peak structure in $\alpha^2F(\omega)$. These force constants are used throughout our Tl calculations.

Two very different Ashcroft pseudopotentials have been obtained, which (when combined with the WSM force constants) give almost identical $\alpha^2F(\omega)$'s; and very good agreement with experiment is obtained. The first pseudopotential Tl(0.875) takes the experimental estimate $m_B = 0.64$; while the second Tl(0.435) has a band mass value of $m_B = 0.44$.

We point out that (from figures 3.4.9 and 3.4.10) thallium seems to be a case where $\alpha^2(\omega)$ shows a strong increase in the low frequency peak region, above its value near the high frequency end of the spectrum. This is significant since it may not always be justified, even as a first approximation, to ignore the frequency dependence of $\alpha^2(\omega)$ when comparing $\alpha^2F(\omega)$ and $F(\omega)$.

FIGURE CAPTIONS - SECTION 3.4

FIGURES 3.4.1 and 3.4.2: Thallium dispersion curves as calculated with the 1A model force constants of reference 58.

FIGURE 3.4.3: The phonon frequency dependence of $\alpha^2F(\omega)$ (solid line) and $F(\omega)$ (dashed line) for Tl, compared with the experimental $\alpha^2F(\omega)$ (dots) of Dynes. These calculations were performed with the 1A model force constants, and the Heine-Abarenkov pseudopotential.

FIGURE 3.4.4: Thallium pseudopotential form factors considered in this section. The dashed curve is the Heine-Abarenkov result and the dots are the Fourier coefficients of Holtham and Priestley. The two "empty-core model" pseudopotential form factors, which we have fit to the experimental $\alpha^2F(\omega)$, are given by the solid lines.

FIGURE 3.4.5: The thallium phonon dispersion curves as measured (dots) by Worlton and Schmunk, and fit by their 1A model force constants (dashed lines). The solid lines show the fit obtained by our WSM force constants.

FIGURES 3.4.6 and 3.4.7: The thallium dispersion curves as calculated with our WSM force constants.

FIGURE 3.4.8: Comparisons of calculated (solid lines) and experimental (dots) $\alpha^2F(\omega)$'s, which illustrate some of the intermediate steps in fitting the pseudopotentials. Figure (a) uses the 1A force constants and the Tl(0.875) pseudopotential. Figure (b) uses the WSM force constants and the Heine-Abarenkov pseudopotential.

FIGURE 3.4.9: A comparison of calculated (solid line) and experimental (dots) $\alpha^2F(\omega)$'s, using the WSM force constants, the Tl(0.875) pseudopotential and $m_B = 0.64$. The dashed curve gives the frequency distribution $F(\omega)$.

FIGURE 3.4.10: A comparison of calculated (solid line) and experimental (dots) $\alpha^2F(\omega)$'s, using the WSM force constants, the Tl(0.435) pseudopotential and $m_B = 0.44$. The frequency distribution is the same as that shown in figure 3.4.9.

Figure 3.4.1

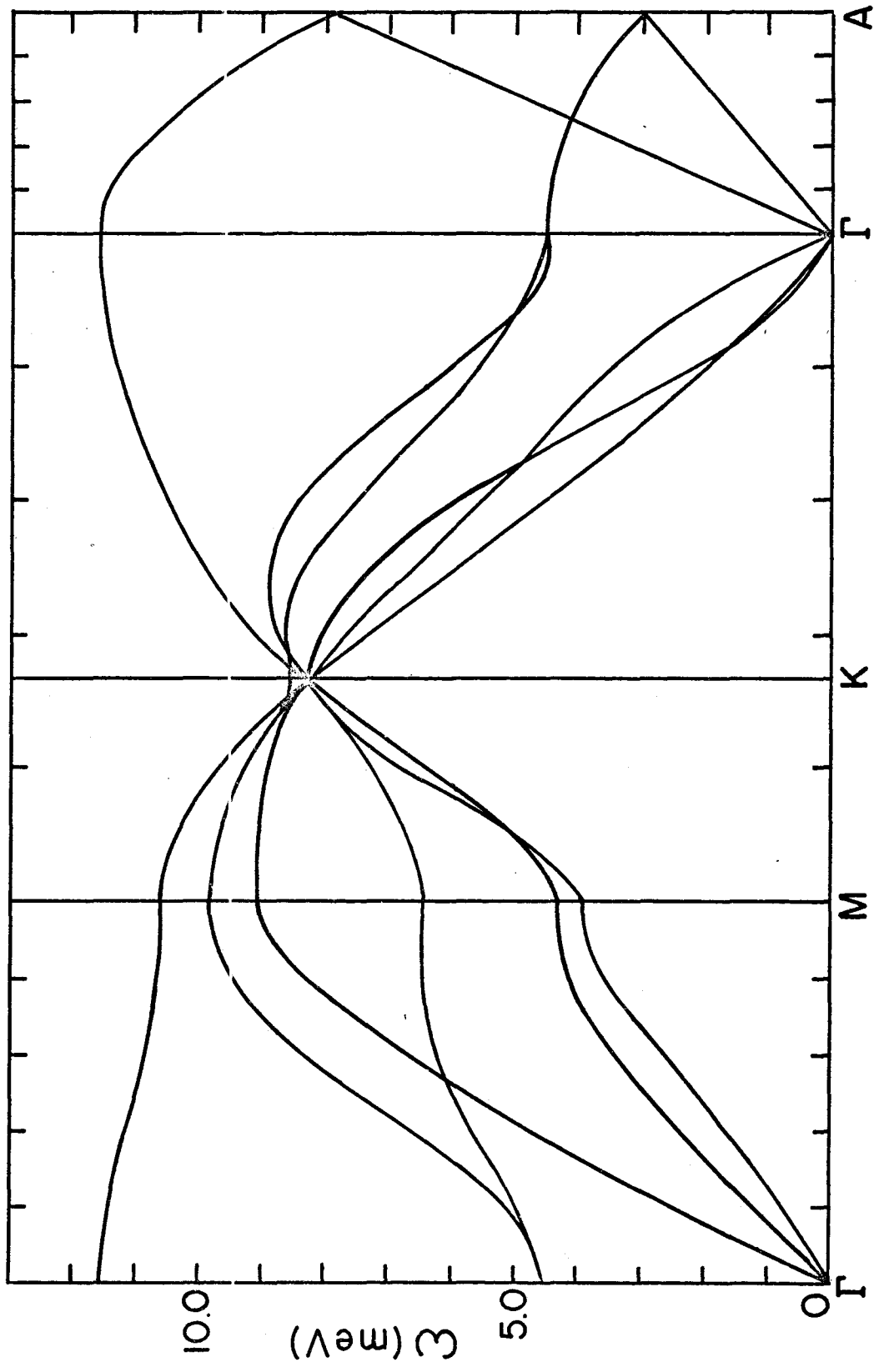

Figure 3.4.2

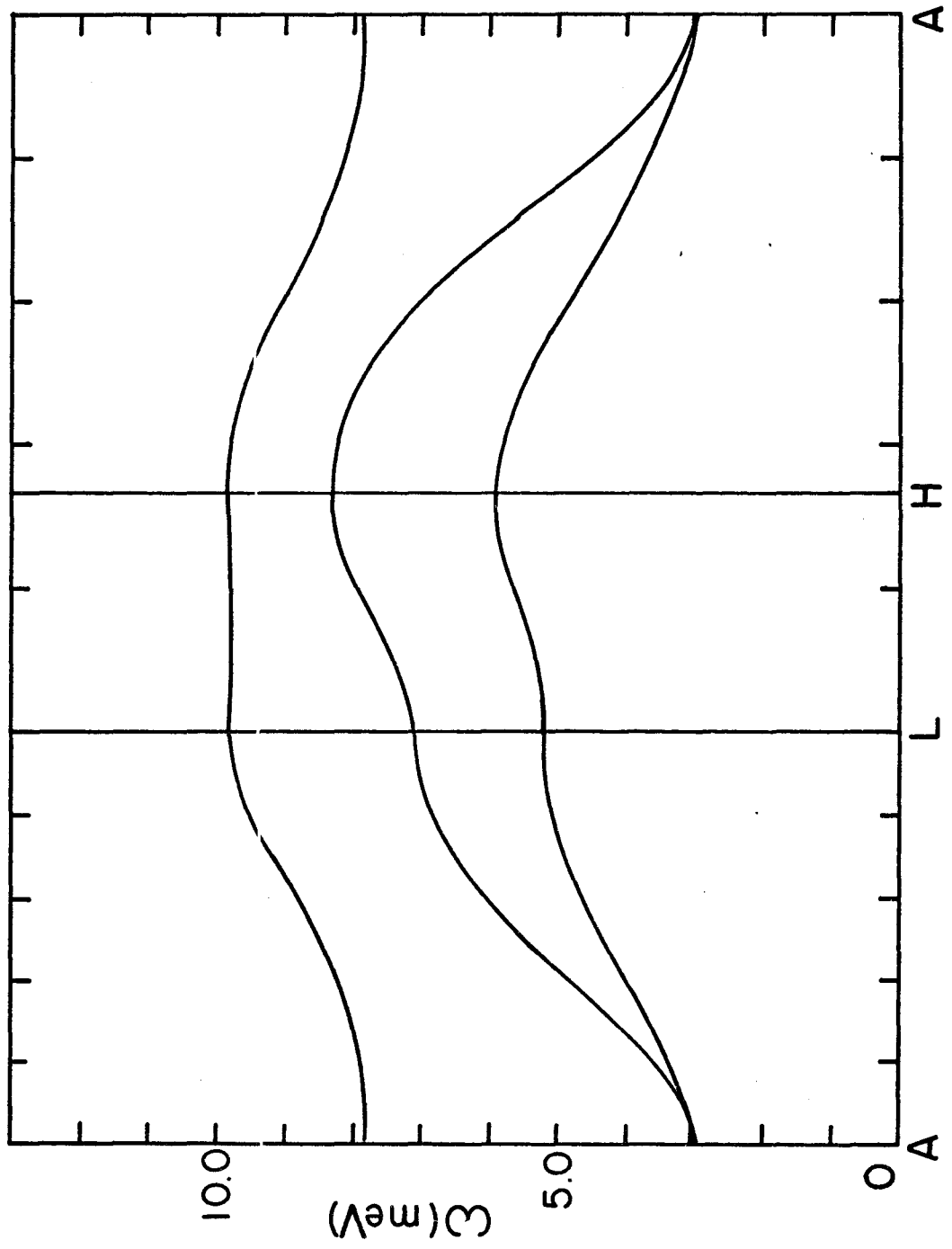

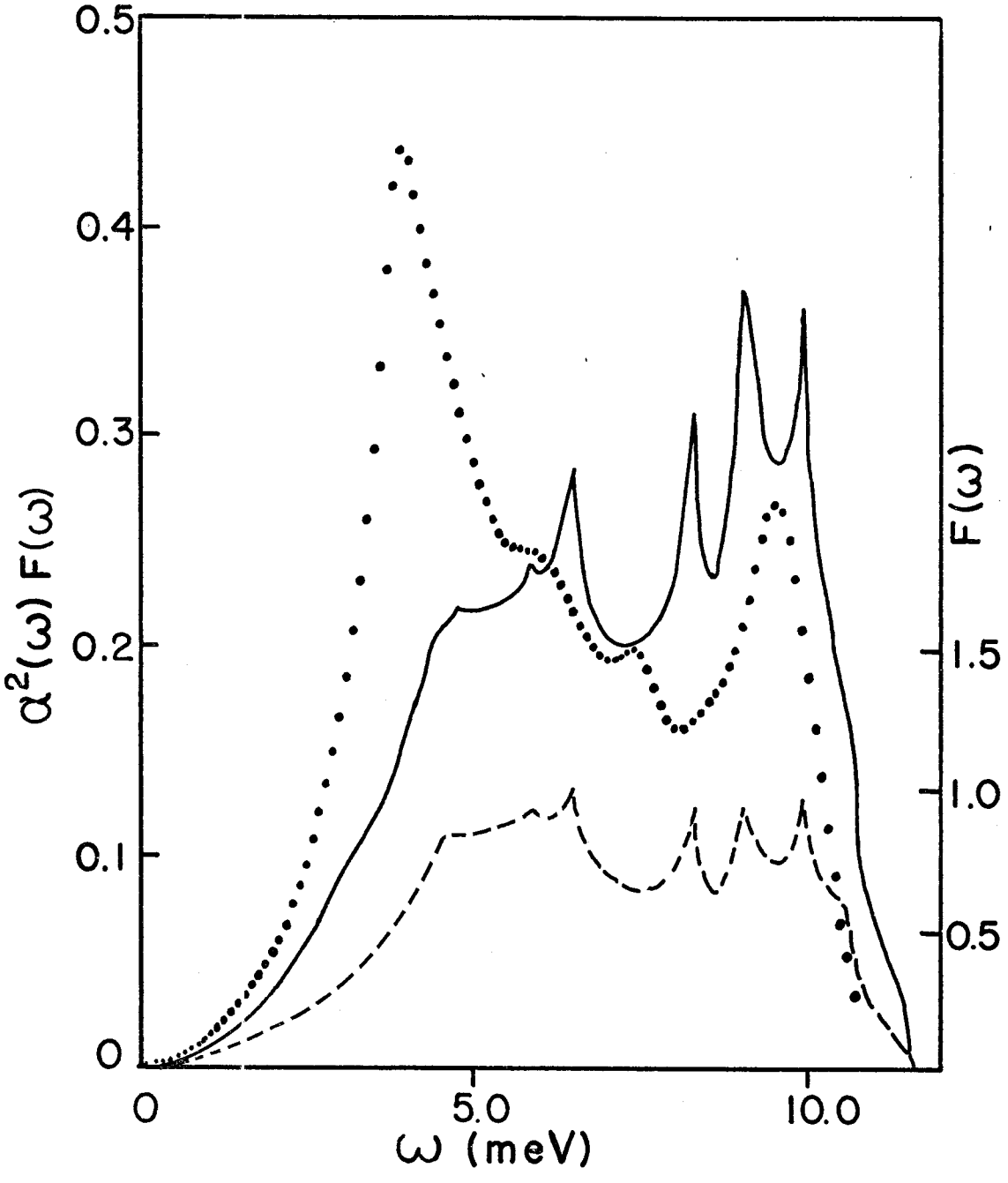
0.5
0.4
0.3
0.2
0.1
0
$\alpha^2(\omega)\,F(\omega)$
F(ω)
1.5
1.0
0.5
0
5.0
10.0
ω (meV)

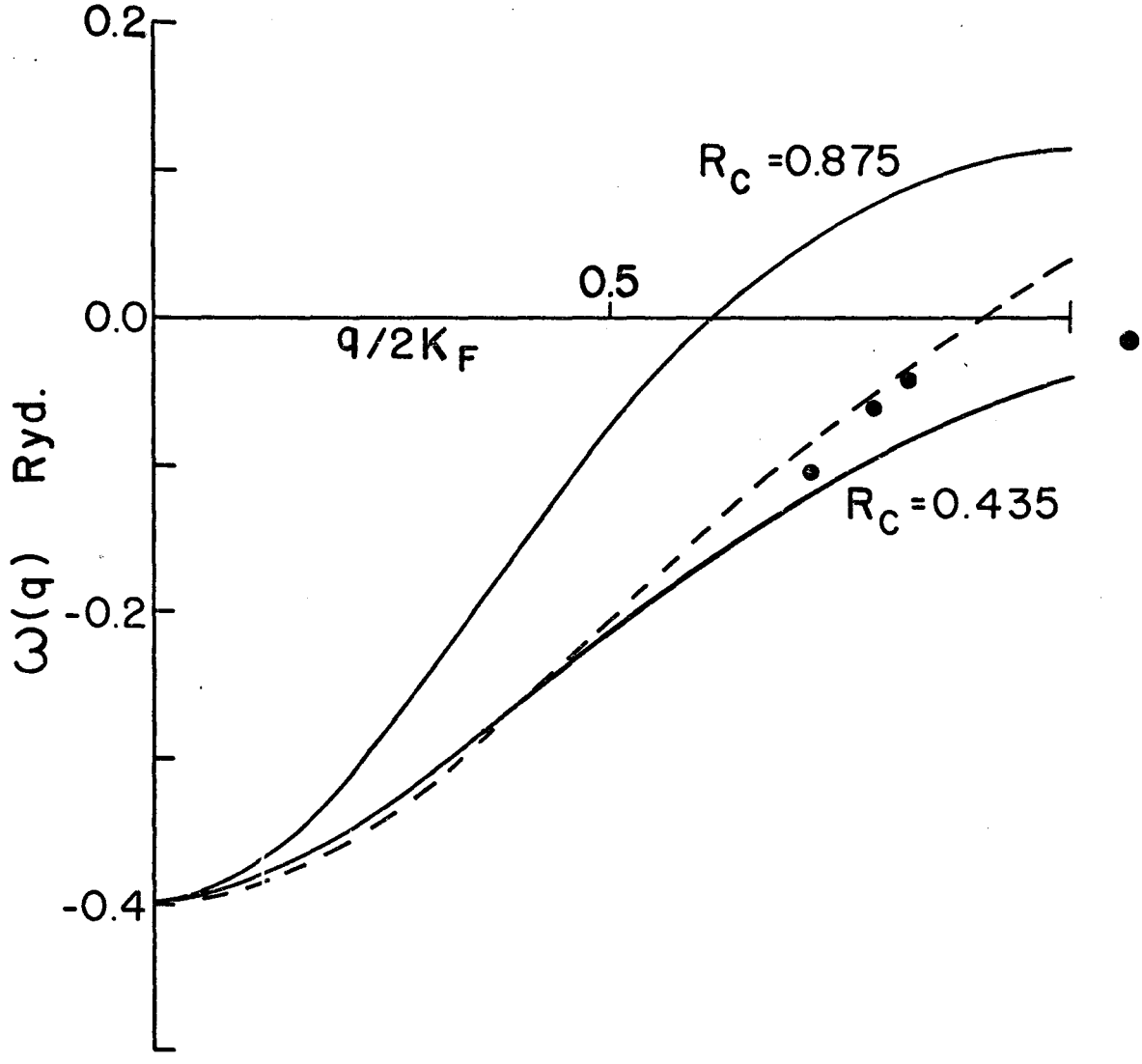
0.2
0.0
-0.2
-0.4
ω(q) Ryd.
0.5
q/2K_F
R_c =0.875
R_c =0.435

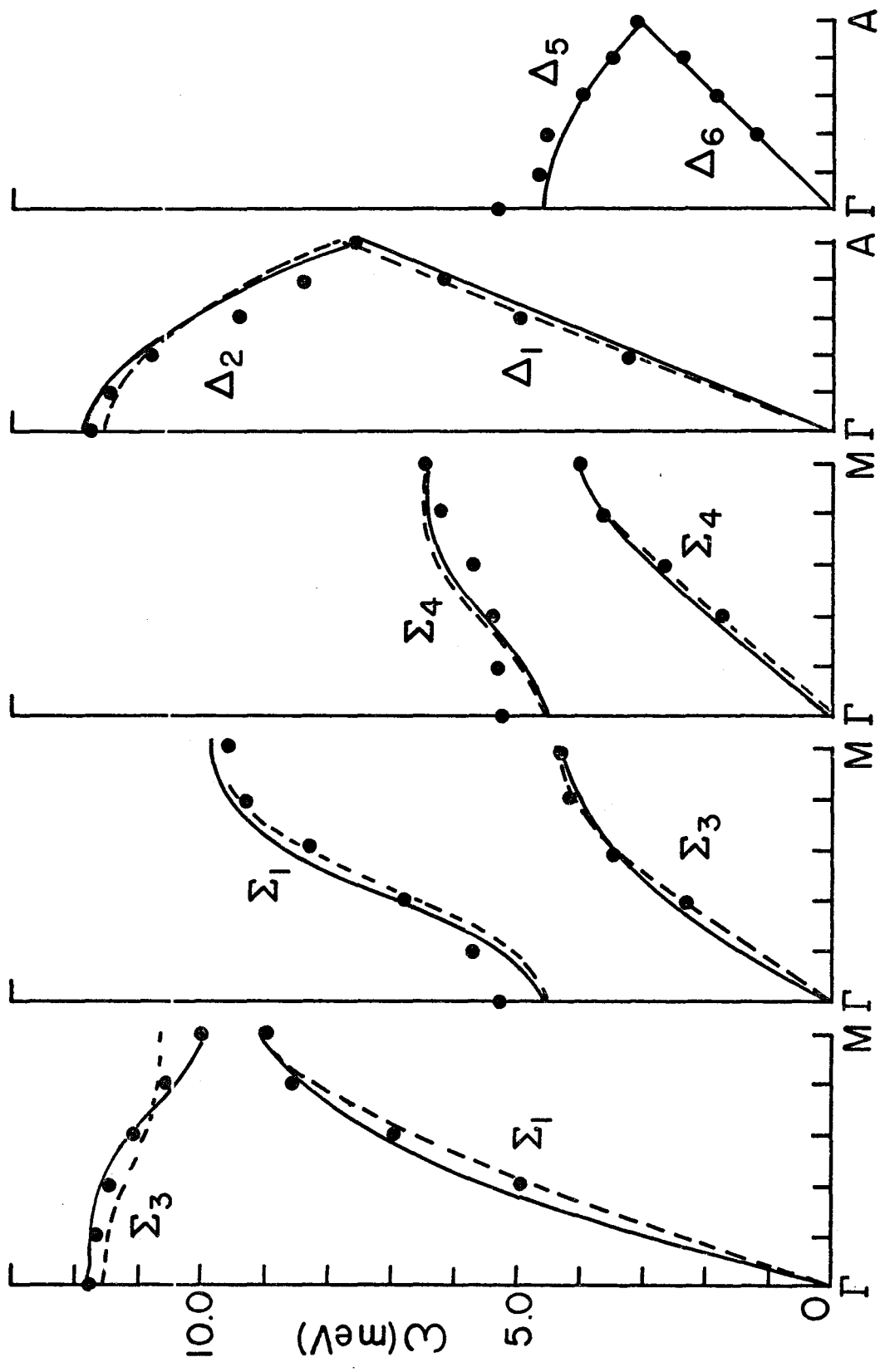
ω(meV)
10.0
5.0
0
Γ
M
Γ
Σ3
Σ1
M
Γ
Σ3
Σ1
M
Γ
Σ4
Σ4
A
Γ
Δ1
Δ2
A
Γ
Δ6
Δ5

Figure 3.4.6

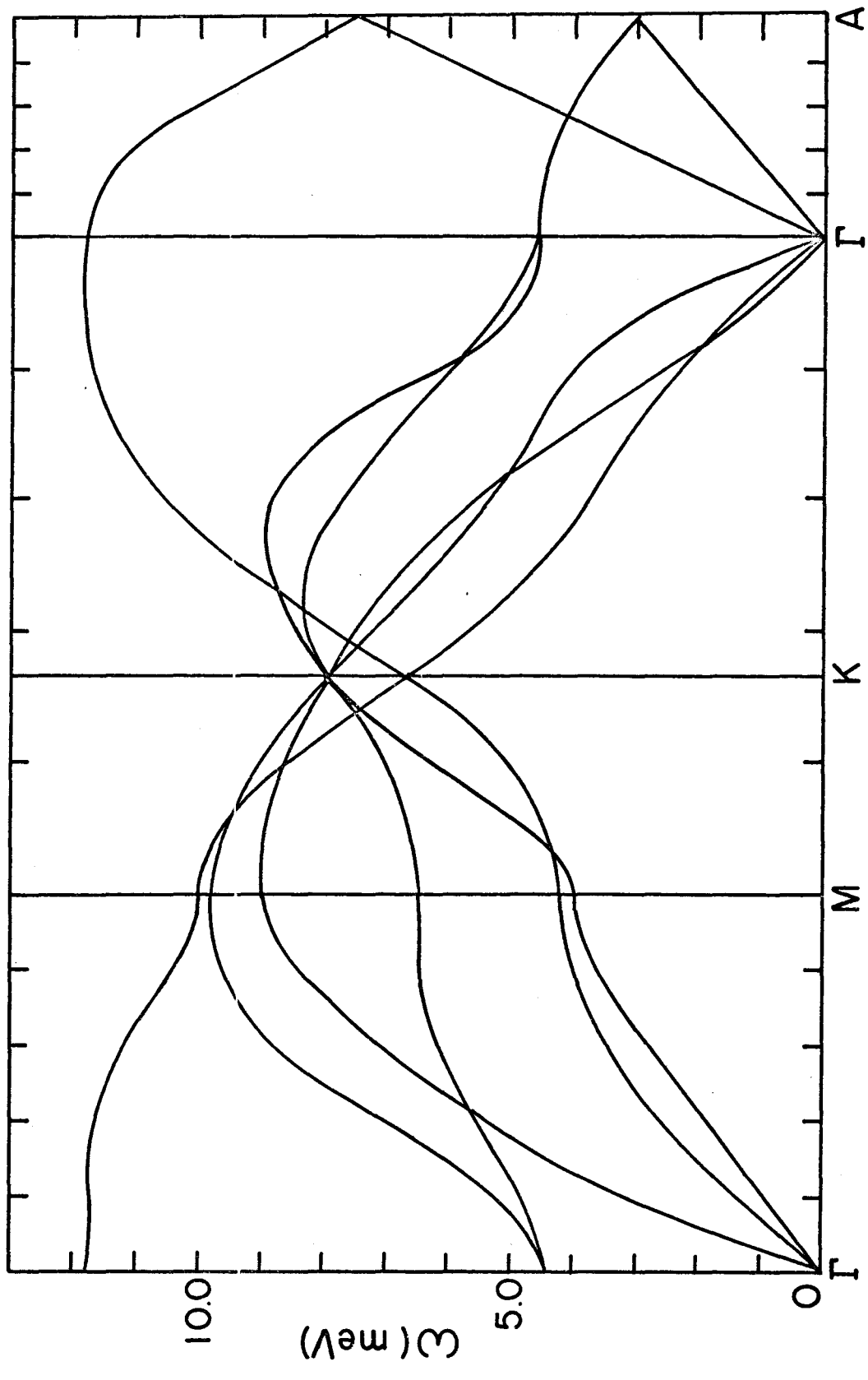

Figure 3.4.7

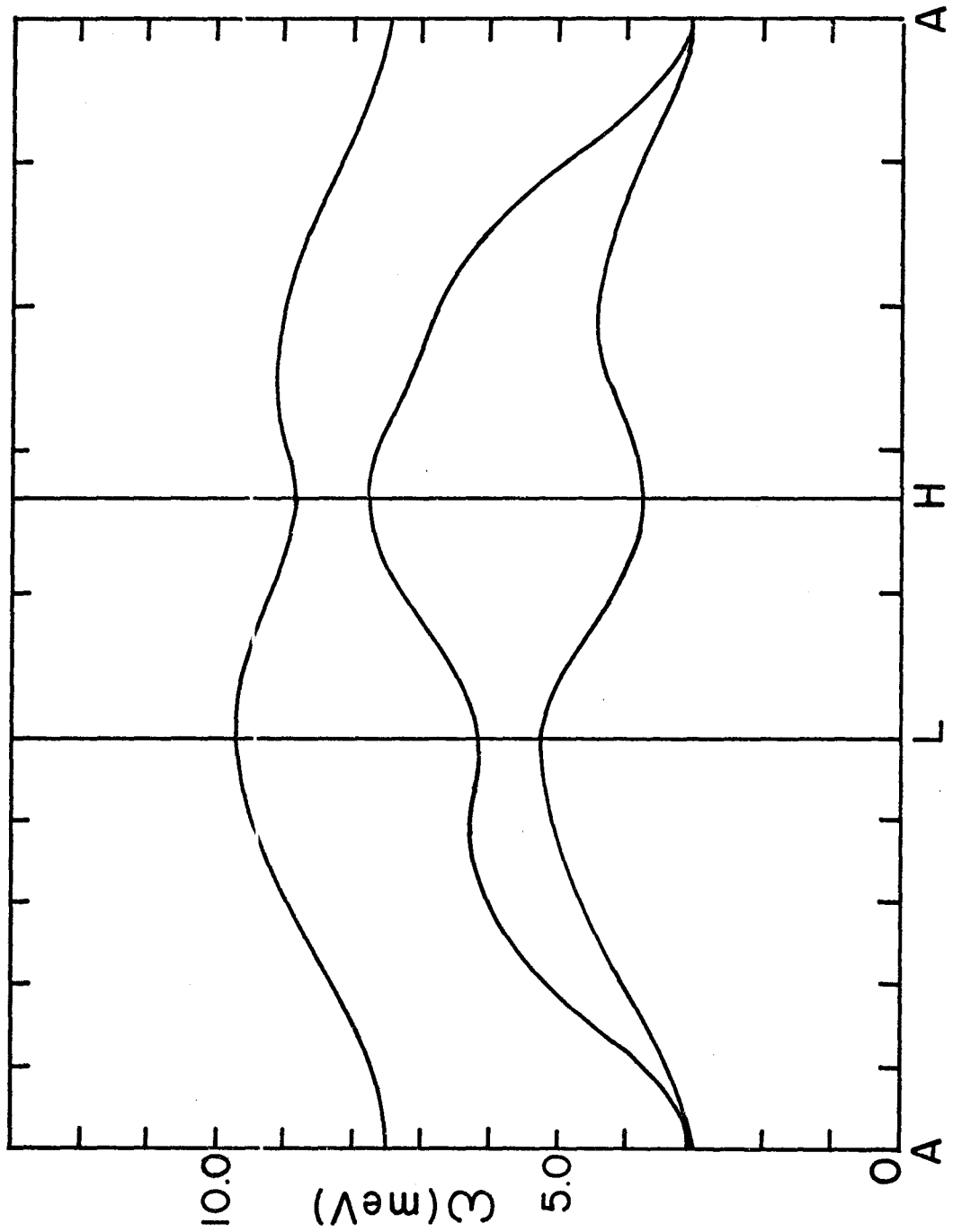

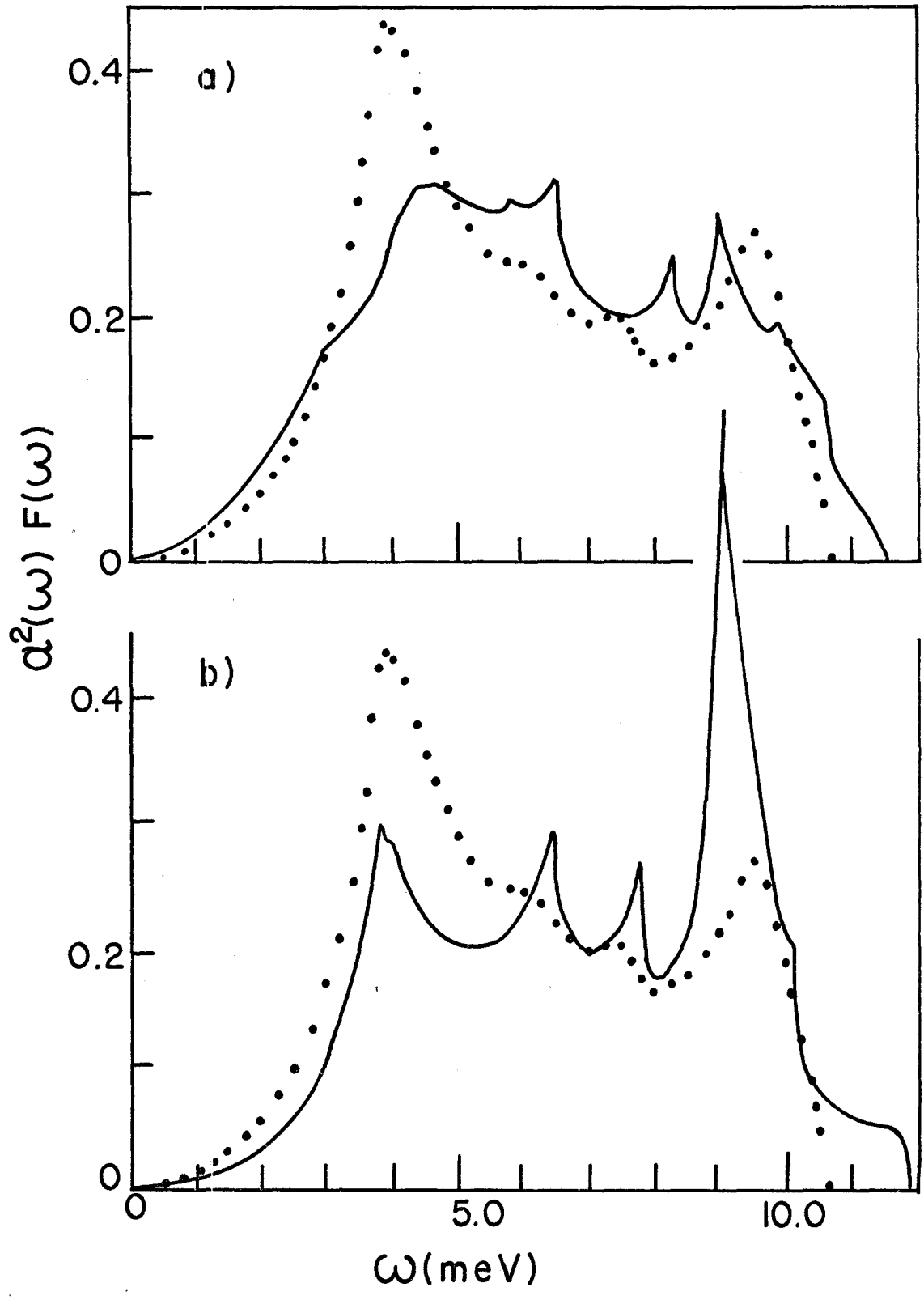
a)
b)
0.4
0.2
0
0.4
0.2
0
0
5.0
10.0
$\alpha^2(\omega)\, F(\omega)$
ω(meV)

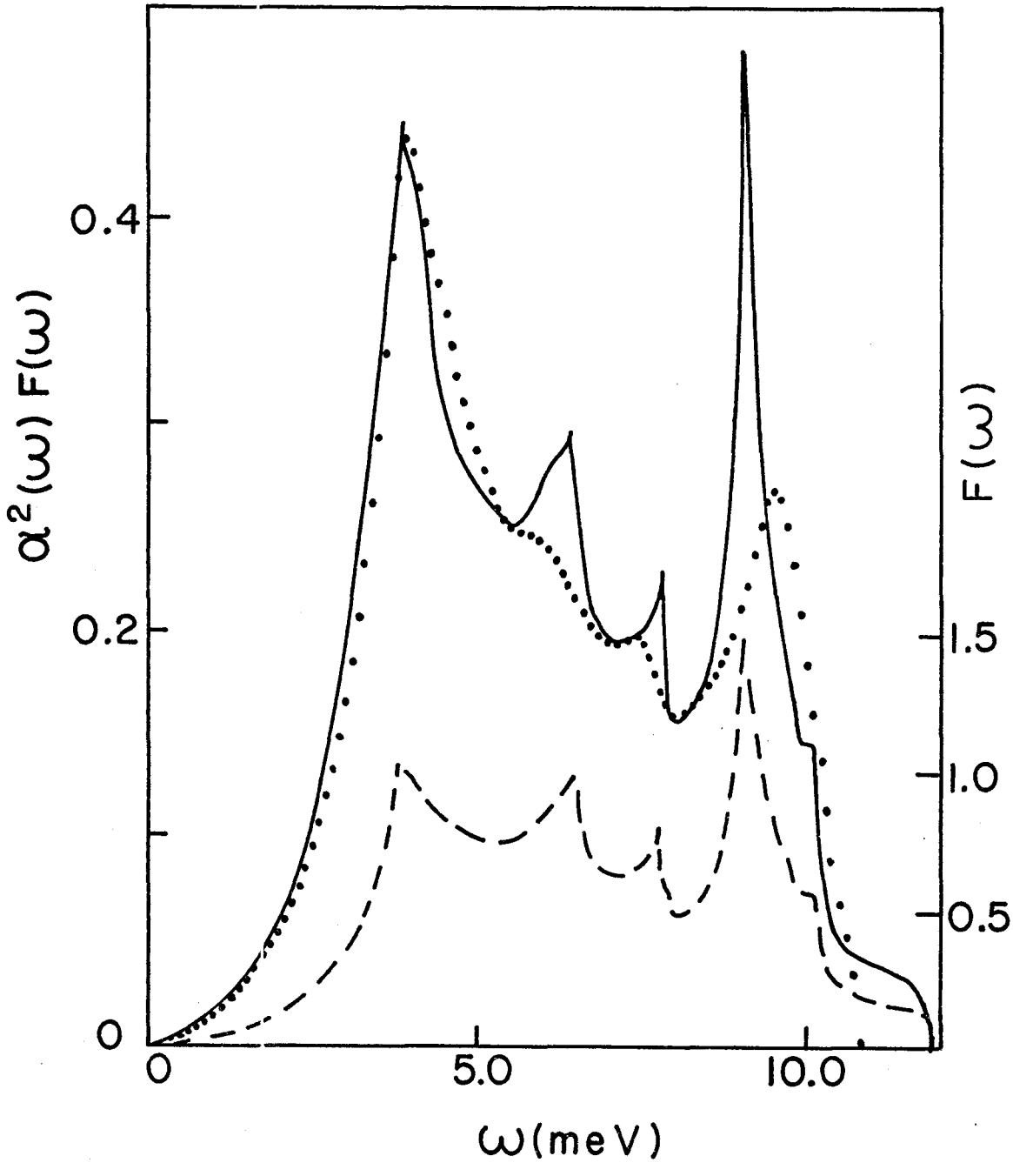
0.4
0.2
0
$\alpha^2(\omega)\,F(\omega)$
0
5.0
10.0
ω(meV)
1.5
1.0
0.5
$F(\omega)$

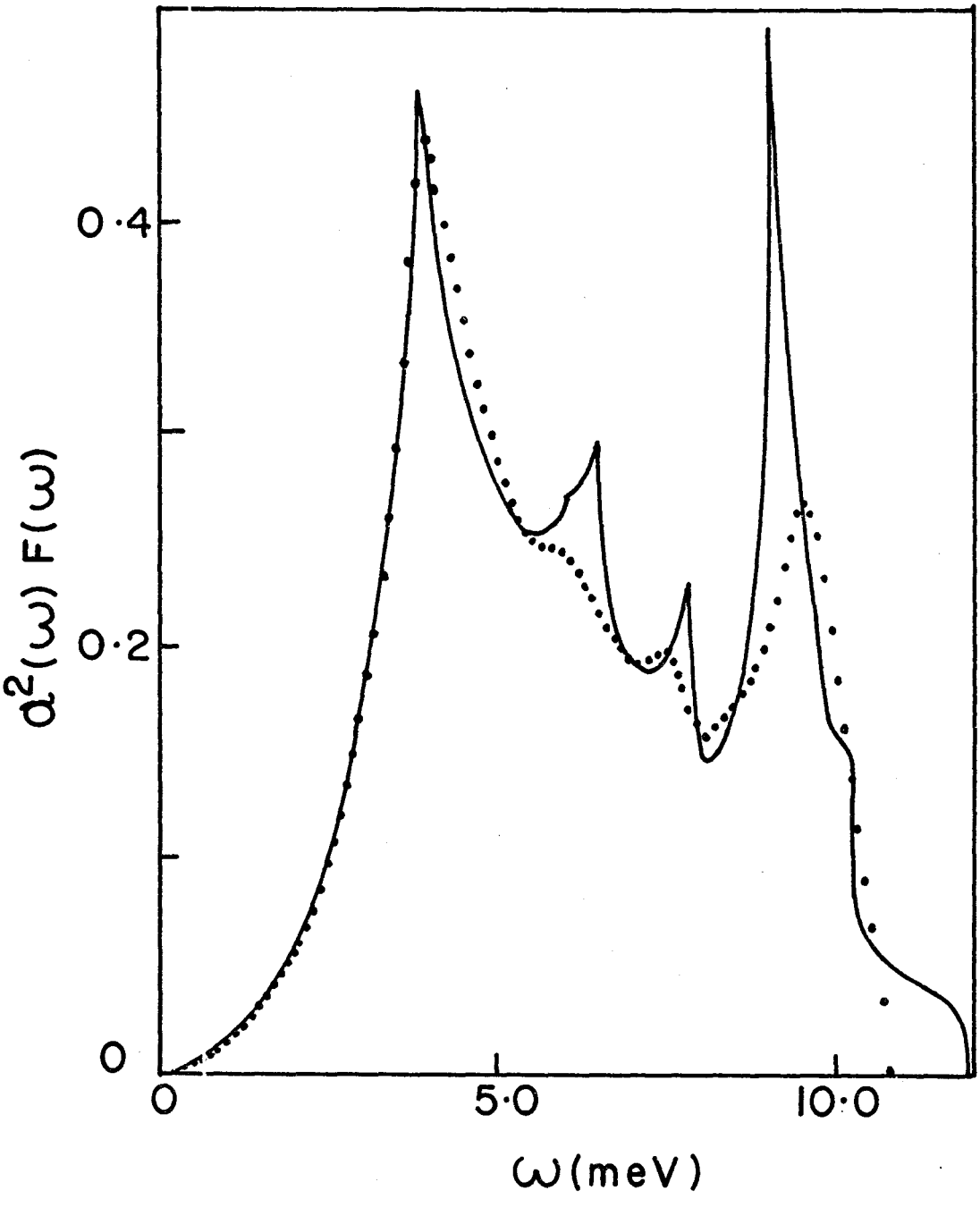
0·4
0·2
0
$\alpha^2(\omega)\,F(\omega)$
0
5·0
10·0
ω(meV)

CHAPTER IV

SUPERCONDUCTING PROPERTIES

4.1 ISOTROPIC SUPERCONDUCTING PROPERTIES: ZINC AND THALLIUM

Leavens and Carbotte [107] have shown that, on the basis of reasonable assumptions, the complicated Eliashberg equations may be reduced to a greatly simplified set of integral equations determining the gap at the gap edge in a weak coupling superconductor. For this class of superconductor the gap is much smaller than the important phonon energies, and this may be used to further reduce the equations to an explicit analytic form for the zero temperature gap. By analogy with BCS theory [13], expressions for the transition temperature and the isotope shift are also obtained. The derivations are discussed in detail in reference 107, and we only outline the main results here. At the end of this section the above formalism is applied to the two zinc and two thallium models described in sections 3.3 and 3.4 respectively.

The Eliashberg equations of the strong coupling theory of superconductivity [28,59] are a set of nonlinear integral equations, which relate normal and superconducting state properties. Within this theory a superconductor is completely specified by two functions $\Delta(\omega,\underline{k})$ and $Z_s(\omega,\underline{k})$, which are the frequency and wavenumber dependent gap and renormalization

functions respectively. For an isotropic superconductor at zero temperature

$$\Delta(\omega)Z_s(\omega) = \int_0^{\omega_c} d\omega' \ \mathrm{Re}\left[\frac{\Delta(\omega')}{\sqrt{\omega'^2-\Delta^2(\omega')}}\right][K_+(\omega,\omega')-\mu^*] \tag{4.1}$$

$$[1-Z_s(\omega)]\omega = \int_0^{\infty} d\omega' \ \mathrm{Re}\left[\frac{\omega'}{\sqrt{\omega'^2-\Delta^2(\omega')}}\right]K_-(\omega,\omega') \tag{4.2}$$

with

$$K_\pm(\omega,\omega') = \int_0^{\infty} d\nu\alpha^2F(\nu)\left[\frac{1}{\omega'+\omega+\nu+i0^+} \pm \frac{1}{\omega'-\omega+\nu-i0^+}\right] \tag{4.3}$$

where ω_c is the upper phonon cutoff frequency. The normal state information is contained in the function $\alpha^2F(\nu)$ and the number μ^*.

The isotropic $\alpha^2F(\nu)$ is given by equation (3.11) in the spherical Fermi surface approximation by

$$\alpha^2F(\nu) = N(0)\iint \frac{d\Omega_{\underline{k}}}{4\pi}\frac{d\Omega_{\underline{k}'}}{4\pi}\sum_j |g_{\underline{k}\underline{k}'j}|^2 \ \delta(\nu-\omega_{\underline{k}-\underline{k}'j}) \tag{4.4}$$

The input data (Chapter III) needed to calculate (4.4) is the band structure density of states at the Fermi surface, the electron-ion pseudopotential, and the phonon frequencies and polarization vectors.

The number μ^* describes, in an average way, the effect of the Coulomb interaction on scattering at the Fermi surface. First principle calculations of μ^* are not

considered to be very reliable at present, and it is usually treated as an adjustable parameter [57]. We shall adopt this attitude, and choose its value such that the correct superconducting transition temperature, T_c, is given by the analytic expression (4.19). This procedure has been followed by Meservey and Schwartz [14] with the BCS T_c equation.

Now we begin the reduction of Leavens and Carbotte. At zero temperature the energy gap $\Delta(\Delta_0) = \Delta_0$ and the renormalization function $Z_s(\Delta_0)$, at the gap edge, are real. The gross frequency dependence of $\Delta(\omega')$ is included by assuming the model

$$\begin{aligned} \Delta(\omega') &= \Delta_0 \quad , \quad \text{for } \Delta_0 < \omega' < \omega_c \\ &= \Delta_c \quad , \quad \text{for } \omega' > \omega_c \end{aligned} \tag{4.5}$$

where

$$\Delta_c = -\mu^* \ln\left(\frac{2\omega_c}{\Delta_0}\right)\Delta_0 \quad ; \tag{4.6}$$

and ω_c is the highest single phonon frequency, which is given by the high frequency cutoff of $\alpha^2F(\omega)$. This gap model ignores detailed retardation effects and damping.

Substituting (4.5) and (4.6) into the Eliashberg equations for the gap at the gap edge; they obtained the following, greatly simplified, set of approximate equations

$$\Delta_0 Z_s(\Delta_0) = \int_0^{\omega_c} d\omega \left[\alpha^2 F(\omega) K(\omega,\omega_c,\Delta_0)\Delta_0 - \mu^* \ell n\left(\frac{2\omega_c}{\Delta_0}\right)\Delta_0 \right] \quad (4.7)$$

$$Z_s(\Delta_0) = 1 + \int_0^{\omega_c} d\omega \alpha^2 F(\omega) \left[L(\omega,\omega_c,\Delta_0) + \frac{2}{\omega+\omega_c} \right] \quad (4.8)$$

$$K(\omega,\omega_c,\Delta_0) \equiv \sum_{i=1}^{2} J_i(\omega,\omega_c,\Delta_0) \quad (4.9)$$

$$L(\omega,\omega_c,\Delta_o) \equiv \frac{1}{\Delta_0} \sum_{i=1}^{2} (-1)^{i+1} p_i J_i(\omega,\omega_c,\Delta_0) \quad (4.10)$$

$$J_i(\omega,\omega_c,\Delta_o) \equiv \frac{1}{\sqrt{p_i^2-\Delta_0^2}} \ell n \left[\frac{\omega_c+p_i-\sqrt{\omega_c^2-\Delta_0^2}+\sqrt{p_i^2-\Delta_0^2}}{\omega_c+p_i-\sqrt{\omega_c^2-\Delta_0^2}-\sqrt{p_i^2-\Delta_0^2}} \times \frac{\Delta_0+p_i-\sqrt{p_i^2-\Delta_0^2}}{\Delta_0+p_i+\sqrt{p_i^2-\Delta_0^2}} \right] \quad (4.11)$$

$$p_1 \equiv \omega + \Delta_0 \quad (4.12)$$

and

$$p_2 \equiv \omega - \Delta_0 \quad ; \quad (4.13)$$

where the condition Δ_0, $|\Delta_c| \ll \omega'$ for $\omega' > \omega_c$ has been used. These results also assume that, since the phonon density of states for low energies is small, the contribution from $\omega < 2\Delta_0$ is not important; and $\alpha^2 F(\omega)$ may be set equal to zero for $\omega \leq 2\Delta_0$. The calculated gaps are not sensitive to the

exact cutoff. The above equations (4.7) through (4.13) will form the basis for our analysis of superconducting properties.

To obtain an analytic expression for Δ_0 two more approximations are required. The important phonon frequencies in weak and medium coupling superconductors are usually much greater than the gap value. Thus, $K(\omega,\omega_c,\Delta_o)$ is expanded in powers of (Δ_0/ω), and to second order in the expansion parameter

$$K(\omega,\omega_c,\Delta_0) = \frac{2}{\omega} \ln\left(\frac{2\omega}{\Delta_0(1+\omega/\omega_c)}\right) \quad . \tag{4.14}$$

This has been shown [107] to be a very good approximation for weak coupling superconductors such as zinc; and a fairly good approximation for medium coupling superconductors, such as thallium. Also, for a weak coupling superconductor it is a good approximation to replace $Z_s(\Delta_0)$ by $Z_n(0)$, the zero frequency normal state renormalization function, where [59]

$$Z_n(0) = 1 + \lambda \tag{4.15}$$

and

$$\lambda \equiv 2 \int_0^{\omega_c} \frac{d\omega}{\omega} \alpha^2 F(\omega) \tag{4.16}$$

The isotropic $\alpha^2F(\omega)$ functions for the zinc and thallium models are given in figures 3.3.5, 3.3.8 and 3.4.9, 3.4.10 respectively. Table 4.1 compares $Z_s(\Delta_0)$ from equations (4.7) and (4.8) and $Z_n(0)$ from (4.15), the details will be given later.

TABLE 4.1

COMPARISON OF SUPERCONDUCTING AND NORMAL STATE RENORMALIZATION PARAMETERS

	$Z_n(0)$	$Z_s(\Delta_0)$	$\frac{Z_n(0)}{Z_s(\Delta_0)}$
Zn(MEPM)	1.425	1.424	1.001
Zn(DWL)	1.338	1.338	1.000
Tl(0.875)	1.838	1.822	1.009
Tl(0.435)	1.832	1.815	1.009

Equation (4.15) is an excellent approximation for Zn. For medium coupling Tl it is accurate to within $\tilde{\sim}$ 1%, which is the approximate accuracy of the entire Eliashberg formulation [20].

Substituting (4.14) and (4.15) into equation (4.7), and defining the parameter

$$\bar{\lambda} \equiv 2 \int_0^{\omega_c} \frac{d\omega}{\omega} \alpha^2 F(\omega) \ell n(1 + \frac{\omega_c}{\omega}) \quad , \tag{4.17}$$

the following equation for the zero temperature gap is obtained

$$\Delta_0 = 2\omega_c \exp \left[- \frac{1 + \lambda + \bar{\lambda}}{\lambda - \mu^*} \right] \quad . \tag{4.18}$$

We mention in passing that if Δ_0 as given by equation (4.18) is used as an initial value in the iteration of the simplified integral equations (4.7) and (4.8); then convergence to within 0.01% is obtained in a few seconds on the CDC6400 computer.

To obtain an approximate analytic expression for the superconducting transition temperature, T_c, the weak coupling version of (4.7) is used. The generalization to finite temperature is made by analogy with BCS theory; and the effect of thermal phonons is ignored. Then on the basis of reasonable approximations, such as were used to obtain (4.18), this finite temperature equation is reduced to

$$k_B T_c = 1.134 \ \omega_c \exp \left[- \frac{1 + \lambda(T_c) + \bar{\lambda}}{\lambda - \mu^*} \right] \quad . \tag{4.19}$$

The temperature dependent electron-phonon mass enhancement $\lambda(T)$ will be discussed in section 5.1, under normal state properties. For the moment we merely point out that in the superconducting temperature range $\lambda(T)$ is a slowly increasing function of T. The value $\lambda(T_c)$ is at most a few percent larger than $\lambda = \lambda(0)$, for both Zn and Tl.

From equations (4.18) and (4.19) the following ratio is found

$$\left(\frac{2\Delta_0}{k_B T_c}\right) = 3.53 \exp\left[\frac{\lambda(T_c) - \lambda}{\lambda - \mu^*}\right] \quad . \tag{4.20}$$

The exponential factor in (4.20) gives a small positive correction to the BCS ratio value of 3.53.

An expression for the isotope shift exponent, β, may be obtained by differentiating both sides of equation (4.19) with respect to the average ionic mass M,

$$\beta = \frac{1}{2} \frac{\left(1 - \dfrac{(1 + \lambda(T_c) + \bar{\lambda})}{(\lambda - \mu^*)^2} \mu^{*2}\right)}{\left(1 + T_c \dfrac{d\lambda(T_c)}{dT_c} \Big/ (\lambda - \mu^*)\right)} \quad . \tag{4.21}$$

This result assumes that T_c is proportional to $M^{-\beta}$, and the approximate analytic form for μ^* is taken from reference (24).

Tables 4.2 and 4.3 collect the parameter values used in and calculated from the equations given in this section. We will now review the models and discuss the tables in detail for Zn and Tl, respectively.

TABLE 4.2

ZINC PARAMETERS - CALCULATED AND FITTED

PARAMETER	Zn EXPERIMENT	Zn (MEPM)	Zn (DWL)
ω_c (meV)	25.85 (a)	25.33	26.20
λ		0.425	0.338
$\overline{\lambda}$		0.599	0.436
T_c (°K)	0.849 (b)	0.849	0.849
$\lambda(T_c)/\lambda(0)$		1.0006	1.0004
μ^*		0.086	0.043
Δ_0^{IT} (meV)		0.1295	0.1293
Δ_0^{AN} (meV)		0.1290	0.1290
$(2\Delta_0^{AN}/k_B T_c)$		3.53	3.53
$\frac{d\lambda(T)}{dT}\Big\|_{T_c}$ ($°K^{-1}$)		0.0	0.0
β	0.37 (b)	0.435	0.481
m_B		0.59	0.59
m^*	0.86 (c)	0.84	0.79

(a) Reference 55

(b) Reference 108

(c) Reference 38

TABLE 4.3

THALLIUM PARAMETERS - CALCULATED AND FITTED

PARAMETER	Tl EXPERIMENT†	Tl(0.875)	Tl(0.435)
ω_c (meV)	10.75	10.75	10.75
λ	0.780	0.838	0.832
$\overline{\lambda}$	0.983	1.070	1.051
T_c (°K)	2.33	2.33	2.33
$\lambda(T_c)/\lambda(0)$		1.014	1.012
μ^*	0.127	0.127	0.127
Δ_0^{IT} (meV)	0.369	0.380	0.380
Δ_0^{AN} (meV)	0.369	0.360	0.359
$(2\Delta_0^{AN}/k_B T_c)$	3.68	3.59	3.58
$\frac{d\lambda(T)}{dT}\Big\|_{T_c}$ ($°K^{-1}$)		0.008	0.008
β		0.442	0.442
m_B		0.64	0.44
m^*	1.13	1.18	0.81

†All of the experimental values are taken from references 57 and 102, except the m* value which is from reference 101.

In Zn the availability of the accurate empirical Stark-Falicov pseudopotential [54] allows us to set the pseudopotential and band mass [90] with some confidence. Two models for the force constants were chosen. The MEPM force constants show good agreement with the measured phonons of reference 55. The other model, DWL, is based on less extensive phonon data, and shows poorer agreement with experiment. In particular, the lowest frequency phonon branches of DWL are significantly higher than both the experimental and MEPM results.

In table 4.2 the upper phonon cutoff frequencies ω_c are taken from the force constant fits of MEPM and DWL. The isotropic $\alpha^2F(\omega)$ functions are calculated as described in section 3.2, then λ and $\bar{\lambda}$ are given by equations (4.16) and (4.17) respectively. The small values for the ratio $\lambda(T_c)/\lambda(0)$ show that for Z_n, we may take $\lambda(T_c) = \lambda(0)$ and $(d\lambda(T)/dT)|_{T_c} = 0$.

Using equation (4.19), μ^* is fit to the experimental value of T_c, and then the gap value Δ_0^{AN} is obtained from the analytical formula (4.18). Since $\lambda(T_c) = \lambda(0)$, equation (4.20) gives just the BCS ratio $(2\Delta_0/k_BT_c) = 3.53$. Using Δ_0^{AN} as the starting value in equations (4.7) and (4.8), these equations are iterated to convergence to determine Δ_0^{IT}. It is apparent that, for weak coupling superconductors, the analytic gap expression (4.18) is a very good approximation to the integral equations (4.7) and (4.8)

The above parameter values allow the calculation of the isotope shift coefficient, β, from equation (4.21). Although the MEPM model β is certainly much closer to experiment, neigher model shows very good agreement. Using $m_B = 0.59$ and $m^* = m_B(1+\lambda)$ the predicted specific heat masses are obtained. We recall that the good agreement between the MEPM value and experiment was one of the constraints used to determine the force constant modification. However, the DWL value is significantly smaller than experiment. One further point remains to be mentioned, the values $\mu^* \geq 0.09$ appear to be the general rule [24,38]; and again the MEPM model appears to be the most reasonable.

For Tl we use one force constant model, WSM, which gives a good fit to the measured dispersion curves; and also reproduces the peak structure of $\alpha^2F(\omega)$, as observed in tunneling experiments [57]. It was found that two very different pseudopotentials, denoted Tl(0.875) and Tl(0.435), gave almost identical results in showing very good agreement with the experimental $\alpha^2F(\omega)$.

The thallium table 4.3 was obtained by the same procedure as discussed earlier for zinc, except that the ω_c value is obtained from experiment. We note that all of the gap values are in very close agreement, as is to be expected since we fit to T_c. For medium coupling superconductors the analytic gap equation (4.18) appears to be a good approximation to the integral equations (4.7) and (4.8)

The only significant difference between the two Tl pseudopotentials appears in the m_B and m* values. The band mass values were determined by fitting to the experimental $\alpha^2F(\omega)$. Since the calculated λ's are essentially the same, the difference in m_B shows up in the predicted specific heat mass, through equation (3.27). The Tl(0.875) model is in good agreement with experiment, while Tl(0.435) value is significantly lower.

4.2 ANISOTROPIC SUPERCONDUCTING PROPERTIES: ZINC

The strong coupling theory of superconductivity characterizes the superconducting state by a renormalization function $Z_s(\omega,\underline{k})$ and a gap $\Delta(\omega,\underline{k})$ which are associated with an electronic state of wavevector $\underline{k}$. Both of these functions depend on the orientation of $\underline{k}$ with respect to the crystal axes. In a pure single crystal superconductor the electrons are able to take maximum advantage of this anisotropy in forming the superconducting state. If there are impurities present, a "dirty" superconductor [109], the electronic states become smeared over the Fermi surface, the energy gap becomes essentially isotropic; and the effect is a weakening of the superconducting state.

It has been experimentally observed [110-113] that the addition of impurities lowers the superconducting transition temperature. Markowitz and Kadanoff [44] were able to account for this effect by considering the simple anisotropic pairing potential

$$V_{\underline{kk}'} = (1 + a(\Omega))V(1 + a(\Omega'))$$

where Ω and Ω' are the angular coordinates of $\underline{k}$ and $\underline{k}'$. Clem [114] used the above matrix elements, and weak coupling BCS formalism, to investigate the effects of energy gap

anisotropy on the thermodynamic properties of a pure single crystal superconductor.

Bennett [46] performed a realistic first order calculation of the gap anisotropy in lead, due to anisotropy in the phonon density of states. Band structure effects were later included as a perturbation. He assumed that whenever $\Delta(\omega,\underline{k})$ appeared in an integrand of the strong coupling equations it could, to first order, be replaced by the isotropic value $\Delta(\omega)$ for dirty lead. This directly relates the energy gap anisotropy to the anisotropy in the phonon kernels, equation (4.3). He assumed that the coupling function $\alpha^2(\omega,\theta,\phi)$ was constant, independent of both direction and energy. Also, he expressed both the phonon dispersion curves and the directional frequency distributions in series of Kubic harmonics, which were truncated after three terms.

In this section we closely follow the work of Leavens and Carbotte [51]. Reference 51 contains detailed discussions of their method, which we only briefly sketch here. Bennett's reduction procedure is applied to the simplified integral equations (4.7) and (4.8), to give the first order equations for the directional energy gap

$$\Delta_0^{(1)}(\theta,\phi) = \frac{1}{Z_s^{(1)}(\theta,\phi)_0}\left[\int_{\Delta_0}^{\omega_c} d\omega\ \alpha^2F(\omega,\theta,\phi)K(\omega,\omega_c,\Delta_0) - \mu^*\ \ln\left(\frac{2\omega_c}{\Delta_0}\right)\right]\Delta_0 \qquad (4.22)$$

and

$$Z_s^{(1)}(\theta,\phi)_0 = 1 + \int_{\Delta_0}^{\omega_c} d\omega\ \alpha^2F(\omega,\theta,\phi)\left[L(\omega,\omega_c,\Delta_0) + \frac{2}{\omega+\omega_c}\right] , \tag{4.23}$$

where $K(\omega,\omega_c,\Delta_0)$ and $L(\omega,\omega_c,\Delta_0)$ are given by equations (4.9) through (4.13). In these equations Δ_0 is the solution obtained by iterating (4.7) and (4.8) to convergence using the isotropic $\alpha^2F(\omega)$.

Beyond this point Leavens and Carbotte do not follow Bennett's method. Rather, the phonon frequencies and polarization vectors are obtained from Born-von Kármán force constant models. From this information the combined anisotropy, arising from the directional dependence of both the phonon frequency distributions and the electron-phonon interaction, may be directly calculated.

We recall that all of the essential information about the phonon anisotropy is contained in the functions

$$\alpha^2F(\omega,\theta,\phi) = N(0) \int \frac{d\Omega_{\underline{k}'}}{4\pi} \sum_j |g_{\underline{k}\underline{k}'j}|^2\ \delta(\omega-\omega_{\underline{k}-\underline{k}'j}) \tag{4.24}$$

where $\underline{k}$ and $\underline{k}'$ are on the assumed spherical Fermi surface. The electron-phonon coupling constant $g_{\underline{k}\underline{k}'j}$ is given by equation (2.23); and $N(0)$ is the free electron density of

states at the Fermi surface, multiplied by the band mass m_B.

Figure 4.2.1 presents the $\alpha^2F(\omega,\theta,\phi)$ functions for three high symmetry directions, as calculated for Zn with the Stark-Falicov local pseudopotential and MEPM force constants. The results for the DWL force constant model will be presented at the end of this section. The predominant feature displayed in figure 4.2.1 is that, as $\underline{k} = (k_F,\theta,\phi)$ is varied from the c-axis ($\theta = 0°$) to the basal plane ($\theta = 90°$), the low frequency peak decreases drastically and the middle range of frequencies is increased in importance. The angular coordinate system, (θ,ϕ) is defined in figure 3.1.1. These directional functions should be compared with the Fermi surface average $\alpha^2F(\omega)$ of figure 3.3.5. All four functions are considerably different.

We point out that the peaks in $\alpha^2F(\omega,\underline{k})$ arise from phonon modes which contribute from "flat" regions of $\omega_{\underline{k}j}$ versus $\underline{k}$ space. As $\underline{k}$ is varied the peak positions will not shift, rather their weightings change as different phonons are picked up by the scattering sphere (see figure 3.2.1). If a peak is made up of contributions from several flat regions, then this change in weighting may give the appearance of a shift in position.

The electron-phonon mass enhancement for an electron at the Fermi surface with wavevector direction (θ,ϕ) is

$$\lambda(\theta,\phi) = 2 \int_0^\infty \frac{d\omega}{\omega} \alpha^2 F(\omega,\theta,\phi) \quad . \tag{4.25}$$

Averaging this parameter over all (θ,ϕ) directions gives the electron-phonon correction to the electronic specific heat mass, m* of equation (3.27). The MEPM model results for $\lambda(\theta,\phi)$ are shown in figure 4.2.2. The maximum value occurs in the c-axis direction and the minimum is in the basal plane. All results in this thesis which are presented in the format of figure 4.2.2 have actually been calculated at eleven points along each ϕ-direction (9° intervals), and a smooth curve has been interpolated between these points.

To obtain the correct gaps $\Delta_0(\underline{k})$ one should obtain $\Delta_0^{(1)}(\underline{k})$ from (4.22) and (4.23), then substitute $\Delta_0^{(1)}(\underline{k})$ into the right hand side of (4.7) and (4.8) to give $\Delta_0^{(2)}(\underline{k})$, and repeat the process until convergence is obtained. However, each iteration involves a large investment in computer time; and doing the many iterations [51] is out of the question.

Leavens and Carbotte calculated both the first and second iteration results for Al. They concluded that the effect of the second iteration is to increase the average value of the gap, while leaving the anisotropy essentially unchanged. Thus, we follow their suggestion and obtain the gap anisotropy from the first order equations (4.22) and (4.23), then the average value $\langle\Delta_0(\underline{k})\rangle$ is obtained from an analytic expression to be discussed below.

To calculate the first order gaps from (4.22) and (4.23) we need the $\alpha^2F(\omega,\theta,\phi)$, discussed previously in this section; and the parameters Δ_0, ω_c, μ^* and m_B, which are given in section 4.1. The resulting gaps $\Delta_0^{(1)}(\theta,\phi)$ are presented in figure 4.2.3, for the moment we ignore the absolute magnitudes.

The gap anisotropy parameter $a_{\underline{k}}$, which is defined by

$$\Delta_0(\underline{k}) = \langle\Delta_0(\underline{k})\rangle(1 + a_{\underline{k}}) \quad , \tag{4.26}$$

may be obtained from the $\Delta_0^{(1)}(\theta,\phi)$ values. Since we assume that successive iterations do not appreciably change the anisotropy, we may write approximately

$$a_{\underline{k}} \tilde{=} \frac{\Delta_0^{(1)}(\underline{k}) - \langle\Delta_0^{(1)}(\underline{k})\rangle}{\langle\Delta_0^{(1)}(\underline{k})\rangle} \quad . \tag{4.27}$$

To completely determine the pure single crystal gaps, equation (4.26), all that remains is the calculation of $\langle\Delta_0(\underline{k})\rangle$.

The average energy gap of a pure single crystal weak coupling superconductor is obtained from equations (4.7) and (4.8). First the anisotropy parameters $a_{\underline{k}}$, $b_{\underline{k}}$ and $\bar{b}_{\underline{k}}$ are defined by equation (4.26) and

$$\lambda(\underline{k}) = \langle\lambda(\underline{k})\rangle(1 + b_{\underline{k}}) \tag{4.28}$$

$$\bar{\lambda}(\underline{k}) = \langle\bar{\lambda}(\underline{k})\rangle(1 + \bar{b}_{\underline{k}}) \tag{4.29}$$

where

$$\langle f(\underline{k})\rangle = \int \frac{d\Omega_{\underline{k}}}{4\pi} f(\underline{k})$$

is the Fermi surface average of any function $f(\underline{k})$. The functions $\lambda(\underline{k})$, equation (4.25), and

$$\bar{\lambda}(\underline{k}) = 2\int_0^\infty \frac{d\omega}{\omega}\,\alpha^2F(\omega,\underline{k})\,\ell n(1 + \frac{\omega_c}{\omega}) \quad , \tag{4.30}$$

are calculated directly from the $\alpha^2F(\omega,\theta,\phi)$. In our previous notation we have

$$\lambda = \langle\lambda(\underline{k})\rangle$$

and

$$\bar{\lambda} = \langle\bar{\lambda}(\underline{k})\rangle \quad .$$

Now definitions (4.26), (4.28) and (4.29) are substituted into (4.7) and (4.8). Since

$$|a_{\underline{k}}| \ , \ |b_{\underline{k}}| \ , \ |\bar{b}_{\underline{k}}| << 1 \quad ,$$

the equations are expanded in terms of these small quantities; and to second order in these parameters Leavens and Carbotte

quote

$$\langle\Delta_0(\underline{k})\rangle = 2\omega_c \exp\left[- \frac{1 + (1 + \frac{1}{2}\langle a^2\rangle + 2\langle ab\rangle)\lambda + (1 + \langle a\bar{b}\rangle)\bar{\lambda} - \frac{1}{2}\langle a^2\rangle\mu^*}{(1 + \langle ab\rangle)\lambda - \mu^*}\right] \tag{4.31}$$

We note that there are no first order terms, since by definition

$$\langle a_{\underline{k}}\rangle = \langle b_{\underline{k}}\rangle = \langle \bar{b}_{\underline{k}}\rangle = 0 \quad .$$

The pure Zn crystal anisotropic gaps, $\Delta_0(\theta,\phi)$ as given by the MEPM force constant model, are shown in figure 4.2.3. These are just the first order gaps scaled by the ratio $\langle\Delta_0(\theta,\phi)\rangle/\langle\Delta_0^{(1)}(\theta,\phi)\rangle$ where equation (4.31) has been used with the parameters $\langle a^2\rangle = 0.014$, $\langle ab\rangle = 0.015$ and $\langle a\bar{b}\rangle = 0.019$. The average gap is indicated in the figure by the arrow placed on the vertical axis.

A number of experiments have been analyzed in terms of gap anisotropy models. They indicate that the maximum gap occurs along the c-axis and the minimum is in the basal plane. This is in agreement with figure 4.2.3. Although the numerical results are somewhat model dependent, we may use them for a qualitative comparison with our calculated

gaps. Table 4.4 summarizes the experimental thermal conductivity [115], microwave-absorption [116], and specific heat [53] results.

TABLE 4.4

EXPERIMENTAL ESTIMATES OF THE Zn SUPERCONDUCTING GAPS IN UNITS OF $k_B T_c$

REFERENCE	$\Delta_c = \Delta(0,0)$	Δ_a MINIMUM IN BASAL PLANE	Δ_c/Δ_a
Reference 115	1.75	1.20	1.46
Reference 116 MODEL A	2.0	1.55	1.29
Reference 116 MODEL B	2.45	1.55	1.58
Reference 53	1.79	1.00	1.79

From figure 4.2.3 our MEPM model gives $\Delta_c = 2.34\ k_B T_c$, $\Delta_a = 1.41\ k_B T_c$ and $(\Delta_c/\Delta_a) = 1.66$; and our calculated results are consistent with experiment.

We may also compare with the ultrasonic attenuation measurements of Lea and Dobbs [117]. Since these results depend on weighted averages of the gaps over the Fermi surface, only a rough qualitative comparison is possible.

However, experiment indicates that the gaps along the $\phi = 30°$ direction are larger than those along $\phi = 0°$. This behaviour is opposite to that seen in figure 4.2.3.

Leavens and Carbotte [51] also obtain the transition temperature, T_c^{PSC}, for a pure single crystal superconductor as

$$k_B T_c^{PSC} = 1.134\omega_c \exp\left[- \frac{1 + (1 + \langle ab \rangle)\lambda(T_c) + (1 + \langle a\bar{b} \rangle)\bar{\lambda}}{(1 + \langle ab \rangle)\lambda - \mu^*} \right] . \qquad (4.32)$$

In deriving this result it is assumed that the anisotropy parameters are independent of temperature in the small temperature range between $T = 0$ and $T = T_c^{PSC}$. We shall see in section 5.1 that this holds very well for $b_{\underline{k}}$; and, therefore, also for $\bar{b}_{\underline{k}}$. Leavens and Carbotte have calculated $a_{\underline{k}}$ in Al at $T = 0$ and $T = 0.98T_c$, and they find no significant variation in the gap anisotropy parameter.

Using the MEPM values of $\langle a^2 \rangle$, $\langle ab \rangle$ and $\langle a\bar{b} \rangle$ in equation (4.32) we have

$$\frac{T_c^{PSC}}{T_c} = 1.06 \quad ,$$

and from equation (4.31)

$$\frac{\langle \Delta_0(\underline{k}) \rangle}{\Delta_0} = 1.03 \quad .$$

Combined with relation (4.20), these give

$$\frac{2\langle \Delta_0(\underline{k}) \rangle}{k_B T_c^{PSC}} = 3.44$$

for Zn, as compared to the BCS ratio of 3.53 for an isotropic weak coupling superconductor. Since T_c^{PSC} is greater than the isotropic result we see that anisotropy has enhanced the superconducting state, as expected.

We now go on to a calculation of the nuclear spin-lattice relaxation rate; and later we consider the electronic specific heat of a pure single crystal superconductor.

The ratio of the superconducting and normal state relaxation rates is given by [59,114]

$$\frac{R_s(T)}{R_N(T)} = \beta \int_{-\infty}^{\infty} d\omega f(\omega)[1 - f(\omega)] \{\langle n(T,\Omega,\omega)\rangle^2 + \langle \bar{n}(T,\Omega,\omega)\rangle^2\} \qquad (4.33)$$

where $\beta = (k_B T)^{-1}$ and

$$f(\omega) = (e^{\beta\omega} + 1)^{-1} \qquad (4.34)$$

is the Fermi-Dirac distribution function. In the above equation $n(T,\Omega,\omega)$ is the temperature dependent anisotropic quasiparticle density of states

$$n(T,\Omega,\omega) \equiv \mathrm{Re}\left[\frac{\omega}{\sqrt{\omega^2 - \Delta_0^2(T,\Omega)}}\right] , \tag{4.35}$$

similarly

$$\overline{n}(T,\Omega,\omega) \equiv \mathrm{Re}\left[\frac{\Delta_0(T,\Omega)}{\sqrt{\omega^2 - \Delta_0^2(T,\Omega)}}\right] . \tag{4.36}$$

The temperature dependent anisotropic gap has been written as $\Delta_0(T,\Omega)$, Ω is the angular position on the Fermi surface; and the $\langle\ \rangle$ denote a Fermi surface average. The energy variable ω is measured relative to the Fermi level, and the sign of the square root is chosen such that

$$\sqrt{\omega^2 - \Delta^2(T,\Omega)} \to \omega \qquad \text{as} \qquad |\omega| \to \infty \quad .$$

It is convenient to use the anisotropy distribution function $P(a)$, first introduced by Clem [114]. This function has the property that $P(a)da$ is the fraction of the Fermi surface for which the gap anisotropy parameter $a(\Omega)$ has a value between a and a + da.

To calculate $P(a)$ some method is needed to interpolate between the gap values which we have determined on the irreducible 1/24th of the hcp Fermi surface. This was

accomplished, following Leavens and Carbotte [51], by fitting the calculated gaps with a least-squares polynomial in both the θ and ϕ variables. The least squares procedure was found to be necessary to eliminate "wiggles" in the gap surface. Then this polynomial was evaluated at approximately 10^5 points, and the P(a) histogram was generated and normalized to unity.

The anisotropy distribution function, P(a), for the zinc MEPM force constant model is shown in figure 4.2.4. We note that this distribution is far from rectangular as was assumed by Clem. However, it must be remembered that the Clem model is meant to reproduce gap anisotropy arising from all sources, while we have only included phonon effects.

The Fermi surface average of any function F of the anisotropic gap $\Delta_0(\Omega)$ can always be written as an integral over P(a),

$$\langle F(\Delta_0(\Omega))\rangle = \int da\ P(a) F(\langle\Delta_0(\Omega)\rangle(1+a)) \quad . \tag{4.37}$$

The first three moments of P(a) are

$$\int P(a)da = 1$$

$$\int a\ P(a)da = 0$$

and

$$\int a^2\ P(a)da = \langle a^2\rangle \quad .$$

As discussed previously, we may take $a(\Omega)$ to be temperature independent. Therefore, $P(a)$ is also independent of temperature, and this allows us to write

$$\langle F(\Delta_0(T,\Omega))\rangle = \int da\ P(a) F(\langle\Delta_0(T,\omega)\rangle(1+a)) \quad , \qquad (4.38)$$

where $\langle\Delta_0(T,\Omega)\rangle$ is the average gap in a pure single crystal at temperature T.

Now we return to the calculation of the nuclear spin-lattice relaxation rate, equation (4.33). In the range $T < 0.3\ T_c$ the temperature variation of the gap may be neglected; and the Fermi surface averages may be calculated once to obtain $R_s(T)/R_N(T)$, see reference 51. However, for $T > 0.3\ T_c$ the averages $\langle n\rangle$ and $\langle\bar{n}\rangle$ must be calculated for each temperature considered, and this is very time consuming. There is a simple way out of this difficulty.

To compute (4.33) over the whole temperature range $0 \leq T \leq T_c$ we transform to the dimensionless variable ω', where

$$\omega = \langle\Delta_0(T,\Omega)\rangle\omega' \quad . \qquad (4.39)$$

Using (4.39) and (4.38) in equation (4.33) gives

$$\frac{R_s(T)}{R_N(T)} = \beta\langle\Delta_0(T,\Omega)\rangle\int_{-\infty}^{\infty} d\omega' f(\langle\Delta_0(T,\Omega)\rangle\omega')(1-f(\langle\Delta_0(T,\Omega)\rangle\omega'))$$

$$\{\rho^2(\omega') + \bar{\rho}^2(\omega')\} \qquad (4.40)$$

where

$$\rho(\omega') = \left\langle \mathrm{Re} \frac{\omega'}{\sqrt{\omega'^2 - (1+a)^2}} \right\rangle \tag{4.41}$$

and

$$\bar{\rho}(\omega') = \left\langle \mathrm{Re} \frac{1}{\sqrt{\omega'^2 - (1+a)^2}} \right\rangle \tag{4.42}$$

are independent of temperature; and need only be calculated once for the whole range $0 \leq T \leq T_c$. The temperature independent quasiparticle density of states $\rho(\omega')$ is plotted in figure 4.2.5; and we see that it reflects the structure of P(a) from figure 4.2.4.

In figure 4.2.6 we show the overlap of the thermal factors in (4.40) with the function $\rho^2(\omega') + \bar{\rho}^2(\omega')$. It is this overlap which determines R_s/R_N. As the temperature is lowered below T_c, less and less of $\rho^2 + \bar{\rho}^2$ is sampled and the nuclear spin-lattice relaxation rate should drop. Our results for this temperature variation are presented in figure 4.2.7 (the dashed DWL curve will be discussed later). A similar calculation has been performed for Al [118], where good qualitative and fair quantitative agreement with experiment was obtained.

In general, the temperature variation of the average gap for a pure single crystal need not be the same as that for an isotropic superconductor. We have evaluated (4.40)

using P(a) of figure 4.2.4, and both a BCS and a rectangular Clem model [114] ($\langle a^2 \rangle = 0.0014$) temperature variation for the average gap. The differences, as expected, were extremely small. All of the $R_S(T)/R_N(T)$ curves presented in this thesis represent either temperature variation equally well.

One last point remains to be mentioned about the spin-lattice relaxation calculation. Although the transformation (4.39) allows ρ and $\bar{\rho}$ to be calculated once for the whole temperature range, figure 4.2.6 shows that we must know these functions for very large ω' values. However, for large ω', the fact that $\langle a^2 \rangle << 1$ may be used to obtain an approximate analytic expression for ρ and $\bar{\rho}$. Expanding the square root in (4.41) and (4.42) to second order in the gap anisotropy parameter and to seventh order in $(\omega)^{-1}$ gives

$$\rho(\omega') \cong \frac{\omega'}{\sqrt{\omega'^2-1}} + \frac{\langle a^2 \rangle}{2\omega'^2}\left[1 + \frac{9}{2\omega'^2} + \frac{75}{8\omega'^4}\right] \qquad (4.43)$$

and

$$\bar{\rho}(\omega') \cong \frac{1}{\sqrt{\omega'^2-1}} + \frac{3\langle a^2 \rangle}{2\omega'^3}\left[1 + \frac{5}{2\omega'^2} + \frac{35}{8\omega'^4}\right] \qquad (4.44)$$

for large ω'.

For all models considered in this thesis the calculation of ρ and $\bar{\rho}$ from the full integral forms (4.41)

and (4.42) was restricted to approximately $\omega' < 3$, for larger ω' the analytic forms (4.43) and (4.44) were used. For this value of $\omega' \approx 3$ the approximate expressions were found to be accurate to better than one part in 10^4.

In the range $0 \leq T < 0.3\ T_c$ the temperature dependence of the energy gap may be neglected and the low temperature electronic specific heat of an anisotropic weak coupling superconductor is given by Clem [114] as

$$C_s(T) = 2N(0)k_B\beta^2 \int_{-\infty}^{\infty} d\omega\ \omega^2 f(\omega)[1-f(\omega)]\langle n(\Omega,\omega)\rangle \quad .$$

The temperature dependence of the anisotropic quasiparticle density of states, $n(\Omega,\omega)$, has been dropped. Making the transformation (4.39) we obtain

$$\frac{C_s(T)}{\gamma T_c} = \frac{3\beta^2}{\pi^2 k_B T_c}\langle\Delta_0(\Omega)\rangle^3 \int_{-\infty}^{\infty} d\omega'\ \omega'^2 f(\langle\Delta_0(\Omega)\rangle\omega')$$

$$[1 - f(\langle\Delta_0(\Omega)\rangle\omega')]\rho(\omega') \qquad (4.45)$$

where $\rho(\omega')$ is given by (4.41), or for large ω' (4.43).

Our results for the zinc MEPM force constant model are shown in figure 4.2.8, where comparison is made with both BCS theory and experiment. The inclusion of anisotropy has raised the specific heat values from those of BCS theory. However, the experimental results of Ducla-Soares and Cheeke [53] are much higher than either. It is apparent

that to explain this experimental data, on the basis of phonons, a much larger anisotropy is needed. It seems more likely that band structure effects must be included in any calculation of the zinc low temperature electronic specific heat.

Thus far we have only discussed the Zn results for the MEPM force constant model. Now we will quickly present the results of the DWL model. Exactly the same procedure was followed for DWL as has been described for MEPM.

Figure 4.2.9 shows the DWL model $\alpha^2F(\omega,\theta,\phi)$ for three high symmetry directions. These functions should be compared with the isotropic result, figure 3.3.8, and all four functions are considerably different. Comparison with figure 4.2.1 shows that the MEPM and DWL $\alpha^2F(\omega,\theta,\phi)$ are similar. However, as was noted in the isotropic case, in DWL the onset of structure and the low frequency peak positions have been significantly shifted towards higher energies. Also, the low energy peak in the DWL (0,0) direction is of considerably less weight than the corresponding peak for MEPM.

The significance of the above differences is apparent in figure 4.2.10 for $\lambda(\theta,\phi)$ and figure 4.2.11 for $\Delta_0(\theta,\phi)$, where the maxima no longer occur in the c-axis direction. As discussed previously, experiment supports the assignment of the largest gap to the (0,0) direction, as is predicted by the MEPM model.

From the gaps of figure 4.2.11 the P(a) function is

derived. This function, shown in figure 4.2.12 is very different from the MEPM model P(a), figure 4.2.4. The DWL result displays considerably less anisotropy (note the change of scale along the a-axis) with $\langle a^2 \rangle = 0.006$, as compared to the MEPM value of $\langle a^2 \rangle = 0.014$. Using the other DWL parameter values of $\langle ab \rangle = 0.008$ and $\langle a\bar{b} \rangle = 0.012$ we obtain, from equations (4.31) and (4.32),

$$\frac{\langle \Delta_0(\underline{k}) \rangle}{\Delta_0} = 1.02$$

$$T_c^{PSC}/T_c = 1.03$$

and

$$\frac{2\langle \Delta_0(\underline{k}) \rangle}{k_B T_c} = 3.49 \quad .$$

The temperature independent quasiparticle density of states $\rho(\omega')$ for the DWL model is shown in figure 4.2.13, and again it is quite different from the MEPM result of figure 4.2.5. The nuclear spin-lattice relaxation rate is shown in figure 4.2.7, where it lies somewhat higher than the MEPM prediction. This is to be expected, since the DWL model shows less anisotropy it should be closer to the BCS result which diverges at $T = T_c$ [59].

The low temperature electronic specific heat has been calculated, but not shown. Because of the smaller anisotropy,

the DWL specific heat values are smaller than the MEPM results; and lie between the BCS and MEPM curves shown in figure 4.2.8. Thus, agreement with experiment is even worse for the DWL model.

In conclusion, the MEPM force constant model shows better agreement than DWL with all experimental results considered: the measured phonons, the specific heat mass, the isotope effect, the low temperature electronic specific heat and the superconducting gaps. The major difference between these two models was in their fit to the low frequency phonon branches. We have seen that these modes play a very important role in superconductivity.

FIGURE CAPTIONS - SECTION 4.2

FIGURE 4.2.1: $\alpha^2F(\omega,\theta,\phi)$ for three high symmetry directions in Zn, calculated with the MEPM force constants. The directions are labeled by (θ,ϕ).

FIGURE 4.2.2: Zinc (MEPM) electron-phonon mass enhancements $\lambda(\theta,\phi)/\lambda(0,0)$ with $\lambda(0,0) = 0.565$. The Fermi surface averaged value is given by the position of the arrow on the vertical axis.

FIGURE 4.2.3: Zinc (MEPM) zero temperature superconducting gaps $\Delta_0(\theta,\phi)/\Delta_0(0,0)$ with $\Delta_0(0,0) = 0.171$ meV. The Fermi surface averaged value is given by the position of the arrow on the vertical axis.

FIGURE 4.2.4: Zinc (MEPM) gap anisotropy distribution function $P(a)$.

FIGURE 4.2.5: Zinc (MEPM) temperature independent quasi-particle density of states $\rho(\omega')$ as a function of ω' (dimensionless).

FIGURE 4.2.6: The overlap of the thermal factors (solid curves) in equation (4.40) with $[(\rho^2(\omega') + \bar{\rho}^2(\omega')]$ (dashed curve). The thermal factors, for temperature $t = T/T_c$, have been multiplied by a factor of 10. The variable ω' is dimensionless, and the functions are calculated using the zinc MEPM force constant model.

FIGURE 4.2.7: Ratio of the Zn superconducting and normal state nuclear spin-lattice relaxation rates $R_S(T)/R_N(T)$ as a function of temperature. Both force constant models are shown: MEPM (solid line) and DWL (dashed line).

FIGURE 4.2.8: Low temperature behaviour of the electronic specific heat of Zn. The lowest solid curve is the BCS result for an isotropic superconductor. The higher solid curve is our MEPM model result, and the experimental data [53] is indicated by the dashed curve.

FIGURE 4.2.9: $\alpha^2F(\omega,\theta,\phi)$ for three high symmetry directions in Zn, calculated with the DWL force constants. The directions are labeled by (θ,ϕ).

FIGURE 4.2.10: Zinc (DWL) electron-phonon mass enhancements $\lambda(\theta,\phi)/\lambda(0,0)$ with $\lambda(0,0) = 0.383$. The Fermi surface averaged value is given by the position of the arrow on the vertical axis.

FIGURE 4.2.11: Zinc (DWL) zero temperature superconducting gaps $\Delta_0(\theta,\phi)/\Delta_0(0,0)$ with $\Delta_0(0,0) = 0.146$ meV. The Fermi surface averaged value is given by the position of the arrow on the vertical axis.

FIGURE 4.2.12: Zinc (DWL) gap anisotropy distribution function $P(a)$.

FIGURE 4.2.13: Zinc (DWL) temperature independent quasiparticle density of states $\rho(\omega')$ as a function of ω' (dimensionless).

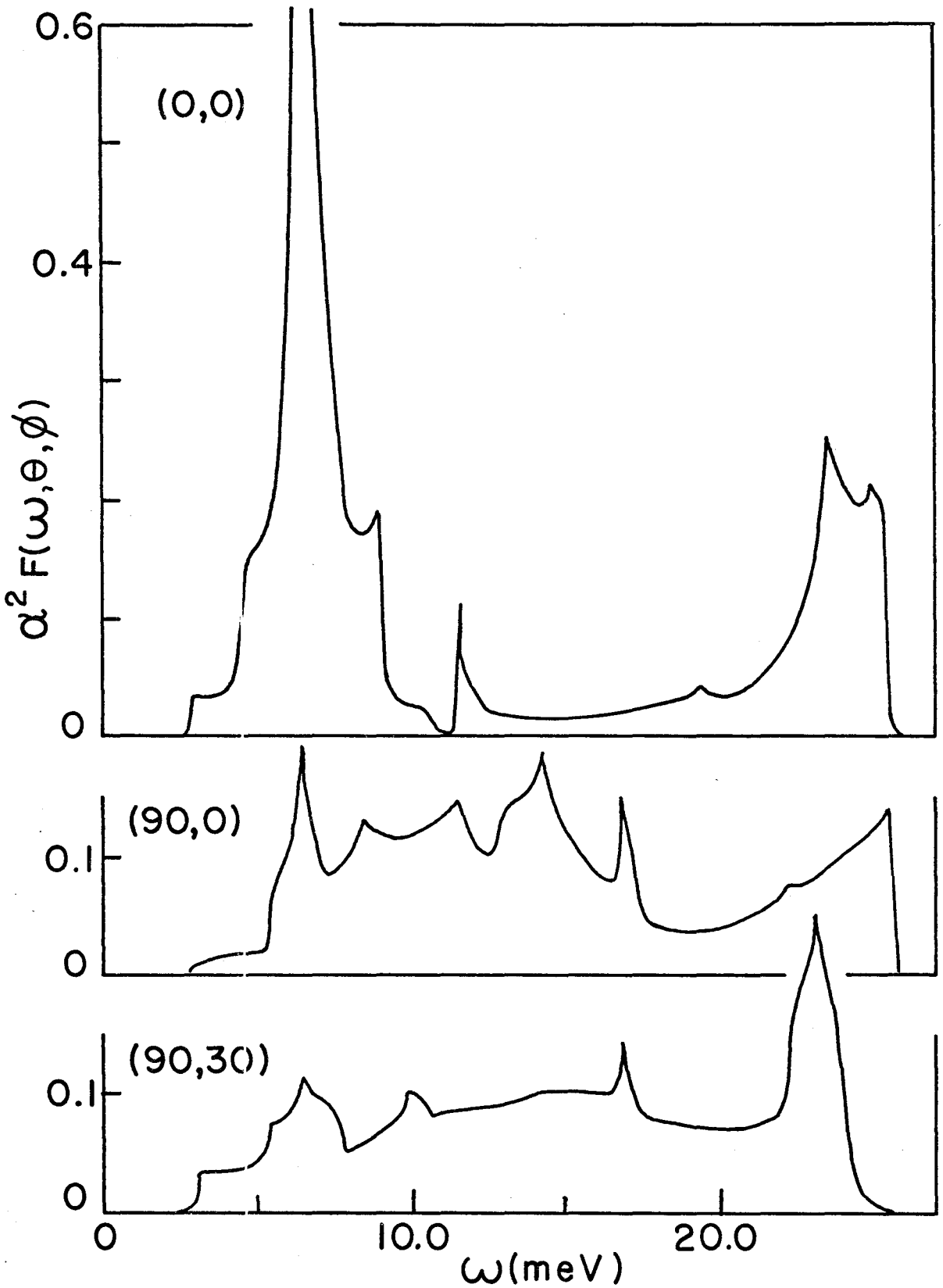
0.6
0.4
0
(0,0)
$\alpha^2 F(\omega,\theta,\phi)$
0.1
0
(90,0)
0.1
0
(90,30)
0
10.0
20.0
ω(meV)

Figure 4.2.2

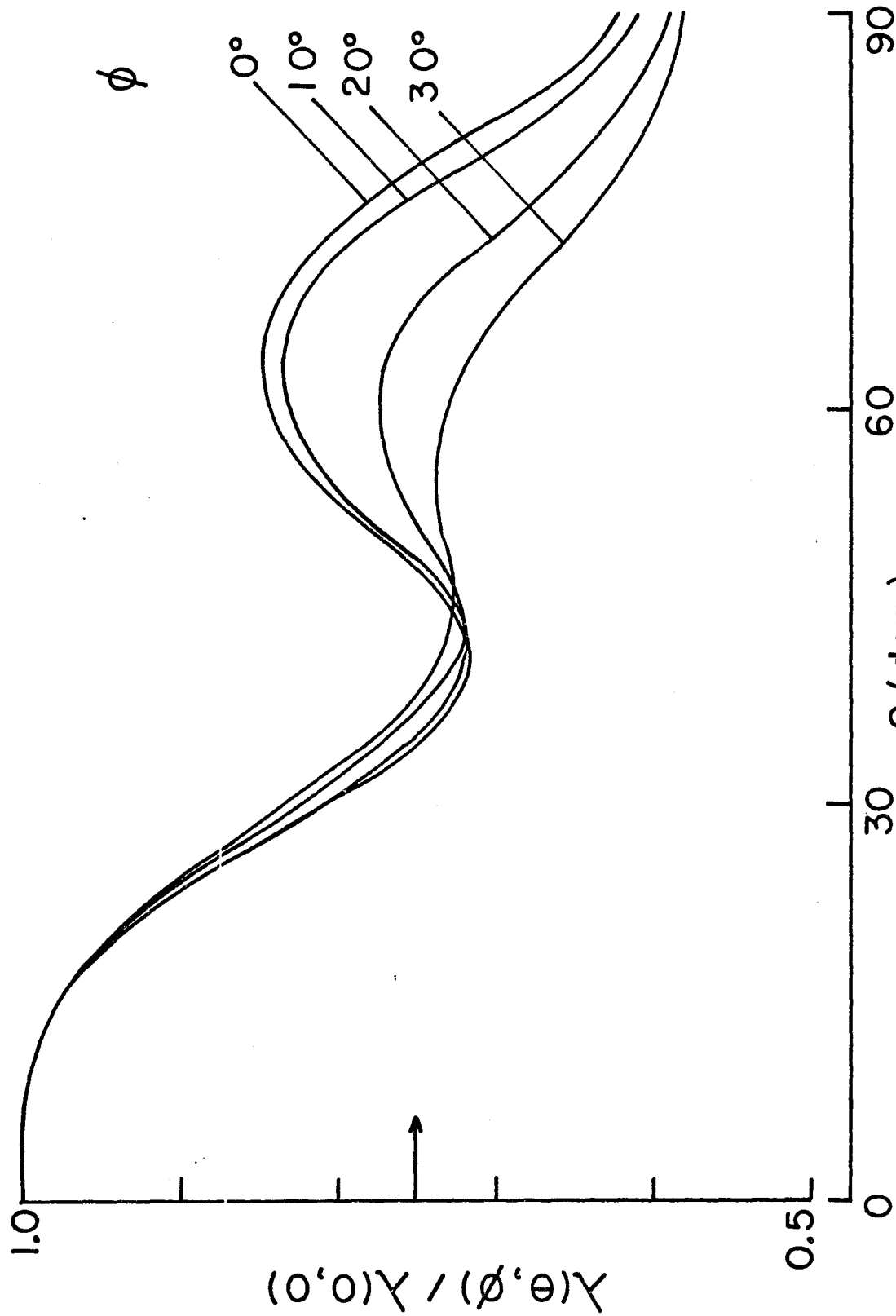

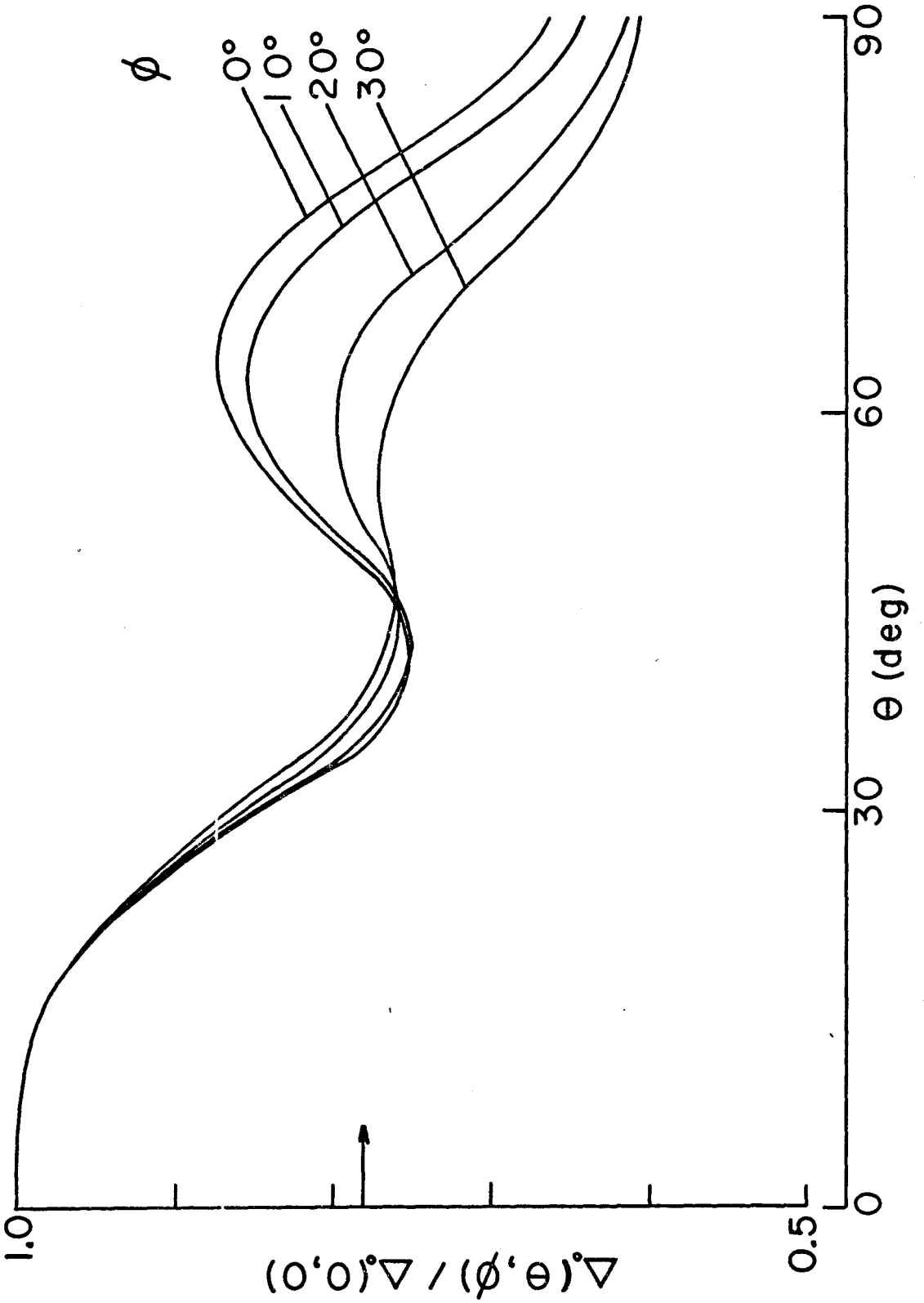
φ
0°
10°
20°
30°
90
60
30
0
θ (deg)
1.0
0.5
Δ°(θ,φ) / Δ°(0,0)

Figure 4.2.4

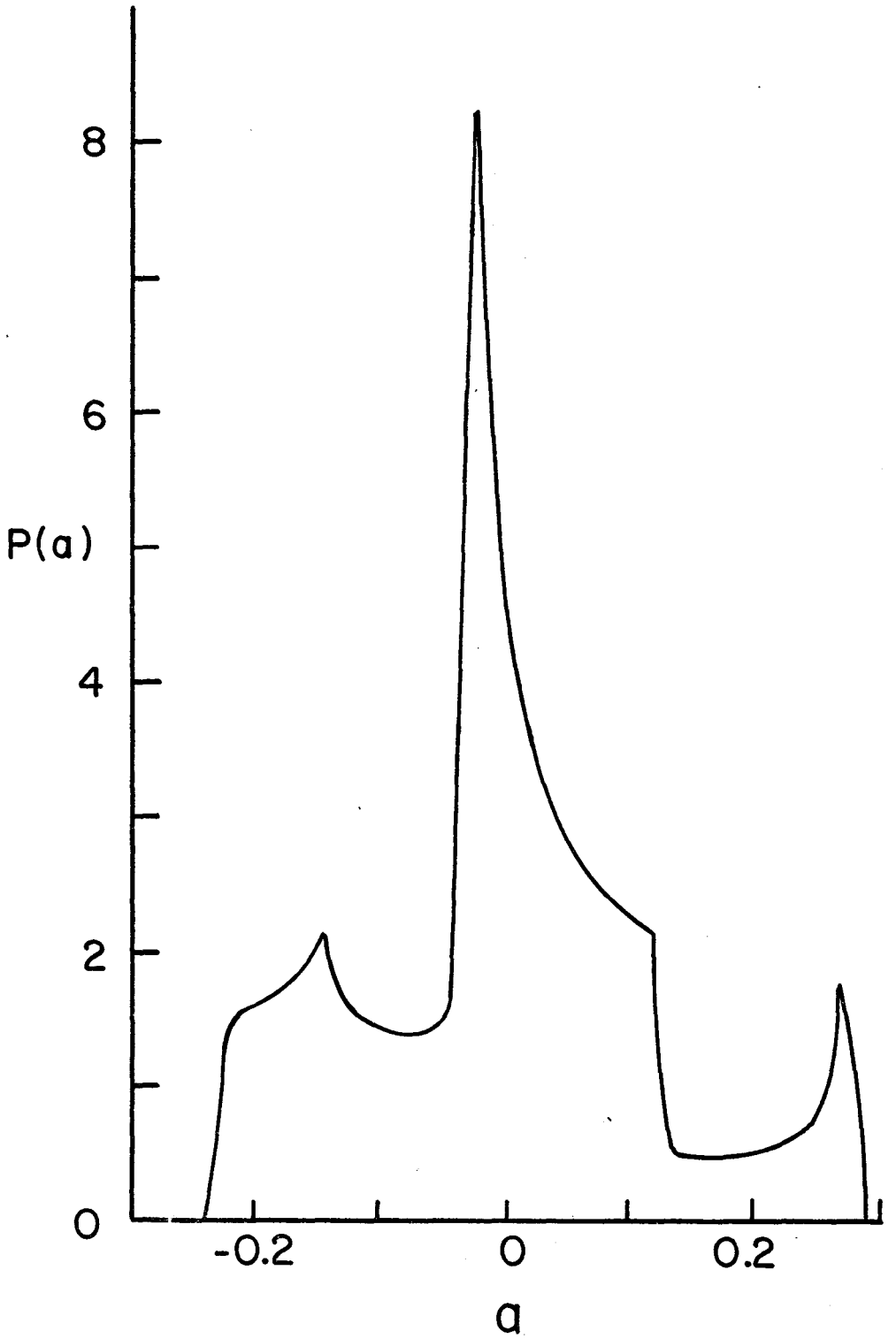

Figure 4.2.5

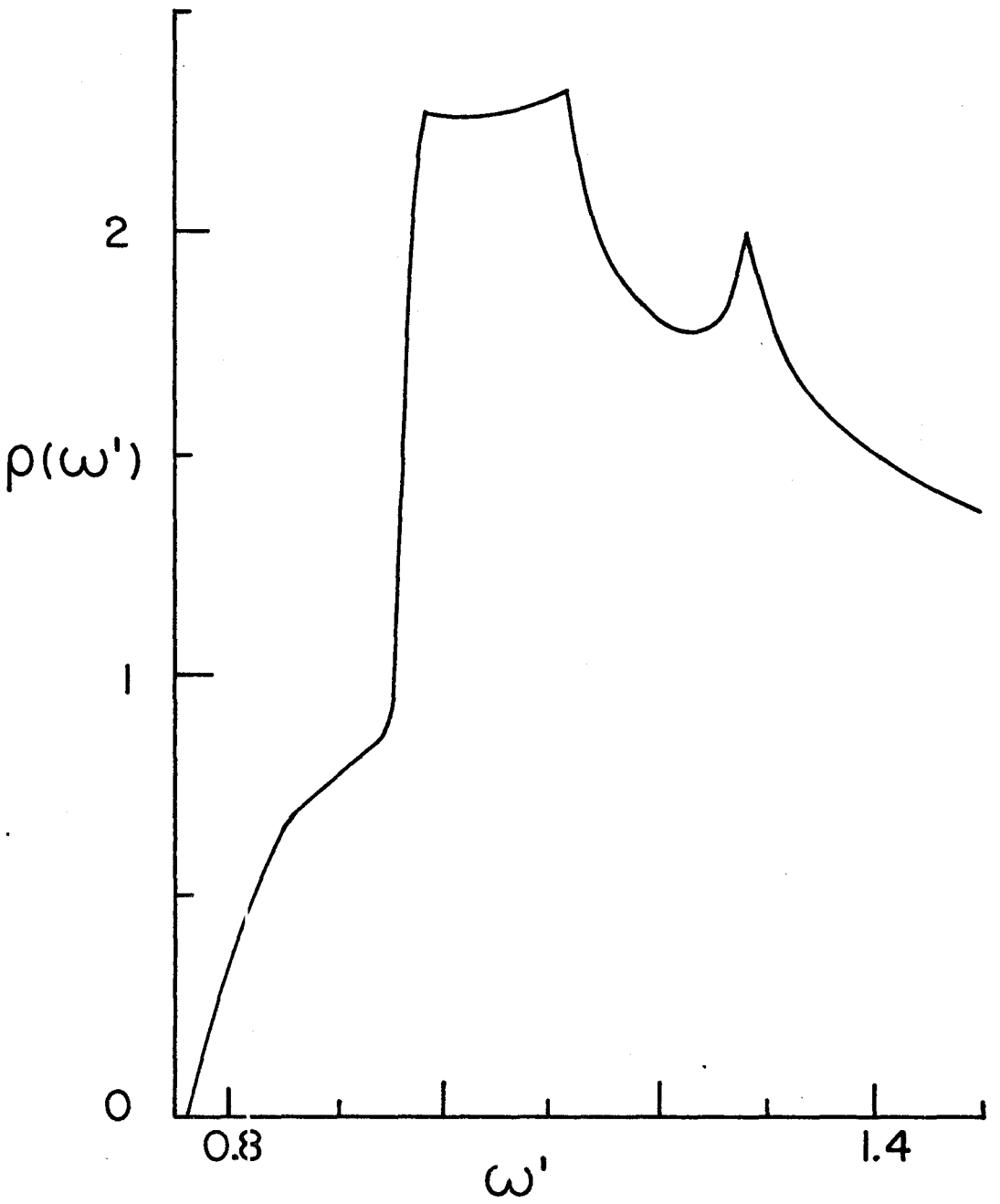

Figure 4.2.6

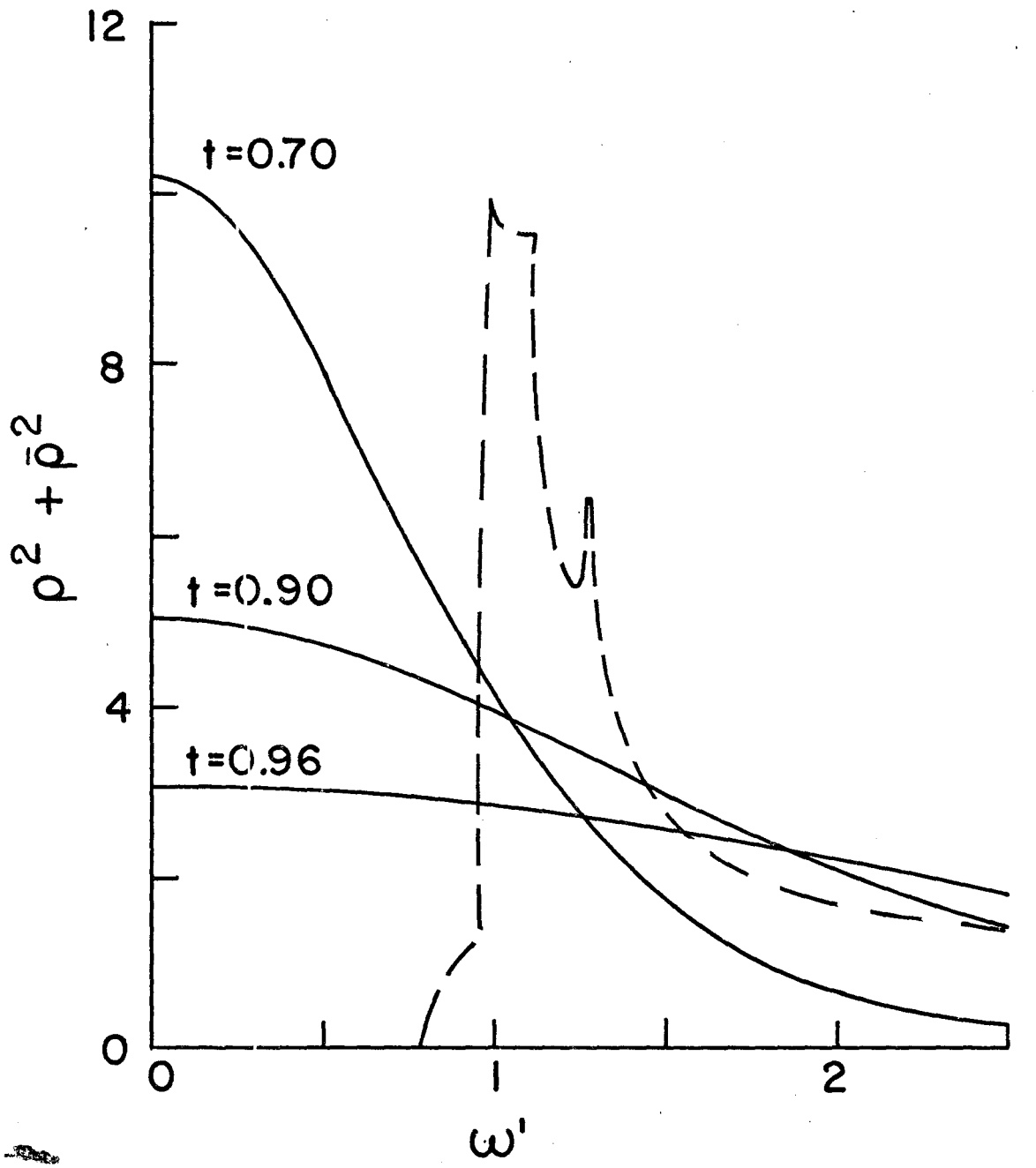

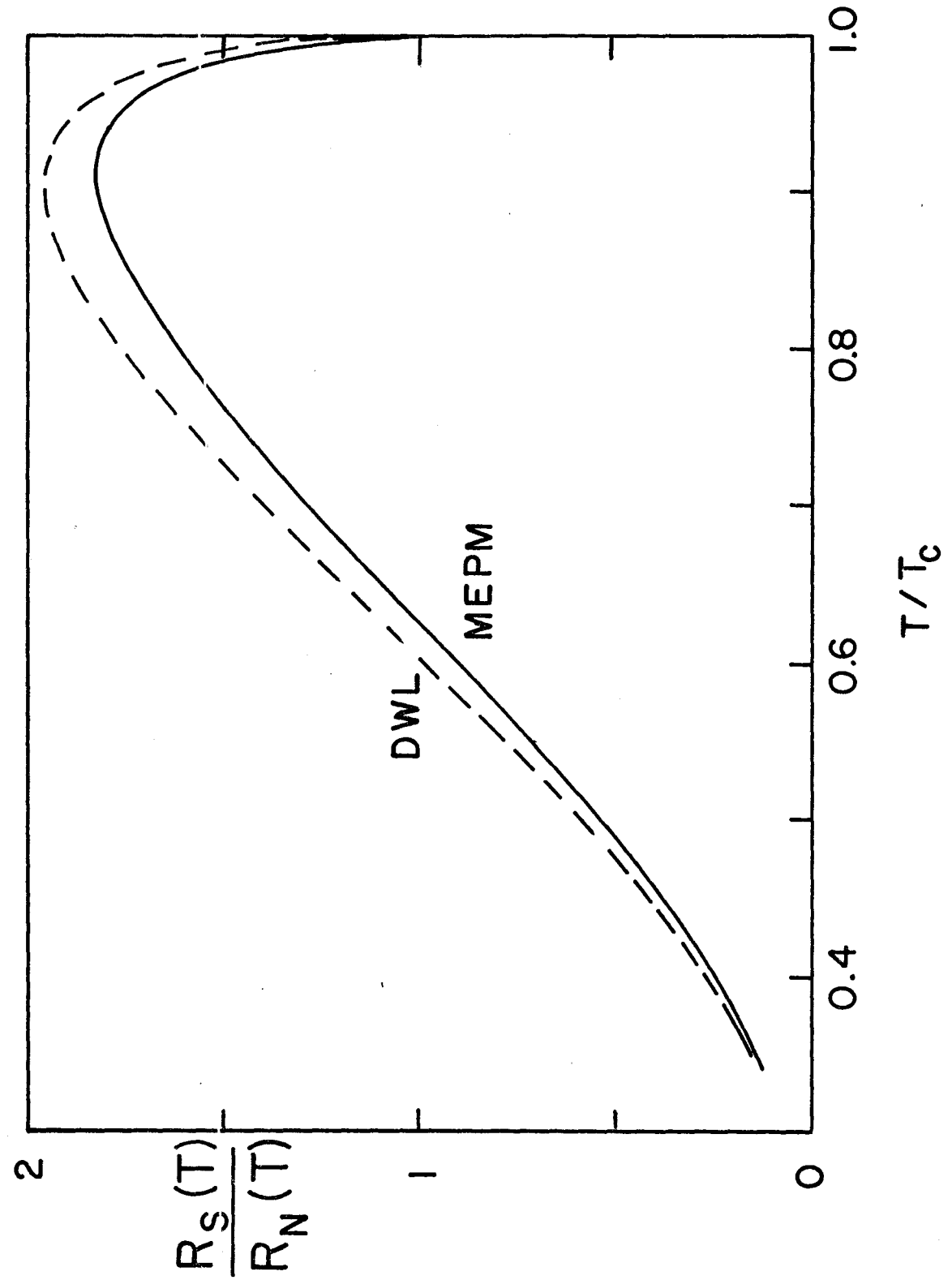
2
1
0
$\frac{R_S(T)}{R_N(T)}$
0.4
0.6
0.8
1.0
T / T_c
DWL
MEPM

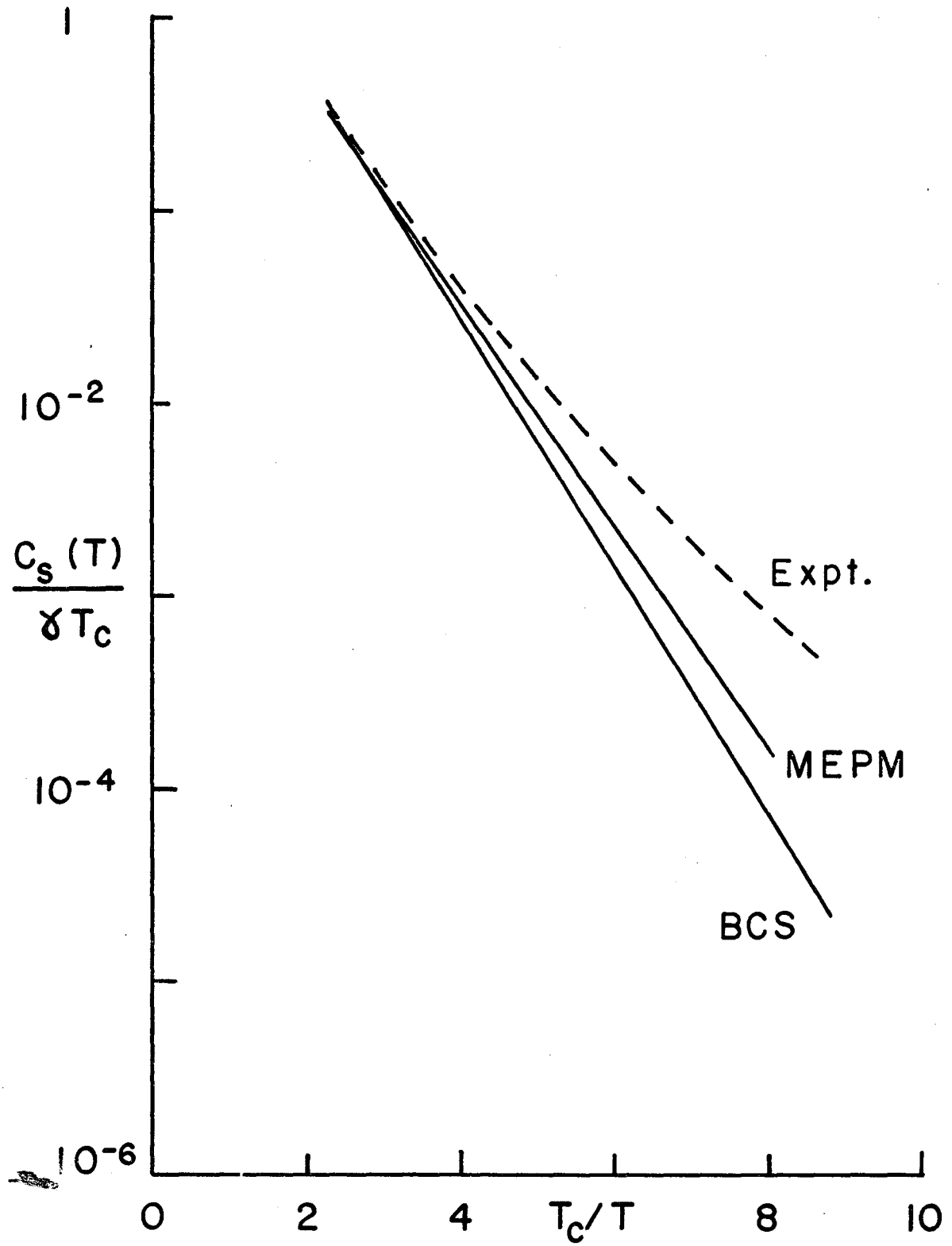
1
10^{-2}
$\frac{C_s(T)}{\gamma T_c}$
10^{-4}
10^{-6}
0
2
4
T_c/T
8
10
Expt.
MEPM
BCS

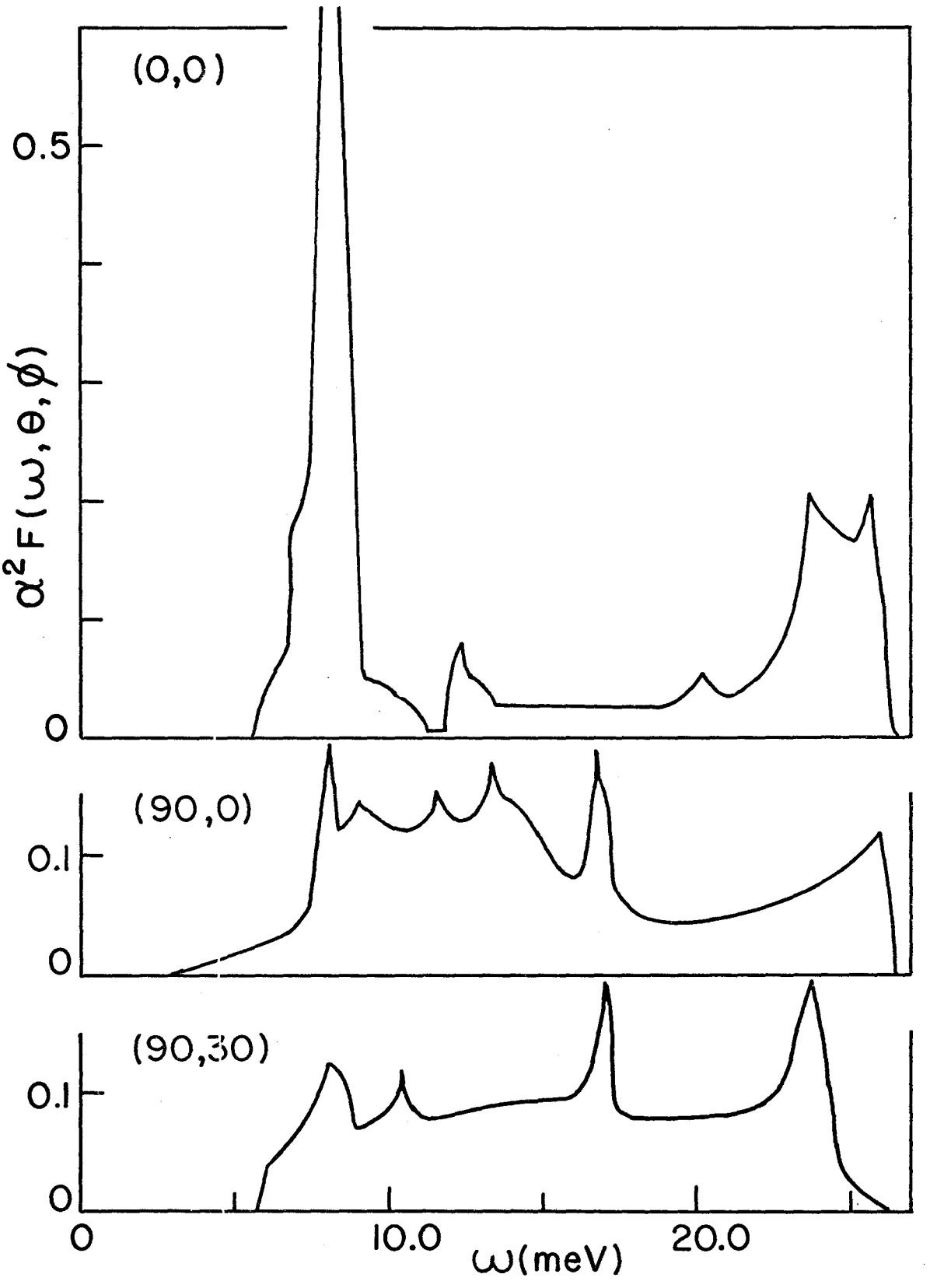
(0,0)
0.5
0
$\alpha^2F(\omega,\theta,\phi)$
(90,0)
0.1
0
(90,30)
0.1
0
0
10.0
20.0
ω(meV)

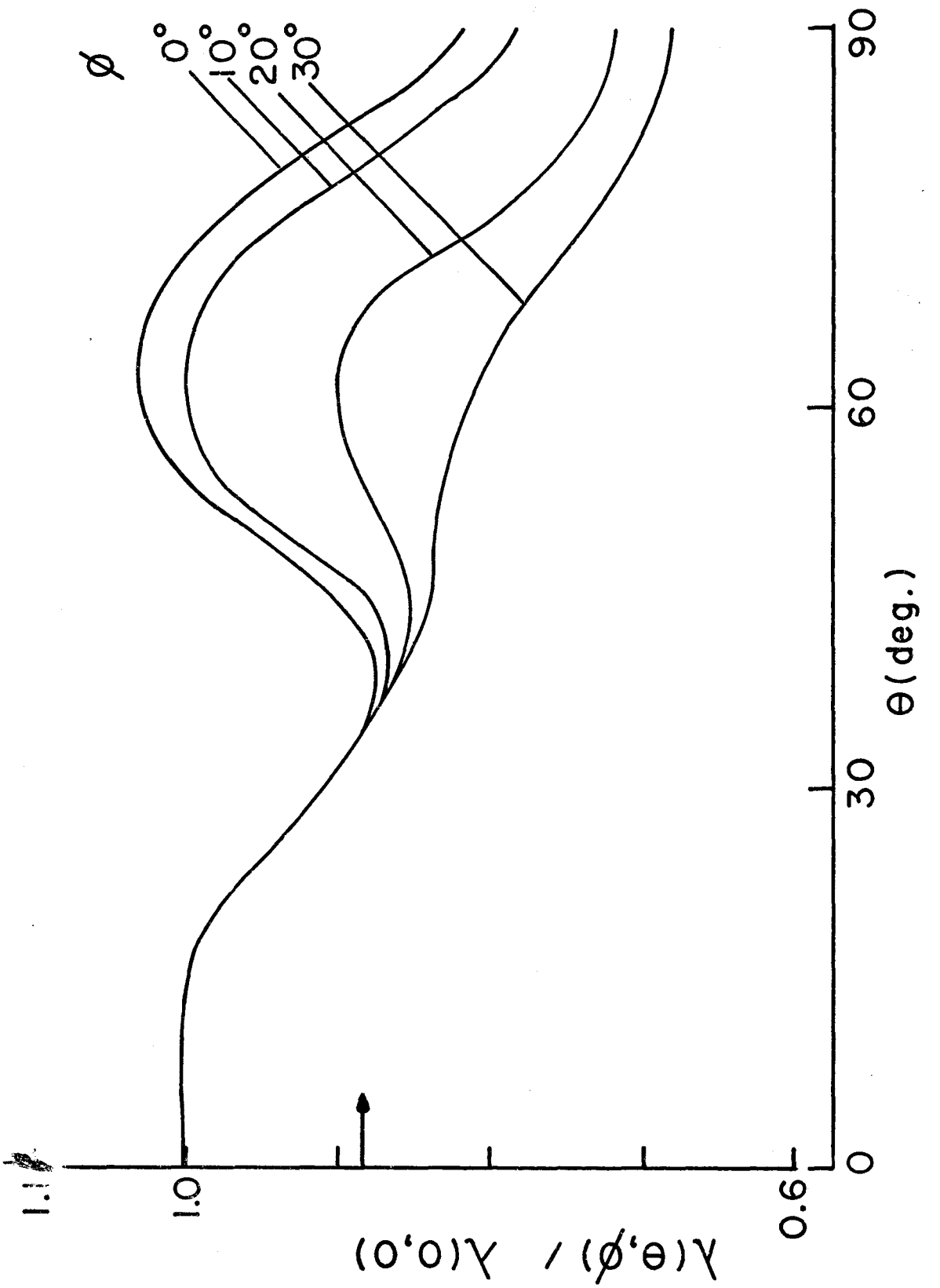
ϕ
0°
10°
20°
30°
90
60
30
0
θ(deg.)
λ(θ,ϕ) / λ(0,0)
0.9
1.0
1.1

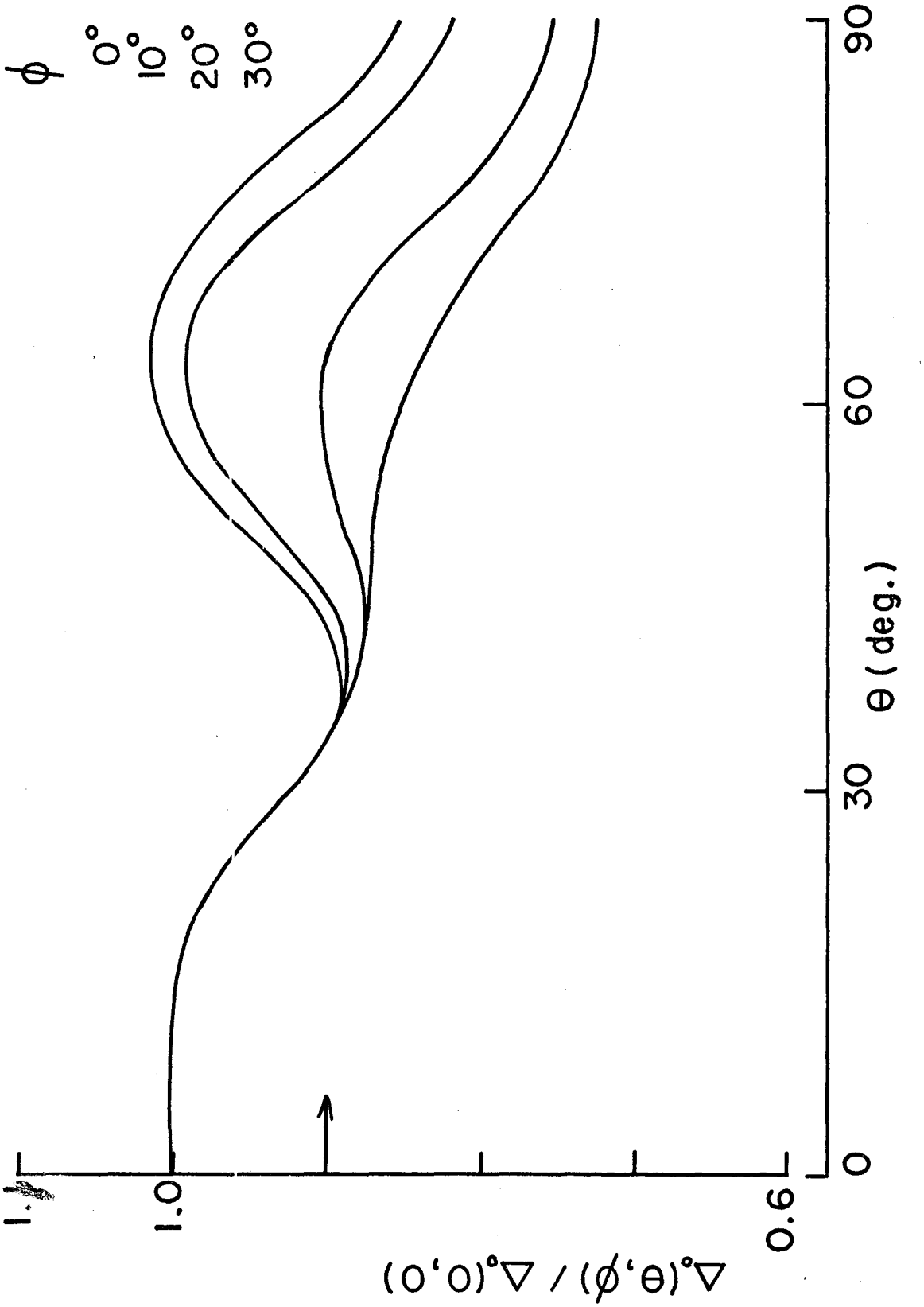
φ
0°
10°
20°
30°
1.4
1.0
0.6
0
30
60
90
θ (deg.)
Δ°(θ,φ) / Δ°(0,0)

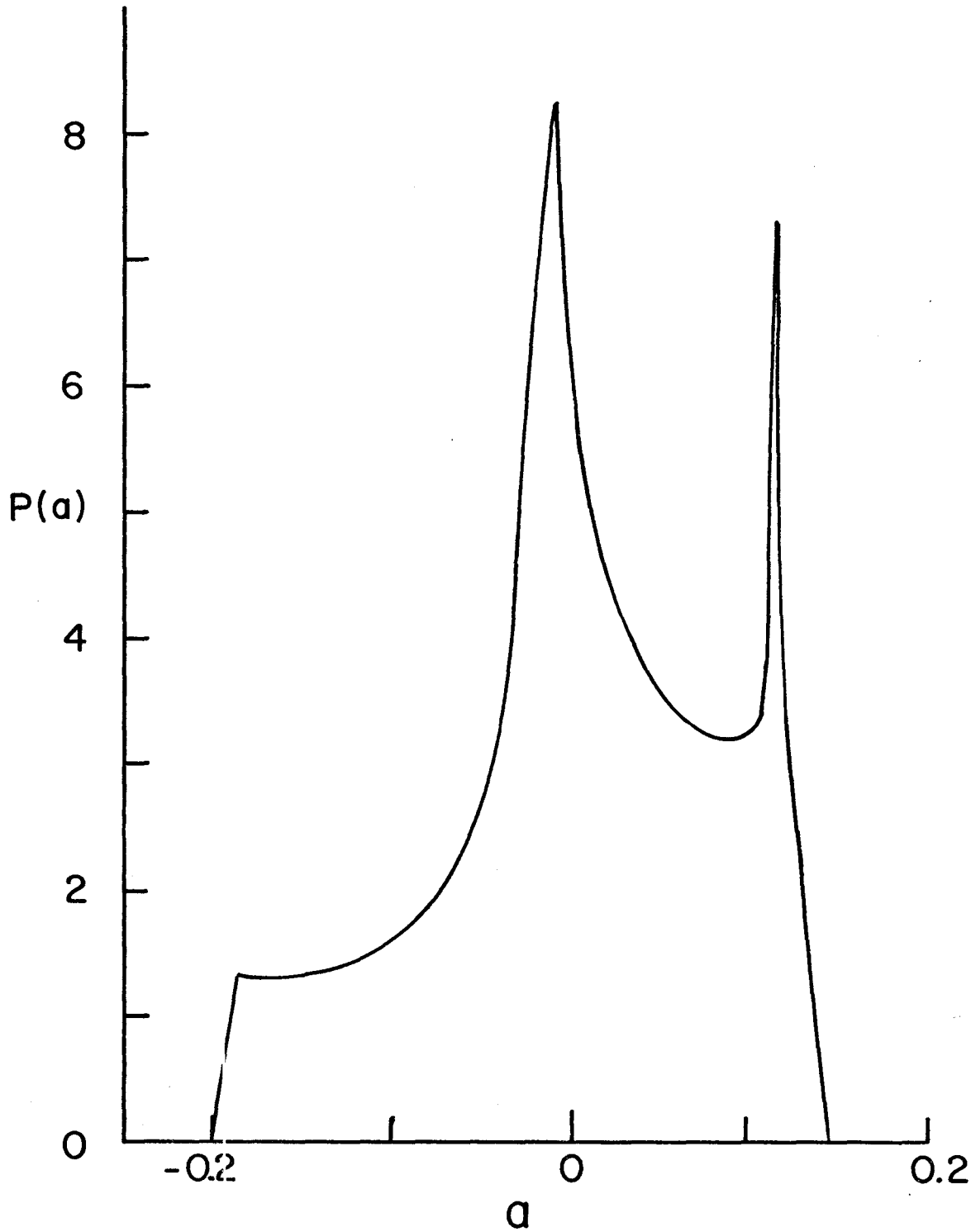
8
6
P(a)
4
2
0
-0.2
0
0.2
a

Figure 4.2.13

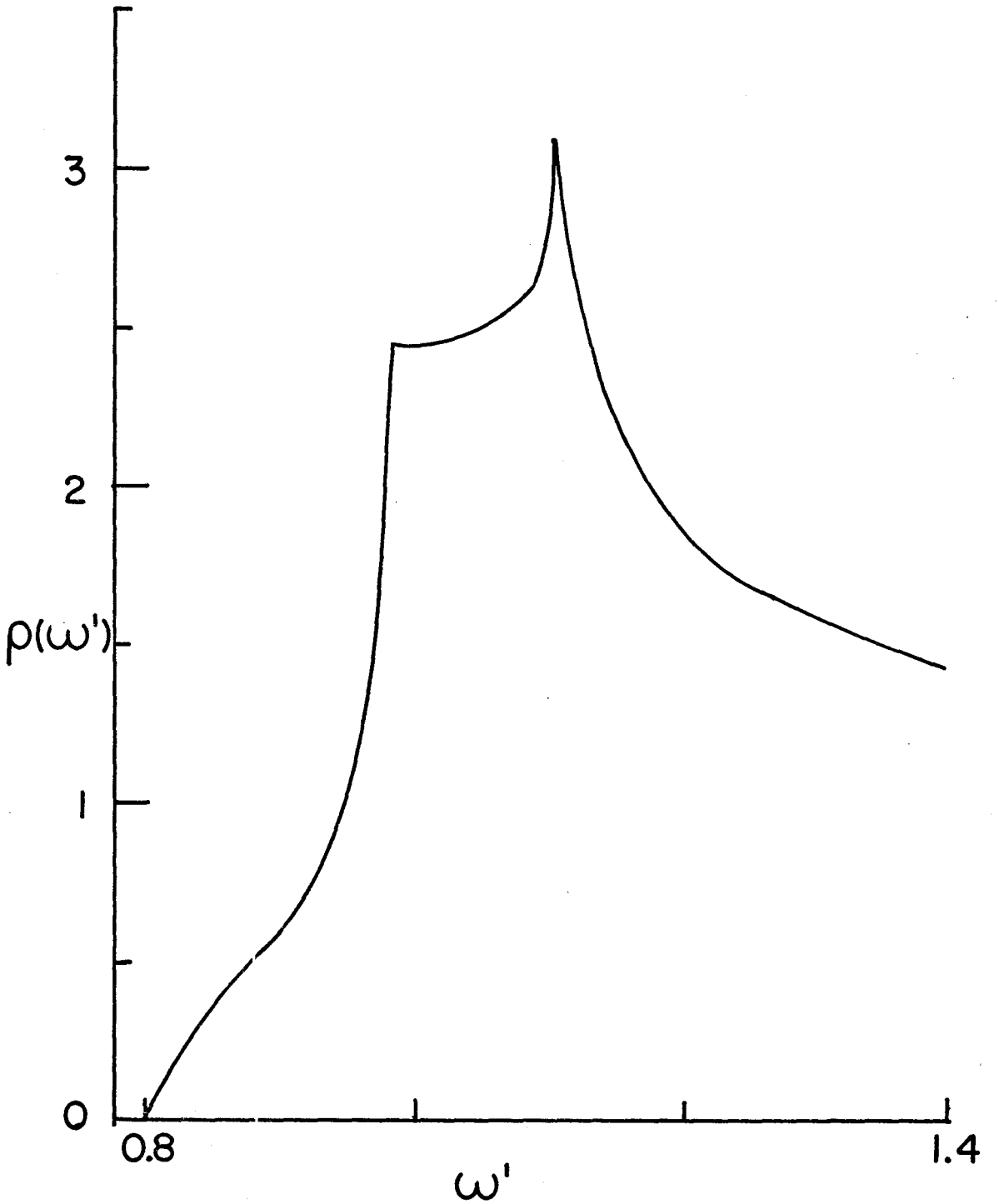

4.3 ANISOTROPIC SUPERCONDUCTING PROPERTIES: THALLIUM

In this section we present our results for the anisotropic superconducting properties of thallium. As discussed in section 3.4, we carry through all the calculations with two Tl models. Both use the WSM force constants and Ashcroft form pseudopotentials. One has a pseudopotential parameter $R_c = 0.875$ Å and band mass $m_B = 0.64$, while the other uses $R_c = 0.435$ Å and $m_B = 0.44$. The models are presented together, and comparison is made between them. The method of calculation is the same as that discussed for zinc in the previous section.

We recall that both Tl models give almost identical results for the isotropic $\alpha^2F(\omega)$; and agreement with experiment is very good, figures 3.4.9 and 3.4.10. The three high symmetry direction $\alpha^2F(\omega,\theta,\phi)$'s for the Tl(0.875) and Tl(0.435) models are shown in figures 4.3.1 and 4.3.2 respectively. We note that, for each model, the isotropic and each of the directional functions are quite different.

Comparing figures 4.3.1 and 4.3.2 it is observed that, although there is qualitative agreement between the directional results for these two models, there are also rather large differences. These differences arise solely as a result of the different weightings which the two pseudopotentials give the phonon modes through the $L(\underline{q};j)$ factor in equation (3.20).

Unlike Zn, the Tl low frequency peak of $\alpha^2F(\omega,0,0)$ is not very much larger than those observed in the basal plane directions. At the same time, the basal plane functions have a much larger contribution from frequencies significantly lower than the low frequency peak value. These observations lead one to expect that neither the directional mass enhancement nor the superconducting gap will show a maximum along the c-axis direction ($\theta = 0°$, $\phi = 0°$). This is indeed the case, as is shown in figures 4.3.3 and 4.3.4, where we give $\lambda(\theta,\phi)$ and $\Delta_0(\theta,\phi)$ respectively. As can be observed in Zn (section 4.2) and Al [50], the electron-phonon mass enhancement parameters and the gaps are highly correlated. However, the gap curves appear to be "smoother" and more uniform.

A very qualitative comparison may be made between longitudinal ultrasonic attenuation measurements [119] and our gaps of figure 4.3.4. Sound propagation along the (90,0) direction picks up larger gap values than propagation along (90,30). Since the important electrons for ultrasonic attenuation are those with velocity vectors perpendicular to the direction of propagation, experiment indicates that $\Delta_0(\theta,0) < \Delta_0(\theta,30)$. This is the ordering given by our Tl models. However, it must be remembered that this is a very rough comparison, because ultrasonic attenuation involves weighted angular averages over the gaps.

The gap variation as a function of angle, figure 4.3.4, is similar for both Tl models. The gap anisotropy

distribution functions P(a) are shown in figure 4.3.5. The structures of these two functions are somewhat different. These differences are directly related to the absolute and secondary maxima and minima of figure 4.3.4.

The minimum gap value for the Tl(0.875) model occurs at approximately (72,0). Since the $\Delta_0(\theta,\phi)$ enter the calculation of P(a) with a weight of $\sin(\theta)$, there will be a strong contribution from this region and P(a) will show a sharp strong increase for the most negative a-values. The Tl(0.435) model has the minimum at (0,0) and from the $\sin(\theta)$ weighting there will be a weak contribution to the most negative a-region. When the a-values reach the region of the secondary minimum at (72,0) there will be a sharp increase in P(a). This effect is seen in figure 4.3.5 as a negative-a "tail" in P(a) for Tl(0.435), which is absent in the Tl(0.875) function.

Now let us consider the effect of the maxima. The Tl(0.875) model has a secondary maximum $\Delta_0(90,30)$, as the a-variable is increased beyond the value corresponding to this gap there will be a sharp decrease in P(a). This decrease will be followed by a peak from gaps in the region $\theta \cong 30°$, since these gap values are all larger than $\Delta_0(90,30)$. As seen in figure 4.3.5, this structure is absent for the Tl(0.435) model, because the gap maxima at $\theta = 90°$ and $\theta \cong 35°$ are of almost the same magnitude. Thus, small shifts in the gap variation over the Fermi surface may produce large changes in P(a).

The R_c = 0.875 (0.435) model gives anisotropy parameters: $\langle a^2 \rangle$ = 0.0024 (0.0017), $\langle ab \rangle$ = 0.0046 (0.0033) and $\langle a\bar{b} \rangle$ = 0.0073 (0.0053). Then equation (4.32) with λ, $\lambda(T_c)$, $\bar{\lambda}$ and μ^* values from section 4.1 gives

$$\frac{T_c^{PSC}}{T_c} = 1.006 \ (1.004) \quad .$$

As discussed in section 4.2, the presence of anisotropy has enhanced the strength of the superconducting state. Phonon anisotropy was found to have a much smaller effect on the average gap than on T_c, and for thallium we set $(\langle \Delta_0(\underline{k}) \rangle / \Delta_0) = 1.0$.

Figure 4.3.6 shows the calculated temperature independent quasiparticle densities of states. The structure of the P(a) functions is directly reflected in the $\rho(\omega')$. The nuclear spin-lattice relaxation rates are shown in figure 4.3.7. As expected the Tl(0.435) results, which show less anisotropy, lie slightly above the Tl(0.875) curve in the temperature range indicated. We have also calculated the low temperature electronic specific heats. Since the anisotropy is very small, these values lie between the BCS and MEPM curves of figure 4.2.8.

In summary, both of our thallium pseudopotentials give very similar anisotropic superconducting properties. Small differences are observed in the variation of the mass enhancements and gaps as of function of position on the Fermi surface.

FIGURE CAPTIONS - SECTION 4.3

FIGURE 4.3.1: $\alpha^2F(\omega,\theta,\phi)$ for three high symmetry directions in Tl, calculated with the R_c = 0.875 Å pseudopotential. The directions are labeled by (θ,ϕ).

FIGURE 4.3.2: $\alpha^2F(\omega,\theta,\phi)$ for three high symmetry directions in Tl, calculated with the R_c = 0.435 Å pseudopotential. The directions are labeled by (θ,ϕ).

FIGURE 4.3.3: Thallium electron-phonon mass enhancements $\lambda(\theta,\phi)/\lambda(0,0)$ with $\lambda(0,0) = 0.707$ for the Tl(0.875) model, and $\lambda(0,0) = 0.681$ for the Tl(0.435) model. The Fermi surface averaged values are given by the positions of the arrows on the vertical axes.

FIGURE 4.3.4: Thallium zero temperature superconducting gaps $\Delta_0(\theta,\phi)/\Delta_0(0,0)$ where $\Delta_0(0,0) = 0.349$ meV for the Tl(0.875) model and $\Delta_0(0,0) = 0.338$ meV for the Tl(0.435) model. The Fermi surface averaged values are given by the positions of the arrows on the vertical axes.

FIGURE 4.3.5: Tl(0.875) and Tl(0.435) gap anisotropy distribution functions P(a).

FIGURE 4.3.6: Tl(0.875) and Tl(0.435) temperature independent quasiparticle densities of states $\rho(\omega')$ as a function of ω' (dimensionless).

FIGURE 4.3.7: Ratio of the thallium superconducting and normal state nuclear spin-lattice relaxation rates $R_S(T)/R_N(T)$ as a function of temperature. The results for both models Tl(0.875) and Tl(0.435) are shown.

Figure 4.3.1

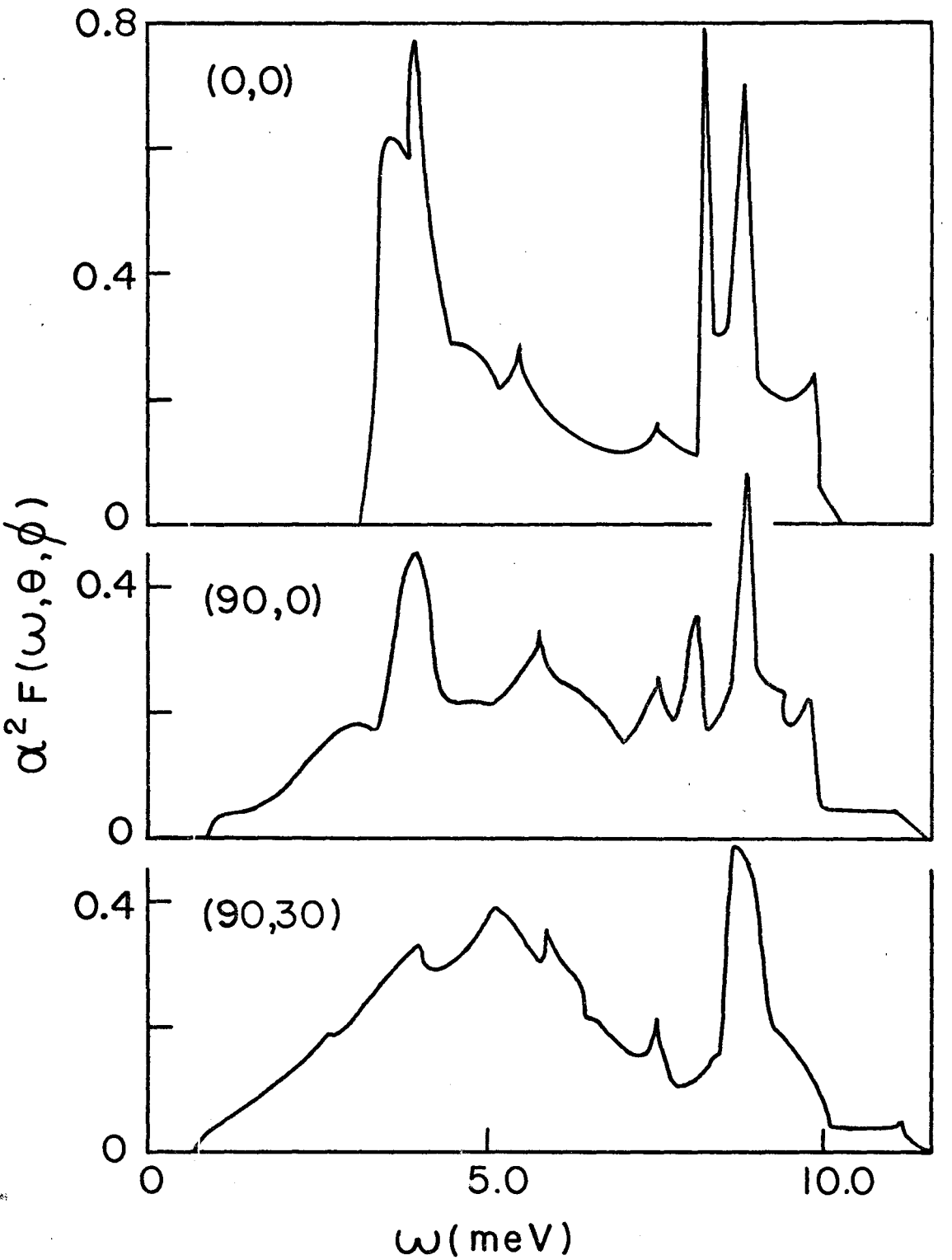
0.8
0.4
0
(0,0)
0.4
0
(90,0)
0.4
0
(90,30)
$\alpha^2 F(\omega,\theta,\phi)$
0
5.0
10.0
ω(meV)

Figure 4.3.2

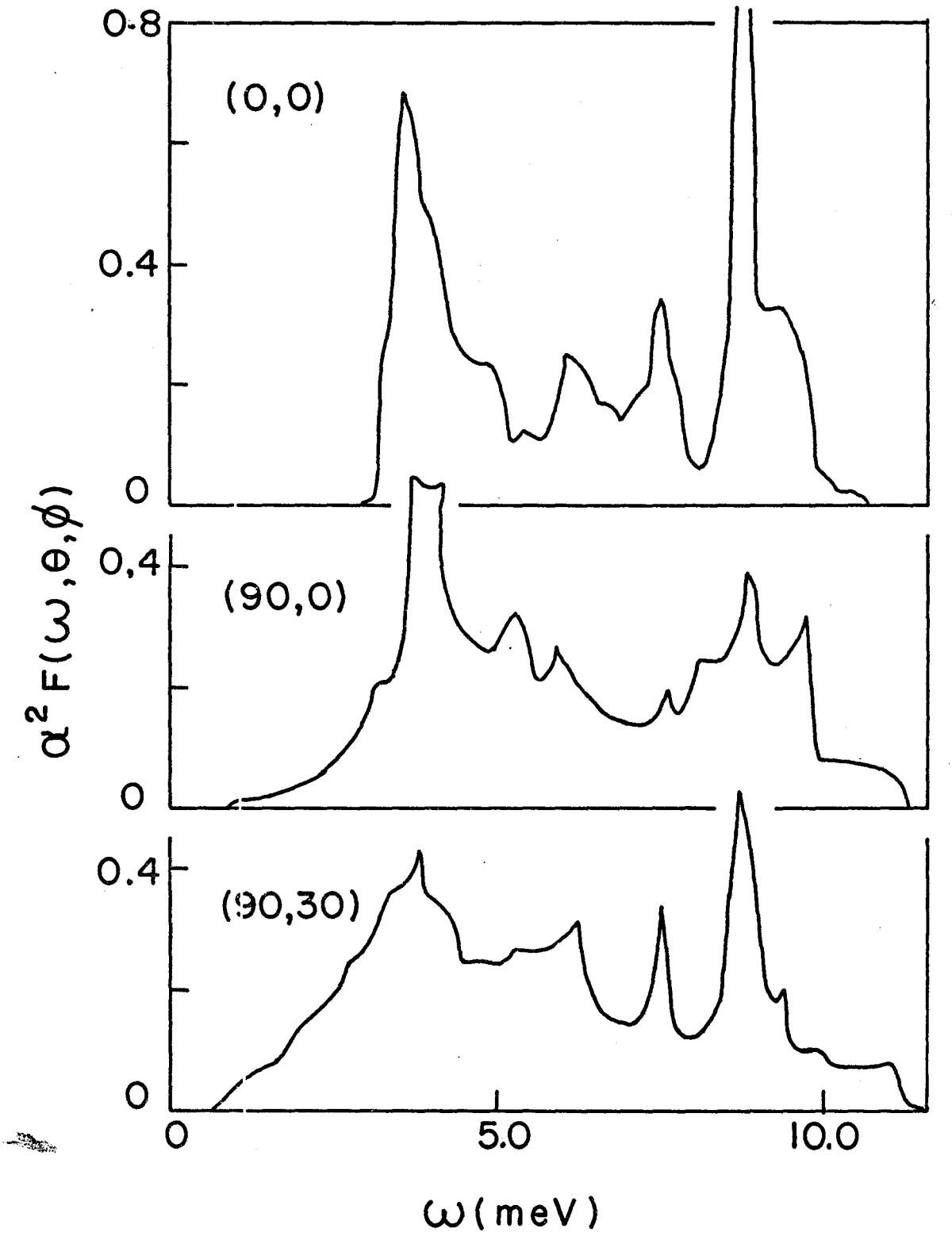
0.8
0.4
0
(0,0)
0.4
0
(90,0)
0.4
0
(90,30)
0
5.0
10.0
$\alpha^2 F(\omega,\theta,\phi)$
ω(meV)

Figure 4.3.3

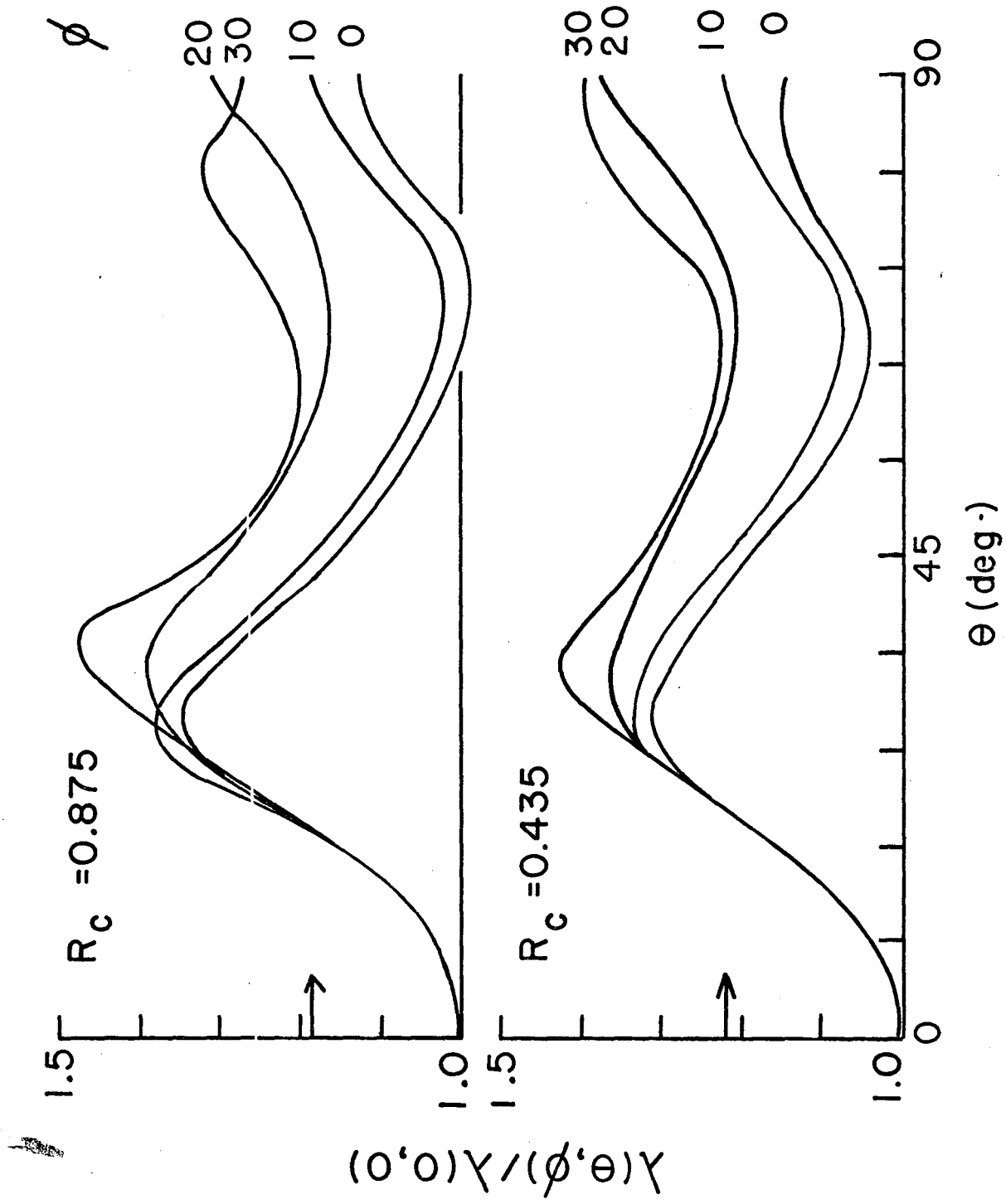
φ
20
30
10
0
R_c =0.875
1.5
1.0
R_c =0.435
30
20
10
0
1.5
1.0
0
45
90
θ (deg.)
λ(θ,φ)/λ(0,0)

Figure 4.3.4

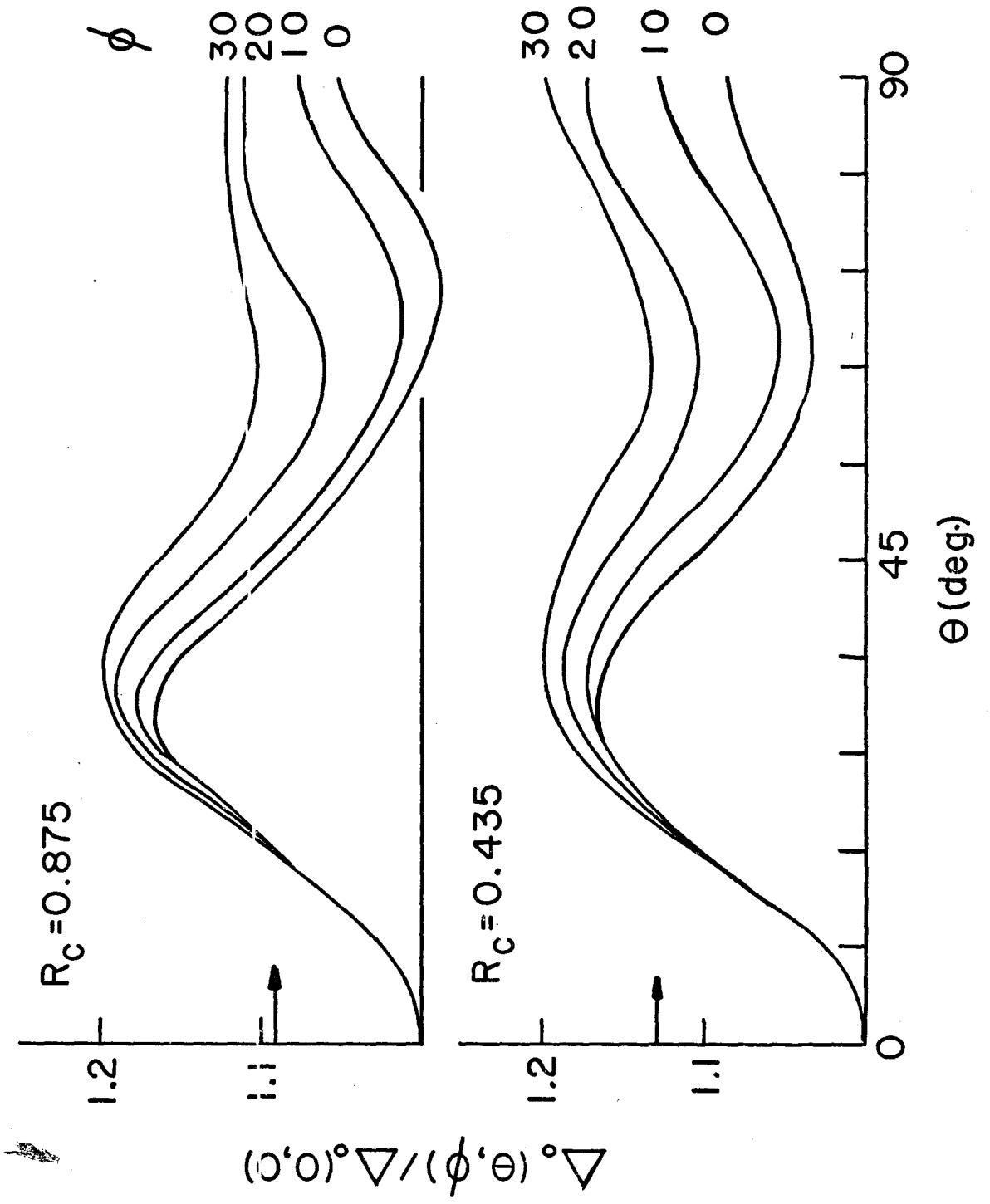
ϕ
30
20
10
0
R_c=0.875
R_c=0.435
1.2
1.1
0
45
90
θ(deg.)
$\Delta_\circ(\theta,\phi)/\Delta_\circ(0,0)$

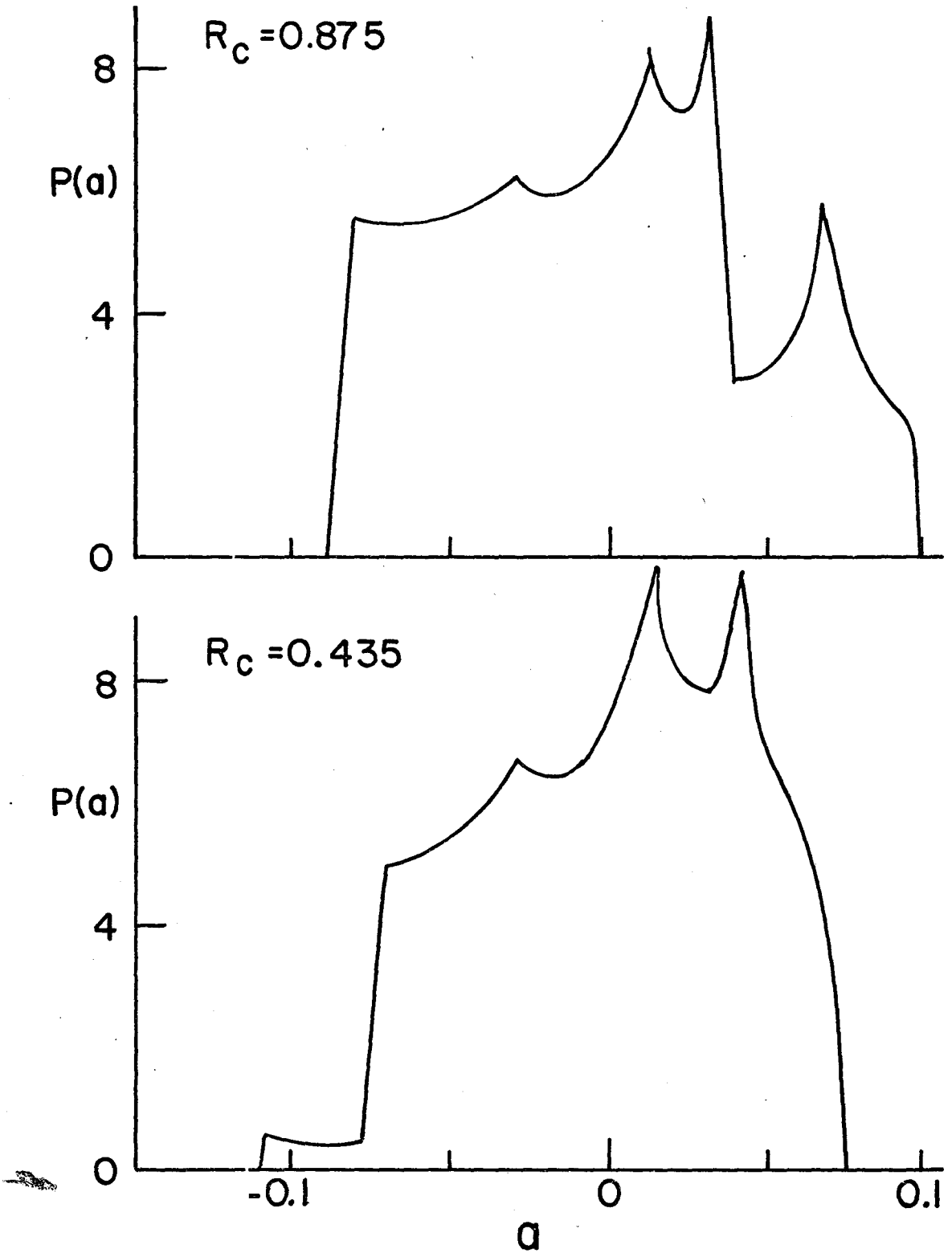
R_c =0.875
8
P(a)
4
0
R_c =0.435
8
P(a)
4
0
-0.1
0
0.1
a

Figure 4.3.6

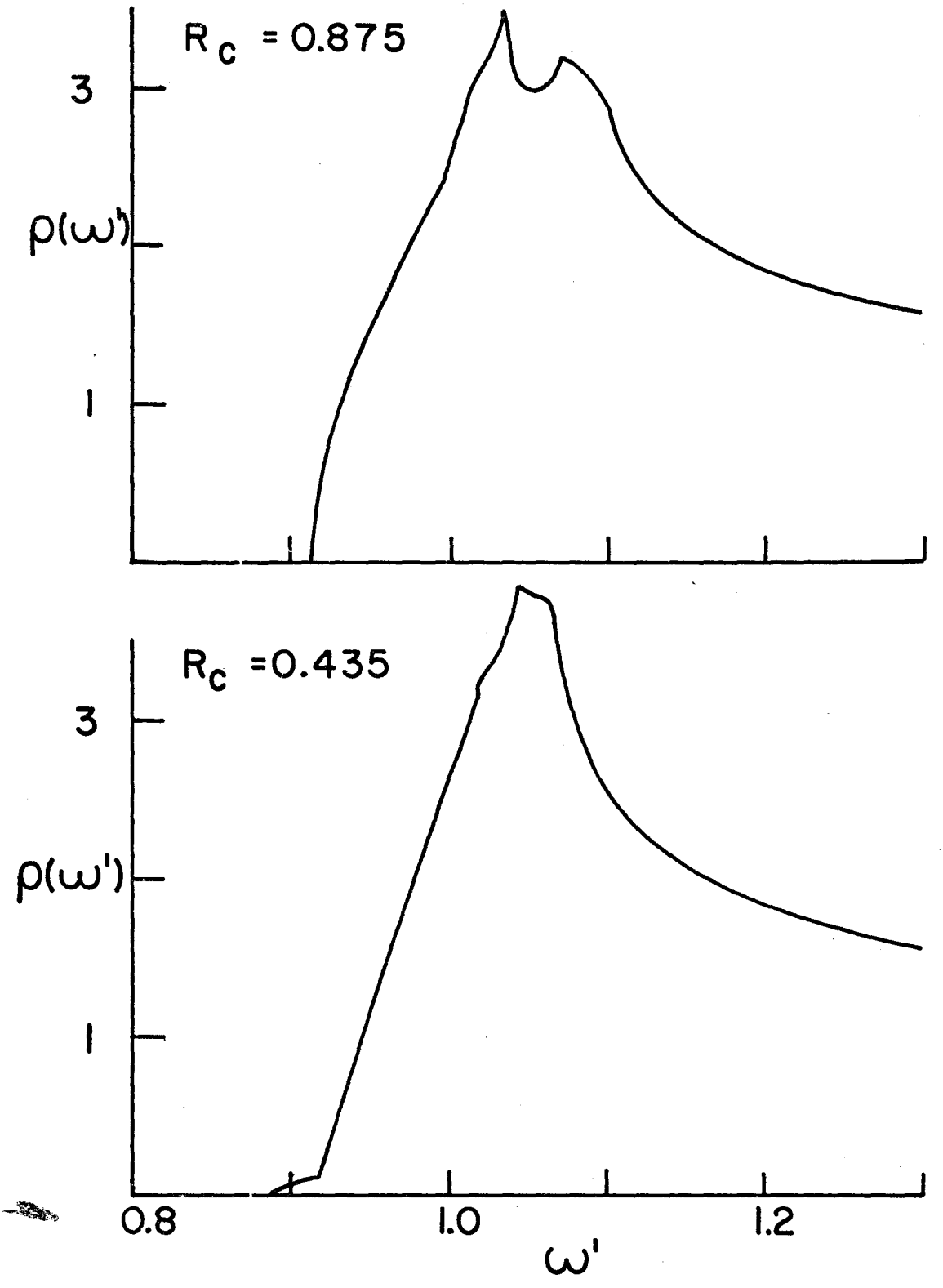

Figure 4.3.7

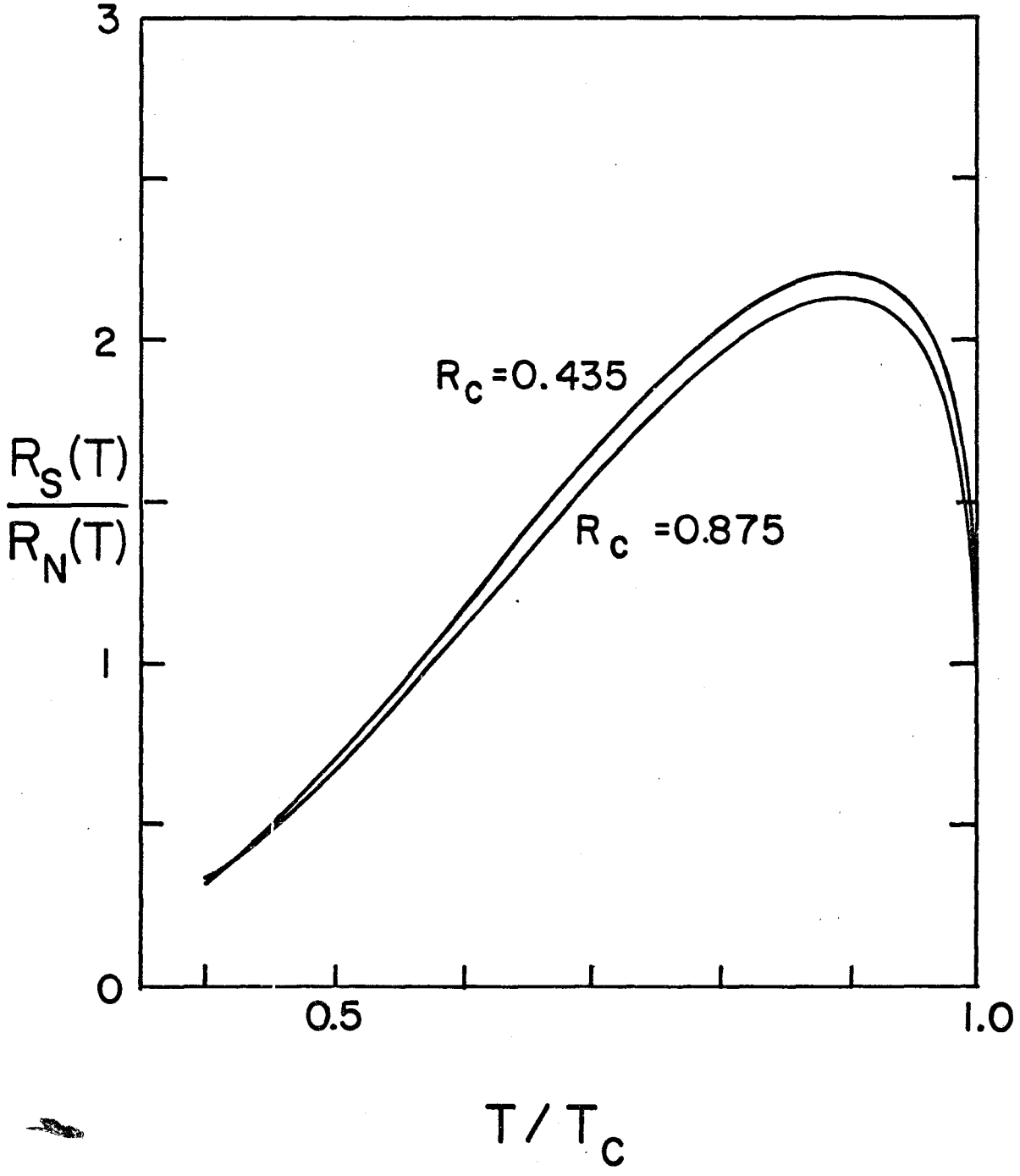

CHAPTER V

NORMAL STATE PROPERTIES

5.1 ANISOTROPY IN THE TEMPERATURE VARIATION OF THE ELECTRON-PHONON MASS ENHANCEMENT AND SCATTERING TIMES: ZINC AND THALLIUM

In this section we investigate the effect of finite temperature (T) on the electron-phonon mass enhancements $\lambda(\underline{k},T)$, and the electron-phonon scattering times $\tau_{el-ph}(\underline{k},T)$. Because of the similar qualitative behaviour shown by these properties for all models considered, we present our Zn and Tl results together.

Grimvall [120] has shown theoretically that the renormalization, λ, of the electronic effective mass due to the electron-phonon interaction can have a significant temperature variation. This temperature dependence can in principle be measured in a cyclotron resonance experiment [121-123]. Data have been reported on $\lambda(T)$ in zinc [124], lead [125] and mercury [126,127]. For the moment we merely note that the directional quantities $\lambda(\underline{k},T)$ are relevant to these experiments, and not necessarily the isotropic result $\lambda(T)$. This point will be illustrated in section 5.2.

The energy of an electron near the Fermi surface in a state $|\underline{k}>$ will be modified by the electron-phonon

interaction. It can be expressed as [92]

$$E_{\underline{k}} = \varepsilon_{\underline{k}} + \text{Re } \Sigma\ (\underline{k},E_{\underline{k}}) \tag{5.1}$$

where $\varepsilon_{\underline{k}} = \hbar^2k^2/2m$, m is the bare electron mass and $\Sigma(\underline{k},E_{\underline{k}})$ is the electron self-energy due to the electron-phonon interaction. The electron-phonon mass enhancement factor for an electron of momentum $\hbar\underline{k}$ is

$$\lambda_{\underline{k}} = -\frac{\partial}{\partial\omega}\,[\text{Re } \Sigma\ (\underline{k},\omega)]\Big|_{\omega=E_{\underline{k}}=0} \tag{5.2}$$

where the energy is measured relative to the Fermi level. The electron self-energy is given by

$$\Sigma(\underline{k},\omega) = \int_0^\infty d\omega' \int_{-\infty}^{\infty} dE_{\underline{k}'}\ \alpha^2F(\omega,\underline{k}') \times \left[\frac{1 + n(\omega') - f(E_{\underline{k}'})}{\omega - E_{\underline{k}'} - \omega' - i0^+} + \frac{n(\omega') + f(E_{\underline{k}'})}{\omega - E_{\underline{k}'} + \omega' - i0^+}\right] \tag{5.3}$$

where $f(E_{\underline{k}'})$ and $n(\omega')$ are the Fermi-Dirac and Bose-Einstein distribution functions, respectively.

Using (5.2) and (5.3) we may write $\lambda(\underline{k},T)$ as a simple frequency integration over a thermal factor $G(\frac{\omega}{T})$ independent of the material, and the function $\alpha^2F(\omega,\underline{k})$ characteristic of the material and direction under

consideration; that is

$$\lambda(\underline{k},T) = 2\int_0^\infty \frac{d\omega}{\omega}\,\alpha^2F(\omega,\underline{k})\,G(\tfrac{\omega}{T}) \tag{5.4}$$

where

$$G(\tfrac{\omega}{T}) = \frac{1}{2}\,(\frac{\hbar\omega}{2k_BT})^2\int_{-\infty}^{\infty}\frac{dX}{(\frac{\hbar\omega}{2k_BT})^2 - X^2}\cdot\frac{1}{\cosh^2X}\quad . \tag{5.5}$$

Therefore, the problem of calculating (5.4) reduces to a knowledge of $\alpha^2F(\omega,\underline{k})$, where we recall that

$$\alpha^2F(\omega,\underline{k}) = N(0)\int\frac{d\Omega_{\underline{k}'}}{4\pi}\sum_j|g_{\underline{k}\underline{k}'j}|^2\,\delta(\omega-\omega_{\underline{k}-\underline{k}'j}) \tag{5.6}$$

in the spherical Fermi surface approximation. These functions have already been obtained in sections 4.2 and 4.3. We note that for T = 0, expression (5.4) reduces to the correct zero temperature equation (4.25).

The function $G(\frac{\omega}{T})$ is plotted in figure 5.1.1, and the isotropic $\lambda(T)$'s for our Zn and Tl models are shown in figure 5.1.2. These isotropic functions are obtained by taking the Fermi surface average of equation (5.4). Because of the similarity of $\alpha^2F(\omega)$ calculated from our two thallium pseudopotentials, the single Tl curve represents both models Tl(0.875) and Tl(0.435) equally well.

The qualitative behaviour seen in figure 5.1.2 is characteristic of all $\lambda(T)$ and $\lambda(\underline{k},T)$; there is an initial

rise from the zero temperature value, a maximum is reached at relatively "low" temperatures, followed by a decrease to zero for $T \to \infty$. This behaviour is a direct consequency of the $G(\frac{\omega}{T})$ function shown in figure 5.1.1. The thermal function starts from zero for $(\hbar\omega/2k_BT) = 0$, reaches a maximum of ≈ 1.2 at $(\hbar\omega/2k_BT) \approx 1.9$ and then asymptotically approaches unity.

Therefore, for a given temperature, the phonon modes which are most heavily weighted are those of energy $\hbar\omega \approx 4k_BT$; and we would expect λ to be maximum when T is of the order of 1/4 the energy of the "most important" lower frequency modes. The Tl low energy peak occurs at $\hbar\omega_P \approx 4$ meV and by the above discussion the λ maximum should be at $T_M \approx 11°K$, for the zinc MEPM model $\hbar\omega_P \approx 6$ meV with $T_M \approx 18°K$, and for the zinc DWL model $\hbar\omega_P \approx 8$ meV with $T_M \approx 23°K$. For temperatures larger than T_M, the smaller than unity region of $G(\frac{\omega}{T})$ begins to "cutoff" the low frequency part of the α^2F spectrum and λ decreases. This is essentially the behaviour seen in figure 5.1.2.

Figures 5.1.3 through 5.1.6 show $\lambda(\theta,\phi,T)/\lambda(\theta,\phi,0)$, and the Fermi surface averaged variation $\lambda(T)/\lambda(0)$ for both Zn and Tl models in the low temperature region. The Tl temperature scale has been expanded relative to the Zn scale. The results for our Zn models are very different. Relative to the DWL model, the MEPM electron-phonon mass enhancements show more anisotropy, increase much faster as a

function of temperature and peak at a lower temperature. For our Tl models the (0,0), (90,30) and Fermi surface average results are very similar; but it is interesting that the (90,0) curves are considerably different.

The limiting values of $G(\frac{\omega}{T})$ are given by [92]

$$G(\frac{\omega}{T}) \simeq 1 + (\frac{\pi^2}{3})(\frac{k_B T}{\hbar\omega})^2 \qquad \text{for} \quad \hbar\omega >> k_B T \tag{5.7}$$

$$G(\frac{\omega}{T}) \simeq \frac{7\zeta(3)}{2\pi^2}(\frac{\hbar\omega}{k_B T})^2 \qquad \text{for} \quad \hbar\omega << k_B T \tag{5.8}$$

where $\zeta(x)$ denotes the Riemann zeta function. In the case where the contribution to λ from small ω is not important (see the appendix), the first limiting expansion gives $\lambda(T) - \lambda(0) \sim T^2$, for small T. This T^2 variation has been observed [124,127].

Figures 5.1.7 and 5.1.8 show the change in anisotropy of $\lambda(\theta,\phi,T)$ as a function of temperature for the Zn(MEPM) and Tl(0.435) models respectively. We have plotted the ratio of $\lambda(\theta,\phi,T)$ to the isotropic value $\lambda(T)$, and the qualitative behaviour is very similar for both metals. The anisotropy remains approximately constant for very small temperatures. Then it reaches a maximum for some temperature $\lesssim T_M$. Where we recall that $\lambda(T_M)$ is the maximum value as shown in figure 1.2; and the position of this maximum is primarily determined by the low frequency peak of $\alpha^2F(\omega)$. This is followed by a rapid decrease in anisotropy as the temperature is

increased further. The temperature variation of the anisotropy shown in these figures illustrates the importance of the low frequency phonon modes for anisotropy calculations in both zinc and thallium.

The decrease in anisotropy of the electron-phonon mass enhancement as the temperature is increased is illustrated in another way in figures 5.1.9-Zn(MEPM), 5.1.10-Tl(0.435), and 5.1.11-Tl(0.875). Here, for each model, we have plotted $\lambda(\theta,\phi,T)/\lambda(0,0,T)$ at two temperatures: T = 0°K and T = 60°K for zinc, and T = 0°K and T = 26°K for thallium. Comparing the results at the two temperatures allows a quick determination of which $\lambda(\underline{k},T)$ are strongly influenced by the low frequency phonon modes. For example, in zinc (figure 5.1.9) at 60°K the region $\theta \lesssim 0°$ has been decreased relative to the other mass enhancements. Similarly for thallium the two maxima along $\phi = 30°$ at 26°K have been decreased in magnitude relative to the other values.

The lifetime of an electron in a state $|\underline{k}>$ on the Fermi surface, due to the electron-phonon interaction, is given by the imaginary part of the self-energy as [123]

$$\tau^{-1}_{\text{el-ph}} = 2 \text{ Im } \Sigma (\underline{k},\omega) \quad . \tag{5.9}$$

From (5.3) the zero frequency lifetime $\tau_{\text{el-ph}}(\underline{k},T)$ as a function of temperature and position on the Fermi surface

is

$$\tau^{-1}_{\text{el-ph}}(\underline{k},T) = \frac{4\pi}{\hbar}\int d\omega\ \alpha^2F(\omega,\underline{k})\left[\frac{1}{e^{\beta\omega}+1}+\frac{1}{e^{\beta\omega}-1}\right]. \tag{5.10}$$

The Fermi surface average of the electron-phonon scattering times are presented in figure 5.1.12. We have only drawn the MEPM model for Zn; and because the $\alpha^2F(\omega)$ functions are so similar for both Tl models, the curve labeled Tl represents either model equally well.

Figures 5.1.13-Zn(MEPM), 5.1.14-Tl(0.435) and 5.1.15-Tl(0.875) show $\tau_{\text{el-ph}}(\theta,\phi,T)/\tau_{\text{el-ph}}(0,0,T)$ for T = 20°K and T = 300°K. It is apparent that the anisotropy in the electron-phonon lifetimes decreases as the temperature is increased. We have not shown the very low temperature scattering times because the thermal factor in (5.10) is peaked at $\omega = 0$, and as T is decreased the low frequency phonons are emphasized more and more. This is the region of our $\alpha^2F(\omega,\underline{k})$ functions which we consider to be the least well determined because of the breakdown of the one OPW approximation, for certain directions. This point has been discussed in section 3.2 and the appendix.

FIGURE CAPTIONS - SECTION 5.1

FIGURE 5.1.1: The thermal factor $G(\frac{\omega}{T})$ of equation (5.5), which determines the temperature variation of the electron-phonon mass enhancements.

FIGURE 5.1.2: The temperature variation of the Fermi surface averaged electron-phonon mass enhancements $\lambda(T)/\lambda(0)$ for all four models considered in this thesis. The two zinc models are labeled by MEPM and DWL. The curve labeled Tl represents both thallium models, to within the accuracy of this graph.

FIGURE 5.1.3: The solid lines give the Zn(MEPM) temperature variation of the directional electron-phonon mass enhancements $\lambda(\theta,\phi,T)/\lambda(\theta,\phi,0)$ for three high symmetry directions. The dashed curve is the Zn(MEPM) Fermi surface averaged result $\lambda(T)/\lambda(0)$.

FIGURE 5.1.4: As in figure 5.1.3, but for the Zn(DWL) model.

FIGURE 5.1.5: As in figure 5.1.3, but for the Tl(0.435) model.

FIGURE 5.1.6: As in figure 5.1.3, but for the Tl(0.875) model.

FIGURE 5.1.7: Zn(MEPM) temperature variation of the anisotropy in the electron-phonon mass enhancements for three high symmetry directions, labeled by (θ,ϕ). One other direction (63,0) is also presented.

FIGURE 5.1.8: Tl(0.435) temperature variation of the anisotropy in the electron-phonon mass enhancements for three high symmetry directions, labeled by (θ,ϕ).

FIGURE 5.1.9: Comparison at two temperatures of the Zn(MEPM) electron-phonon mass enhancements as a function of position (θ,ϕ) on the Fermi surface, with $\lambda(0,0,0°K) = 0.565$ and $\lambda(0,0,60°K) = 0.330$.

FIGURE 5.1.10: Tl(0.435), as in figure 5.1.9 with $\lambda(0,0,0°K) = 0.681$ and $\lambda(0,0,26°K) = 0.656$.

FIGURE 5.1.11: Tl(0.875), as in figure 5.1.9 with $\lambda(0,0,0°K) = 0.707$ and $\lambda(0,0,26°K) = 0.679$.

FIGURE 5.1.12: The temperature variation of the Fermi surface averaged electron-phonon scattering times $\tau_{el-ph}(T)$ for the Zn(MEPM) and Tl models. The results for the Tl(0.435) and Tl(0.875) models are equally well represented by the single Tl curve.

FIGURE 5.1.13: Comparison at two temperatures of the Zn(MEPM) electron-phonon scattering times as a function of position (θ,ϕ) on the Fermi surface, with $\tau_{el-ph}(0,0,20°K) = 5.72\times10^{-13}$ sec. and $\tau_{el-ph}(0,0,300°K) = 7.36\times10^{-15}$ sec.

FIGURE 5.1.14: Tl(0.435) as in figure 5.1.13 with $\tau_{el-ph}(0,0,20°K) = 2.92\times10^{-13}$ sec. and $\tau_{el-ph}(0,0,300°K) = 6.01\times10^{-15}$ sec.

FIGURE 5.1.15: Tl(0.875) as in figure 5.1.13 with $\tau_{el-ph}(0,0,20°K) = 2.76\times10^{-13}$ sec. and $\tau_{el-ph}(0,0,300°K) = 5.79\times10^{-15}$ sec.

Figure 5.1.1

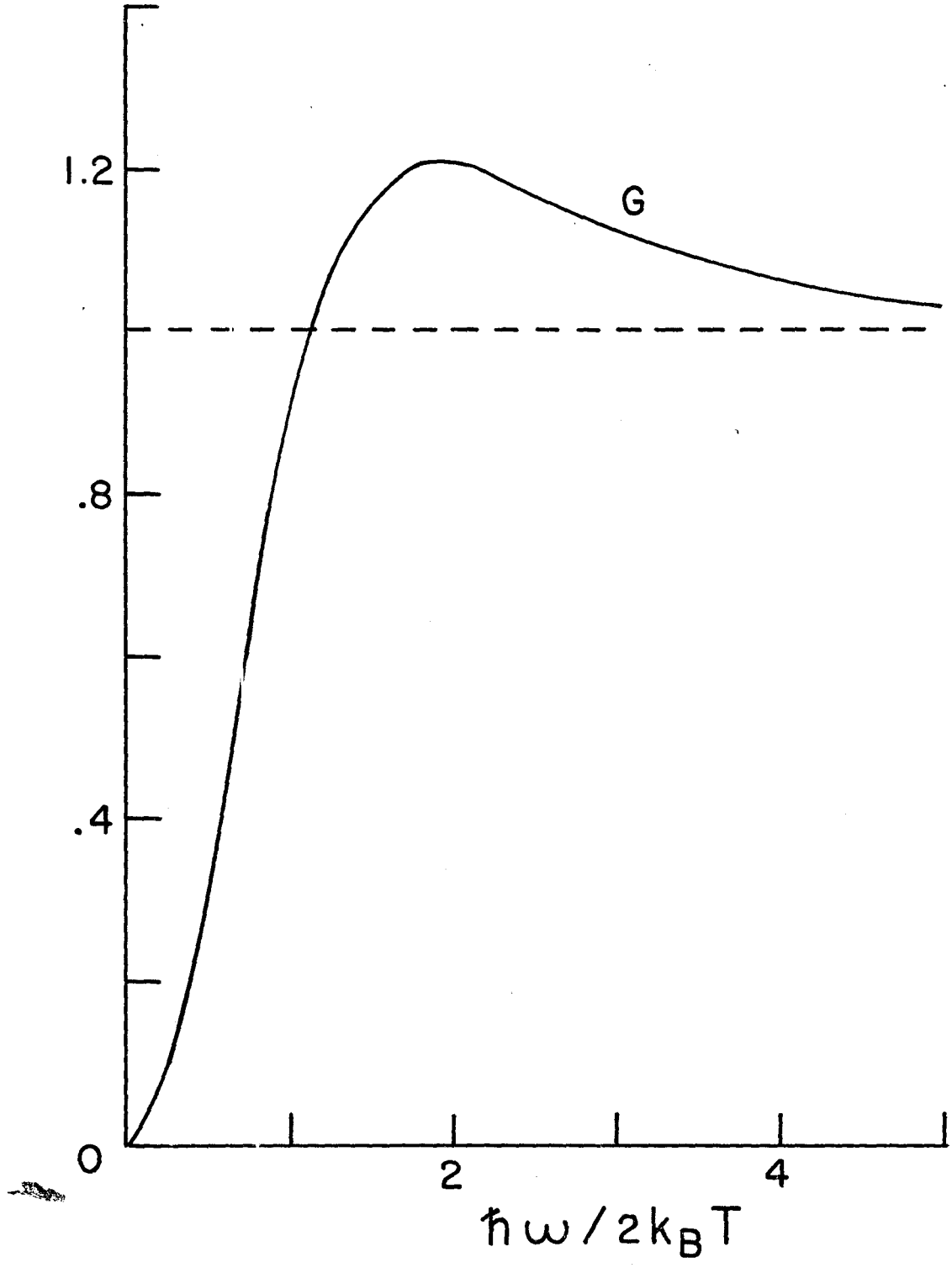

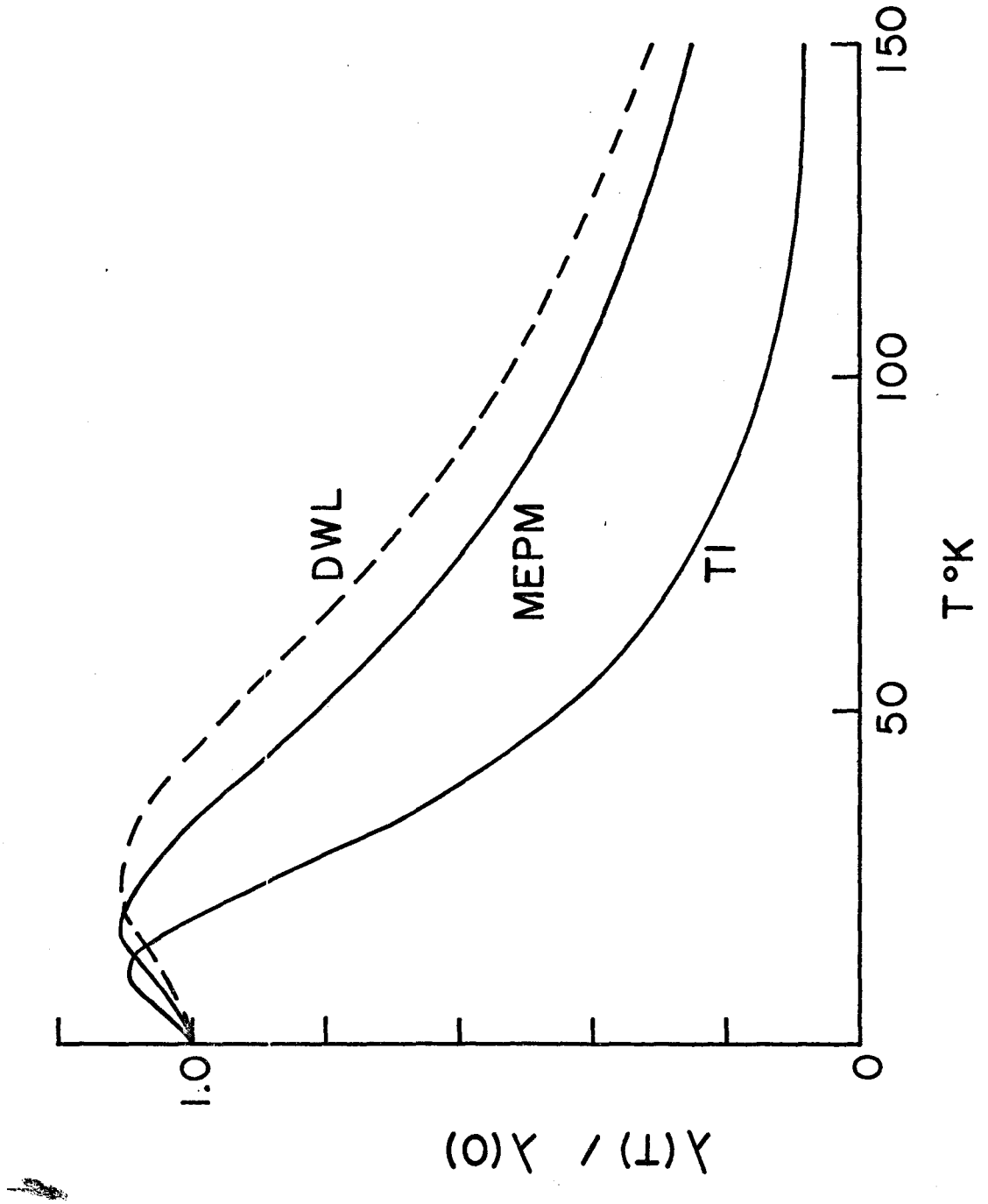
DWL
MEPM
TI
150
100
50
0
T °K
1.0
λ(T) / λ(0)

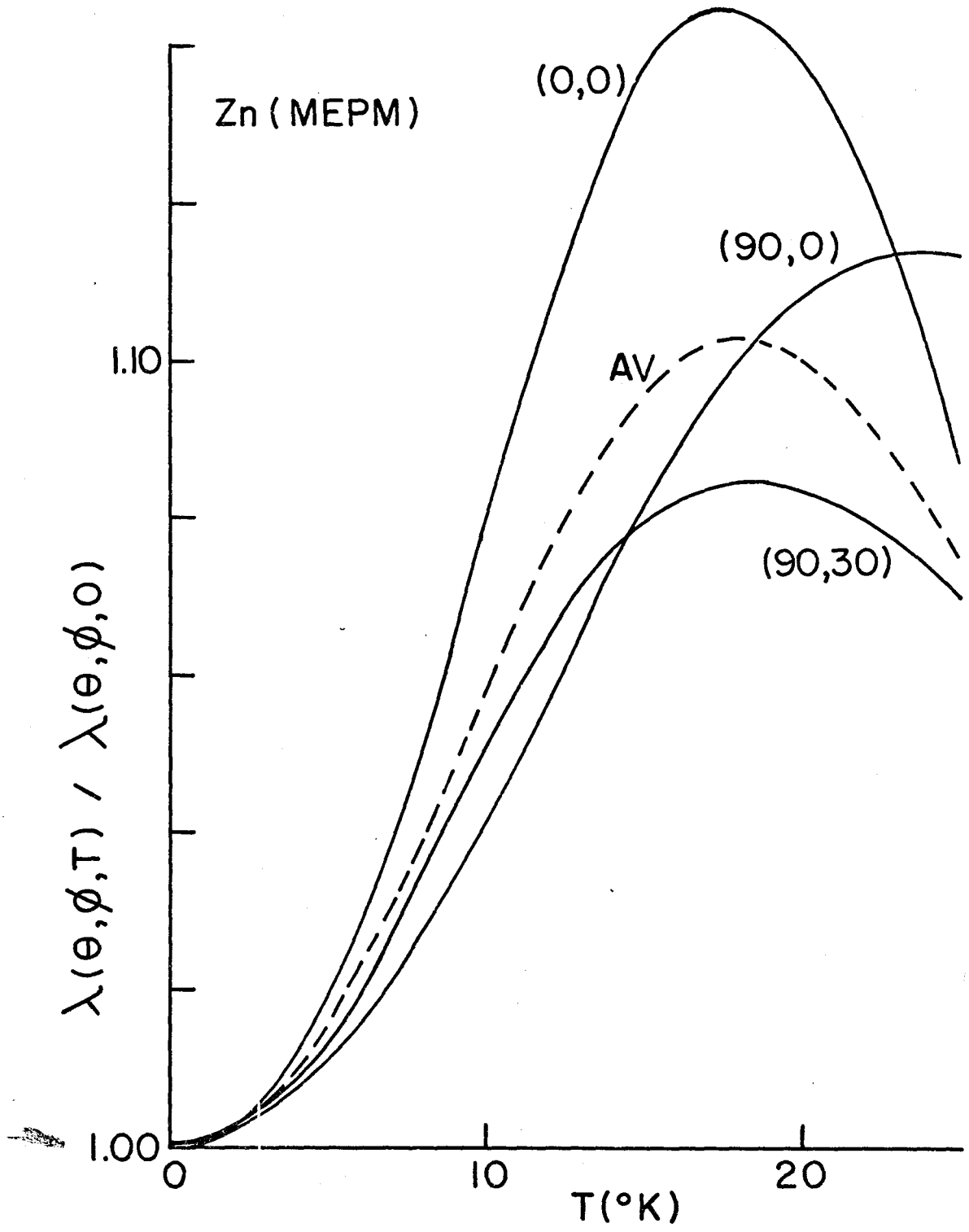
Zn (MEPM)
(0,0)
(90,0)
AV
(90,30)
1.10
1.00
0
10
20
T(°K)
λ(θ,φ,T) / λ(θ,φ,0)

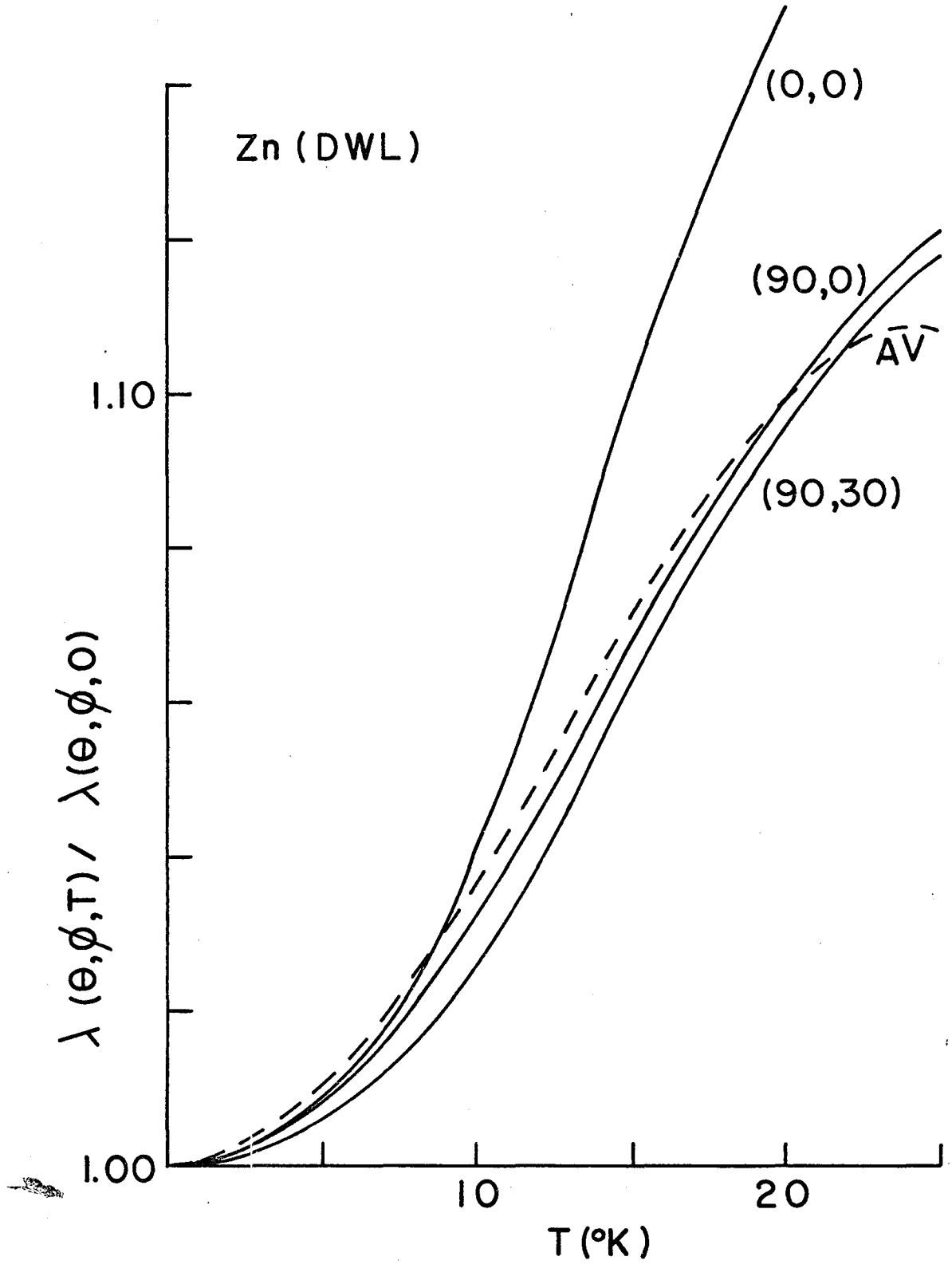
Zn (DWL)
(0,0)
(90,0)
$\bar{A}\bar{V}$
(90,30)
1.10
1.00
$\lambda(\theta,\phi,T)$ / $\lambda(\theta,\phi,0)$
10
20
T (°K)

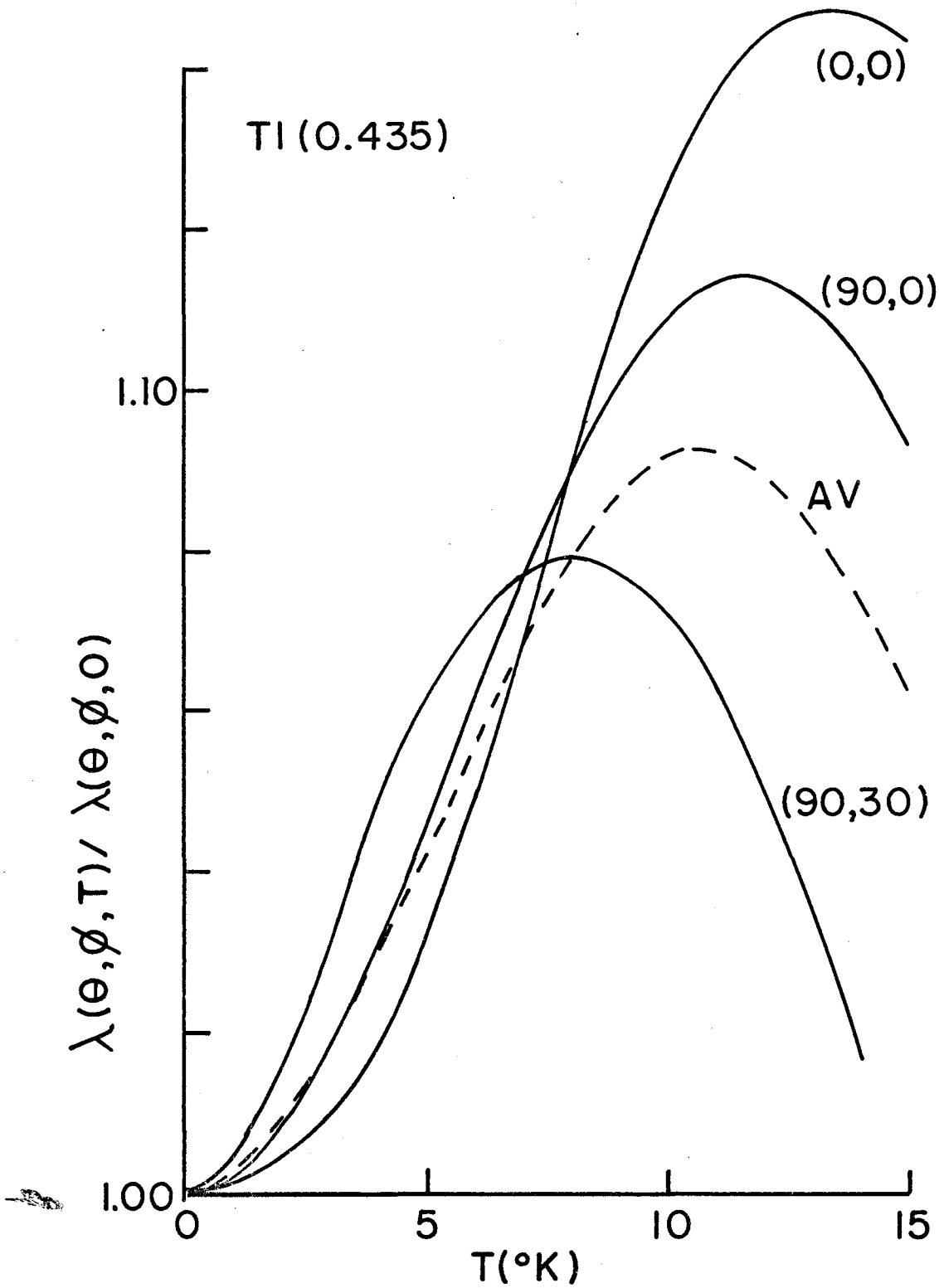
(0,0)
Tl (0.435)
(90,0)
1.10
AV
(90,30)
λ(θ,φ,T)/ λ(θ,φ,0)
1.00
0
5
10
15
T(°K)

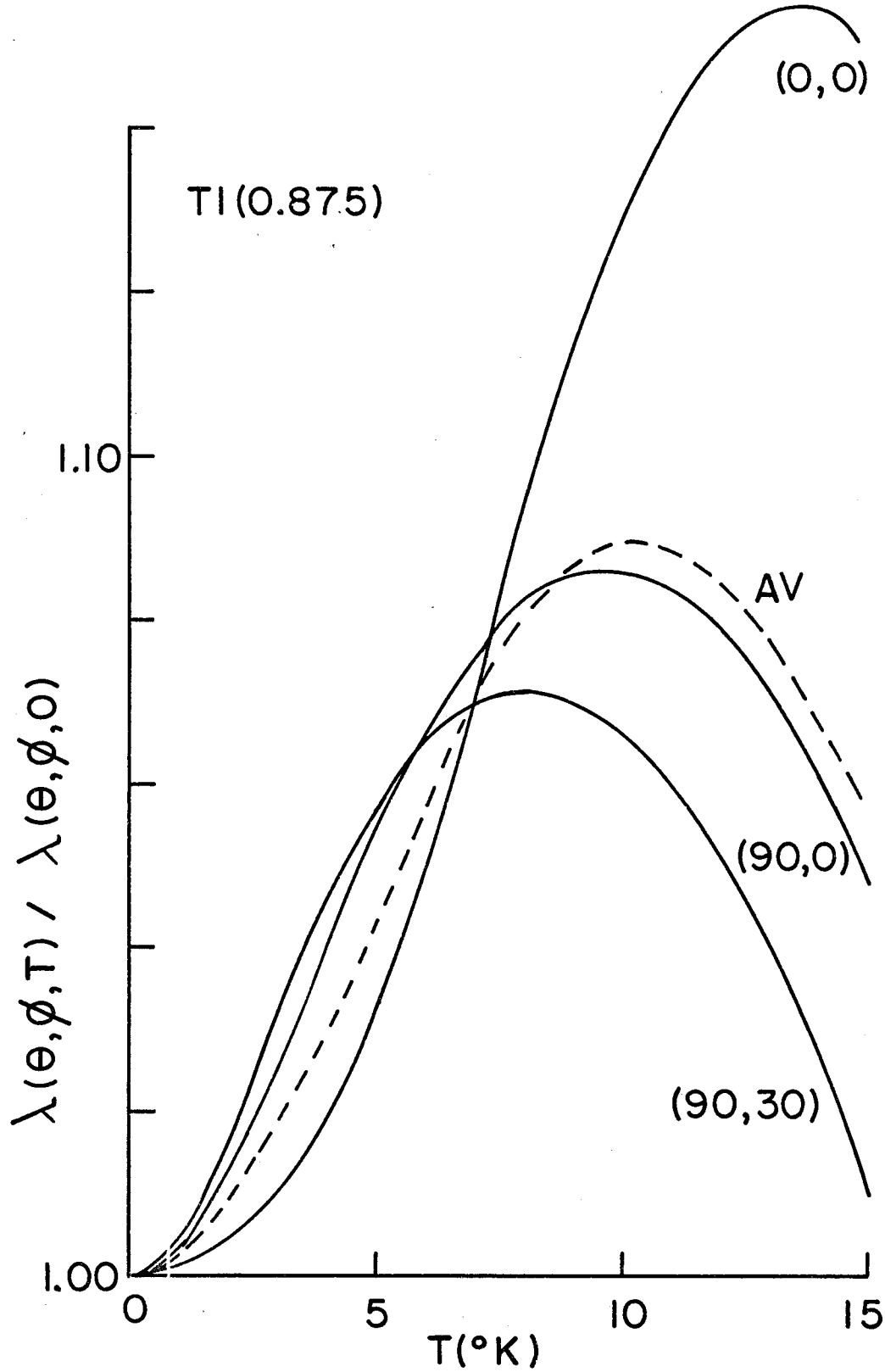
(0,0)
Tl(0.875)
1.10
AV
(90,0)
(90,30)
λ(θ,φ,T) / λ(θ,φ,0)
1.00
0
5
10
15
T(°K)

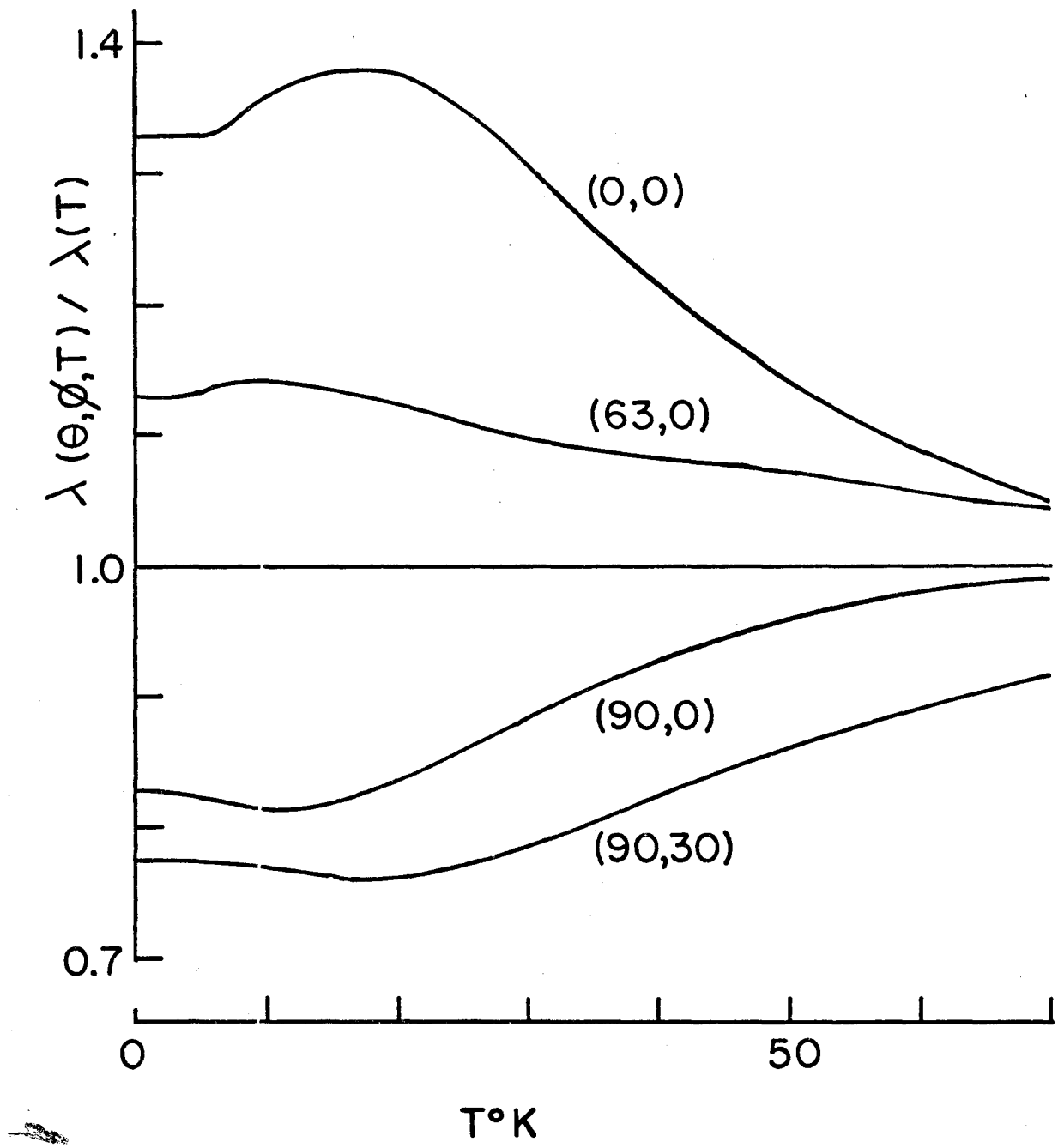
1.4
1.0
0.7
λ (θ,φ,T) / λ(T)
(0,0)
(63,0)
(90,0)
(90,30)
0
50
T°K

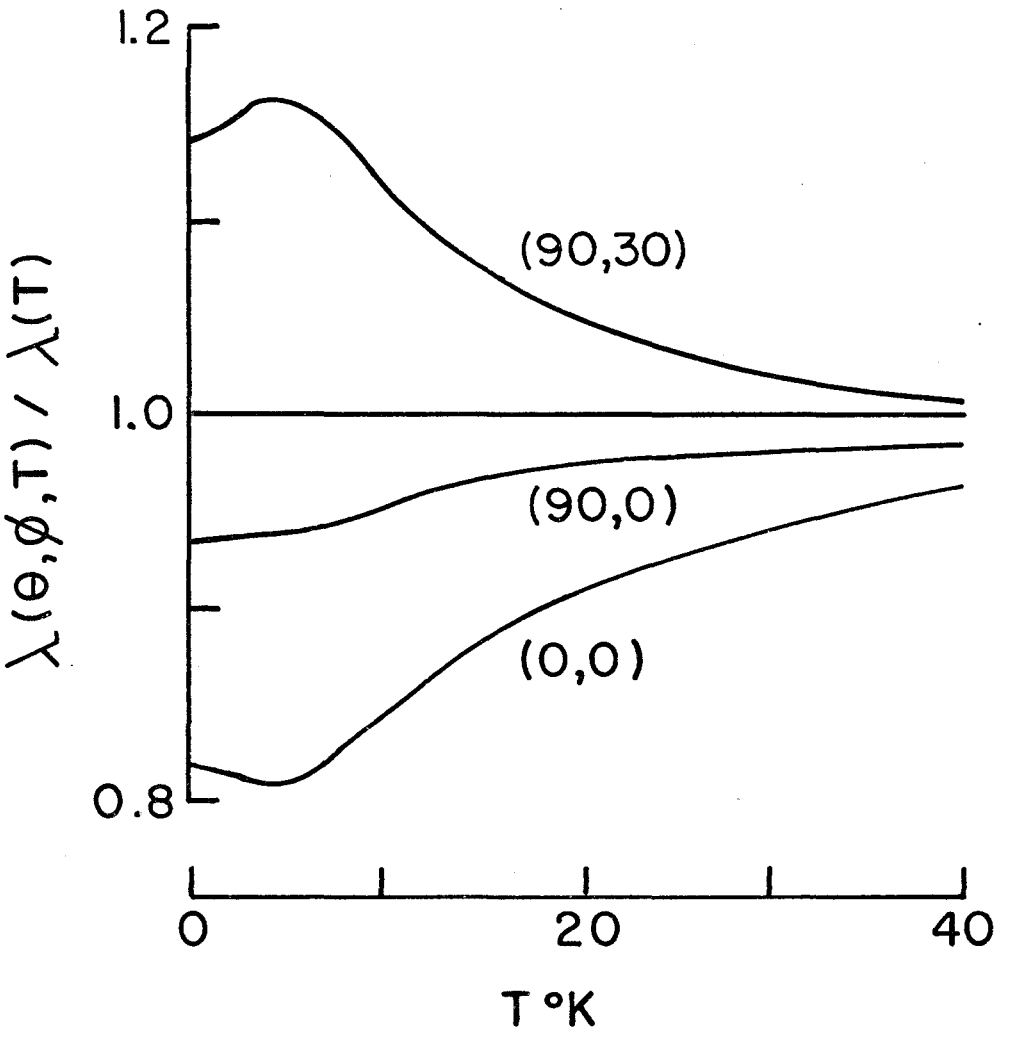
1.2
1.0
0.8
λ(θ,φ,T) / λ(T)
(90,30)
(90,0)
(0,0)
0
20
40
T °K

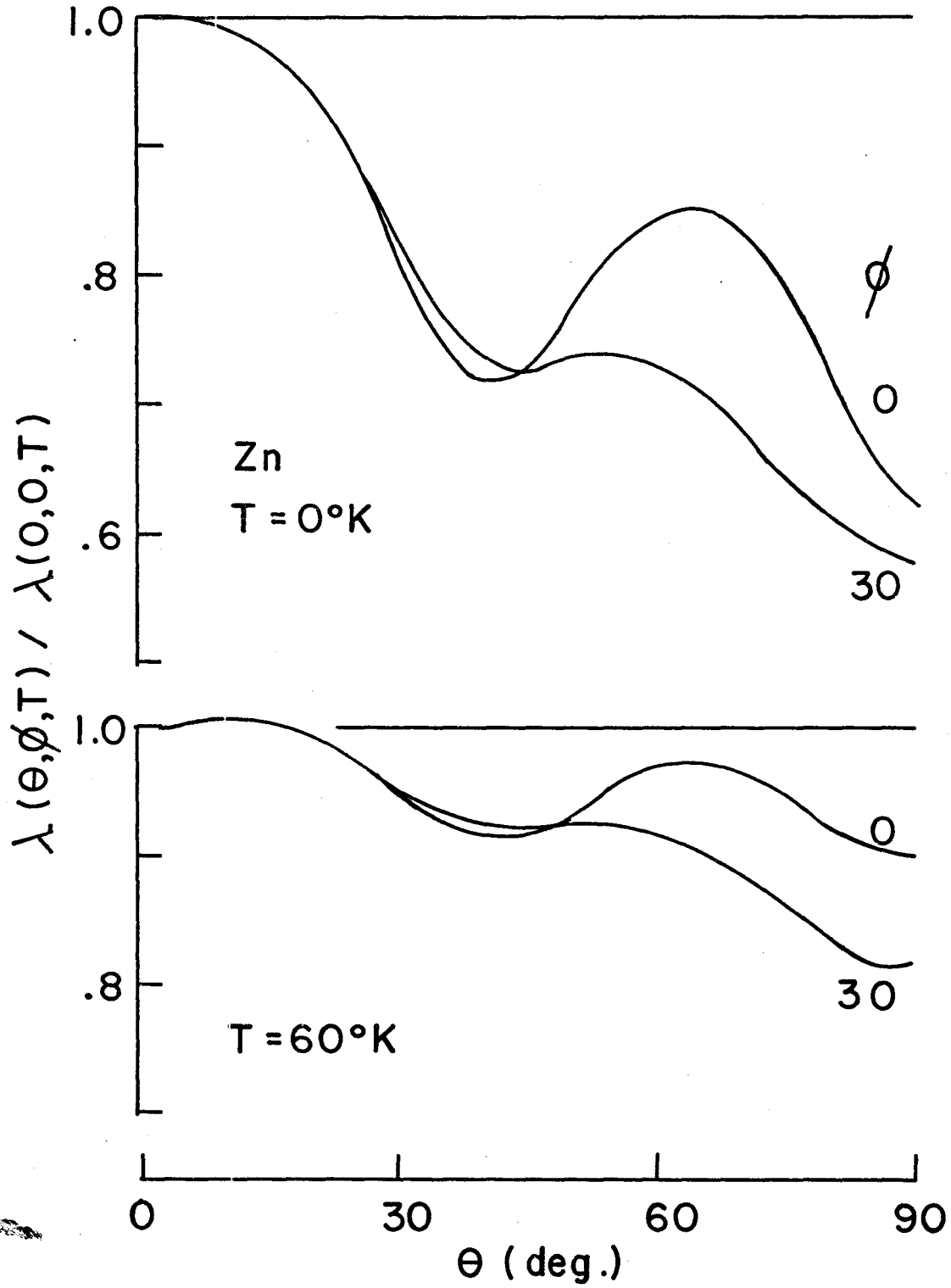
1.0
.8
.6
Zn
T = 0°K
ϕ
0
30
1.0
.8
T = 60°K
0
30
λ (θ,ϕ,T) / λ(0,0,T)
0
30
60
90
θ (deg.)

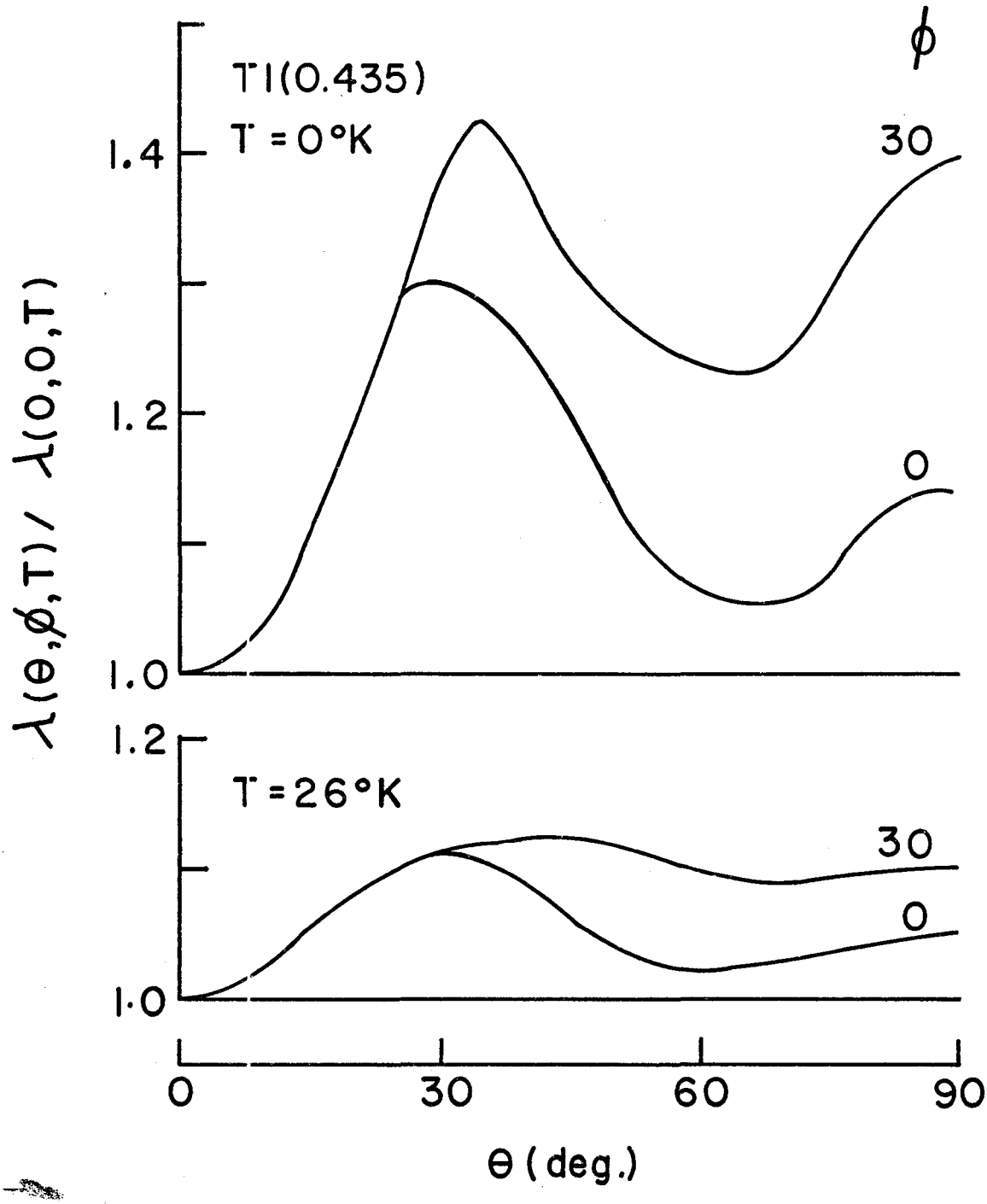
Tl(0.435)
T = 0°K
φ
30
0
1.4
1.2
1.0
λ(θ,φ,T) / λ(0,0,T)
T = 26°K
30
0
1.2
1.0
0
30
60
90
θ (deg.)

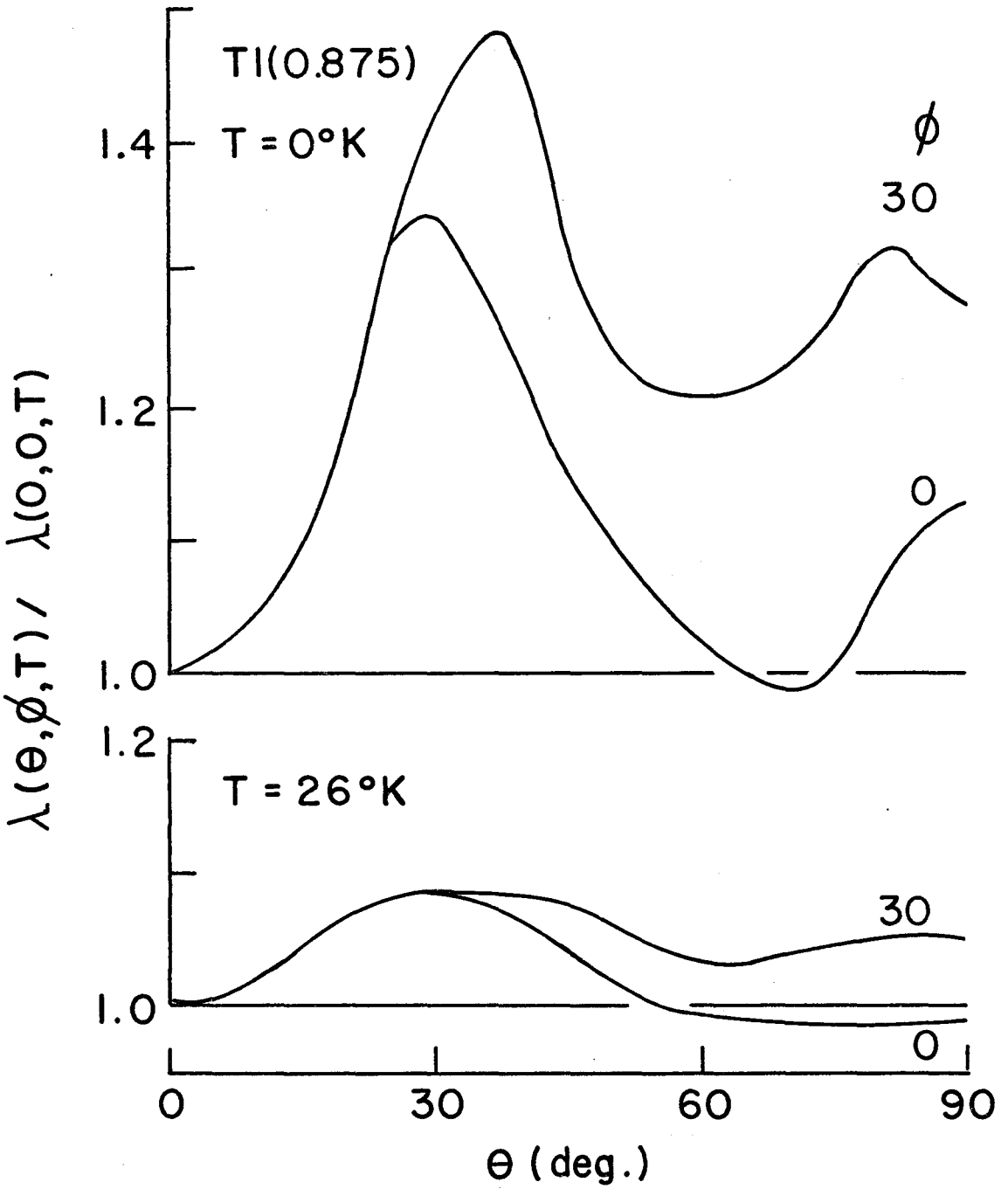
Tl(0.875)
T = 0°K
1.4
1.2
1.0
φ
30
0
T = 26°K
1.2
1.0
30
0
λ(θ,φ,T) / λ(0,0,T)
0
30
60
90
θ (deg.)

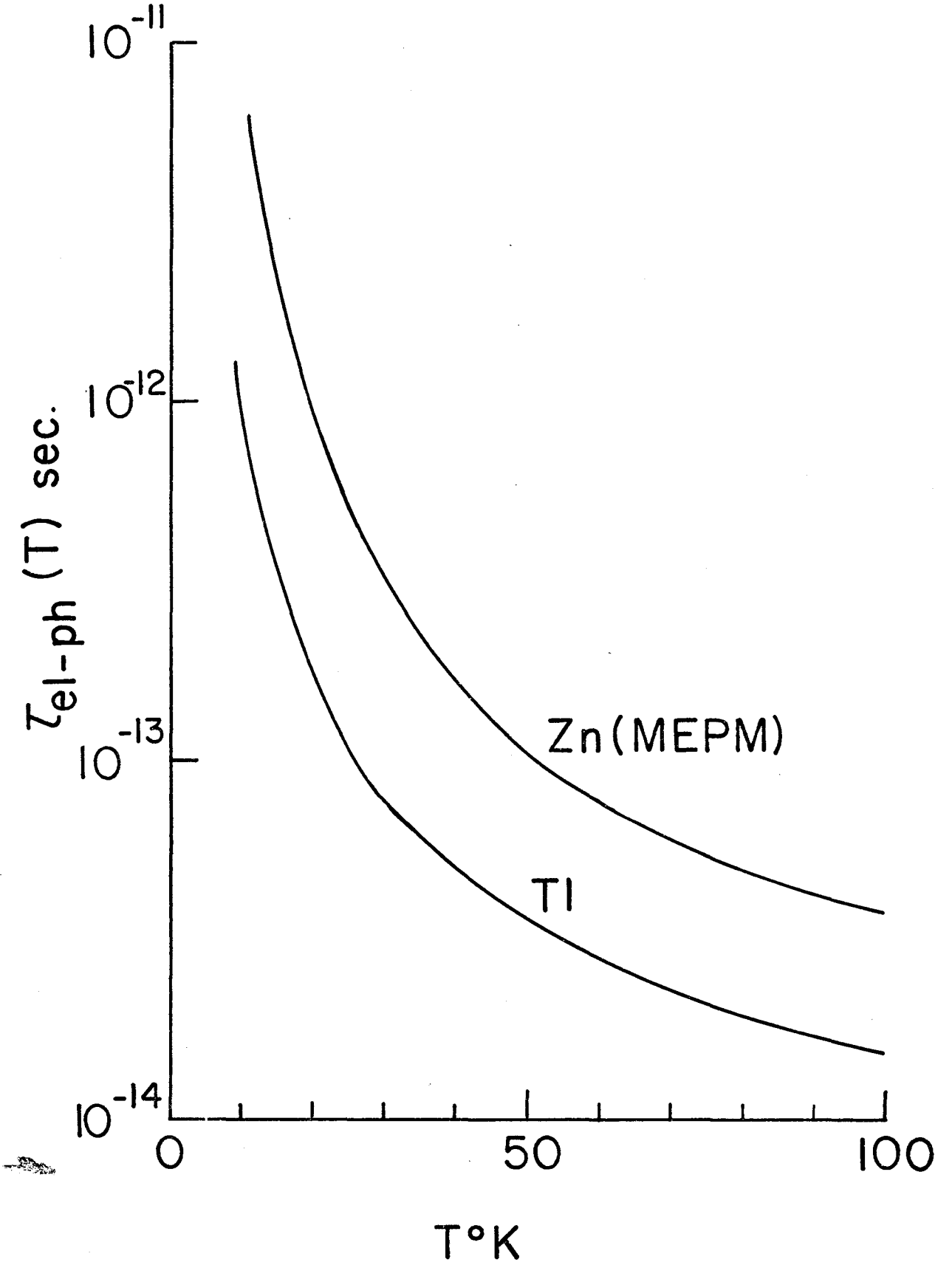
10^{-11}
10^{-12}
10^{-13}
10^{-14}
τ_{el-ph} (T) sec.
Zn (MEPM)
Tl
0
50
100
T°K

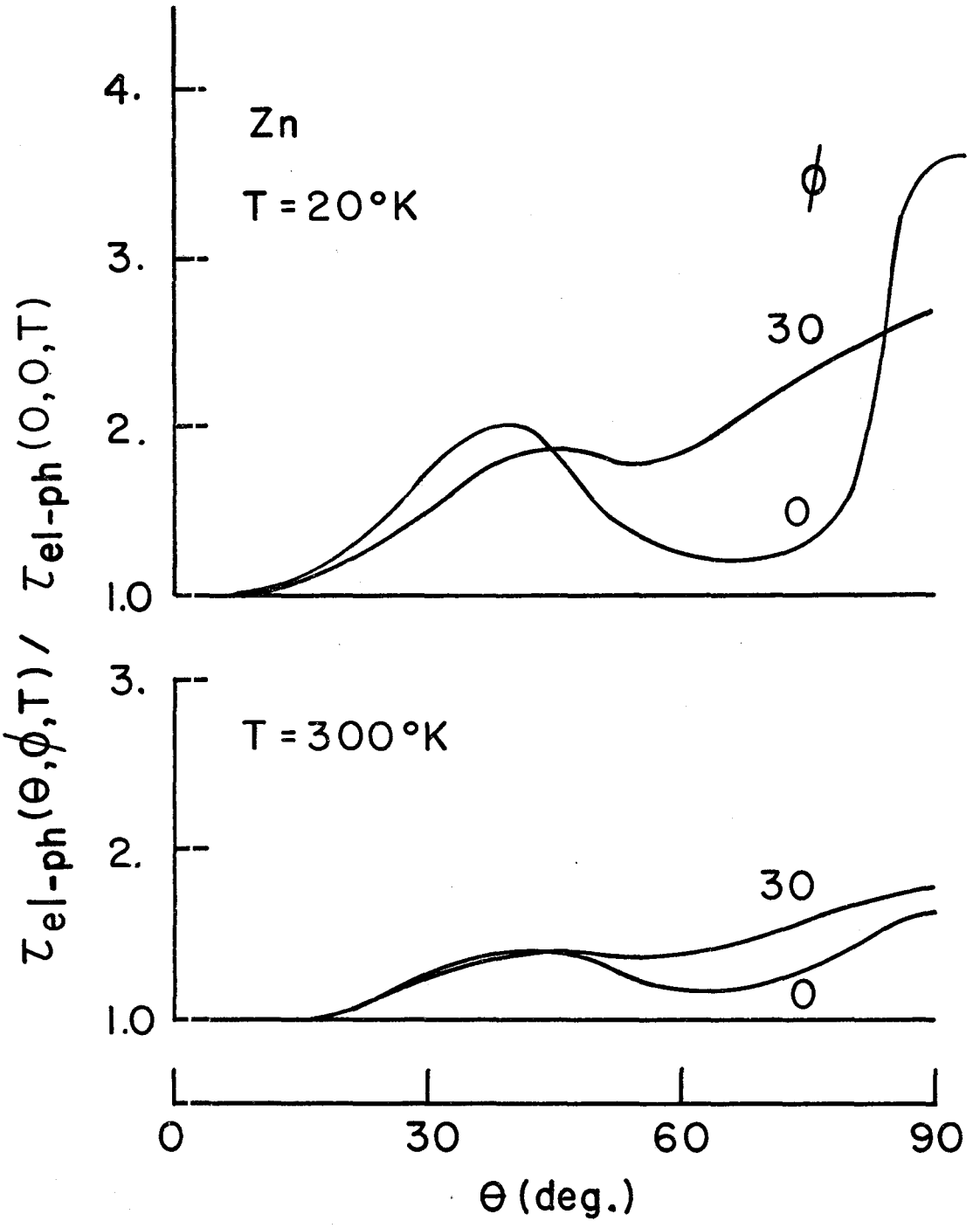
Zn
T = 20°K
T = 300°K
ϕ
30
0
4.
3.
2.
1.0
0
30
60
90
θ (deg.)
$\tau_{el-ph}(\theta,\phi,T) / \tau_{el-ph}(0,0,T)$

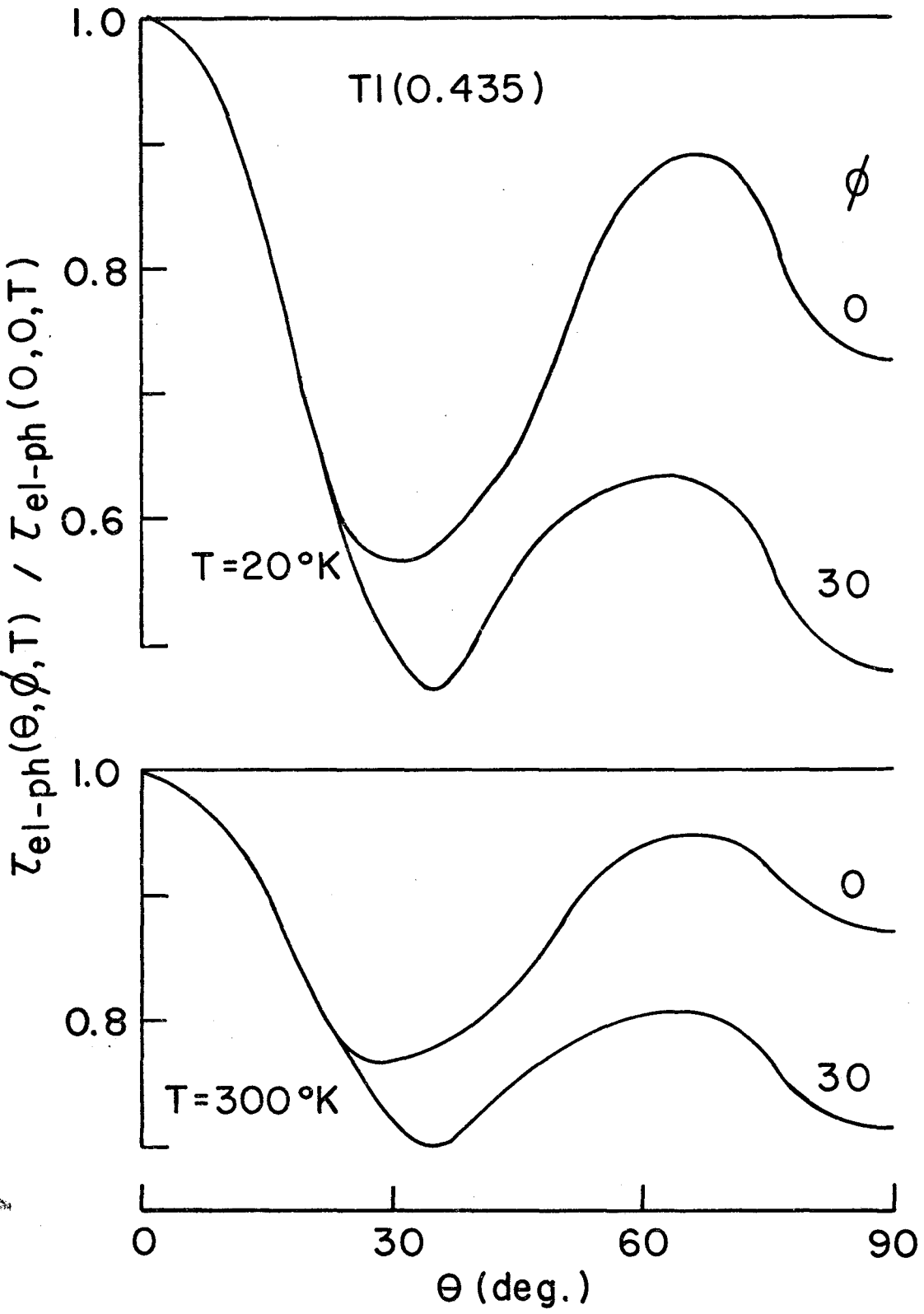
1.0
0.8
0.6
Tl(0.435)
ϕ
0
30
T=20°K
$\tau_{el-ph}(\theta,\phi,T)$ / $\tau_{el-ph}(0,0,T)$
1.0
0.8
0
30
T=300°K
0
30
60
90
θ (deg.)

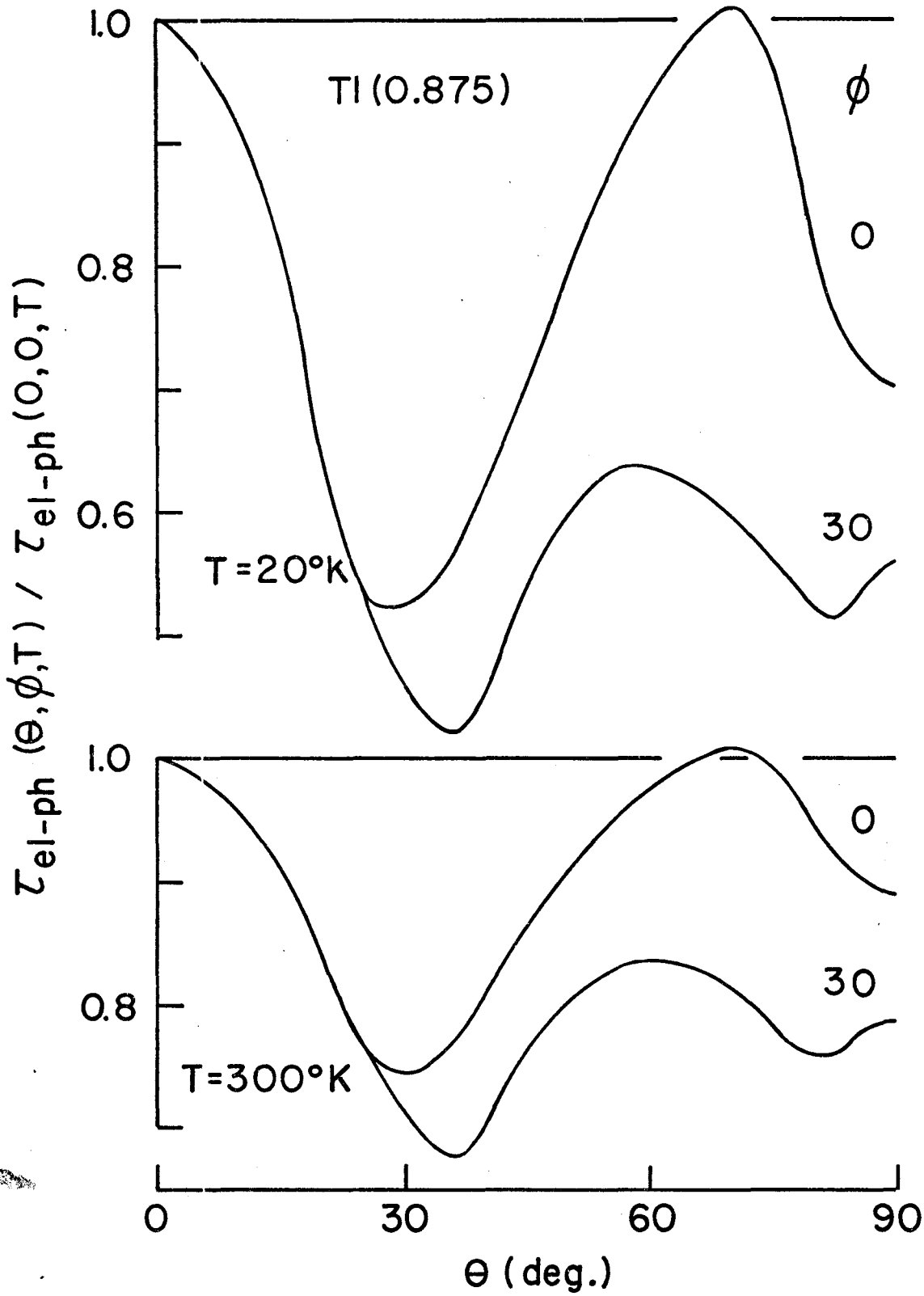
1.0
0.8
0.6
Tl (0.875)
ϕ
0
30
T=20°K
1.0
0.8
0
30
T=300°K
0
30
60
90
Θ (deg.)
τel-ph (Θ,ϕ,T) / τel-ph (0,0,T)

5.2 ANISOTROPY IN THE TEMPERATURE VARIATION OF THE ELECTRON-PHONON MASS ENHANCEMENT ON THE ZINC THIRD BAND LENS

The temperature (T) variation of the electronic effective mass λ, due to the electron-phonon interaction, can be measured in a cyclotron resonance experiment. In this section we will only be concerned with zinc for which metal Sabo [124] has obtained results for three distinct cyclotron orbits on the third band lens: the limit point orbit (the magnetic field $\underline{H} \parallel$ c-axis), the rim orbit ($\underline{H} \parallel$ c-axis) and the belt orbit ($\underline{H} \perp$ c-axis).

In the range of temperature studied by Sabo, he found that $\lambda(T)/\lambda(0)$ could be fit very well by a T^2 law with a different proportionality constant for each orbit. This "T^2" dependence has been discussed in section 5.1. Allen and Cohen [92] have reported a calculation of $\lambda(T)$ in Zn, which is in rough qualitative agreement with experiment. However, their calculation is for the Fermi surface average of the mass renormalization, a quantity which is not directly relevant to cyclotron orbits.

In this section we present the results of our calculations for the directional average effective masses, for each of the three orbits measured by Sabo. We shall restrict our discussion mainly to the zinc MEPM model results, and only mention the DWL model for comparison purposes.

The lens part of the Zn Fermi surface is defined in our angular coordinate system by $0° \leq \theta \leq 36.2°$. It is believed to be very free electron like [86,128,129]. Thus, as is the case throughout this thesis, we base our calculations on the spherical Fermi surface approximation and only include the anisotropy in λ that arises from the phonons. No effects of band structure anisotropy are included.

The unrenormalized cyclotron effective mass is given by a line integral over the Fermi surface orbit in $\underline{k}$-space [92]

$$m_c(0_{\underline{k}}) = \frac{\hbar^2}{2\pi} \oint \frac{d\ell}{\hat{n}_{\underline{k}} \cdot \nabla_{\underline{k}} \varepsilon_{\underline{k}}} \quad , \tag{5.11}$$

where $\varepsilon_{\underline{k}}$ is the free electron energy; and $\hat{n}_{\underline{k}}$ is a unit vector at $\underline{k}$ normal to the orbit $0_{\underline{k}}$ and in the plane perpendicular to the magnetic field. Using relations (5.1), (5.2) and (5.3) of section 5.1, the renormalized cyclotron effective mass as a function of temperature becomes

$$m_c^*(0_{\underline{k}},T) = m_c(0_{\underline{k}})[1 + \lambda(0_{\underline{k}},T)] \tag{5.12}$$

where

$$\lambda(0_{\underline{k}},T) = \left(\oint \frac{\lambda(\underline{k},T)d\ell}{\hat{n}_{\underline{k}} \cdot \nabla_{\underline{k}} \varepsilon_{\underline{k}}}\right) \Big/ \left(\oint \frac{d\ell}{\hat{n}_{\underline{k}} \cdot \nabla_{\underline{k}} \varepsilon_{\underline{k}}}\right) \tag{5.13}$$

with

$$\lambda(\underline{k},T) = 2\int_0^\infty \frac{d\omega}{\omega}\,\alpha^2F(\omega,\underline{k})G(\tfrac{\omega}{T}) \quad . \tag{5.14}$$

The material independent thermal factor $G(\frac{\omega}{T})$ is defined by (5.5), and the functions $\alpha^2F(\omega,\underline{k})$ have been written many times (5.6).

The $\alpha^2F(\omega,\underline{k})$ are averaged over the cyclotron orbit $0_{\underline{k}}$ using the procedure described by equation (3.24). This gives an $\alpha^2F(\omega,0_{\underline{k}})$ for the orbit from which the temperature variation of $\lambda(0_{\underline{k}},T)$ can be calculated using (5.14). The zinc MEPM force constant model results for the limiting point and rim orbit are compared in figure 5.2.1. We note that important differences exist between these two functions. These differences arise predominantly from a modulation of magnitude and not from a shifting of peak positions. In particular, the low frequency peak has more relative importance for the limit point orbit than it does for the rim orbit. It is important to stress that these differences arise solely as a result of phonon anisotropy and have nothing to do with the band structure of zinc. They give rise to differences in both the absolute magnitude and temperature variation of the cyclotron mass for different orbits.

In figure 5.2.2 we have plotted $\lambda(0_{\underline{k}},T)/\lambda(0_{\underline{k}},0)$ for the three orbits considered by Sabo. It is seen that our calculations give considerably different curves for the

three cases:

a) The limit point orbit results (solid line) are compared with the experimental points of Sabo which were read from his published graph. To extract these results from the measured cyclotron mass Sabo needs to assume some value for the orbital band mass $m_c(0_{\underline{k}})$. For the limit point orbit he takes the free electron mass, m. This seems to be a reasonable choice since the limit point orbit samples a region of the true Fermi surface which is believed to be very free electron like.

b) Our results for the belt and rim orbits are given in figure 5.2.2 by the dashed curves, with the belt orbit showing the greater temperature variation. We do not include Sabo's results for these orbits because the experimental points are very sensitive to the value assumed for $m_c(0_{\underline{k}})$ and its value for each of these two orbits is quite uncertain. Sabo's choice for the $m_c(0_{\underline{k}})$ gives an ordering of rim and belt results which is opposite to ours. However, he considers that an equally reasonable choice of orbital band masses would reverse the order. Also, Sabo does not specify the orientation of the magnetic field in the basal plane; and since our belt orbits show very little anisotropy ($\lesssim$ 1%) as a function of ϕ, we have drawn the ϕ-averaged belt orbit in figure 5.2.2.

A number of points remain to be mentioned. The reduction of the bare data to the $\lambda(0_{\underline{k}},T)/\lambda(0_{\underline{k}},0)$ curves will depend upon any electron-electron mass enhancement. Sabo did not include this correction. Also, the calculated results contain the low frequency renormalization for umklapp process with small reduced momentum transfer as discussed in section 3.2 and the appendix. It should be pointed out that this renormalization does not affect the limit point orbit results. Although it is important for the belt and rim orbits, we have found that the results for these orbits are not sensitive to the particular renormalization used.

Up to this point we have only considered the MEPM model, it can be seen that the DWL model gives very poor results for the limit point orbit by comparing the (0,0) curves in figures 5.1.3 and 5.1.4. The DWL curve is much lower than experiment. However, both MEPM and DWL predict the same ordering of orbital temperature variations. This may be seen by considering $\lambda(\theta,\phi)/\lambda(0,0)$, figures 4.2.2 and 4.2.10, in the region of third band lens ($0 \leq \theta \leq 36.2°$). For small θ, as θ is increased the main effect is to decrease the importance of the low frequency peak. This shifts the maximum of $\lambda(\theta,\phi,T)$ to higher temperatures, which in term decreases the magnitude of the temperature variation.

In summary, data on the temperature variation of the cyclotron mass may be reduced to give the temperature

variation of the electron-phonon mass enhancement $\lambda(0_{\underline{k}},T)$ for each measured cyclotron orbit. The limit point orbit is not affected by the one OPW low frequency renormalization, and the value of the cyclotron band mass is well determined. For this orbit we find quantitative agreement with experiment. However, it must be stated that the degree of agreement may be somewhat fortuitous. We think it more significant though, that by only including phonon anisotropy we find that at a given temperature the orbital variation of $\lambda(0_{\underline{k}},T)$ is of the same order as is observed experimentally.

FIGURE CAPTIONS - SECTION 5.2

FIGURE 5.2.1: The orbital averages of $\alpha^2F(\omega,\underline{k})$ for: (a) the limit point orbit and (b) the rim orbit. For this figure the free electron value of N(0) has been used, that is m_B has been set equal to unity.

FIGURE 5.2.2: The temperature dependence of $\lambda(0_{\underline{k}},T)/\lambda(0_{\underline{k}},0)$ for the zinc third band orbits considered. The solid line gives our calculated results for the limit point orbit, and the experimental points [124] also correspond to this orbit. The dashed lines (a) and (b) give our results for the belt and rim orbits respectively.

Figure 5.2.1

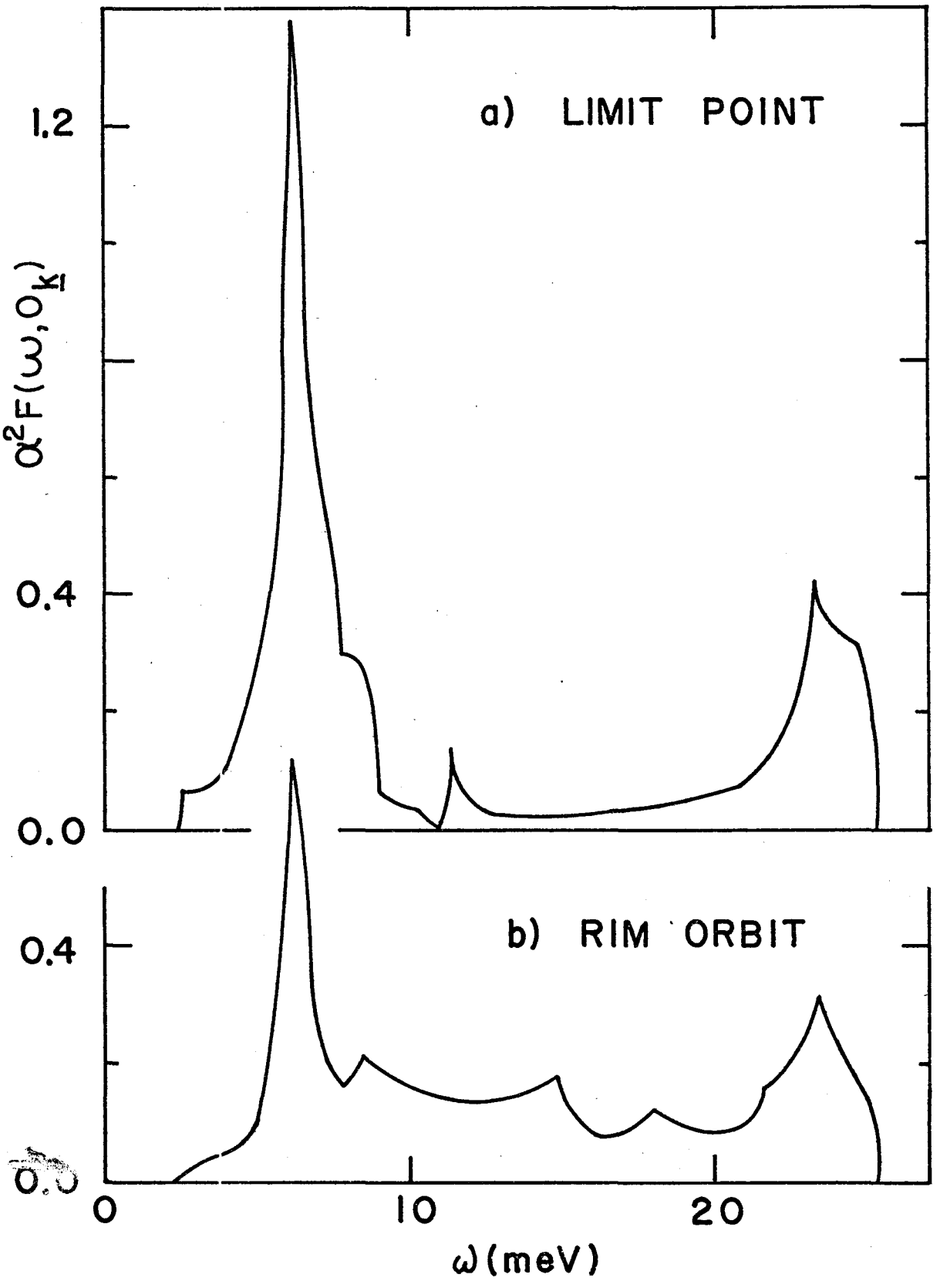
a) LIMIT POINT
b) RIM ORBIT
$\alpha^2F(\omega,O_{\underline{k}})$
1.2
0.4
0.0
0.4
0.0
0
10
20
ω(meV)

Figure 5.2.2

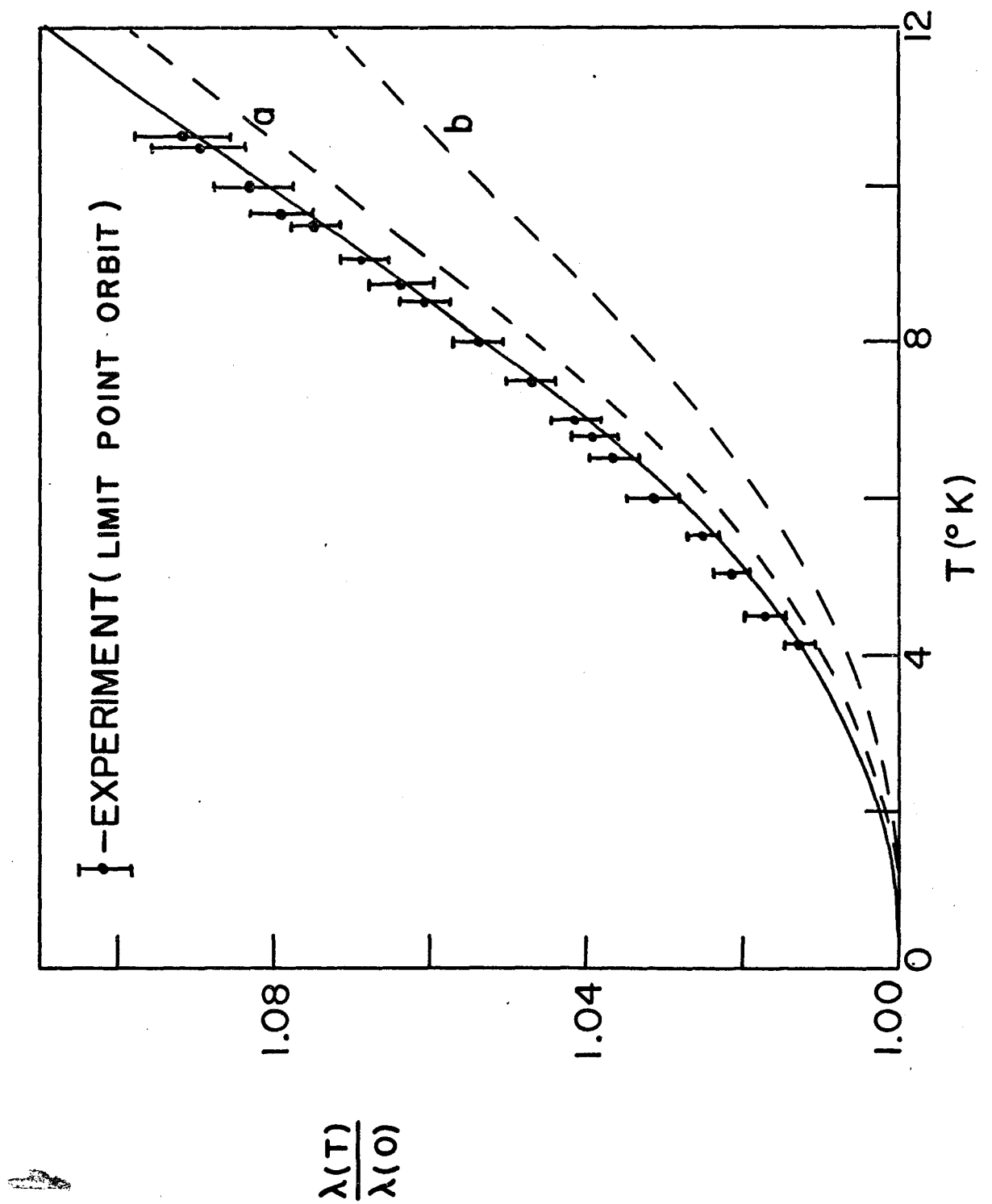

5.3 ANISOTROPY AND THE PHONON-LIMITED RESISTIVITY OF HCP METALS: ZINC AND THALLIUM

In a completely isotropic system, such as a free electron gas, the conductivity tensor $\underset{\sim}{\sigma}$ may be considered as a scalar σ, and the resistivity becomes

$$\rho = \sigma^{-1} = \frac{mv_F}{ne^2\Lambda}$$

where: e is the electronic charge, n is the conduction electron density, m is the free electron mass, v_F is the Fermi velocity, and Λ is the electron mean free path. The mean free path may be written as

$$\Lambda = \tau v_F \quad ,$$

which defines τ, the conduction electron relaxation or scattering time.

In a cubic system the conductivity is isotropic. Since the vector mean free path $\underline{\Lambda}_{\underline{k}}$ is always parallel to the electron velocity $\underline{v}(\underline{k})$, a temperature dependent scattering time function $\tau(\underline{k},T)$ may be defined over the Fermi surface [130]. Then the standard Ziman variational

resistivity formula [131] corresponds to

$$\rho^{V}(T) = \frac{m}{ne^2} \left\langle \frac{1}{\tau(\underline{k},T)} \right\rangle \tag{5.15}$$

where the < > denote a Fermi surface average.

Robinson and Dow [132] (hereafter referred to as RD) have pointed out that (5.15) averages over the resistivities, when actually the conductivities should be averaged to give

$$\rho(T) = \frac{m}{ne^2} \frac{1}{\langle \tau(\underline{k},T) \rangle} \quad . \tag{5.16}$$

These authors give a prescription for calculating $\tau(\underline{k},T)$ in cubic materials from which the resistivity may be obtained via equation (5.16).

Throughout the remainder of this section we suppress the explicit temperature dependence of $\tau(\underline{k},T)$ and write $\tau(\underline{k})$.

It is interesting to note that, in the cubic case, if the $\tau(\underline{k})$ of RD are averaged according to (5.15) then one obtains exactly ρ^{V} as given by the variational formulation. This is not obvious because of the approximations used to obtain $\tau(\underline{k})$ by the RD method. The resistivities of the alkali metals have been calculated [133] using both (5.15) and (5.16), with significant differences obtained at low temperatures. These differences decrease as the temperature is increased. As we will show, essentially the same behaviour is obtained in the hcp metals. A discussion of

the use of relaxation times in the noble metals has recently been given by Springford [134].

Unfortunately the situation in noncubic metals is considerably more complex: the conductivity must be considered in tensor form, it is not possible to define a unique relaxation time function $\tau(\underline{k})$, and there are two accepted formulae for the hcp metal polycrystalline resistivity. However, by applying the RD technique to noncubic metals it is possible to uniquely define an approximate $\tau(\underline{k})$. Also, in the hcp polycrystalline sample limit the results of the RD and variational formulations become equivalent, except for the averaging procedure discussed above.

For an hcp metal the resistivity is given by [135]

$$\underset{\sim}{\sigma}^{-1} = \begin{bmatrix} \sigma_\perp & 0 & 0 \\ 0 & \sigma_\perp & 0 \\ 0 & 0 & \sigma_\parallel \end{bmatrix}^{-1} = \begin{bmatrix} \rho_\perp & 0 & 0 \\ 0 & \rho_\perp & 0 \\ 0 & 0 & \rho_\parallel \end{bmatrix} \tag{5.17}$$

where $\rho_\perp$ is the resistivity observed for electric fields in the basal plane normal to the c-axis, and $\rho_\parallel$ is the resistivity for fields parallel to the c-axis. Thus, to completely specify the resistivity we must calculate $\rho_\perp$ and $\rho_\parallel$, or equivalently, $\sigma_\perp$ and $\sigma_\parallel$. These are obtained from the Boltzmann equation.

The electrons are scattered between states by the emission or absorption of phonons. The Golden Rule transition probability for scattering from $\underline{k}$ to $\underline{k}'$ by the absorption of a phonon or wavevector $\underline{q} = \underline{k}' - \underline{k}$ is

$$\frac{2\pi}{\hbar} \sum_j |\langle \underline{k}' | H_{el\text{-}ph} | \underline{k} \rangle|^2 \, \delta(E_{\underline{k}'} - E_{\underline{k}} - \hbar\omega_{\underline{q}j})$$

where $E_{\underline{k}}$ is the energy of an electron in state $\underline{k}$, relative to the Fermi energy. Using $H_{el\text{-}ph}$ from section 2.2 the above expression becomes

$$\frac{2\pi}{\hbar} \sum_j |g_{\underline{k}\underline{k}'j}|^2 \, n_{\underline{q}j} \, f_{\underline{k}}(1 - f_{\underline{k}'}) \delta(E_{\underline{k}'} - E_{\underline{k}} - \hbar\omega_{\underline{q}j})$$

where $n_{\underline{q}j}$ and $f_{\underline{k}}$ are the phonon and electron distribution functions, respectively; and $g_{\underline{k}\underline{k}'j}$ is the electron-phonon coupling given by equation (2.23).

The total rate of change of the electron distribution function is the difference between scattering into and out of the state $\underline{k}$ caused by the emission and absorption of phonons

$$\left.\frac{\partial f}{\partial t}\right|_{scat.} = \frac{2\pi}{\hbar} \sum_{\underline{k}'j} |g_{\underline{k}\underline{k}'j}|^2$$

$$\times \{[(n_{\underline{q}j} + 1) f'(1-f) - n_{\underline{q}j} f(1-f')] \delta(E' - E - \hbar\omega_{\underline{q}j})$$

$$+ [n_{\underline{q}j} f'(1-f) - (n_{\underline{q}j} + 1) f(1-f')] \delta(E' - E + \hbar\omega_{\underline{q}j})\}$$

(5.18)

To simplify the notation we have used f, E, f' and E' for $f_{\underline{k}}$, $E_{\underline{k}}$, $f_{\underline{k}'}$ and $E_{\underline{k}'}$, respectively. In the absence of magnetic fields and thermal gradients the scattering term appropriate to the Boltzmann equation for the electron system with an applied electric field $\underline{u}$ is (131)

$$\left.\frac{\partial f}{\partial t}\right|_{\text{scat.}} = \frac{e}{\hbar}\,\underline{u}\cdot\frac{\partial f}{\partial \underline{k}} \quad . \tag{5.19}$$

To simplify equations (5.18) and (5.19) it is usual to make the assumption that the phonon system is in equilibrium with $n_{\underline{q}j} = n^{\circ}_{\underline{q}j}$ given by the Bose-Einstein distribution function. The electron distribution is expanded about the equilibrium Fermi-Dirac distribution f° to give

$$f = f^{\circ} - \Phi_{\underline{k}}\,\frac{\partial f^{\circ}}{\partial E} \tag{5.20}$$

where the relation

$$\frac{\partial f^{\circ}}{\partial E} = -\beta\, f^{\circ}(1-f^{\circ}) \tag{5.21}$$

holds with $\beta = (k_B T)^{-1}$.

Equating (5.18) and (5.19), then using (5.20) and (5.21) along with the notation

$$P_{\underline{k}}^{\underline{k}'} = \frac{2\pi}{\hbar} \sum_j |g_{\underline{k}\underline{k}'j}|^2 \, n^\circ_{\underline{q}j} \, f^\circ(1-f'^\circ)$$

$$\{\delta(E' - E - \hbar\omega_{\underline{q}j}) + e^{\beta\hbar\omega_{\underline{q}j}} \, \delta(E' - E + \hbar\omega_{\underline{q}j})\} \tag{5.22}$$

the Boltzmann equation becomes

$$e\underline{v}(\underline{k})\cdot\underline{u} \, \frac{\partial f^\circ}{\partial E} = \beta \sum_{\underline{k}'} (\Phi_{\underline{k}'} - \Phi_{\underline{k}}) P_{\underline{k}}^{\underline{k}'} \quad . \tag{5.23}$$

The solution of this equation determines the phonon-limited resistivity. We shall discuss two methods of solution - first the variational approach, and later the scattering time approximation.

Ziman [131] discusses in detail the variational solution of equation (5.23), and it is sufficient to quote his result that the solution $\Phi_{\underline{k}}$ of the Boltzmann equation minimizes the resistivity ρ^V given by

$$\rho^V = \frac{\beta \iint (\Phi_{\underline{k}'} - \Phi_{\underline{k}})^2 P_{\underline{k}}^{\underline{k}'} \, d\underline{k} d\underline{k}'}{2 \left| \int e\underline{v}(\underline{k}) \Phi_{\underline{k}} \frac{\partial f^\circ}{\partial E} \, d\underline{k} \right|^2} \quad . \tag{5.24}$$

In practice the calculation proceeds by assuming a simple trial function for $\Phi_{\underline{k}}$ which satisfies the symmetry requirements. The usual choice, which we follow is

$$\Phi_{\underline{k}} = \alpha \underline{k}\cdot\underline{u} \quad , \tag{5.25}$$

where α is a constant which cancels from (5.24); and we also assume a spherical Fermi surface where

$$\underline{v}(\underline{k}) = \frac{\hbar \underline{k}}{m} \quad . \tag{5.26}$$

Substituting (5.25) and (5.26) into (5.24) and following the reduction of Ziman, we finally arrive at the variational result for the resistivity

$$\rho^V = \frac{4\pi m\beta}{ne^2 m_B k_F^2} \int d\omega \; R(\omega) \; N(0) \iint \frac{d\Omega_{\underline{k}}}{4\pi} \frac{d\Omega_{\underline{k}'}}{4\pi}$$

$$\times \sum_j |g_{\underline{k}\underline{k}'j}|^2 [(\underline{k} - \underline{k}')\cdot\hat{u}]^2 \; \delta(\omega - \omega_{\underline{q}j}) \tag{5.27}$$

where the thermal factor is given by

$$R(\omega) = \hbar\omega(1 - e^{-\beta\hbar\omega})^{-1} \; (e^{\beta\hbar\omega} - 1)^{-1} \quad , \tag{5.28}$$

$\hat{u}$ is a unit electric field vector and n is the conduction electron density.

It should be noted that ρ^V is independent of the band mass. The electronic band mass density of states, N(0) of equation (5.27), is m_B times the free electron value and the m_B factors cancel from equation (5.27). This may also be seen by referring to equation (5.24) where the energy integrals give a m_B^2 factor in both the numerator and the denominator. This conclusion has been reached by others [136].

It should be pointed out that the thermal factor quoted by Balsley [48] is missing the $\hbar\omega$ factor in the numerator.

Equation (5.27) is calculated in the same manner as $\alpha^2F(\omega)$, which is discussed in section 3.2. To obtain $\rho_{\parallel}^{V}$ one merely takes $\hat{u}$ to be along the c-axis, and $\rho_{\perp}^{V}$ is obtained by placing $\hat{u}$ along the x or y-axis.

There are two formulae [137] available for calculating the resistivity, ρ_{Poly}, of a polycrystalline sample of a hcp metal. One corresponds to averaging the resistivities to give

$$\rho_{Poly} = \frac{1}{3} (\rho_{\parallel} + 2\rho_{\perp}) \quad ; \tag{5.29}$$

and the other averages the conductivities

$$\rho_{Poly} = [\frac{1}{3} (\frac{1}{\rho_{\parallel}} + \frac{2}{\rho_{\perp}})]^{-1} = \frac{3\rho_{\parallel}\rho_{\perp}}{2\rho_{\parallel} + \rho_{\perp}} \quad . \tag{5.30}$$

If there is no anisotropy ($\rho_{\perp} = \rho_{\parallel}$) then these two expressions become the same. From the $\rho_{\parallel}$ and $\rho_{\perp}$ results to be presented later, it is easily determined that ρ_{Poly} from equation (5.29) and (5.30) differ by approximately 2 to 3% for Zn, and at most 0.3% for Tl. These differences will not be significant for our results, and we prefer to chose ρ_{Poly} to be consistent with the Fermi surface averages used to obtain $\rho_{\parallel}$ and $\rho_{\perp}$.

As has been mentioned previously the variational formula averages the resistivities, therefore, we take

$$\rho^{V}_{Poly} = \frac{1}{3}(\rho_{\parallel} + 2\rho_{\perp}) \quad . \tag{5.31}$$

Using this expression, the result (5.27) for $\rho_{\parallel}$ and $\rho_{\perp}$, and the definition of $\alpha^2_{tr}F(\omega)$ from (3.12) and (3.13) we have

$$\rho^{V}_{Poly} = \frac{4\pi m\beta}{ne^2 m_B} \int d\omega \; R(\omega) \; \alpha^2_{tr}F(\omega) \tag{5.32}$$

which is in the form of the resistivity expression given by Allen [138].

Figures 5.3.1, 5.3.2(a) and 5.3.2(b) show the isotropic $\alpha^2_{tr}F(\omega)$ for the zinc MEPM model and the thallium Tl(0.875) and Tl(0.435) models, respectively. Upon comparison with the $\alpha^2F(\omega)$ functions of sections 3.3 and 3.4 we see that the $\alpha^2_{tr}F(\omega)$ functions are qualitatively similar. However, there are significant differences, which are due to the heavier weighting given to large $|\underline{q}|$ processes in $\alpha^2_{tr}F$. In particular we note that $\alpha^2_{tr}F$ may not be obtained from α^2F by the use of a constant scaling factor.

Recalling that the $\alpha^2F(\omega)$ functions for our two Tl models are almost identical, the differences between the $\alpha^2_{tr}F(\omega)$ of figure 5.3.2 appear to be quite striking. The differences in the relative peak heights can be ascribed to the large $|\underline{q}|$ weighting factor of $\alpha^2_{tr}F$, and the pseudopotential

models; while the difference in absolute magnitude is mainly a result of the m_B values for the two Tl models (see section 3.4).

In figure 5.3.3 we compare ρ^V_{Poly} from equation (5.32) with the experimental results compiled by Meaden [137]. The agreement with experiment over the whole temperature range appears to be quite good for Zn and very good for Tl. This agreement is striking when it is considered that the parameters involved in these calculations were entirely determined by the phonons and zero temperature experimental results. No attempt has been made to incorporate the effect of volume changes [139], the anisotropic expansion of Zn and Tl [140], or the temperature dependence of the phonons [58].

The resistivity curve labeled Zn is for the MEPM force constant model. The zinc DWL model was dropped for this section because in all the previous work described in this thesis it did not give results as good as the MEPM model. Borchi et al. [136] have used formula (5.32) to calculate the resistivity of Be, Mg and Zn, with Zn results similar to those seen in figure 5.3.3.

The Tl curve of figure 5.3.3 represents both Tl(0.435) and Tl(0.875) model results, to within the accuracy of the graph. This is to some extent fortuitous since, when fitting the pseudopotential to the experimental $\alpha^2F(\omega)$ function, small shifts in R_c can be allowed. These changes would tend to separate the two Tl model results for ρ^V_{Poly} in the figure.

However, it does seem significant that two very different pseudopotentials can give almost identical results for $\alpha^2F(\omega)$ and the resistivity, both in excellent agreement with experiment.

Our results for $\rho_{\parallel}^{V}$ and $\rho_{\perp}^{V}$ will be presented towards the end of this section, after we derive the scattering time resistivity formulae. In our discussion of the scattering time approximation for noncubic metals we closely follow the formalism of Taylor [141] and the method of RD, which they used for the cubic case.

The total current density $\underline{J}$ is given by

$$\underline{J} = \frac{e}{V} \sum_{\underline{k}} \underline{v}(\underline{k}) f \tag{5.33}$$

where V is the total volume and the summation is over both spin directions. The electron distribution function f, shortened notation for $f_{\underline{k}}$, is expanded about the equilibrium Fermi-Dirac distribution f° and only terms linear in the electric field $\underline{u}$ are retained. This statement implies that the total change in f, caused by $\underline{u}$, is just the sum of the changes which would be caused by the three components of $\underline{u}$ acting separately. In this case we may define [141] a "vector mean free path" $\underline{\Lambda}_{\underline{k}}$ which is independent of $\underline{u}$, and which satisfies

$$f = f^\circ - e\underline{\Lambda}_{\underline{k}} \cdot \underline{u} \frac{\partial f^\circ}{\partial E} \tag{5.34}$$

This expansion corresponds to that used in the variational approach, except that for the trial function, $\Phi_{\underline{k}}$ of equation (5.25), $\underline{k}$ has been replaced by the general vector $\underline{\Lambda}_{\underline{k}}$ to give

$$\Phi_{\underline{k}} = e\underline{\Lambda}_{\underline{k}} \cdot \underline{u} \quad . \tag{5.35}$$

Now substituting (5.34) into (5.33), and noting that in equilibrium the current density is zero

$$\underline{J} = - \frac{e^2}{V} \sum_{\underline{k}} \underline{v}(\underline{k}) \underline{\Lambda}_{\underline{k}} \cdot \underline{u} \frac{\partial f^\circ}{\partial E} \tag{5.36}$$

is obtained.

The conductivity tensor $\underset{\sim}{\sigma}$ is defined by

$$\underline{J} = \underset{\sim}{\sigma} \cdot \underline{u} \quad ,$$

thus

$$\underset{\sim}{\sigma} = - \frac{e^2}{V} \sum_{\underline{k}} \underline{v}(\underline{k}) \underline{\Lambda}_{\underline{k}} \frac{\partial f^\circ}{\partial E} \quad . \tag{5.37}$$

It is seen that the vector $\underline{\Lambda}_{\underline{k}}$ provides a complete description of the conductivity with three independent numbers for each point of $\underline{k}$-space. Using (5.35) in the Boltzmann equation (5.23), and integrating the right hand side over E' and the whole equation over E leaves [142]

$$\underline{v}(\underline{k}) = 4\pi\beta \int d\omega\ R(\omega)\ N(0) \int \frac{d\Omega_{\underline{k}'}}{4\pi} \sum_j |g_{\underline{k}\underline{k}'j}|^2$$

$$\times (\underline{\Lambda}_{\underline{k}} - \underline{\Lambda}_{\underline{k}'})\ \delta(\omega - \omega_{\underline{q}j}) \quad . \tag{5.38}$$

The thermal factor $R(\omega)$ is given by (5.28), and the above equation is written in vector form.

The problem of calculating the conductivity tensor has been reduced to solving equation (5.38) for $\underline{\Lambda}_{\underline{k}}$. Taylor [130] has given a formal solution for $\underline{\Lambda}_{\underline{k}}$ in terms of an infinite sum. However, this sum is very slowly converging and the time required to calculate more than the first term or so is prohibitive. Instead we prefer to proceed in analogy with the derivation of RD, and assume that

$$\underline{\Lambda}_{\underline{k}} \cong \tau(\underline{k})\underline{v}(\underline{k}) \quad , \tag{5.39}$$

where the equality holds for cubic systems. Then equation (5.38) becomes

$$\underline{k} = 4\pi\beta \int d\omega\ R(\omega)\ N(0) \int \frac{d\Omega_{\underline{k}'}}{4\pi} \sum_j |g_{\underline{k}\underline{k}'j}|^2$$

$$\times \{\tau(\underline{k})\underline{k} - \tau(\underline{k}')\underline{k}'\}\ \delta(\omega - \omega_{\underline{q}j}) \tag{5.40}$$

where we have used the spherical Fermi surface relation $\underline{v}(\underline{k}) \sim \underline{k}$. In the curly brackets $\tau(\underline{k})\underline{k}'$ is added and

subtracted to obtain

$$\{\tau(\underline{k})(\underline{k} - \underline{k}') + [\tau(\underline{k}) - \tau(\underline{k}')]\underline{k}'\} \quad ,$$

and

$$1 = 4\pi\beta \int d\omega\ R(\omega)\ N(0) \int \frac{d\Omega_{\underline{k}'}}{4\pi} \sum_j |g_{\underline{k}\underline{k}'j}|^2$$

$$\times \{\tau(\underline{k})(1 - \cos(\underline{k},\underline{k}')) + [\tau(\underline{k}) - \tau(\underline{k}')]\frac{\underline{k}\cdot\underline{k}'}{k_F^2}\}$$

$$\times \delta(\omega - \omega_{\underline{q}j}) \qquad (5.41)$$

where $\underline{k}\cdot$ has been taken on both sides of (5.40).

At this point it is observed that the first term in the curly brackets is always positive, while the second term is positive and negative. In fact, for a general point $\underline{k}$ the second term will pass through zero 24 times as the $\underline{k}'$ integral is performed. The contribution from this term is expected to be small and we shall neglect it, as did RD in the cubic case [132].

Finally we obtain the scattering time formula

$$\frac{1}{\tau(\underline{k})} = 4\pi\beta \int d\omega\ R(\omega)\ \alpha_{tr}^2 F(\omega,\underline{k}) \qquad (5.42)$$

where we have used the definition (3.12) of $\alpha_{tr}^2 F(\omega,\underline{k})$. The anisotropic resistivities $\rho_{\parallel}$ and $\rho_{\perp}$ are now simply obtained

by using the $\tau(\underline{k})$, obtained from equation (5.42), in the conductivity equation (5.37). It is interesting to note that the τ's depend on the m_B value through $\alpha^2_{tr}F$. This dependence drops out when the integral in (5.37) is performed to obtain the conductivities, or equivalently, the resistivities.

We shall take the polycrystalline sample resistivity ρ^{ST}_{Poly}, in the scattering time approximation, to be given by (5.30) which is consistent with averaging the conductivities to obtain $\rho^{ST}_{\parallel}$ and $\rho^{ST}_{\perp}$. Therefore, we may write, in terms of the scattering times of equation (5.42),

$$\rho^{ST}_{Poly} = \frac{m}{ne^2 m_B} \frac{1}{\langle \tau(\underline{k}) \rangle} \quad , \tag{5.43}$$

and equation (5.32) for the variational result becomes

$$\rho^{V}_{Poly} = \frac{m}{ne^2 m_B} \left\langle \frac{1}{\tau(\underline{k})} \right\rangle \quad . \tag{5.44}$$

It is seen that the variational and scattering time results are in direct correspondence, except for the averaging procedure for $\tau(\underline{k})$. Again we point out that (5.43) and (5.44) are independent of m_B, since $\tau^{-1} \sim m_B$.

Calculations using the formalism outlined in this section were performed using the Zn(MEPM) model, and both Tl(0.435) and Tl(0.875) models. In figures 5.3.4, 5.3.5 and 5.3.6 we plot $\alpha^2_{tr}F(\omega,\underline{k})$ for three high symmetry directions

in each of the three models mentioned above. Comparing with the results of sections 4.2 and 4.3 it is seen that α^2F and $\alpha^2_{tr}F$ are qualitatively similar; but that they differ by more than a constant scaling factor. The differences can be ascribed to the heavier weighting given to the large $|\underline{q}|$ scattering processes in $^2_{tr}F$. There is also a considerable $\underline{k}$ dependence within each model. The two Tl models differ both in absolute magnitude and in the relative peak heights. The difference in absolute magnitude is mainly due to the band mass values, where $m_B = 0.44$ for Tl(0.435) and $m_B = 0.64$ for Tl(0.875).

Figures 5.3.7, 5.3.8 and 5.3.9 show the scattering times $\tau(\theta,\phi)/\tau(0,0)$ at two temperatures T = 20°K and T = 300°K. The most obvious features are that there is a considerable variation as a function of Fermi surface position, and the anisotropy decreases as a function of temperature. It is also interesting to compare these results with the electron-phonon scattering times of section 5.1, and we note that these two scattering times show very similar variations with direction.

The temperature variation of $\langle\tau(\theta,\phi)\rangle$ is shown in figure 5.3.10, and by equation (5.43) the scattering times go as ρ^{-1}. However, as indicated in figure 5.3.3, the resistivities of the two Tl models are almost the same while the scattering times are considerably different. This is caused by the difference in band mass values since $\tau \sim m_B^{-1}$ while ρ is independent of m_B.

The effect of the two different averaging procedures in equations (5.43) and (5.44) is shown in figure 5.3.11 where $(\rho^{V}_{Poly}/\rho^{ST}_{Poly}) = (\langle\tau^{-1}(\underline{k})\rangle/\langle\tau(\underline{k})\rangle^{-1})$ is plotted. The variational result is larger than the scattering time polycrystalline resistivity. This difference may be very large at low temperatures, and it decreases as the temperature is increased. However, in a highly anisotropic material this effect may be significant even at room temperatures [133]. For example, in our Zn calculation the difference in averaging procedures is 9% at 60°K and 5% at 300°K. If the material is not very anisotropic, then for higher temperatures this effect becomes insignificant as compared to other uncertainties. For our Tl models the difference is only $\tilde{\sim}$ 1% at 40°K, although it gains in importance for the very low temperature resistivities. We note that if ρ^{ST}_{Poly} had been plotted in figure 5.3.3, then agreement with the experimental low temperature resistivities would be improved.

In the final two figures we present a very sensitive test for any resistivity calculation in a noncubic material. The quantity $\rho_{\parallel}/\rho_{\perp}$ has been plotted, where the solid line uses the scattering time formula (5.37) and the dotted line is the variational result (5.27).

Comparison of these curves in figure 5.3.12 for Zn and 5.3.13 for the Tl models indicates that they agree qualitatively in both temperature dependence and magnitude. However, there are considerable quantitative differences

between the variational and scattering time $\rho_{\parallel}/\rho_{\perp}$ ratios. Also, figure 5.3.13 illustrates that this ratio can be extremely dependent on the pseudopotential used. In fact, of all the properties calculated in this thesis the $\rho_{\parallel}/\rho_{\perp}$ ratio is the most sensitive test for differentiating between the two Tl pseudopotentials.

The variational formula (5.27) for $\rho_{\parallel}$ and $\rho_{\perp}$ represents a much smaller investment in computing time than is required for the complete scattering time approximation. However, (5.27) calculates averages of the form $\langle\tau^{-1}\rangle$ when actually the correct averages should be $\langle\tau\rangle^{-1}$. We may use our scattering time results to investigate the effect of this averaging on $\rho_{\parallel}/\rho_{\perp}$.

The calculation of $\rho_{\parallel}$ and $\rho_{\perp}$ in the scattering time approximation has already been discussed, and the results are shown as the solid curves in the last two figures. We have repeated exactly the same procedure except that the averaging was done over τ^{-1} rather than τ. The results are displayed in figures 5.3.12 and 5.3.13 as the dashed curves. In all cases, for T > 10°K the variational type average has decreased the calculated anisotropy. Therefore, it appears as if the variational formula (5.27) will underestimate the $\rho_{\parallel}/\rho_{\perp}$ ratio which would be obtained by a variational calculation using the correct $\langle\tau\rangle^{-1}$ averages. This may be quite significant as in the Tl(0.435) model where the averaging procedure causes a difference of a factor of two in $(\rho_{\parallel}/\rho_{\perp})-1$.

In figure 5.3.12 we include a number of experimental determinations [143-145] of the zinc $\rho_{\parallel}/\rho_{\perp}$ ratio. It is seen that our calculated ratio is in qualitative agreement with that observed experimentally. This is significant in that we have only included phonon anisotropy, and all anisotropic band structure effects have been neglected.

The degree of agreement seen in figure 5.3.12 is about as good as can be expected considering the uncertainties in the Zn force constant model used. As stated earlier, we expect the MEPM force constants to place an upper limit on the effects of phonon anisotropy in Zn. Thus, the overestimate of $\rho_{\parallel}/\rho_{\perp}$ is not surprising.

Behaviour similar to that seen in figure 5.3.12 has been observed in tin by Case and Gueths [146]. These authors interpret their results in terms of a model ellipsoidal Fermi surface; while our results and those of Balsley [48] would indicate that the phonons may be the predominant source of anisotropy in the $\rho_{\parallel}/\rho_{\perp}$ ratio.

In summary, we have obtained expressions for ρ_{Poly}, $\rho_{\parallel}$ and $\rho_{\perp}$ using both the variational approach and the scattering time approximation. We find good agreement between experiment and our calculated polycrystalline resistivities for both Zn and Tl. By only including the effects of phonon anisotropy we find qualitative agreement with experiment for the zinc $\rho_{\parallel}/\rho_{\perp}$ ratio.

FIGURE CAPTIONS - SECTION 5.3

FIGURE 5.3.1 Zn(MEPM) Fermi surface averaged "transport frequency distribution" $\alpha^2_{tr}F(\omega)$. The function $\alpha^2_{tr}F$ is dimensionless.

FIGURE 5.3.2 Fermi surface averaged "transport frequency distributions" $\alpha^2_{tr}F(\omega)$ for (a) the Tl(0.875) model, and (b) the Tl(0.435) model.

FIGURE 5.3.3 The polycrystalline sample resistivity ρ_{Poly} in units of $\mu\Omega$-cm. The experimental values for zinc (×) and thallium (o) are from Meaden [137]. The solid curves are calculated using the variational formula (5.32). The curve labeled Zn is for the MEPM force constant model; and the Tl curve represents both Tl(0.435) and Tl(0.875) models equally well.

FIGURE 5.3.4 Zn(MEPM) model electron-phonon "transport frequency distributions" $\alpha^2_{tr}F(\omega,\underline{k})$ for three high symmetry directions. The directions are labeled by (θ,ϕ) where $\underline{k} = (k_F,\theta,\phi)$.

FIGURE 5.3.5 Tl(0.435) model, as in figure 5.3.4.

FIGURE 5.3.6 Tl(0.875) model, as in figure 5.3.4.

FIGURE 5.3.7 Comparison at two temperatures of the Zn(MEPM) transport scattering times as a function of position (θ,ϕ) on the Fermi surface, with $\tau(0,0,20^{o}K)=2.89\times10^{-13}$ sec. and $\tau(0,0,300^{o}K)=6.36\times10^{-15}$ sec.

FIGURE 5.3.8 Tl(0.435), as in figure 5.3.7, with $\tau(0,0,20^{o}K)=1.86\times10^{-13}$ sec. and $\tau(0,0,300^{o}K)=6.35\times10^{-15}$ sec.

FIGURE 5.3.9 Tl(0.875), as in figure 5.3.7, with $\tau(0,0,20^{o}K)=1.20\times10^{-13}$ sec. and $\tau(0,0,300^{o}K)=3.98\times10^{-15}$ sec.

FIGURE 5.3.10 The temperature dependence of the Fermi surface averaged transport scattering times $\langle\tau(\underline{k},T)\rangle$. The curve labeled Zn is for the zinc MEPM force constant model, and both thallium models are shown.

FIGURE 5.3.11 Comparison of the polycrystalline resistivities, as a function of temperature, ρ^{V}_{Poly} and ρ^{ST}_{Poly} calculated by the variational equation (5.32) and the scattering time equation (5.43)

respectively. The zinc graph is for the MEPM force constant model; and the thallium graph has the solid line for the Tl(0,435) model, and the dashed line for the Tl(0.875) model. The vertical scale for the thallium curves has been expanded by a factor of four relative to the zinc scale.

FIGURE 5.3.12 Temperature dependence of the Zn(MEPM) resistivity ratio $\rho_{\parallel}/\rho_{\perp}$. The solid curve is $\rho_{\parallel}^{ST}/\rho_{\perp}^{ST}$ calculated in the scattering time approximation by equations (5.37) and (5.39), where the $\tau(\underline{k})$ are given by (5.42). The dotted curve is $\rho_{\parallel}^{V}/\rho_{\perp}^{V}$ calculated by the variational approach, equation (5.27). The dashed curve is the resistivity ratio as calculated in the scattering time approximation except that the average in (5.37) has been taken over $\tau^{-1}(\underline{k})$, (a "variational" average). The experimental points (⊡), (⊙) and (×) are from references 143, 144 and 145 respectively.

FIGURE 5.3.13 As in figure 5.3.12, except that the curves are for the two thallium models : Tl(0.435) and Tl(0.875).

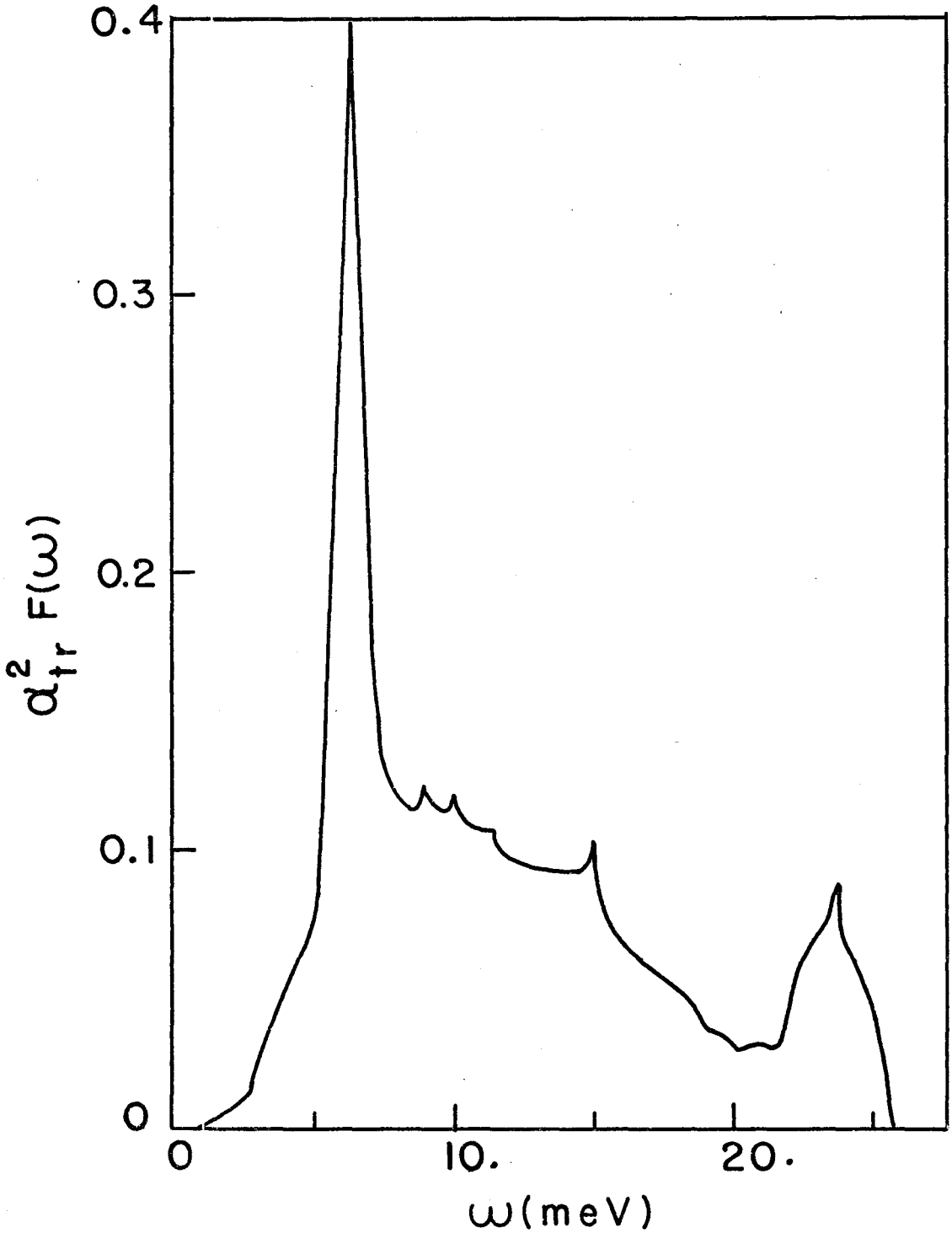
0.4
0.3
0.2
0.1
0
$\alpha^2_{tr} F(\omega)$
0
10.
20.
ω(meV)

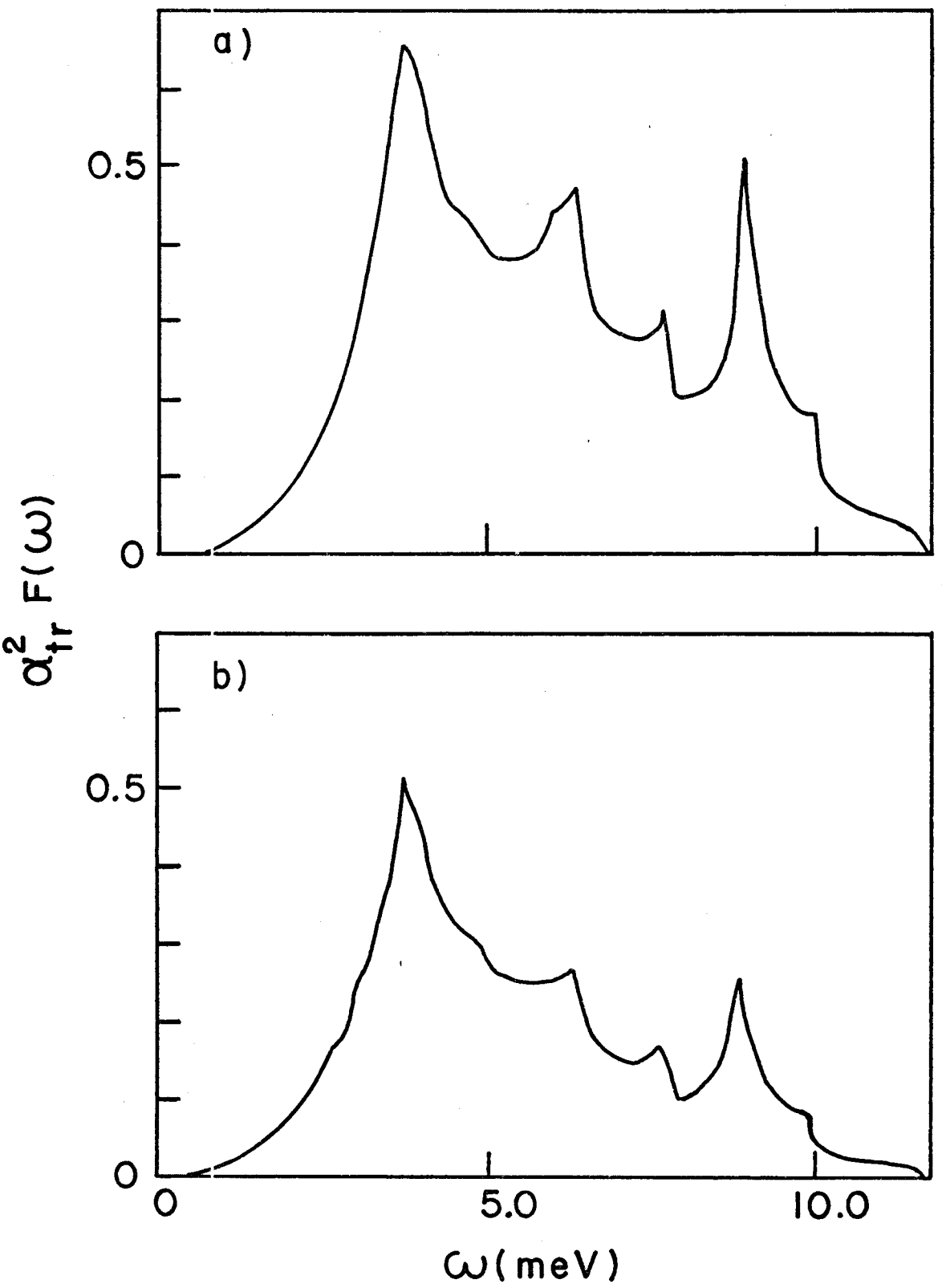
a)
b)
0.5
0
0.5
0
0
5.0
10.0
$\alpha^2_{tr} F(\omega)$
ω(meV)

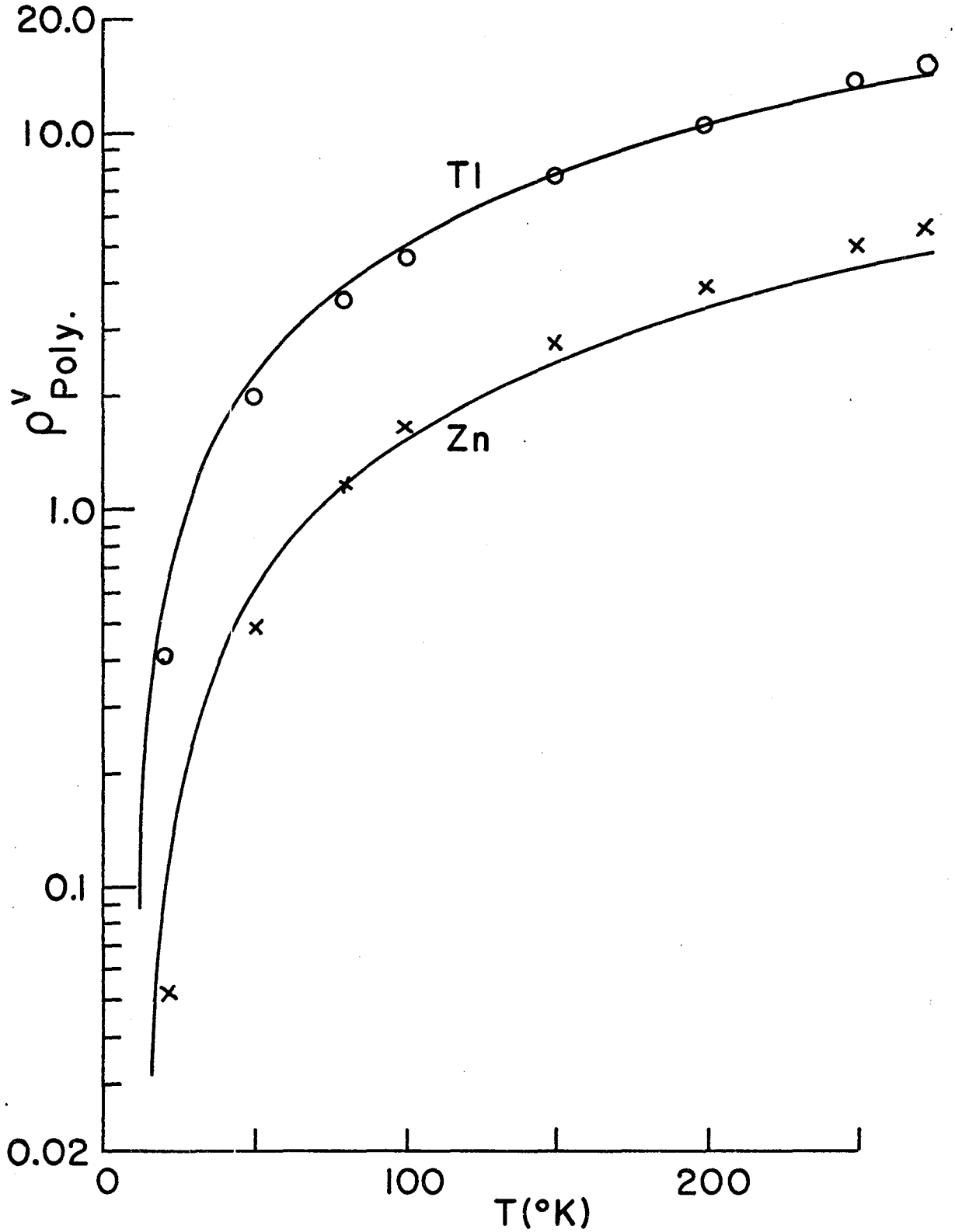
20.0
10.0
1.0
0.1
0.02
$\rho^{v}_{Poly.}$
Tl
Zn
0
100
200
T(°K)

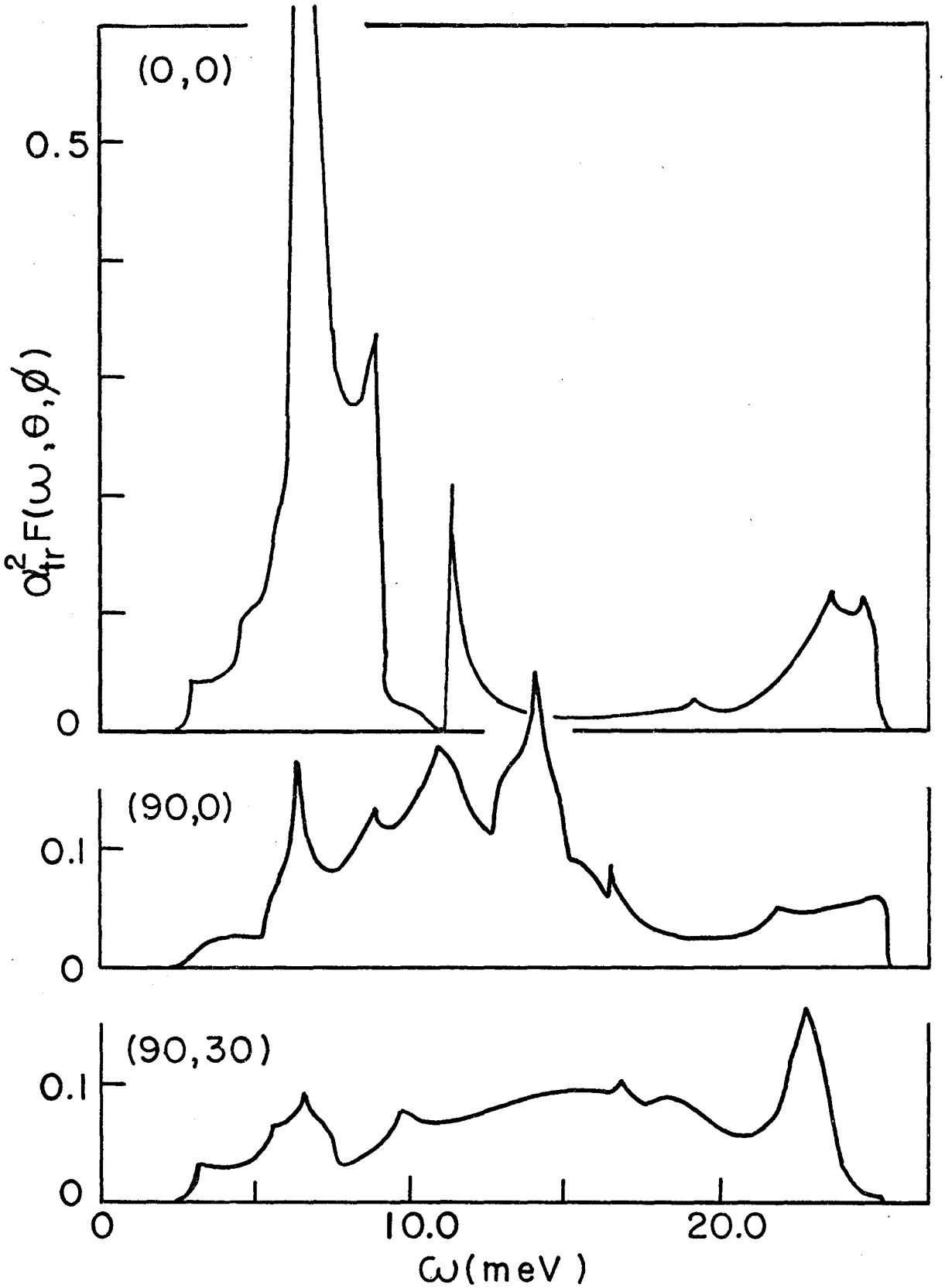
(0,0)
0.5
0
$\alpha^2_{tr}F(\omega,\theta,\phi)$
(90,0)
0.1
0
(90,30)
0.1
0
0
10.0
20.0
ω(meV)

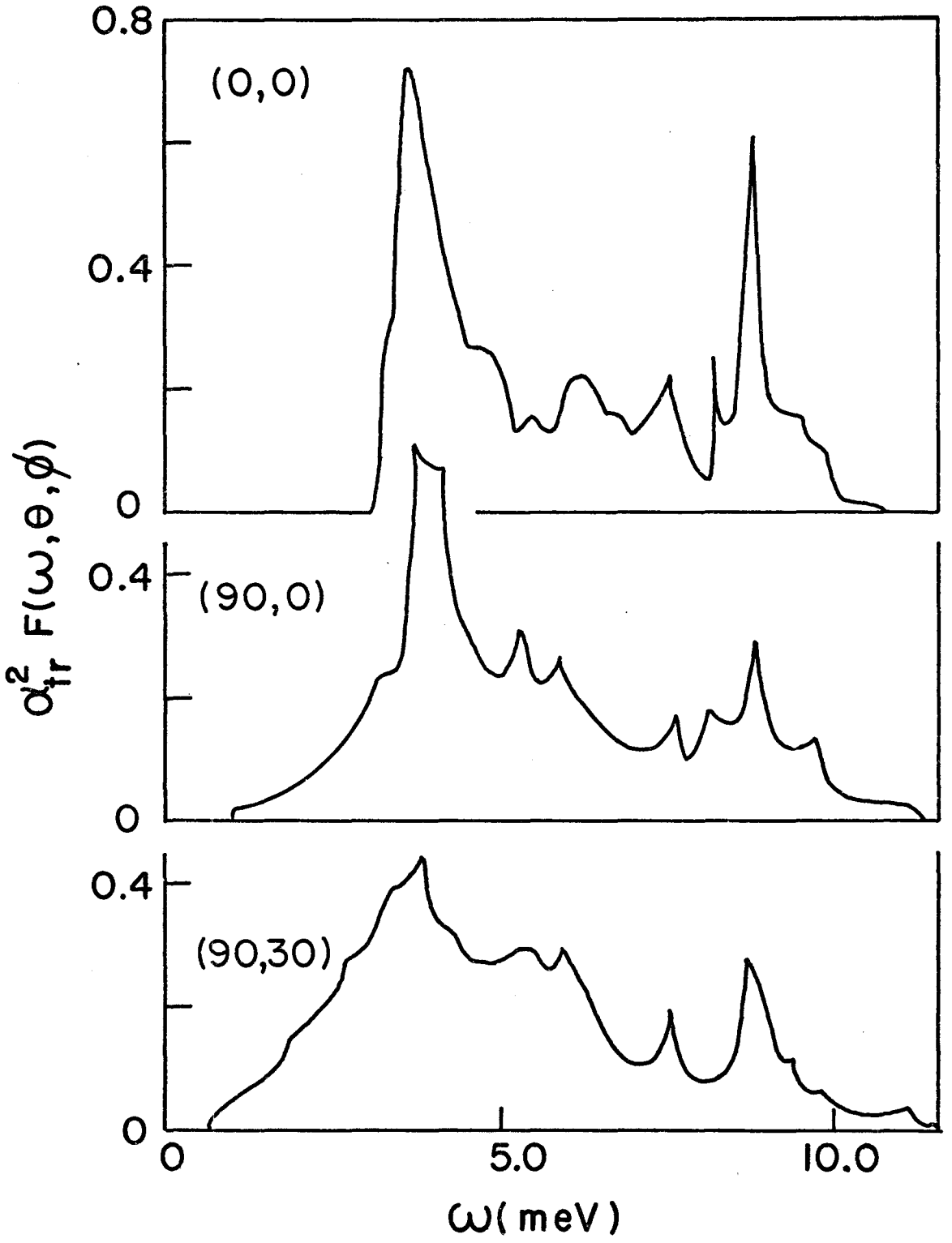
0.8
0.4
0
(0,0)
0.4
0
(90,0)
0.4
0
(90,30)
0
5.0
10.0
ω(meV)
$\alpha^2_{tr} F(\omega,\theta,\phi)$

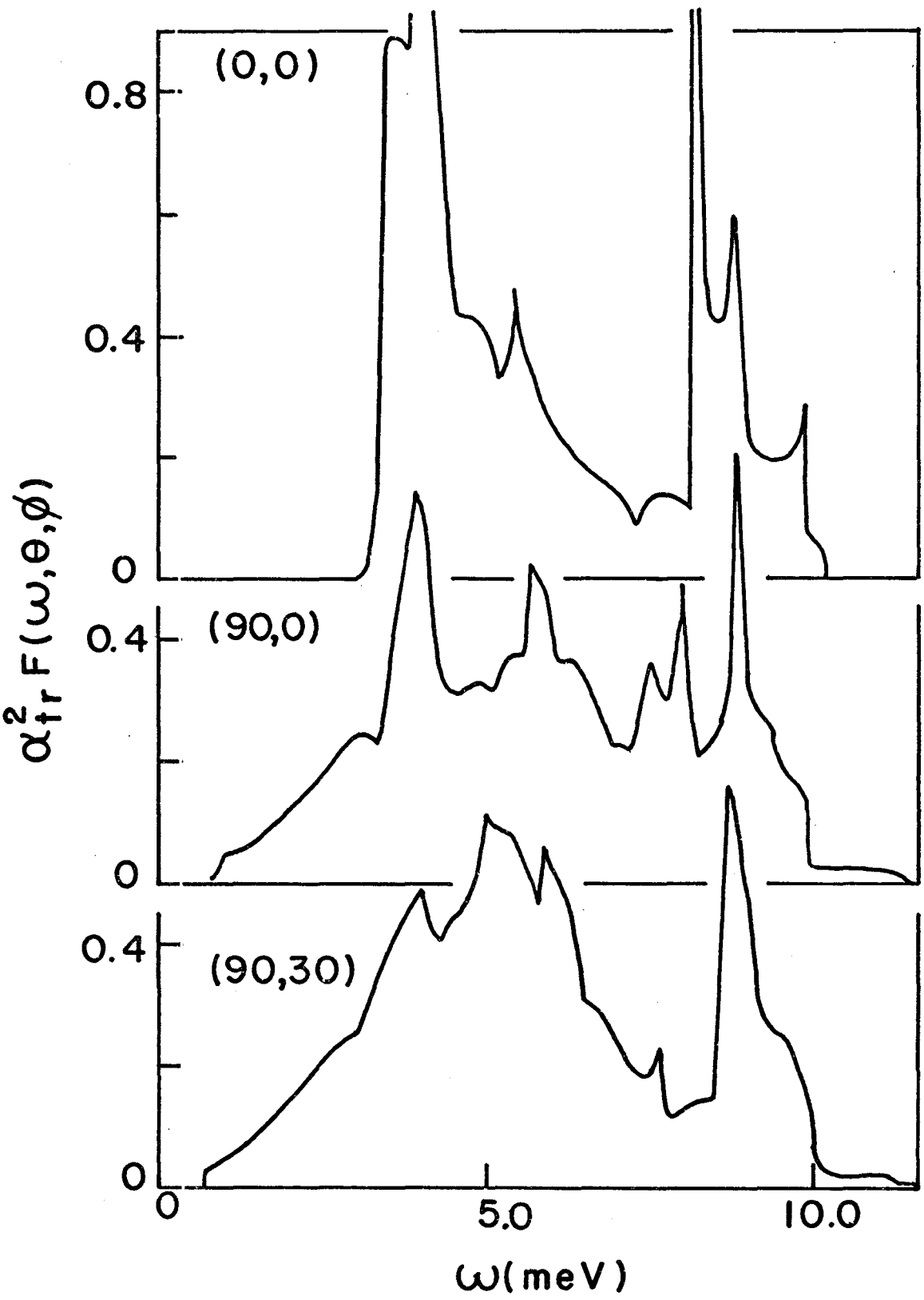
(0,0)
(90,0)
(90,30)
0.8
0.4
0
0.4
0
0.4
0
0
5.0
10.0
ω(meV)
$\alpha^2_{tr}F(\omega,\theta,\phi)$

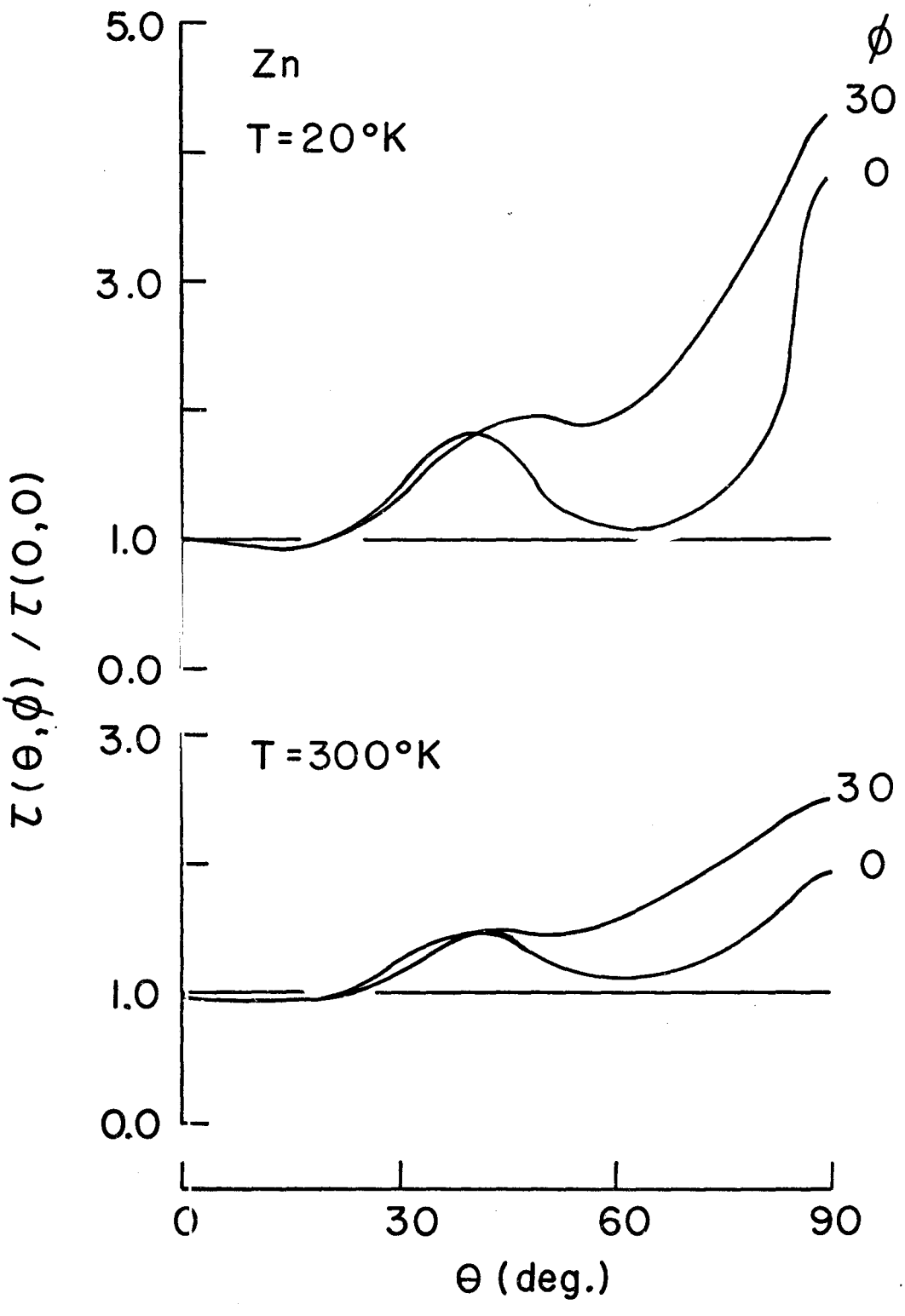
Zn
T=20°K
T=300°K
φ
30
0
30
0
5.0
3.0
1.0
0.0
3.0
1.0
0.0
I(θ,φ) / I(0,0)
0
30
60
90
θ (deg.)

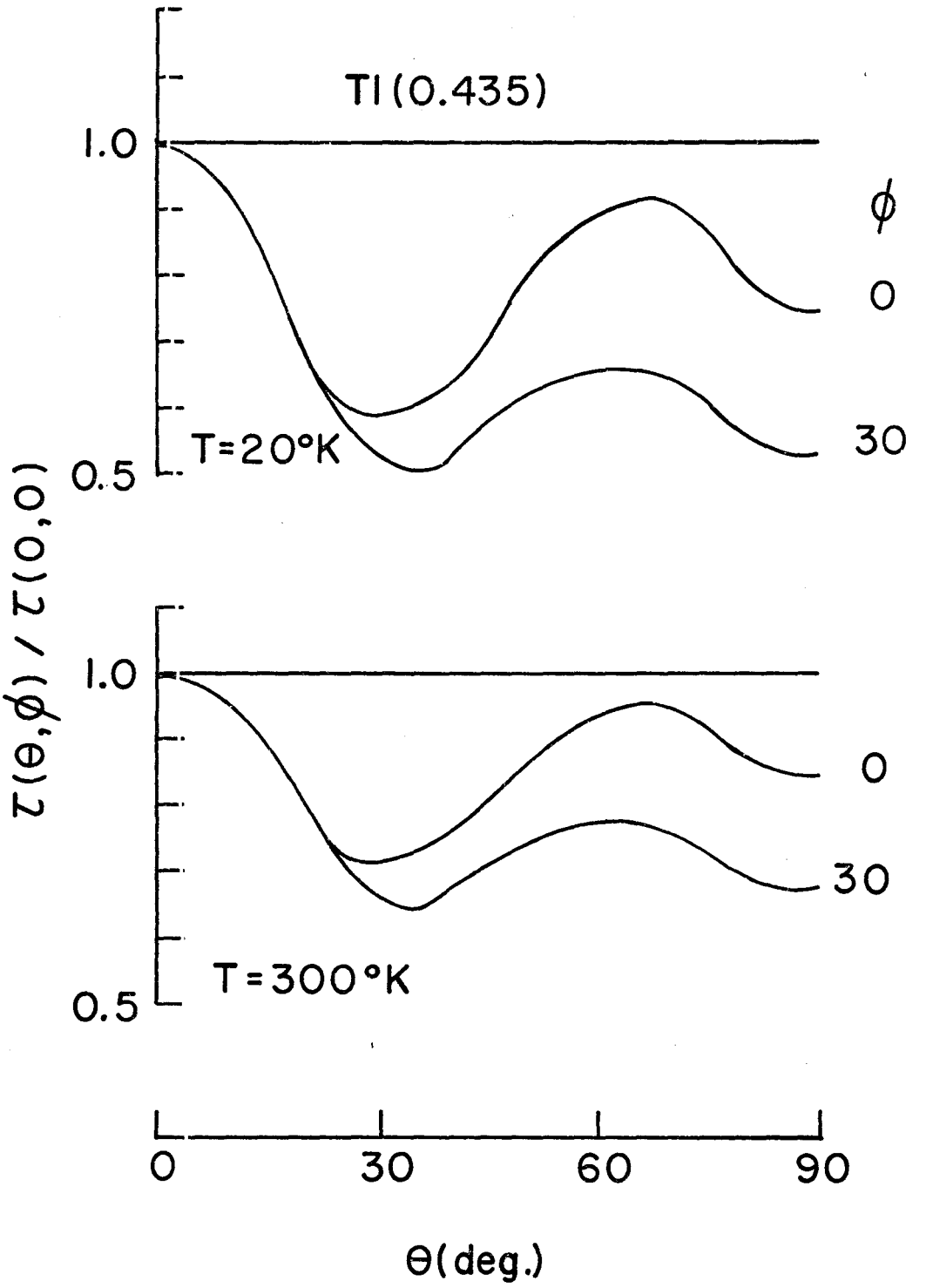
Tl(0.435)
1.0
0.5
T=20°K
ϕ
0
30
1.0
0.5
T=300°K
0
30
τ(θ,ϕ) / τ(0,0)
0
30
60
90
θ(deg.)

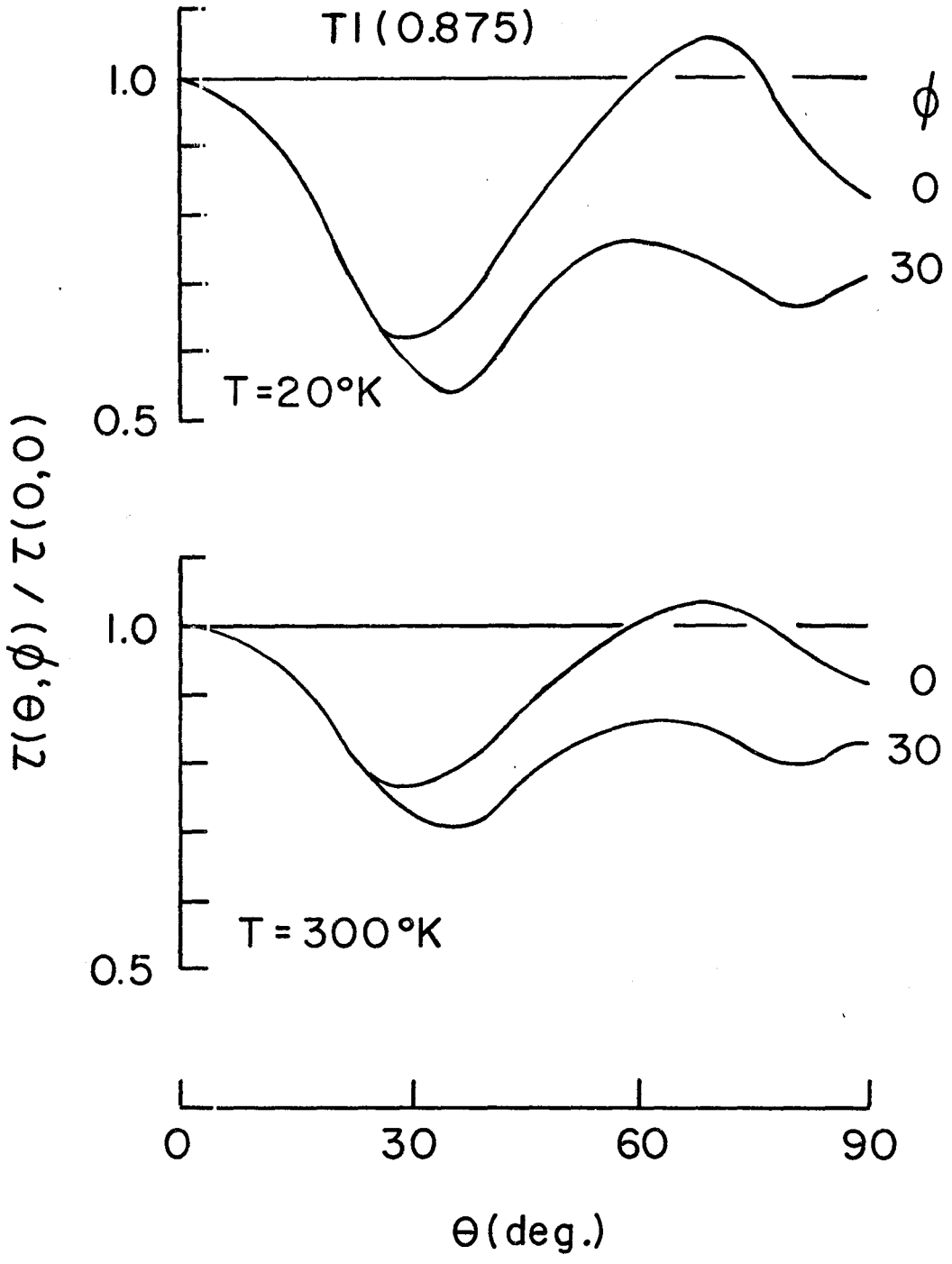
Tl(0.875)
1.0
0.5
T=20°K
φ
0
30
1.0
0.5
T=300°K
0
30
I(θ,φ) / I(0,0)
0
30
60
90
θ(deg.)

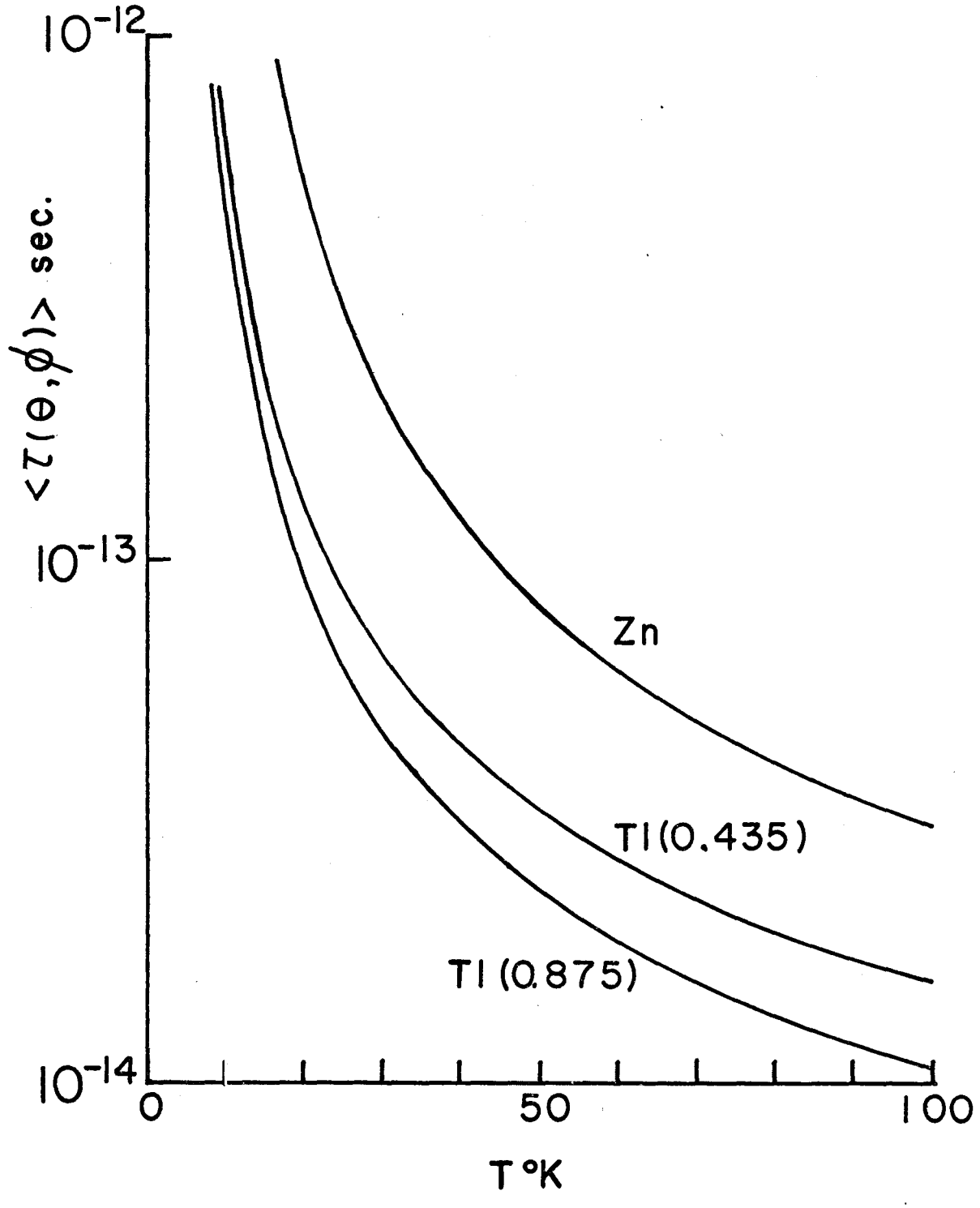
10^{-12}
10^{-13}
10^{-14}
$\langle \tau(\theta,\phi) \rangle$ sec.
Zn
Tl(0.435)
Tl(0.875)
0
50
100
T °K

Figure 5.3.11

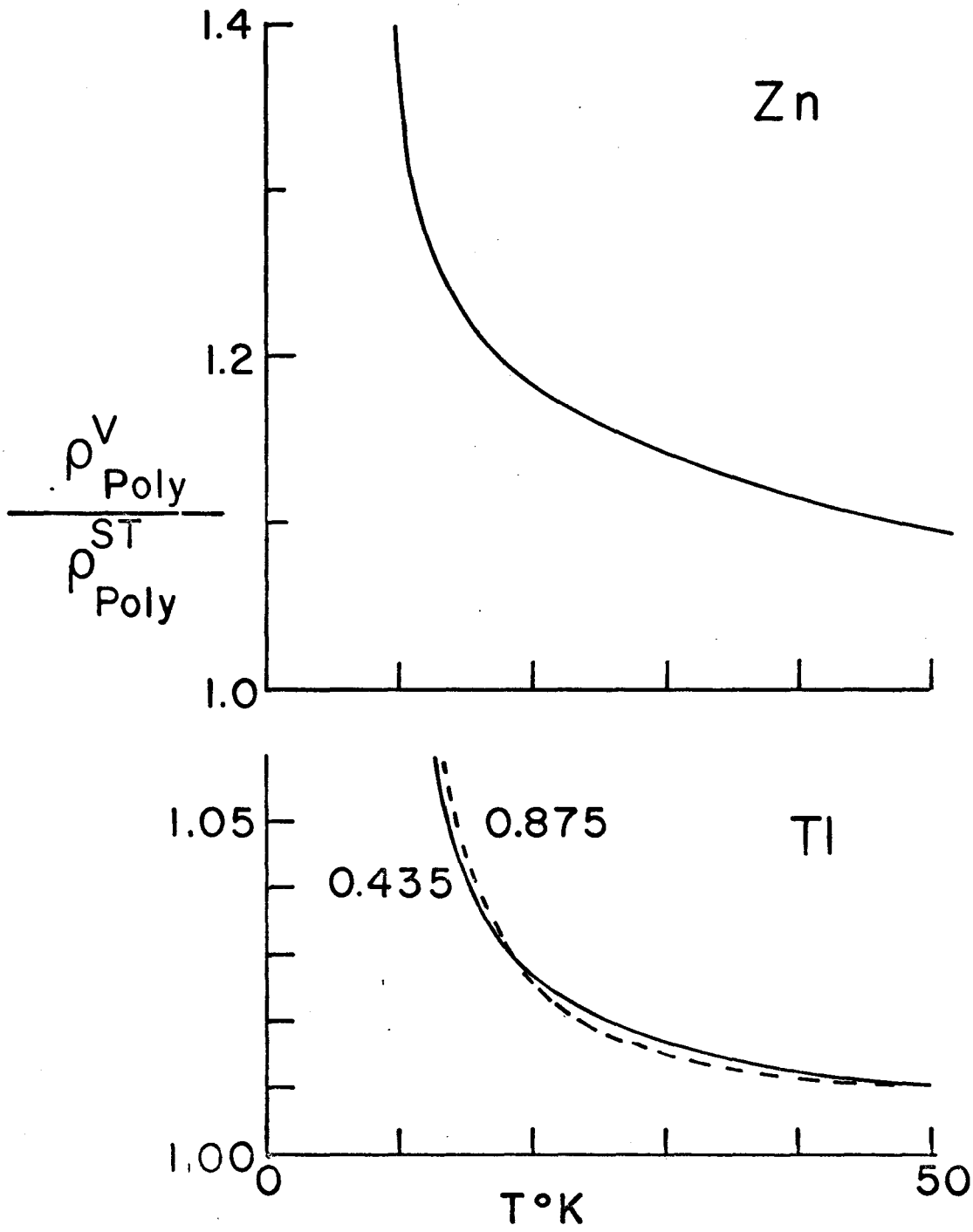
1.4
1.2
1.0
Zn
$\frac{\rho^{V}_{Poly}}{\rho^{ST}_{Poly}}$
1.05
1.00
0.875
0.435
Tl
0
50
T°K

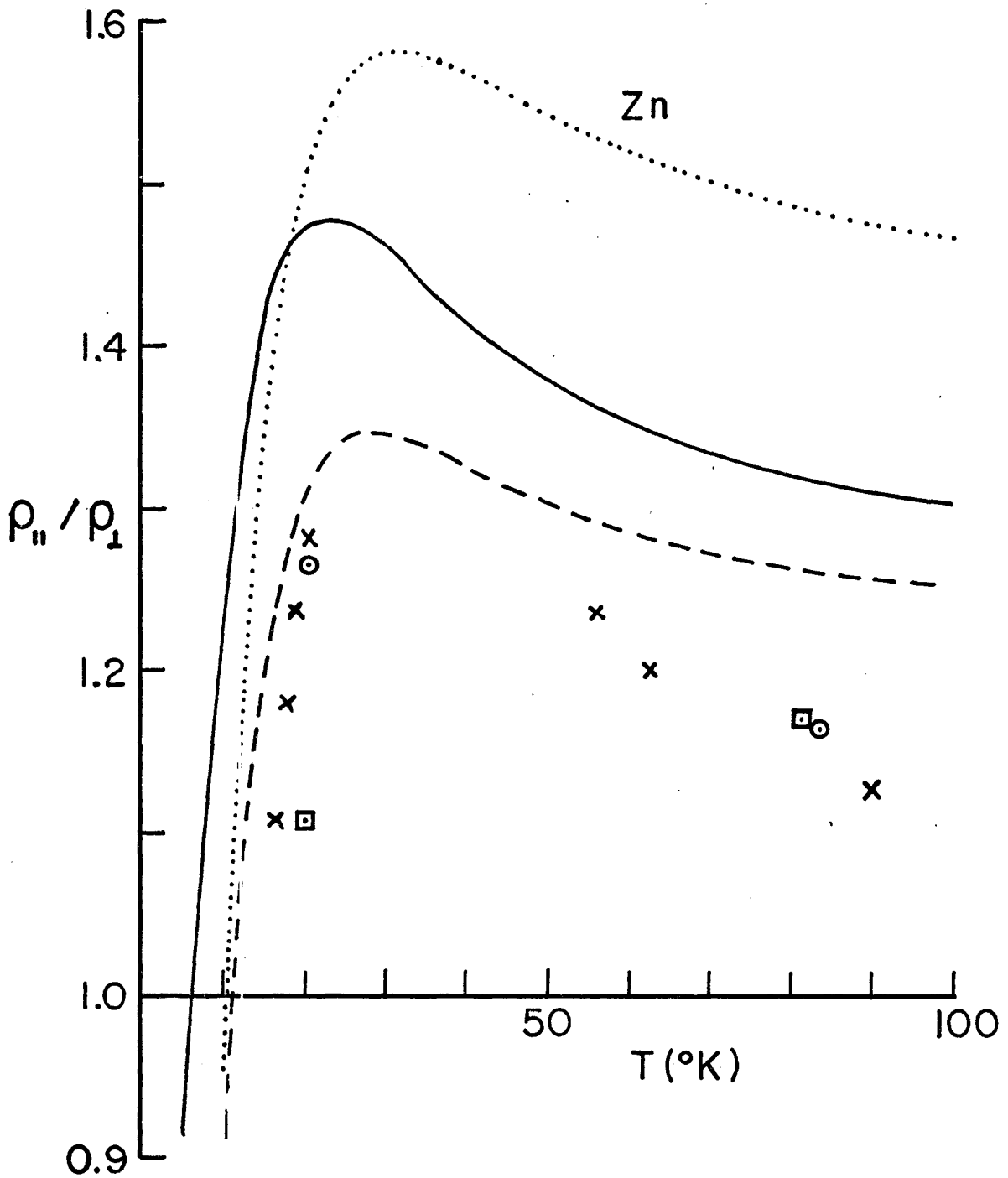
1.6
1.4
1.2
1.0
0.9
$\rho_{\parallel} / \rho_{\perp}$
Zn
50
100
T (°K)

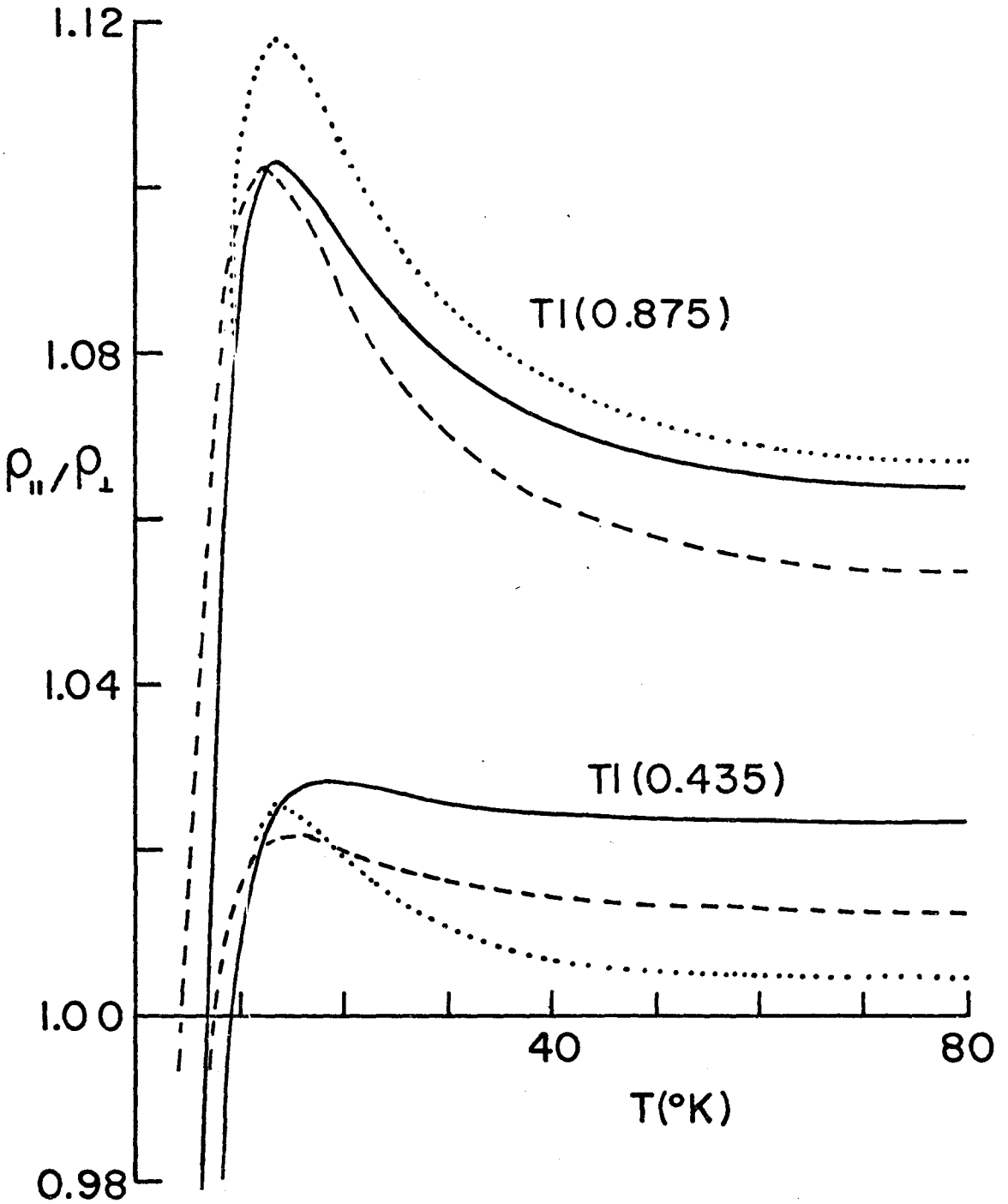
1.12
1.08
1.04
1.00
0.98
$\rho_{\parallel}/\rho_{\perp}$
Tl(0.875)
Tl(0.435)
40
80
T(°K)

CHAPTER VI

CONCLUSIONS

A unified approach, employing effective phonon frequency distributions α^2F and $\alpha^2_{tr}F$, was used to investigate the electron-phonon interaction in the hexagonal close-packed metals. Particular emphasis was placed on the effects of phonon anisotropy, which arises from both the directional dependence of the phonon frequency distributions and the anisotropy in the electron-phonon interaction.

Zinc and thallium were used as models in this detailed numerical investigation; and many superconducting and normal state properties were calculated. Experimental phonon information was included by the use of Born-von Kármán force constant models, and pseudopotentials were used to describe the electron-ion interaction. The major assumption made throughout this work was that the true Fermi surface could be replaced by a spherical model with a modified electronic density of states. Inclusion of the actual Fermi surface would have greatly increased the complexity of the calculations.

The local form of the Stark-Falicov pseudopotential was employed throughout the zinc calculations. Using the modified axially symmetric model, a set of zinc force constants (MEPM) was derived which reproduced both the measured phonon dispersion curves and the electronic specific

heat effective mass. Very recent neutron measurements indicate that this MEPM model should place an upper limit on the effects of phonon anisotropy in zinc.

Recent experiments in thallium have indicated that there are rather alarming discrepancies between the phonon frequency distribution $F(\omega)$ derived from inelastic neutron scattering experiments and the superconducting phonon frequency distribution $\alpha^2F(\omega)$ obtained from tunneling measurements. We have shown that these discrepancies are more apparent than real, and result from the force constant model and pseudopotential used to process the neutron data. In fact, we have used tunneling data to obtain information about the phonon dispersion curves that have not been directly measured by neutron spectroscopy.

It was observed that thallium appears to be a case where $\alpha^2(\omega)$ shows a strong frequency dependence. This is significant since it may not always be justified, even as a first approximation, to ignore the frequency dependence of $\alpha^2(\omega)$ when comparing $\alpha^2F(\omega)$ and $F(\omega)$.

The thallium force constant model used throughout this work was determined by fitting the calculated phonons to both the measured dispersion curves and the peak positions of the experimentally determined $\alpha^2F(\omega)$. Two very different "empty-core model" pseudopotentials were found which gave almost identical $\alpha^2F(\omega)$'s, both in good agreement with experiment. One pseudopotential gives good agreement with

the experimental electronic specific heat mass; but it does not agree with the structure factors determined by Holtham and Priestley [106]. The other thallium model is in better agreement with the Holtham and Priestley results; but the specific heat mass is much lower than experiment. In general these pseudopotentials gave very similar results for most of the other calculated properties; except the anisotropic resistivity ratio discussed towards the end of this section.

We have performed the first realistic microscopic calculation of the gap anisotropy in pure superconducting hcp crystals. The superconducting gaps as a function of position on the Fermi surface were determined by:

a) performing a first order iteration of an approximate set of strong coupling equations discussed by Leavens and Carbotte [51], and

b) obtaining the pure single crystal average gap from the analytic formula derived by the same authors.

The gaps showed considerable variation as a function of Fermi surface position. The maximum deviation from the average gap value was as much as 29% for Zn and 11% for Tl.

It was found that phonon effects were sufficient to explain the experimentally observed positions and magnitudes of the Zn maximum and minimum gaps, and also the ϕ-variation (figure 3.1.1) of the Tl gaps. We have only made a very rough qualitative comparison between the gap ϕ-variation

and the results of longitudinal ultrasonic attenuation measurements. As a function of ϕ, our Zn gaps show an ordering which is opposite to that indicated by experiment. However, even in this case the phonon effects are still significant and must be allowed for in any more detailed calculation.

We have used this gap anisotropy to calculate the transition temperature, the low temperature electronic specific heat and the nuclear spin-lattice relaxation rate for pure single crystal superconducting Zn and Tl. The results for the Zn electronic specific heat indicate that phonon anisotropy is not sufficient to explain experiment, and band structure effects must be included in the calculation of this property.

The isotropic or "dirty-limit" superconducting properties were also calculated, using the formalism of Leavens and Carbotte [107].

The electron-phonon mass enhancements are obtained from the real part of the electron self-energy. These mass enhancements and the imaginary part of the electron self-energy were calculated as a function of temperature and position on the Fermi surface. The anisotropy in the imaginary part of the self-energy increases as the temperature decreases. As the temperature is increased from zero, the anisotropy in λ remains constant for very low temperatures, reaches a maximum for temperatures of the order of $\frac{1}{4}$ the

lowest important phonon energy, and then rapidly approaches zero as the temperature is further increased.

We have calculated the temperature variations of the electron-phonon mass enhancements for three cyclotron orbits on the Zn third band lens, which were measured by Sabo [124]. Quantitative agreement with experiment is obtained for the limit point orbit results. However, it must be stated that the degree of agreement may be fortuitous. We think it more significant that, by only including phonon anisotropy, the orbital variation of the mass enhancements is of the same order of magnitude as is observed experimentally.

We have defined large-angle transport scattering times for noncubic crystals in terms of effective "transport" phonon frequency distributions, $\alpha^2_{tr}F$. It was observed that, in general, the shape of the $\alpha^2_{tr}F$ functions may be considerably different from either α^2F or F. The transport scattering times were calculated as a function of temperature and position on the Fermi surface. They display a large amount of anisotropy at low temperatures, which decreases as the temperature is increased.

These scattering times, $\tau(\underline{k})$, were used to calculate the isotropic polycrystalline resistivities, ρ_{Poly}, and the anisotropic single crystal resistivities, $\rho_{\parallel}$ and $\rho_{\perp}$. The calculated ρ_{Poly} was found to be in good agreement with experiment for both Zn and Tl. The qualitative behaviour of the resistivity ratio $\rho_{\parallel}/\rho_{\perp}$ was found to be the same for

all cases considered. At high temperatures the ratio is approximately constant and greater than unity. As the temperature is lowered, $\rho_{\parallel}/\rho_{\perp}$ increases monotonically to a maximum value at $\approx$ 25°K in Zn and $\approx$ 13°K in Tl. A further decrease in temperature results in a sharp drop in the resistivity ratio. This behaviour has been experimentally observed in zinc; and we emphasize that it appears to be a direct result of phonon anisotropy.

The resistivities ρ_{Poly}, $\rho_{\parallel}$ and $\rho_{\perp}$ were also calculated using the variational approach. The scattering time and variational polycrystalline resistivity formulae are in direct correspondence, except that the Fermi surface averages are taken to be $\langle\tau(\underline{k})\rangle^{-1}$ and $\langle\tau^{-1}(\underline{k})\rangle$ respectively. The variational average, while incorrect, involves a much smaller investment in computer time; however, we have observed that it will tend to overestimate the low temperature ρ_{Poly}. The resistivity ratios were also calculated, and they were found to be qualitatively the same as the scattering time results.

As stated earlier the two Tl pseudopotentials tend to give very similar results for most properties, including the qualitative behaviour of the resistivity ratios. However, the quantitative $\rho_{\parallel}/\rho_{\perp}$ results are quite different. For example, the low temperature maxima are $\approx$ 1.10 for the Tl(0.875) model and $\approx$ 1.03 for the Tl(0.435) model.

For comparison purposes most of the zinc calculations were repeated with another set of force constants (DWL), which were based on less extensive phonon data. In general, the DWL model gave low frequency phonon branches which were higher than both experiment and the MEPM model results. It was found that, for all properties calculated in this thesis, the DWL model did not give as good agreement with experiment as the MEPM model did. Comparison of the results for these two force constant models illustrates the importance of the low frequency phonon branches in phonon anisotropy effects.

REFERENCES

(1) H. K. Onnes, Commun. Phys. Lab. Univ. Leiden, No. 119b (1911).

(2) W. Meissner and R. Ochsenfeld, Naturwissenschaften 21, 787 (1933).

(3) C. J. Gorter and H. Casimir, Physica 1, 306 (1934).

(4) H. London and F. London, Proc. Roy. Soc. (London) A149, 71 (1935).

(5) V. L. Ginzburg and L. D. Landau, Zh. Eksperim. i Theor. Fiz. 20, 1064 (1950).

(6) A. B. Pippard, Proc. Roy. Soc. (London) A216, 547 (1953).

(7) H. Fröhlich, Phys. Rev. 79, 845 (1950).

(8) E. Maxwell, Phys. Rev. 78, 477 (1950).

(9) C. A. Reynolds, B. Serin, W. H. Wright and L. B. Nesbitt, Phys. Rev. 78, 487 (1950).

(10) W. S. Corak and C. B. Satterthwaite, Phys. Rev. 102, 662 (1956).

(11) W. S. Corak, B. B. Goodman, C. B. Satterthwaite and A. Wexler, Phys. Rev. 102, 656 (1956).

(12) L. N. Cooper, Phys. Rev. 104, 1189 (1956).

(13) J. Bardeen, L. N. Cooper and J. R. Schrieffer, Phys. Rev. 108, 1175 (1957).

(14) R. Meservey and B. B. Schwartz, in Superconductivity, edited by R. D. Parks (Marcel Dekker, Inc., New York, 1969).

(15) D. M. Ginsberg and L. C. Hebel, in Superconductivity, edited by R. D. Parks (Marcel Dekker, Inc., New York, 1969).

(16) I. Giaever, Phys. Rev. Letters 5, 147 (1960).

(17) I. Giaever, H. R. Hart, Jr. and K. Megerle, Phys. Rev. 126, 941 (1962).

(18) J. M. Rowell, P. W. Anderson and D. E. Thomas, Phys. Rev. Letters 10, 334 (1963).

(19) W. L. McMillan and J. M. Rowell, Phys. Rev. Letters 14, 108 (1965).

(20) W. L. McMillan and J. M. Rowell, in Superconductivity, edited by R. D. Parks (Marcel Dekker, Inc., New York, 1969).

(21) C. B. Duke, Tunneling in Solids, (Academic Press, Inc., New York, 1969).

(22) G. M. Eliashberg, Zh. Eksperim. i Teor. Fiz. 38, 966 (1960); Soviet Phys. JETP 11, 696 (1960).

(23) Y. Nambu, Phys. Rev. 117, 648 (1960).

(24) P. Morel and P. W. Anderson, Phys. Rev. 125, 1263 (1962).

(25) D. J. Scalapino, J. R. Schrieffer and J. W. Wilkins, Phys. Rev. 148, 263 (1966).

(26) A. B. Migdal, Zh. Eksperim. i Teor. Fiz. 34, 1438 (1958); Soviet Phys. JETP 7, 996 (1958).

(27) L. P. Gor'kov, Zh. Eksperim. i Teor. Fiz. 34, 735 (1958); Soviet Phys. JETP 7, 505 (1958).

(28) J. R. Schrieffer, Theory of Superconductivity, (W. A. Benjamin, Inc., New York, 1964).

(29) Both theoretical and experimental aspects are discussed in the two volume set Superconductivity, edited by R. D. Parks (Marcel Dekker, Inc., New York, 1969).

(30) V. Ambegaokar and J. Woo, Phys. Rev. 139, A1818 (1965).

(31) D. J. Scalapino, Y. Wada and J. C. Swihart, Phys. Rev. Letters 14, 102 (1965).

(32) J. C. Swihart, D. J. Scalapino and Y. Wada, Phys. Rev. Letters 14, 106 (1965).

(33) T. M. Wu, Phys. Rev. Letters 19, 508 (1967).

(34) J. P. Carbotte and R. C. Dynes, Phys. Letters 25A, 685 (1967).

(35) W. L. McMillan, Phys. Rev. 167, 331 (1968).

(36) J. P. Carbotte and R. C. Dynes, Phys. Rev. 172, 476 (1968).

(37) R. C. Dynes, J. P. Carbotte, D. W. Taylor and C. K. Campbell, Phys. Rev. 178, 713 (1969).

(38) P. B. Allen and M. L. Cohen, Phys. Rev. 187, 525 (1969).

(39) G. I. Rochlin, Phys. Rev. 153, 513 (1967).

(40) B. L. Blackford, Ph.D. Thesis, Dalhousie University, Halifax, Nova Scotia, Canada (unpublished) (1969).

(41) N. V. Zavaritskii, Zh. Eksperim. i Teor. Fiz. 43, 1123 (1962); Soviet Phys. JETP 16, 793 (1963).

(42) N. V. Zavaritskii, Zh. Eksperim. i Teor. Fiz. 48, 837 (1965); Soviet Phys. JETP 21, 557 (1965).

(43) V. L. Pokrovskii, Zh. Eksperim. i Teor. Fiz. 40, 641 (1961); Soviet Phys. JETP 13, 447 (1961).

(44) D. Markowitz and L. P. Kadanoff, Phys. Rev. 131, 563 (1963).

(45) B. T. Geilikman and V. Z. Kresin, Zh. Eksperim. i Teor. Fiz. 40, 970 (1961); Soviet Phys. JETP 13, 677 (1961).

(46) A. J. Bennett, Phys.Rev. 140, A1902 (1965).

(47) A. J. Bennett, Phys. Rev. 153, 482 (1967).

(48) J. F. Balsley, Ph.D. Thesis, Indiana University, Bloomington, Indiana, U.S.A. (unpublished) (1969).

(49) J. F. Balsley and J. C. Swihart, Low Temperature Physics, LT12 (editor E. Kanda), Keigaku, Tokyo, (1971); Section B, p. 303.

(50) C. R. Leavens and J. P. Carbotte, Solid State Commun. 9, 75 (1971).

(51) C. R. Leavens and J. P. Carbotte, Annals of Physics, April (1972).

(52) M. Born and K. Huang, Dynamical Theory of Crystal Lattices (Oxford University Press, 1954).

(53) E. Ducla-Soares and J. D. N. Cheeke, Low Temperature Physics, LT12 (editor E. Kanda), Keigaku, Tokyo, (1971); Section B, p. 305.

(54) R. W. Stark and L. M. Falicov, Phys. Rev. Letters 19, 795 (1967).

(55) D. L. McDonald, M. M. Elcombe and A. W. Pryor, J. Phys. C: Solid St. Phys. 2, 1857 (1969).

(56) T. D. Clark, J. Phys. C: Solid St. Phys. 1, 732 (1968).

(57) R. C. Dynes, Phys. Rev. B2, 644 (1970).

(58) T. G. Worlton and R. E. Schmunk, Phys. Rev. B3, 4115 (1971).

(59) D. J. Scalapino, in Superconductivity, edited by R. D. Parks (Marcel Dekker, Inc., New York, 1969).

(60) B. N. Brockhouse, E. D. Hallman and S. C. Ng, in Magnetic and Inelastic Scattering of Neutrons by Metals, edited by T. J. Rowland and P. A. Beck (Gordon and Breach Science Publishers, Inc., New York, 1969).

(61) L. J. Sham and J. M. Ziman, Solid State Phys. 15, 221 (1963).

(62) A. A. Maradudin, E. W. Montroll and G. H. Weiss, Theory of Lattice Dynamics in the Harmonic Approximation (Academic Press Inc., New York, 1963).

(63) A. A. Maradudin and S. H. Vosko, Reviews of Mod. Phys. 40, 1 (1968).

(64) R. C. Dynes and J. P. Carbotte, Phys. Rev. 175, 913 (1968).

(65) B. N. Brockhouse, T. Arase, G. Caglioti, K. R. Rao and A. D. B. Woods, Phys. Rev. 128, 1099 (1962).

(66) H. F. Bezdek and L. Finegold, Phys. Rev. B4, 1390 (1971).

(67) R. C. Dynes, J. P. Carbotte and E. J. Woll Jr., Solid State Commun. 6, 101 (1968).

(68) R. Stedman, L. Almqvist and G. Nilsson, Phys. Rev. 162, 549 (1967).

(69) W. A. Harrison, Pseudopotentials in the Theory of Metals (W. A. Benjamin, Inc., New York, 1966).

(70) V. Heine, Solid State Phys. 24, 1 (1970).

(71) J. C. Phillips, Phys. Rev. 112, 685 (1958).

(72) J. C. Phillips and L. Kleinman, Phys. Rev. 116, 287 (1959).

(73) M. H. Cohen and V. Heine, Phys. Rev. 122, 1821 (1961).

(74) J. M. Ziman, Principles of the Theory of Solids (Cambridge University Press, 1964).

(75) M. L. Cohen and V. Heine, Solid State Phys. 24, 37 (1970).

(76) G. F. Koster, Solid State Phys. 5, 173 (1957).

(77) R. E. DeWames, T. Wolfram and G. W. Lehman, Phys. Rev. 138, A717 (1965).

(78) L. J. Slutsky and C. S. Garland, J. Chem. Phys. 26, 787 (1957).

(79) M. F. Collins, Proc. Phys. Soc. (London) 80, 362 (1962).

(80) G. W. Lehman, T. Wolfram and R. E. DeWames, Phys. Rev. 128, 1593 (1962).

(81) T. Wolfram, G. W. Lehman and R. E. DeWames, Phys. Rev. 129, 2483 (1963).

(82) G. Gilat and L. J. Raubenheimer, Phys. Rev. 144, 390 (1966).

(83) L. J. Raubenheimer and G. Gilat, Phys. Rev. 157, 586 (1967).

(84) L. J. Raubenheimer and G. Gilat, South African Atomic Energy Board Rep., No. PEL-178, (1968).

(85) Z. Kam and G. Gilat, Phys. Rev. 175, 1156 (1968).

(86) R. J. Higgins, J. A. Marcus and D. H. Whitmore, Phys. Rev. 137, A1172 (1965).

(87) Y. Ishizawa and W. R. Datars, Phys. Rev. B2, 3875 (1970).

(88) P. Soven, Phys. Rev. 137, A1706 (1965); 137, A1717 (1965).

(89) C. Kittel, Introduction to Solid State Physics (John Wiley and Sons, Inc., New York, 1966) p.209.

(90) P. B. Allen, M. L. Cohen, L. M. Falicov and R. V. Kasowski, Phys. Rev. Letters 21, 1794 (1968).

(91) E. Pytte, J. Phys. Chem. Solids 28, 93 (1967).

(92) P. B. Allen and M. L. Cohen, Phys. Rev. B1, 1329 (1970).

(93) P. B. Allen, private communication.

(94) T. M. Rice, Phys. Rev. 175, 858 (1968).

(95) C. W. Garland and J. Silverman, J. Chem. Phys. 34, 781 (1961).

(96) G. Seidel and P. H. Keesom, Phys. Rev. 112, 1083 (1958).

(97) N. E. Phillips, Phys. Rev. Letters 1, 363 (1958).

(98) J. M. Rowell and R. C. Dynes, in Phonons, edited by M. Nusimovici (Richard Abel and Co., Portland, Oregon, 1971).

(99) L. Almqvist and R. Stedman, J. Phys. F: Metal Phys. 1, 785 (1971).

(100) H. Lipson and A. R. Stokes, Nature 148, 437 (1941).

(101) B. J. C. van der Hoeven, Jr. and P. H. Keesom, Phys. Rev. 135, A631 (1964).

(102) R. C. Dynes, private communication.

(103) A. O. E. Animalu and V. Heine, Phil. Mag. 12, 1249 (1965).

(104) V. Heine and I. Abarenkov, Phil. Mag. 9, 451 (1964).

(105) N. W. Ashcroft, Phys. Letters 23, 48 (1966).

(106) P. M. Holtham and M. G. Priestley, J. Phys. F: Metal Phys. 1, 621 (1971).

(107) C. R. Leavens and J. P. Carbotte, Canadian J. Phys. 49, 724 (1971).

(108) R. E. Fassnacht and J. R. Dillinger, Phys. Rev. 164, 565 (1967).

(109) P. W. Anderson, J. Phys. Chem. Solids 11, 26 (1959).

(110) E. A. Lynton, B. Serin and M. Zucker, J. Phys. Chem. Solids 3, 165 (1957).

(111) G. Chanin, E. A. Lynton and B. Serin, Phys. Rev. 114, 719 (1959).

(112) D. P. Seraphim, C. Chiou and D. J. Quinn, Acta Met. 9, 861 (1961).

(113) R. I. Gayley, Jr., E. A. Lynton and B. Serin, Phys. Rev. 126, 43 (1962).

(114) J. R. Clem, Annals of Physics 40, 268 (1966).

(115) N. V. Zavaritskii, Zh. Eksperim. i Teor. Fiz. 39, 1193 (1960); Soviet Phys. JETP 12, 831 (1961).

(116) D. A. Hays, Phys. Rev. B1, 3631 (1970).

(117) M. J. Lea and E. R. Dobbs, Phys. Letters 27A, 556 (1968).

(118) J. P. Carbotte and P. T. Truant, Canadian J. Phys. March (1972).

(119) H. J. Willard, Jr., R. W. Shaw and G. L. Salinger, Phys. Rev. 175, 362 (1968).

(120) G. Grimvall, J. Phys. Chem. Solids 29, 1221 (1968).

(121) S. Nakajima and M. Watabe, Prog. Theor. Phys. 29, 341 (1963).

(122) S. Nakajima and M. Watabe, Prog. Theor. Phys. 30, 772 (1963).

(123) J. W. Wilkins, Observable Many-Body Effects in Metals, (Nordita, Copenhagen, 1968).

(124) J. J. Sabo, Jr., Phys. Rev. B1, 1325 (1970).

(125) P. Goy, Phys. Letters 31A, 584 (1970).

(126) R. G. Poulsen and W. R. Datars, Solid State Commun. 8, 1969 (1970).

(127) S. H. Choh and W. R. Datars, Physics in Canada 27, 62 (1971).

(128) M. P. Shaw, P. I. Sampath and T. G. Eck, Phys. Rev. 142, 399 (1966).

(129) M. P. Shaw, T. G. Eck and D. A. Zych, Phys. Rev. 142, 406 (1966).

(130) P. L. Taylor, Proc. Roy. Soc. (London) A275, 200 (1963).

(131) J. M. Ziman, Electrons and Phonons (Oxford University Press, 1960).

(132) J. E. Robinson and J. D. Dow, Phys. Rev. 171, 815 (1968).

(133) B. Hayman and J. P. Carbotte, accepted for publication, J. Phys. F: Metal Phys. (1972).

(134) M. Springford, Advances in Phys. 20, 493 (1971).

(135) T. L. Martin, Jr. and W. F. Leonard, Electrons and Crystals, (Brooks/Cole Publishing Co., Belmont, California, 1970).

(136) E. Borchi, S. De Gennaro and P. L. Tasselli, private communication.

(137) G. T. Meaden, Electrical Resistance of Metals, (Plenum Press, New York, 1965).

(138) P. B. Allen, Phys. Rev. B3, 305 (1971).

(139) B. Hayman and J. P. Carbotte, Canadian J. Phys. 49, 1952 (1971).

(140) R. W. Meyerhoff and J. F. Smith, J. Applied Phys. 33, 219 (1962).

(141) P. L. Taylor, A Quantum Approach to the Solid State (Prentice-Hall, Inc., Englewood Cliffs, New Jersey, 1970).

(142) M. P. Greene and W. Kohn, Phys. Rev. 137, A513 (1965).

(143) E. Grüneisen and E. Goens, Z. Physik 26, 250 (1924).

(144) W. Meissner, Z. Physik 38, 647 (1926).

(145) B. N. Aleksandrov and I. G. D'Yakov, Zh. Eksperim. i Teor. Fiz. 43, 852 (1962); Soviet Phys. JETP 16, 603 (1963).

(146) S. K. Case and J. E. Gueths, Phys. Rev. B2, 3843 (1970).

APPENDIX

ONE OPW LOW FREQUENCY RENORMALIZATION

As discussed in section 3.2, for certain $\underline{k}$ directions the one OPW coupling constant $\alpha^2(\omega,\underline{k})$ artificially diverges as ω approaches zero. This leads to an approximate linear behaviour of the low frequency region of the Fermi surface average $\alpha^2F(\omega)$. There is some evidence to suggest that this region should actually vary quadratically with ω. Allen and Cohen [92] have proposed a simple method for removing this difficulty. They suggest that the lowest $1/5^{th}$ of the $\alpha^2F(\omega)$ spectrum should be multiplied by $5\omega/\omega_c$, where ω_c is the maximum phonon frequency. Throughout this thesis we follow their suggestion, with the minor modifications discussed below, and apply this renormalization to all isotropic and directional phonon distribution functions.

The zinc MEPM force constant model displays the most anisotropy of the four models (two Zn and two Tl) considered in this work. Thus, this should be the most sensitive test of the low frequency renormalization.

The contribution to the $0 \leq \omega \leq \omega_c/5$ region for the zinc MEPM model is made up of three parts:

a) normal processes,

b) umklapp processes of large reduced momentum transfer, which occur in the region of the

H-point where the lowest frequency is less than $\omega_c/5$ (figure 3.3.4),

c) umklapp processes of small reduced momentum transfer, which cause the divergence of the one OPW coupling constant.

These three contributions were separated and only the umklapp processes of small reduced momentum transfer were renormalized in this region.

Three renormalizations were considered: multiplication by $5\omega/\omega_c$ which has been used throughout this thesis, multiplication by $(5\omega/\omega_c)^2$, and the final form considered was to take the unrenormalized α^2F and set the lowest 1% of the spectrum equal to zero. The superconducting results given by the three renormalizations are shown in table A.1.

It is apparent from these results that the particular method of renormalization chosen is not important. This is reasonable since the strongest weight given to the low frequencies is much weaker than ω^{-2}, and the low ω regions will not be important as long as they show roughly the correct behaviour.

Because of the insensitivity of the MEPM results to the low frequency renormalization, the DWL phonon distribution functions were renormalized by multiplying by $5\omega/\omega_c$ in the region $0 \leq \omega \leq \omega_c/5$. We note that for the DWL force constant model there are no large reduced momentum contributions to this region.

TABLE A.1

COMPARISON OF ZINC SUPERCONDUCTING PARAMETERS CALCULATED WITH THE "MEPM" FORCE CONSTANTS FOR THREE DIFFERENT LOW FREQUENCY RENORMALIZATIONS

PARAMETER	Zn(MEPM) $\left(\frac{5\omega}{\omega_c}\right)$	Zn(MEPM) $\left(\frac{5\omega}{\omega_c}\right)^2$	Zn(MEPM)*
λ	0.425	0.416	0.448
$\overline{\lambda}$	0.599	0.577	0.664
μ^*	0.086	0.083	0.094
Δ_0^{IT}	0.1295	0.1294	0.1299
β	0.435	0.439	0.425
m^*	0.84	0.84	0.85
$\langle a^2 \rangle$	0.014	0.014	0.015
$\langle ab \rangle$	0.015	0.015	0.016
$\langle a\overline{b} \rangle$	0.019	0.020	0.022
T_c^{PSC}/T_c	1.06	1.06	1.06
$\langle \Delta_0(\underline{k}) \rangle / \Delta_0$	1.03	1.03	1.03

* The lowest 1% of the α^2F spectrum is set equal to zero for this column.

Similarly for the thallium models, the low frequency regions $0 \leq \omega \leq \omega_c/4$ were multiplied by $4\omega/\omega_c$. The Tl renormalization was extended to 1/4 of the frequency range because this seemed to be indicated upon comparison with the experimental $\alpha^2F(\omega)$.

It should be mentioned that the very low temperature scattering times will show some sensitivity to this renormalization because the thermal factors are strongly peaked at the origin and the distribution functions will be heavily weighted in the renormalization region. A multiple OPW calculation would be needed to accurately calculate these quantities for very low temperatures, and this is beyond the scope of this work.